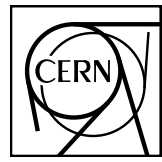


# EUROPEAN ORGANIZATION FOR NUCLEAR RESEARCH



ALICE-ANA-2018-xxx  
February 25, 2019

## **$\Lambda K$ and $\Xi^- K^\pm$ Femtoscopy in Pb-Pb Collisions at $\sqrt{s_{NN}} = 2.76$ TeV from the LHC ALICE Experiment**

Jesse T. Buxton<sup>1</sup>

1. Department of Physics, The Ohio State University, Columbus, Ohio, USA

Email: jesse.thomas.buxton@cern.ch

### **Abstract**

I present the first femtoscopic analysis of  $\Lambda K$  correlations in Pb-Pb collisions at  $\sqrt{s_{NN}} = 2.76$  TeV measured by the ALICE experiment at the Large Hadron Collider (LHC). All pair combinations of  $\Lambda$  and  $\bar{\Lambda}$  with  $K^+$ ,  $K^-$  and  $K_S^0$  are analyzed. The femtoscopic correlations result from strong final-state interactions, and are fit with a parametrization allowing us to both characterize the emission source and measure the scattering parameters for the particle pairs. We observe a large difference in the  $\Lambda K^+$  and  $\Lambda K^-$  correlations in pairs with low relative momenta ( $k^* \lesssim 100$  MeV/c). This might suggest an effect arising from different quark-antiquark interactions within the pairs ( $s\bar{s}$  in  $\Lambda K^+$  and  $u\bar{u}$  in  $\Lambda K^-$ ), or from different net strangeness for each system. To gain further insight into this hypothesis, we are currently conducting a  $\Xi^- K^\pm$  femtoscopic analysis, for which I present preliminary results.



## Contents

<b>1</b>	<b>Introduction</b>	<b>7</b>
<b>2</b>	<b>Data Sample and Software</b>	<b>7</b>
2.1	Data Sample . . . . .	7
2.2	Software . . . . .	7
<b>3</b>	<b>Data Selection</b>	<b>7</b>
3.1	Event Selection and Mixing . . . . .	7
3.2	$K^\pm$ Track Selection . . . . .	8
3.3	V0 Selection . . . . .	8
3.4	General V0 Reconstruction . . . . .	8
3.4.1	$\Lambda$ Reconstruction . . . . .	11
3.4.2	$K_S^0$ Reconstruction . . . . .	13
3.5	V0 Purity Estimation . . . . .	15
3.6	V0 Purity Background Estimation . . . . .	15
3.7	$\Xi$ Reconstruction . . . . .	16
3.8	Pair Selection . . . . .	18
<b>4</b>	<b>Correlation Functions</b>	<b>22</b>
4.1	Typical Correlation Function Construction . . . . .	22
4.2	Stavinskiy Correlation Function Construction . . . . .	24
<b>5</b>	<b>Fitting</b>	<b>27</b>
5.1	Model: $\Lambda K_S^0$ , $\Lambda K^\pm$ , $\Xi^- K_S^0$ . . . . .	27
5.2	Model: $\Xi^- K^\pm$ . . . . .	27
5.3	Momentum Resolution Corrections . . . . .	28
5.4	Residual Correlations . . . . .	33
5.5	Non-Flat Background . . . . .	41
5.6	LednickyFitter . . . . .	44
5.7	Coulomb Fitter . . . . .	47
<b>6</b>	<b>Systematic Errors</b>	<b>48</b>
6.1	Systematic Errors: $\Lambda K_S^0$ . . . . .	48
6.1.1	Particle and Pair Cuts . . . . .	48

6.1.2	Non-Flat Background . . . . .	48
6.1.3	Fit Range . . . . .	48
6.2	Systematic Errors: $\Lambda K^\pm$ . . . . .	49
6.2.1	Particle and Pair Cuts . . . . .	49
6.2.2	Non-Flat Background . . . . .	49
6.2.3	Fit Range . . . . .	49
6.3	Systematic Errors: $\Xi K^\pm$ . . . . .	49
6.3.1	Particle and Pair Cuts . . . . .	49
<b>7</b>	<b>Results and Discussion</b>	<b>51</b>
7.1	Results: $\Lambda K_S^0$ and $\Lambda K^\pm$ . . . . .	51
7.1.1	3 Residual Correlations Included in Fit . . . . .	52
7.1.2	10 Residual Correlations Included in Fit . . . . .	59
7.1.3	No Residual Correlations Included in Fit . . . . .	66
7.1.4	Fit Method Comparisons . . . . .	72
7.1.5	Discussion of $m_T$ -Scaling . . . . .	77
7.2	Results: $\Xi K^\pm$ . . . . .	82
<b>8</b>	<b>To Do</b>	<b>83</b>
<b>9</b>	<b>Additional Figures</b>	<b>88</b>
9.1	Residuals . . . . .	88
9.1.1	$\Lambda K^+$ Residuals . . . . .	88
9.1.2	$\Lambda K^-$ Residuals . . . . .	94
9.1.3	$\Lambda K_S^0$ Residuals . . . . .	100
9.2	Spherical Harmonics . . . . .	106

## List of Figures

1	V0 Reconstruction	10
2	$K_S^0$ contamination in $\Lambda(\bar{\Lambda})$ collection	13
3	$\Lambda(\bar{\Lambda})$ contamination in $K_S^0$ collection	14
4	$V0(\Lambda, \bar{\Lambda}, K_S^0)$ Purities	16
5	V0 Purity Background Estimation	17
6	$\Xi$ Reconstruction	17
7	$\Xi^-(\bar{\Xi}^+)$ Purity	18
8	Average Separation of $\Lambda(\bar{\Lambda})$ and $K_S^0$ Daughters	20
9	Average Separation of $\Lambda(\bar{\Lambda})$ Daughter and $K^\pm$	20
10	Average Separation of $\Xi$ Daughters and $K^\pm$	21
11	$\Lambda K$ Correlation Functions	23
12	Correlation Functions: $\Lambda K^+$ vs $\Lambda K^-$ for 0-10% Centrality	23
13	$\Lambda K$ Stavinskiy Correlation Functions (Correct)	25
14	$\Lambda K$ Stavinskiy Correlation Functions (Correct and Incorrect)	26
15	Momentum Resolution: Sample $k_{\text{True}}^*$ vs. $k_{\text{Rec}}^*$	29
16	Particle Contaminations Visible in $k_{\text{True}}^*$ vs. $k_{\text{Rec}}^*$	30
17	Momentum Resolution Corrections: Methods Comparison	32
18	Residual Contributions Cartoon	33
19	Sample Transform Matrices for $\Lambda K^+$ Analysis	34
20	Sample Transform Matrices for $\bar{\Lambda} K^+$ Analysis	35
21	Reconstruction Efficiencies	36
22	$\Sigma^0 K^+$ Transform	39
23	$\Lambda K^{*0}$ Transform	40
24	Compare Non-Femtoscopic Backgrounds	41
25	Backgrounds with THERMINATOR, $K_S^0$ Tweak	42
26	Backgrounds with THERMINATOR	43
27	Correlation with background decomposition (THERM)	44
28	Background reduction methods with THERMINATOR	45
29	Extracted Scattering Parameters: 3 Residuals in Fit	52
30	$m_T$ Scaling of Radii: 3 Residuals in Fit	52
31	$\Lambda(\bar{\Lambda}) K_S^0$ Fits with 3 Residuals	53
32	$\Lambda K^+(\bar{\Lambda} K^-)$ Fits with 3 Residuals	54

33	$\Lambda K^- (\bar{\Lambda} K^+)$ Fits with 3 Residuals . . . . .	55
34	$\Lambda (\bar{\Lambda}) K_S^0$ Fits showing 3 Residuals . . . . .	56
35	$\Lambda K^+ (\bar{\Lambda} K^-)$ and $\Lambda K^- (\bar{\Lambda} K^+)$ Fits with 3 Residuals . . . . .	57
36	Extracted Scattering Parameters: 3 Residuals in Fit . . . . .	59
37	$m_T$ Scaling of Radii: 10 Residuals in Fit . . . . .	59
38	$\Lambda K_S^0 (\bar{\Lambda} K_S^0)$ Fits with 10 Residuals . . . . .	60
39	$\Lambda K^+ (\bar{\Lambda} K^-)$ Fits with 10 Residuals . . . . .	61
40	$\Lambda K^- (\bar{\Lambda} K^+)$ Fits with 10 Residuals . . . . .	62
41	$\Lambda (\bar{\Lambda}) K_S^0$ Fits showing 10 Residuals . . . . .	63
42	$\Lambda K^+ (\bar{\Lambda} K^-)$ and $\Lambda K^- (\bar{\Lambda} K^+)$ Fits with 10 Residuals . . . . .	64
43	Extracted Scattering Parameters: No Residuals in Fit . . . . .	66
44	$m_T$ Scaling of Radii: No Residuals in Fit . . . . .	67
45	$\Lambda K_S^0 (\bar{\Lambda} K_S^0)$ Fits with No Residuals . . . . .	68
46	$\Lambda K^+ (\bar{\Lambda} K^-)$ Fits, with NO residual correlations included, with No Residuals . . . . .	69
47	$\Lambda K^- (\bar{\Lambda} K^+)$ Fits with No Residuals . . . . .	70
48	Compare Fit Parameters: Background treatment . . . . .	72
49	Compare Fit Parameters: Number of residuals . . . . .	73
50	Compare Fit Parameters: Free vs fixed $\lambda$ . . . . .	74
51	Compare Fit Parameters: Shared vs unique $\lambda$ . . . . .	75
52	Compare Fit Parameters: Shared vs. Separate Radii . . . . .	76
53	$m_T$ Scaling of Radii: 3 Residuals in Fit (with individual $m_T$ highlighted) . . . . .	77
54	$\Lambda K^+ C_{00}$ and $\Re C_{11}$ Spherical Harmonic Components (0-10%) . . . . .	79
55	Short Overall . . . . .	80
56	Short Caption . . . . .	81
57	Short Caption . . . . .	81
58	$\Xi K^\pm$ Results . . . . .	82
59	$\Xi K^\pm$ Data with Coulomb-Only Bands, 0-10% Centrality . . . . .	83
60	Effect of Strong Force Inclusion on Coulomb-Only Curve for $\Xi K^\pm$ systems . . . . .	84
61	$\Xi K^\pm$ Global Coulomb-Only Fit (Set 1) . . . . .	85
62	$\Xi K^\pm$ Global Coulomb-Only Fit (Set 2) . . . . .	86
63	$\Xi^- K^+$ Coulomb-Only Fit . . . . .	86
64	$\Xi^- K^-$ Coulomb-Only Fit . . . . .	87
65	Residuals: $\Sigma^0 K^+$ to $\Lambda K^+$ (0-10% Centrality) . . . . .	88

66	Residuals: $\Xi^0 K^+$ to $\Lambda K^+$ (0-10% Centrality) . . . . .	89
67	Residuals: $\Xi^- K^+$ to $\Lambda K^+$ (0-10% Centrality) . . . . .	89
68	Residuals: $\Sigma^{*+} K^+$ to $\Lambda K^+$ (0-10% Centrality) . . . . .	90
69	Residuals: $\Sigma^{*-} K^+$ to $\Lambda K^+$ (0-10% Centrality) . . . . .	90
70	Residuals: $\Sigma^{*0} K^+$ to $\Lambda K^+$ (0-10% Centrality) . . . . .	91
71	Residuals: $\Lambda K^{*0}$ to $\Lambda K^+$ (0-10% Centrality) . . . . .	91
72	Residuals: $\Sigma^0 K^{*0}$ to $\Lambda K^+$ (0-10% Centrality) . . . . .	92
73	Residuals: $\Xi^0 K^{*0}$ to $\Lambda K^+$ (0-10% Centrality) . . . . .	92
74	Residuals: $\Xi^- K^{*0}$ to $\Lambda K^+$ (0-10% Centrality) . . . . .	93
75	Residuals: $\Sigma^0 K^-$ to $\Lambda K^-$ (0-10% Centrality) . . . . .	94
76	Residuals: $\Xi^0 K^-$ to $\Lambda K^-$ (0-10% Centrality) . . . . .	95
77	Residuals: $\Xi^- K^-$ to $\Lambda K^-$ (0-10% Centrality) . . . . .	95
78	Residuals: $\Sigma^{*+} K^-$ to $\Lambda K^-$ (0-10% Centrality) . . . . .	96
79	Residuals: $\Sigma^{*-} K^-$ to $\Lambda K^-$ (0-10% Centrality) . . . . .	96
80	Residuals: $\Sigma^{*0} K^-$ to $\Lambda K^-$ (0-10% Centrality) . . . . .	97
81	Residuals: $\Lambda \bar{K}^{*0}$ to $\Lambda K^-$ (0-10% Centrality) . . . . .	97
82	Residuals: $\Sigma^0 \bar{K}^{*0}$ to $\Lambda K^-$ (0-10% Centrality) . . . . .	98
83	Residuals: $\Xi^0 \bar{K}^{*0}$ to $\Lambda K^-$ (0-10% Centrality) . . . . .	98
84	Residuals: $\Xi^- \bar{K}^{*0}$ to $\Lambda K^-$ (0-10% Centrality) . . . . .	99
85	Residuals: $\Sigma^0 K_S^0$ to $\Lambda K_S^0$ (0-10% Centrality) . . . . .	100
86	Residuals: $\Xi^0 K_S^0$ to $\Lambda K_S^0$ (0-10% Centrality) . . . . .	101
87	Residuals: $\Xi^- K_S^0$ to $\Lambda K_S^0$ (0-10% Centrality) . . . . .	101
88	Residuals: $\Sigma^{*+} K_S^0$ to $\Lambda K_S^0$ (0-10% Centrality) . . . . .	102
89	Residuals: $\Sigma^{*-} K_S^0$ to $\Lambda K_S^0$ (0-10% Centrality) . . . . .	102
90	Residuals: $\Sigma^{*0} K_S^0$ to $\Lambda K_S^0$ (0-10% Centrality) . . . . .	103
91	Residuals: $\Lambda K^{*0}$ to $\Lambda K_S^0$ (0-10% Centrality) . . . . .	103
92	Residuals: $\Sigma^0 K^{*0}$ to $\Lambda K_S^0$ (0-10% Centrality) . . . . .	104
93	Residuals: $\Xi^0 K^{*0}$ to $\Lambda K_S^0$ (0-10% Centrality) . . . . .	104
94	Residuals: $\Xi^- K^{*0}$ to $\Lambda K_S^0$ (0-10% Centrality) . . . . .	105
95	$\Lambda K^+$ $C_{00}$ and $\Re C_{11}$ Spherical Harmonic Components . . . . .	106
96	$\Lambda K^+$ First Six Components of Spherical Harmonic Decomposition (0-10%) . . . . .	107
97	$\Lambda K^-$ $C_{00}$ and $\Re C_{11}$ Spherical Harmonic Components . . . . .	108
98	$\Lambda K^-$ First Six Components of Spherical Harmonic Decomposition (0-10%) . . . . .	109

99	$\Lambda K_S^0 C_{00}$ and $\Re C_{11}$ Spherical Harmonic Components . . . . .	110
100	$\Lambda K_S^0$ First Six Components of Spherical Harmonic Decomposition (0-10%) . . . . .	111

---

## 10 1 Introduction

11 We present results from a femtoscopic analysis of  $\Lambda K$  and  $\Xi^- K^\pm$  correlations in Pb-Pb collisions at  
 12  $\sqrt{s_{NN}} = 2.76$  TeV by the ALICE experiment at the LHC. All pair combinations of  $\Lambda$  and  $\bar{\Lambda}$  with  $K^+$ ,  
 13  $K^-$  and  $K_S^0$  are analyzed. The femtoscopic correlations are the result of strong final-state interactions,  
 14 and are fit with a parametrization based on a model by R. Lednicky and V. L. Lyuboshitz [1]. This  
 15 allows us to both characterize the emission source and measure the scattering parameters for the particle  
 16 pairs. We observe a large difference in the  $\Lambda K^+(\bar{\Lambda} K^-)$  and  $\Lambda K^-(\bar{\Lambda} K^+)$  correlations in pairs with low  
 17 relative momenta ( $k^* \lesssim 100$  MeV). The results suggest an effect arising from different quark-antiquark  
 18 interactions in the pairs, i.e.  $s\bar{s}$  in  $\Lambda K^+(\bar{\Lambda} K^-)$  and  $u\bar{u}$  in  $\Lambda K^-(\bar{\Lambda} K^+)$ , or from different net strangeness for  
 19 each system. To gain further insight into this hypothesis, we currently are conducting a  $\Xi K$  femtoscopic  
 20 analysis.

## 21 2 Data Sample and Software

### 22 2.1 Data Sample

23 The analysis used “pass 2” reconstructed Pb-Pb data from LHC11h (AOD145). The runlist was selected  
 24 from runs with global quality tag “1” in the ALICE Run Condition Table. Approximately 40 million  
 25 combined central, semi-central, and minimum bias events were analyzed. Runs from both positive (++)  
 26 and negative (--) magnetic field polarity settings were used.

27 Run list: 170593, 170572, 170388, 170387, 170315, 170313, 170312, 170311, 170309, 170308, 170306,  
 28 170270, 170269, 170268, 170230, 170228, 170207, 170204, 170203, 170193, 170163, 170159, 170155,  
 29 170091, 170089, 170088, 170085, 170084, 170083, 170081, 170040, 170027, 169965, 169923, 169859,  
 30 169858, 169855, 169846, 169838, 169837, 169835, 169591, 169590, 169588, 169587, 169586, 169557,  
 31 169555, 169554, 169553, 169550, 169515, 169512, 169506, 169504, 169498, 169475, 169420, 169419,  
 32 169418, 169417, 169415, 169411, 169238, 169167, 169160, 169156, 169148, 169145, 169144, 169138,  
 33 169099, 169094, 169091, 169045, 169044, 169040, 169035, 168992, 168988, 168826, 168777, 168514,  
 34 168512, 168511, 168467, 168464, 168460, 168458, 168362, 168361, 168342, 168341, 168325, 168322,  
 35 168311, 168310, 168315, 168108, 168107, 168105, 168076, 168069, 167988, 167987, 167985, 167920,  
 36 167915

37 Analysis was also performed on the LHC12a17a\_fix (AOD149) Monte Carlo HIJING events for certain  
 38 checks. THERMINATOR2 was also used for certain aspects, such as generation of transform matrices  
 39 describing feed-down contributions, estimation of  $\lambda$  parameters, and non-femtoscopic background  
 40 modeling.

### 41 2.2 Software

42 The analysis was performed on the PWGCF analysis train using AliRoot v5-09-29-1 and AliPhysics  
 43 vAN-20180505-1.

44 The main classes utilized include: AliFemtoVertexMultAnalysis, AliFemtoEventCutEstimators, AliFemto  
 45 toESDTrackCutNSigmaFilter, AliFemtoV0TrackCutNSigmaFilter, AliFemtoXiTrackCut, AliFemtoV0PairCut,  
 46 AliFemtoV0TrackPairCut, AliFemtoXiTrackPairCut, and AliFemtoAnalysisLambdaKaon. All of these  
 47 classes are contained in /AliPhysics/PWGCF/FEMTOSCOPY/AliFemto and .../AliFemtoUser.

## 48 3 Data Selection

### 49 3.1 Event Selection and Mixing

50 The events used in this study were selected with the class AliFemtoEventCutEstimators according to the  
 51 following criteria:

- Triggers
  - minimum bias (kMB)
  - central (kCentral)
  - semi-central (kSemiCentral)
- z-position of reconstructed event vertex must be within 10 cm of the center of the ALICE detector
- the event must contain at least one particle of each type from the pair of interest

The event mixing was handled by the AliFemtoVertexMultAnalysis class, which only mixes events with like vertex position and centrality. The following criteria were used for event mixing:

- Number of events to mix = 5
- Vertex position bin width = 2 cm
- Centrality bin width = 5

The AliFemtoEventReaderAODChain class is used to read the events. Event flattening is not currently used. FilterBit(7). The centrality is determined by the “V0M” method of AliCentrality, set by calling AliFemtoEventReaderAOD::SetUseMultiplicity(kCentrality). We utilize the SetPrimaryVertexCorrectionTPCPoints switch, which causes the reader to shift all TPC points to be relative to the event vertex.

### 3.2 $K^\pm$ Track Selection

Charged kaons are identified using the AliFemtoESDTrackCutNSigmaFilter class. The specific cuts used in this analysis are as follows:

The purity of the  $K^\pm$  collections was estimated using the HIJING MC data, for which the true identity of each reconstructed  $K^\pm$  particle is known. Therefore, the purity may be estimated as:

$$Purity(K^\pm) = \frac{N_{true}}{N_{reconstructed}} \quad (1)$$

Purity( $K^+$ )  $\approx$  Purity( $K^-$ )  $\approx$  97%

### 3.3 V0 Selection

#### 3.4 General V0 Reconstruction

$\Lambda(\bar{\Lambda})$  and  $K_S^0$  particles are electrically neutral, and cannot be directly detected, but must instead be reconstructed through detection of their decay products, or daughters. This process is illustrated in Figure 1, and the main cuts used are shown in Tables 2 and 3. In general, particles which are topologically reconstructed in this fashion are called V0 particles. The decay channel  $\Lambda \rightarrow p\pi^-$  was used for the identification of  $\Lambda$  hyperons (and, similarly the charge-conjugate decay for the  $\bar{\Lambda}$  identification), and  $K_S^0 \rightarrow \pi^+\pi^-$  for the identification of  $K_S^0$  mesons. The class AliFemtoV0TrackCutNSigmaFilter (which is an extension of AliFemtoV0TrackCut) is used to reconstruct the V0s.

To construct a V0 particle, the charged daughter tracks must first be found. Aside from typical kinematic and PID cuts (using TPC and TOF detectors), the daughter tracks are also exposed to a minimum cut on their impact parameter with respect to the primary vertex. The daughters of a V0 particle should not originate from the primary vertex, but rather from the decay vertex of the V0, hence the minimum cut imposition. The decay vertex of the V0 is assumed to be the point of closest approach between the

<b>K<sup>±</sup> selection</b>	
<b>Kinematic range</b>	
$ \eta $	< 0.8
$p_T$	$0.14 < p_T < 1.5 \text{ GeV}/c$
<b>Track quality and selection</b>	
FilterBit	7
Number of clusters in the TPC	> 80
$\chi^2/N_{DOF}$ for ITS clusters	< 3.0
$\chi^2/N_{DOF}$ for TPC clusters	< 4.0
XY impact parameter	< 2.4 cm
Z impact parameter	< 3.0 cm
Remove particles with any kink labels	true
N $\sigma$ to primary vertex	< 3.0
<b>K<sup>±</sup> identification</b>	
PID Probabilities	
K	> 0.2
$\pi$	< 0.1
$\mu$	< 0.8
p	< 0.1
Most probable particle type	Kaon (fMostProbable=3)
TPC and TOF N $\sigma$ Cuts	
$p < 0.4 \text{ GeV}/c$	$N_{\sigma K, \text{TPC}} < 2$
$0.4 < p < 0.45 \text{ GeV}/c$	$N_{\sigma K, \text{TPC}} < 1$
$0.45 < p < 0.80 \text{ GeV}/c$	$N_{\sigma K, \text{TPC}} < 3 \& N_{\sigma K, \text{TOF}} < 2$
$0.80 < p < 1.0 \text{ GeV}/c$	$N_{\sigma K, \text{TPC}} < 3 \& N_{\sigma K, \text{TOF}} < 1.5$
$p > 1.0 \text{ GeV}/c$	$N_{\sigma K, \text{TPC}} < 3 \& N_{\sigma K, \text{TOF}} < 1$
<b>Misidentification cuts</b>	
Electron Rejection	Reject if $N_{\sigma e^-, \text{TPC}} < 3$
Pion Rejection: Reject if:	
if TOF and TPC available	$N_{\sigma \pi, \text{TPC}} < 3 \& N_{\sigma \pi, \text{TOF}} < 3$
$p < 0.65 \text{ GeV}/c$	$p < 0.5 \text{ GeV}/c$
else	$N_{\sigma \pi, \text{TPC}} < 3$
	$0.5 < p < 0.65 \text{ GeV}/c$
	$N_{\sigma \pi, \text{TPC}} < 2$
$0.65 < p < 1.5 \text{ GeV}/c$	$N_{\sigma \pi, \text{TPC}} < 5 \& N_{\sigma \pi, \text{TOF}} < 3$
$p > 1.5 \text{ GeV}/c$	$N_{\sigma \pi, \text{TPC}} < 5 \& N_{\sigma \pi, \text{TOF}} < 2$

**Table 1:** K<sup>±</sup> selection

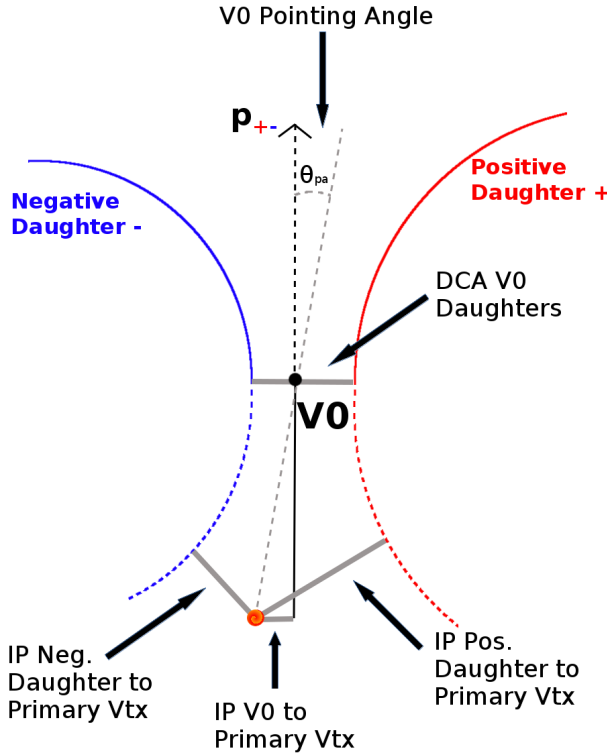


**Fig. 1:** V0 Reconstruction

daughter tracks. To help ensure quality, a maximum value cut is demanded on the distance-of-closest-  
approach between the daughters (DCA V0 Daughters). The positive and negative daughter tracks are  
combined to form the V0 candidate, the momentum of which is simply the sum of the momenta of the  
daughters (calculated at the DCA).

A minimum transverse momentum cut on the V0 candidate is introduced to reduce contamination from  
fake candidates. Opposite to that of the daughter tracks, the V0 candidate is exposed to a maximum cut  
on its impact parameter with respect to the primary vertex. In this case, we do want our V0 candidates  
to be primary, hence the maximum cut imposition. To further strengthen our selection of primary V0  
candidates, we impose a selection on the pointing angle,  $\theta_{pa}$ , between the V0 momentum and the vector  
pointing from the primary vertex to the secondary V0 decay vertex. We want the V0 candidate's momen-  
tum to point back to the primary decay vertex, and therefore a small  $\theta_{pa}$ ; we achieve this by appointing a  
minimum value on  $\cos(\theta_{pa})$  (“Cosine of pointing angle” in Tables 2 and 3).

On occasion,  $\Lambda(\bar{\Lambda})$  particles are misidentified as  $K_S^0$ , and vice versa. To attempt to remove these contam-  
inations without throwing away good candidates, we impose a set of misidentification cuts. The intent  
of these cuts is to judge whether a candidate is more likely a  $\Lambda(\bar{\Lambda})$  or a  $K_S^0$ , and are implemented as  
described below. For a given V0, we calculate the mass assuming different identities ( $\Lambda$ ,  $\bar{\Lambda}$ ,  $K_S^0$ ) of the  
candidate; the mass assuming  $K_S^0$  hypothesis ( $m_{\text{inv}, K_S^0 \text{ hyp.}}$ ) is calculated assuming  $\pi^+\pi^-$  daughters, the  
mass assuming  $\Lambda$  hypothesis ( $m_{\text{inv}, \Lambda \text{ hyp.}}$ ) is calculated assuming  $p\pi^-$  daughters, and the mass assum-  
ing  $\bar{\Lambda}$  hypothesis ( $m_{\text{inv}, \bar{\Lambda} \text{ hyp.}}$ ) is calculated assuming  $\bar{p}\pi^+$  daughters. In addition to the notation just  
introduced, in the following,  $m_{\text{PDG}, K_S^0}$  and  $m_{\text{PDG}, \Lambda(\bar{\Lambda})}$  denote the particle masses of the  $K_S^0$  and  $\Lambda(\bar{\Lambda})$ ,  
respectively, as recorded by the Particle Data Group [?].

For  $\Lambda(\bar{\Lambda})$  selection, a candidate is assumed to be misidentified and is rejected if all of the following  
criteria are satisfied:

$$1. \left| m_{\text{inv}, K_S^0 \text{ hyp.}} - m_{\text{PDG}, K_S^0} \right| < 9.0 \text{ MeV}/c^2$$

111     2. The daughter particles pass daughter cuts intended for  $K_S^0$  reconstruction

112       (a)  $\Lambda$  selection

113           i. p daughter passes  $\pi^+$  cuts intended for  $K_S^0$  reconstruction

114           ii.  $\pi^-$  daughter passes  $\pi^-$  cuts intended for  $K_S^0$  reconstruction.

115       (b)  $\bar{\Lambda}$  selection

116           i.  $\pi^+$  daughter passes  $\pi^+$  cuts intended for  $K_S^0$  reconstruction

117           ii.  $\bar{p}$  daughter passes  $\pi^-$  cuts intended for  $K_S^0$  reconstruction.

118     3.  $|m_{\text{inv}, K_S^0 \text{ hyp.}} - m_{\text{PDG}, K_S^0}| < |m_{\text{inv}, \Lambda(\bar{\Lambda}) \text{ hyp.}} - m_{\text{PDG}, \Lambda(\bar{\Lambda})}|$

119     Similarly, for  $K_S^0$  selection, a candidate is rejected if all of the following criteria are satisfied for the  $\Lambda$   
120     case, or for the  $\bar{\Lambda}$  case:

121     1.  $|m_{\text{inv}, \Lambda(\bar{\Lambda}) \text{ hyp.}} - m_{\text{PDG}, \Lambda(\bar{\Lambda})}| < 9.0 \text{ MeV}/c^2$

122     2. The daughter particles pass daughter cuts intended for  $\Lambda(\bar{\Lambda})$  reconstruction

123       (a)  $\pi^+$  daughter passes  $p(\pi^+)$  daughter cut intended for  $\Lambda(\bar{\Lambda})$  reconstruction

124       (b)  $\pi^-$  daughter passes  $\pi^-(\bar{p})$

125     3.  $|m_{\text{inv}, \Lambda(\bar{\Lambda}) \text{ hyp.}} - m_{\text{PDG}, \Lambda(\bar{\Lambda})}| < |m_{\text{inv}, K_S^0 \text{ hyp.}} - m_{\text{PDG}, K_S^0}|$

126     At this stage, we have a collection of V0 candidates satisfying all of the aforementioned cuts. However,  
127     this collection is still polluted by fake V0s, for which the daughter particles happen to pass all of our cuts,  
128     but which do not actually originate from a V0. Although the two daughter particles appear to reconstruct  
129     a V0 candidate, they are lacking one critical requirement: the system invariant mass does not match that  
130     of our desired V0 species (these can be seen outside of the mass peaks in Fig. ??). Therefore, as our  
131     final single-particle cut, we require the invariant mass of the V0 candidate to fall within the mass peak of  
132     our desired species. Note, however, that some fake V0s still make it past this final cut, as their invariant  
133     mass also happens to fall without our acceptance window.

134     Occasionally, we encounter a situation where two V0 candidates share a common daughter. Not both of  
135     these candidates can be real V0s, and including both could introduce an artificial signal into our data.  
136     To avoid any auto-correlation effects, for each event, we impose a single-particle shared daughter cut on  
137     each collection of V0 candidates. This cut iterates through the V0 collection to ensure that no daughter is  
138     claimed by more than one V0 candidate. If a shared daughter is found between two V0 candidates, that  
139     candidate with a smaller DCA to primary vertex is kept while the other is excluded from the analysis.  
140     Note, this single-particle shared daughter cut is unique from the pair shared daughter cut discussed in  
141     Sec. ??, the latter of which ensure there is no daughter sharing between the particles in a given pair.

142     The specific cuts used to reconstruct our  $\Lambda(\bar{\Lambda})$  and  $K_S^0$  populations, along with plots showing the effect  
143     of the misidentification cuts, are shown in the following sections.

### 144     3.4.1 $\Lambda$ Reconstruction

145     The following cuts, in addition to the misidentification and shared daughter cuts presented in Sec. 3.4,  
146     were used to select good  $\Lambda(\bar{\Lambda})$  candidates:

147     Figure 2a shows the mass assuming  $K_S^0$  hypothesis for the  $\Lambda$  collection, i.e. assume the daughters are  
148      $\pi^+\pi^-$  instead of  $p^+\pi^-$ . Figure 2b is a similar plot, but is for the  $\bar{\Lambda}$  collection, i.e. assume the daughters

<b><math>\Lambda</math> selection</b>	
$ \eta $	< 0.8
$p_T$	> 0.4 GeV/c
$ m_{\text{inv}} - m_{\text{PDG}} $	< 3.8 MeV
DCA to prim. vertex	< 0.5 cm
Cosine of pointing angle	> 0.9993
OnFlyStatus	false
Decay Length	< 60 cm
Shared Daughter Cut	true
Misidentification Cut	true
<b>Daughter Cuts (<math>\pi</math> and <math>p</math>)</b>	
$ \eta $	< 0.8
Number of clusters in the TPC	> 80
Daughter status	kTPCrefit
DCA $\pi p$ Daughters	< 0.4 cm
<b><math>\pi</math>-specific cuts</b>	
$p_T$	> 0.16 GeV/c
DCA to prim vertex	> 0.3 cm
<b>TPC and TOF N<math>\sigma</math> Cuts</b>	
$p < 0.5 \text{ GeV}/c$	$N\sigma_{\text{TPC}} < 3$
$p > 0.5 \text{ GeV}/c$	if TOF & TPC available else $N\sigma_{\text{TOF}} < 3$
<b><math>p</math>-specific cuts</b>	
$p_T$	> 0.5( $p$ ) [0.3( $\bar{p}$ )] GeV/c
DCA to prim vertex	> 0.1 cm
<b>TPC and TOF N<math>\sigma</math> Cuts</b>	
$p < 0.8 \text{ GeV}/c$	$N\sigma_{\text{TPC}} < 3$
$p > 0.8 \text{ GeV}/c$	if TOF & TPC available else $N\sigma_{\text{TOF}} < 3$

**Table 2:**  $\Lambda$  selection

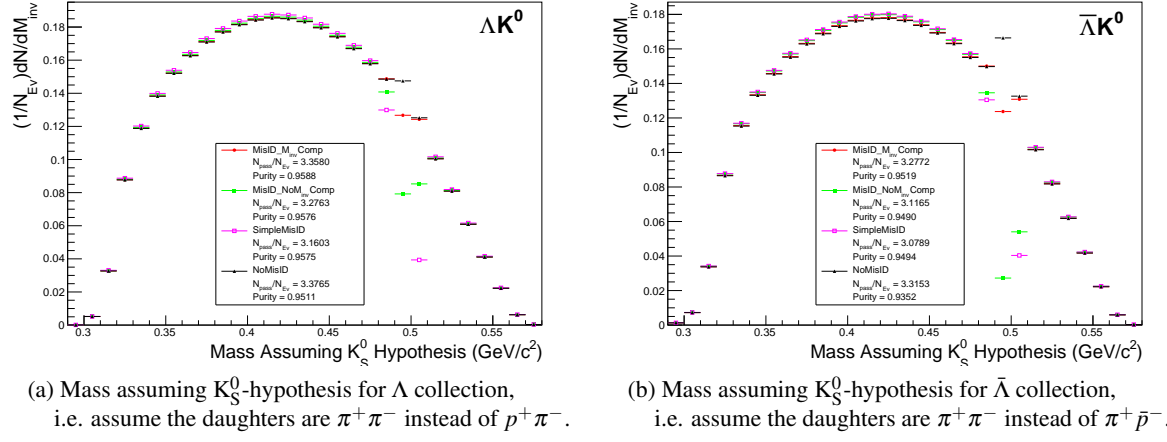


**Fig. 2:** Mass assuming  $K_S^0$ -hypothesis for V0 candidates passing all  $\Lambda$  (2a) and  $\bar{\Lambda}$  (2b) cuts. The “NoMisID” distribution (black triangles) uses the V0 finder without any attempt to remove misidentified  $K_S^0$ . The slight peak in the “NoMisID” distribution around  $m_{\text{inv}} = 0.5 \text{ GeV}/c^2$  contains misidentified  $K_S^0$  particles in our  $\Lambda(\bar{\Lambda})$  collection. “SimpleMisID” (pink squares) simply cuts out the entire peak, which throws away some good  $\Lambda$  and  $\bar{\Lambda}$  particles. “MisID\_NoM<sub>inv</sub>Comp” (green squares) uses the misidentification cut outlined in the text, but does not utilize the final invariant mass comparison step. “MisID\_M<sub>inv</sub>Comp” (red circles) utilizes the full misidentification methods, and is currently used for this analysis. “ $N_{\text{pass}}/N_{\text{ev}}$ ” is the total number of  $\Lambda(\bar{\Lambda})$  particles found, normalized by the total number of events. The purity of the collection is also listed.

are  $\pi^+\pi^-$  instead of  $\pi^+\bar{p}^-$ . The  $K_S^0$  contamination is visible, although not profound, in both, in the slight peaks around  $m_{\text{inv}} = 0.497 \text{ GeV}/c^2$ . If one simply cuts out the entire peak, good  $\Lambda$  particles will be lost. Ideally, the  $\Lambda$  selection and  $K_S^0$  misidentification cuts are selected such that the peak is removed from this plot while leaving the underlying distribution continuous. To attempt to remove these  $K_S^0$  contaminations without throwing away good  $\Lambda$  and  $\bar{\Lambda}$  particles, the misidentification cuts introduced in Sec. 3.4 were imposed.

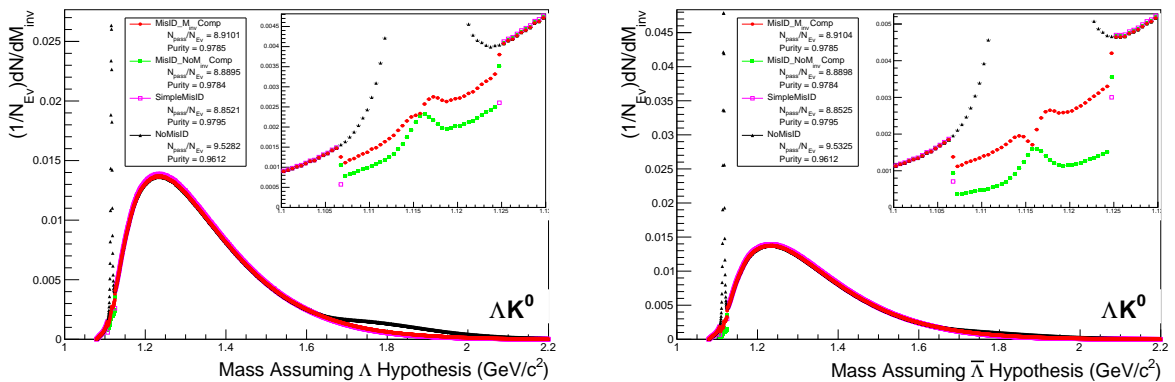
### 3.4.2 $K_S^0$ Reconstruction

The following cuts, in addition to the misidentification and shared daughter cuts presented in Sec. 3.4, were used to select good  $K_S^0$  candidates:

As can be seen in Figure 3, some misidentified  $\Lambda$  and  $\bar{\Lambda}$  particles contaminate our  $K_S^0$  sample. Figure 3a shows the mass assuming  $\Lambda$ -hypothesis for the  $K_S^0$  collection, i.e. assume the daughters are  $p^+\pi^-$  instead of  $\pi^+\pi^-$ . Figure 3b is similar, but shows the mass assuming  $\bar{\Lambda}$ -hypothesis for the collection, i.e. assume the daughters are  $\pi^+\bar{p}^-$  instead of  $\pi^+\pi^-$ . The  $\Lambda$  contamination can be seen in 3a, and the  $\bar{\Lambda}$  contamination in 3b, in the peaks around  $m_{\text{inv}} = 1.115 \text{ GeV}/c^2$ . Additionally, the  $\bar{\Lambda}$  contamination is visible in Figure 3a, and the  $\Lambda$  contamination visible in Figure 3b, in the region of excess around  $1.65 < m_{\text{inv}} < 2.1 \text{ GeV}/c^2$ . This is confirmed as the number of misidentified  $\Lambda$  particles in the sharp peak of Figure 3a (misidentified  $\bar{\Lambda}$  particles in the sharp peak of Figure 3b) approximately equals the excess found in the  $1.65 < m_{\text{inv}} < 2.1 \text{ GeV}/c^2$  region of Figure 3a (Figure 3b).

The peaks around  $m_{\text{inv}} = 1.115 \text{ GeV}/c^2$  in Figure 3 contain both misidentified  $\Lambda(\bar{\Lambda})$  particles and good  $K_S^0$ . If one simply cuts out the entire peak, some good  $K_S^0$  particles will be lost. Ideally, the  $K_S^0$  selection and  $\Lambda(\bar{\Lambda})$  misidentification cuts can be selected such that the peak is removed from this plot while leaving the underlying distribution continuous. To attempt to remove these  $\Lambda$  and  $\bar{\Lambda}$  contaminations without throwing away good  $K_S^0$  particles, the misidentification cuts introduced in Sec. 3.4 were imposed.

<b><math>K_S^0</math> selection</b>	
$ \eta $	< 0.8
$p_T$	> 0.2 GeV/c
$m_{PDG} - 13.677 \text{ MeV} < m_{\text{inv}} < m_{PDG} + 2.0323 \text{ MeV}$	
DCA to prim. vertex	< 0.3 cm
Cosine of pointing angle	> 0.9993
OnFlyStatus	false
Decay Length	< 30 cm
Shared Daughter Cut	true
Misidentification Cut	true
<b><math>\pi^\pm</math> Daughter Cuts</b>	
$ \eta $	< 0.8
Number of clusters in TPC	> 80
Daughter Status	kTPCcrefit
DCA $\pi^+ \pi^-$ Daughters	< 0.3 cm
$p_T$	> 0.15 GeV/c
DCA to prim vertex	> 0.3 cm
TPC and TOF $N\sigma$ Cuts	
$p < 0.5 \text{ GeV}/c$	$N\sigma_{\text{TPC}} < 3$
$p > 0.5 \text{ GeV}/c$	if TOF & TPC available else
	$N\sigma_{\text{TPC}} < 3 \text{ \& } N\sigma_{\text{TOF}} < 3$
	$N\sigma_{\text{TOF}} < 3$

Table 3:  $K_S^0$  selection(a) Mass assuming  $\Lambda$ -hypothesis for  $K_S^0$  collection, i.e. assume the daughters are  $p^+ \pi^-$  instead of  $\pi^+ \pi^-$ .(b) Mass assuming  $\bar{\Lambda}$ -hypothesis for  $K_S^0$  collection, i.e. assume the daughters are  $\pi^+ \bar{p}^-$  instead of  $\pi^+ \pi^-$ .

**Fig. 3:** Mass assuming  $\Lambda$ -hypothesis (3a) and  $\bar{\Lambda}$ -hypothesis (3b) for  $K_S^0$  collection. The “NoMisID” distribution (black triangles) uses the V0 finder without any attempt to remove misidentified  $\Lambda$  and  $\bar{\Lambda}$ . The peak in the “NoMisID” distribution around  $m_{\text{inv}} = 1.115 \text{ GeV}/c^2$  contains misidentified  $\Lambda$  (3a) and  $\bar{\Lambda}$  (3b) particles in our  $K_S^0$  collection. “SimpleMisID” (pink squares) simply cuts out the entire peak, which throws away some good  $K_S^0$  particles. “MisID\_NoM<sub>inv</sub>Comp” (green squares) uses the misidentification cut outlined in the text, but does not utilize the final invariant mass comparison step. “MisID\_M<sub>inv</sub>Comp” (red circles) utilizes the full misidentification methods, and is currently used for this analysis. “N<sub>pass</sub>/N<sub>ev</sub>” is the total number of  $K_S^0$  particles found, normalized by the total number of events. The purity of the collection is also listed. Also note, the relative excess of the “NoMisID” distribution around  $1.65 < m_{\text{inv}} < 2.1 \text{ GeV}/c^2$  shows misidentified  $\bar{\Lambda}$  (3a) and  $\Lambda$  (3b) particles in our  $K_S^0$  collection.

172 **3.5 V0 Purity Estimation**

173 In order to obtain a true and reliable signal, one must ensure good purity of the V0 collection. The purity  
 174 of the collection is calculated as:

$$Purity = \frac{Signal}{Signal + Background} \quad (2)$$

175 To access both the signal and background, the invariant mass distribution ( $m_{inv}$ ) of all V0 candidates  
 176 must be constructed immediately before the final invariant mass cut, as shown in Fig. 4 for  $\Lambda$ ,  $\bar{\Lambda}$  and  $K_S^0$   
 177 candidates in the 0-10% centrality bin. Fig. 4a presents the  $p\pi^-$  invariant mass distribution showing the  
 178  $\Lambda$  peak, Fig. 4b presents the  $\bar{p}\pi^+$  invariant mass distribution showing the  $\bar{\Lambda}$  peak, and Fig. 4c presents  
 179 the  $\pi^+\pi^-$  invariant mass distribution showing the  $K_S^0$  peak.

180 It is vital that this distribution be constructed immediately before the final  $m_{inv}$  cut, otherwise it would be  
 181 impossible to estimate the background. These distributions are used to calculate the collections' purities  
 182 (defined in Eq. 2). As shown in Figure 4, the background is fit (with a polynomial) outside of the peak  
 183 region of interest to obtain an estimate for the background within the region. Within the  $m_{inv}$  cut limits,  
 184 the background is assumed to be the region below the fit while the signal is that above the fit. The  $\Lambda$  and  
 185  $\bar{\Lambda}$  purities were found to be  $\approx 95\%$ , and the  $K_S^0$  purity was found to be  $\approx 98\%$ .

186 **3.6 V0 Purity Background Estimation**

187 As previously stated, the backgrounds in the  $m_{inv}$  distributions are modeled by a polynomial which is  
 188 fit outside of the final cut region in an attempt to estimate the background within the cut region. As  
 189 this estimate of the background under the mass peak is vital for our estimate of our V0 purity, it is  
 190 important for us to ensure that our estimate is accurate. More specifically, it is necessary that we ensure  
 191 the background is well described by a polynomial fit within the cut region.

192 To better understand our background, we studied V0 candidates reconstructed with daughters from dif-  
 193 ferent events. These mixed-event V0s certainly do not represent real, physical V0s (a single V0 cannot  
 194 have daughters living in two different events!), but, rather, represent a large portion of the background  
 195 creeping into our analysis.

196 The standard AliFemto framework is not equipped to handle this situation, as most are not interested in  
 197 these fake-V0s. Therefore, we built the `AliFemtoV0PurityBgdEstimator` class to handle our needs. In ad-  
 198 dition to finding fake-V0s using mixed-event daughters, we also used our `AliFemtoV0PurityBgdEstimator`  
 199 class to find real-V0s using same-event daughters. The purpose here was to compare our simple V0 finder  
 200 (in `AliFemtoV0PurityBgdEstimator`) to the established V0 finder used in standard AliFemto analyses.

201 Figure 5 shows the results of our study. In the figures, the black points, marked "Data", correspond to  
 202 V0s found using the standard V0-finder, and to the V0s used in my analyses. The red points show real  
 203 V0s reconstructed with our personal V0-finder (in `AliFemtoV0PurityBgdEstimator`) using same-event  
 204 daughters, and the blue points show fake-V0s reconstructed with our personal V0-finder using mixed-  
 205 event daughters. Both the red and blue points have been scaled by different factors (listed in the figure's  
 206 legends) to nicely align all three data on a single plot.

207 Figure 5 shows that our personal V0-finder does a good, but not perfect, job of matching the shape of the  
 208  $m_{inv}$  plots obtained from the data. The scale factor listed in the legend reveals that we are only finding  
 209  $1/3 - 1/2$  of the V0s found by the standard V0-finder. These two points are not of concern, as our purpose  
 210 here was to gain a sense of the broad shape of the background. It is revealed in Fig. 5, when studying  
 211 the red and blue points, that the background distribution within the mass peak region is simply a smooth  
 212 connection of the backgrounds outside of the cut region, as we assumed. Therefore, our method of fitting  
 213 the background outside of the cut region, fitting with a smooth polynomial, and extrapolating to the cut

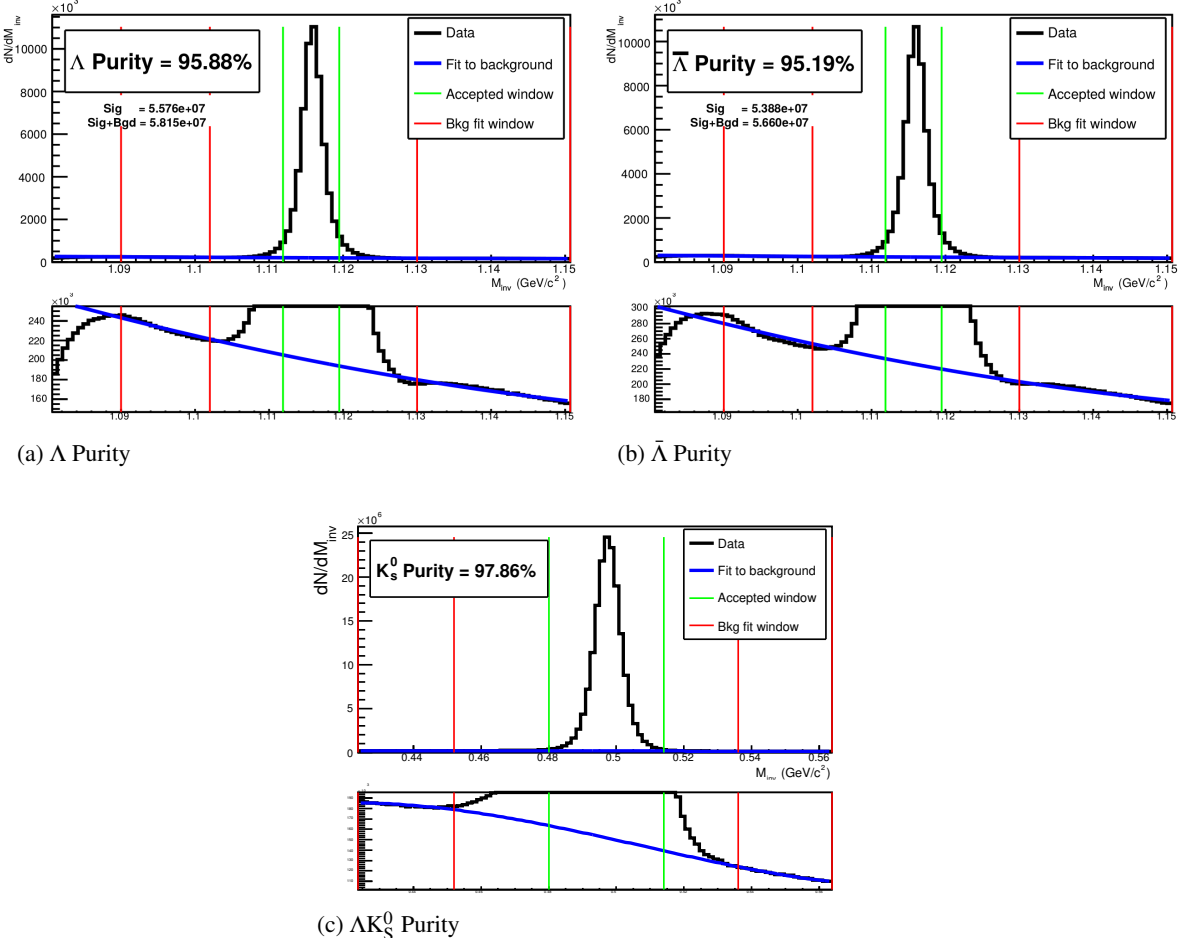


**Fig. 4:** Invariant mass ( $m_{\text{inv}}$ ) distribution for all  $\Lambda$  (a),  $\bar{\Lambda}$  (b), and  $K_S^0$  (c) candidates immediately before the final invariant mass cut. The bottom figures are zoomed to show the background with fit. The vertical green lines represent the  $m_{\text{inv}}$  cuts used in the analyses, the red vertical lines delineate the regions over which the background was fit, and the blue line shows the background fit. These distributions are used to calculate the collection purities,  $\text{Purity}(\Lambda) \approx \text{Purity}(\bar{\Lambda}) \approx 95\%$ , and  $\text{Purity}(K_S^0) \approx 98\%$ .

214 region is justified.

### 215 3.7 $\Xi$ Reconstruction

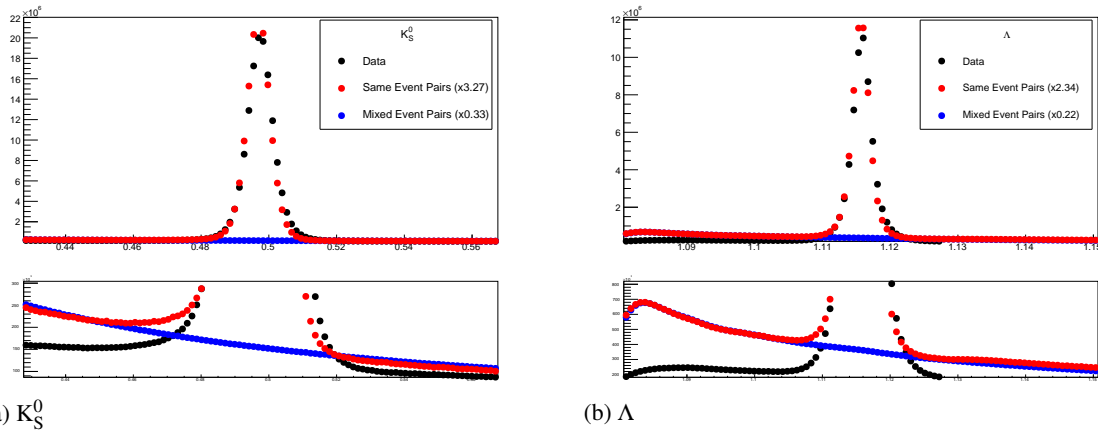
216 Our motivation for studying  $\Xi^- K^\pm$  systems is to attempt to better understand the striking difference in  
 217 the  $\Lambda K^+$  and  $\Lambda K^-$  data at low  $k^*$  (Figure 12).

218 The reconstruction of  $\Xi$  particles is one level above V0 reconstruction. V0 particles are topologically  
 219 reconstructed by searching for the charged daughters' tracks into which they decay. With  $\Xi$  particles, we  
 220 search for the V0 particle and charged daughter into which the  $\Xi$  decays. In the case of  $\Xi^-$ , we search  
 221 for the  $\Lambda$  (V0) and  $\pi^-$  (track) daughters. We will refer to this  $\pi$  as the “bachelor  $\pi$ ”.

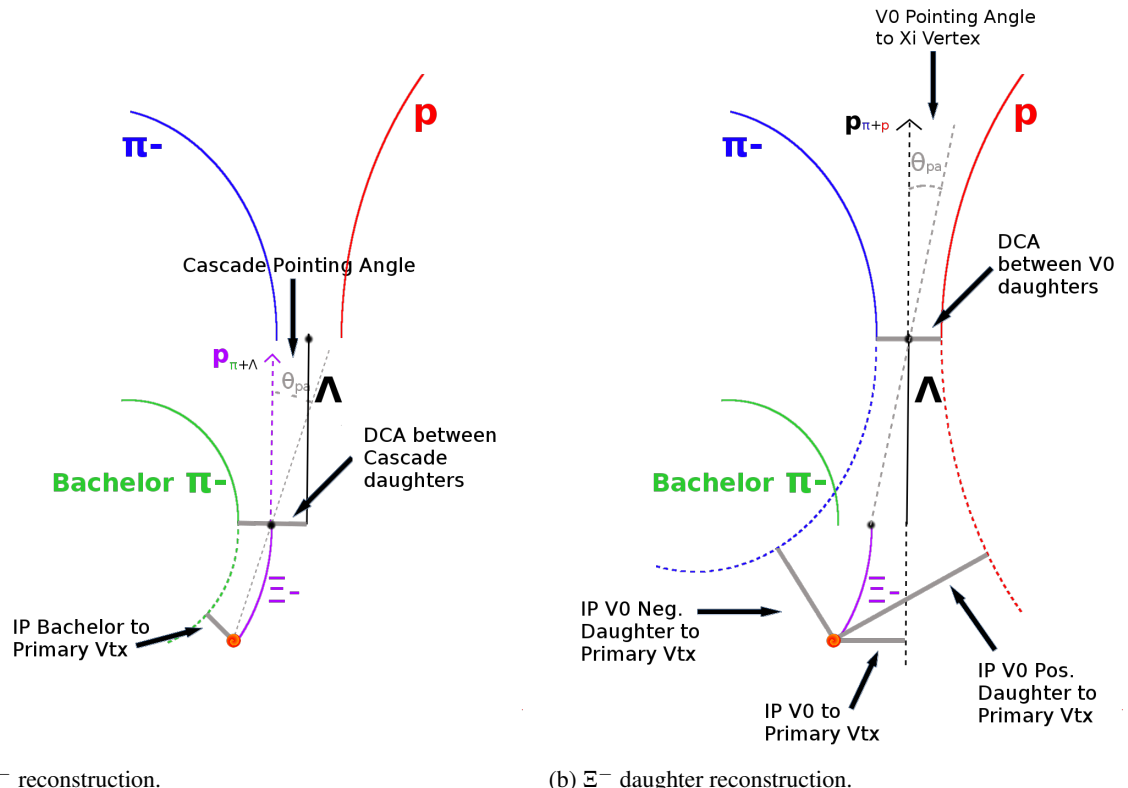
222 The following cuts were used to select good  $\Xi^-$  ( $\bar{\Xi}^+$ ) candidates:

#### 223 1. Shared Daughter Cut for $\Xi$ Collection

- 224 – Iterate through  $\Xi$  collection to ensure that no daughter is used in more than one  $\Xi$  candidate
- 225 – Remove any candidate in which the bachelor  $\pi$  is also a daughter of the  $\Lambda$  (implemented in  
 226 `AliFemtoXiTrackPairCut` class)



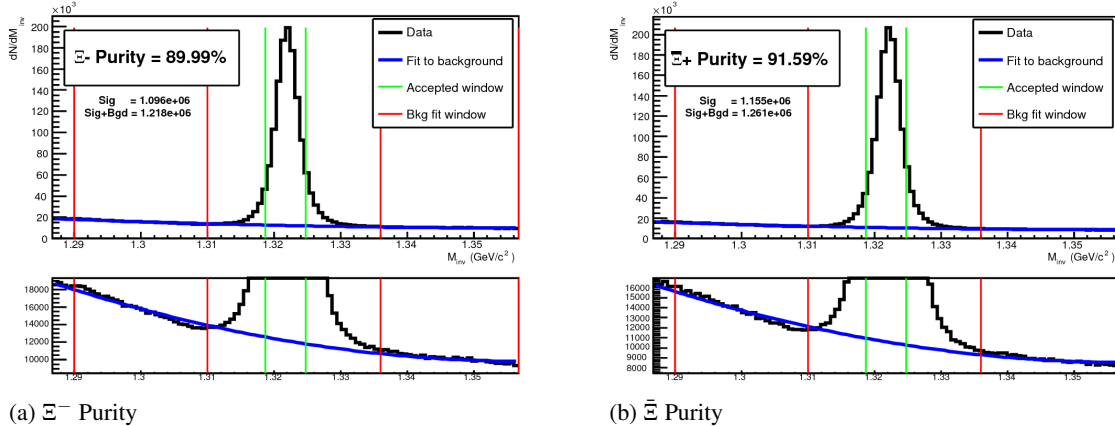
**Fig. 5:** V0 Purity Background Estimation. The black points, marked "Data", correspond to real V0s found using the standard V0-finder (i.e. the V0s used in my analyses). The red points, marked "Same Event Pairs", show real V0s reconstructed with our personal V0-finder in AliFemtoV0PurityBgdEstimator. These data are scaled by a factor (listed in the legend) to match their *Signal + Background* value in the cut region with that of the data. The blue points, marked "Mixed Event Pairs", show fake-V0s reconstructed with our personal V0-finder using mixed-event daughters. The blue points are scaled by a factor (listed in the legend) to closely match the red points in the side-band region.



**Fig. 6:** (Left)  $\Xi^-$  reconstruction (DCA to primary vertex for  $\Xi^-$  not shown). (Right)  $\Xi^-$  daughter reconstruction.

<sup>227</sup> The purity of our  $\Xi$  and  $\bar{\Xi}$  collections are calculated just as those of our V0 collections 3.3. Figure 7,  
<sup>228</sup> which is used to calculate the purity, shows the  $m_{\text{inv}}$  distribution of our  $\Xi(\bar{\Xi})$  candidates just before the  
<sup>229</sup> final  $m_{\text{inv}}$  cut. Currently, we have  $\text{Purity}(\Xi^-) \approx 90\%$  and  $\text{Purity}(\bar{\Xi}^+) \approx 92\%$ .

$\Xi$ selection	
$ \eta $	< 0.8
$p_T$	> 0.8 GeV/c
$ m_{\text{inv}} - m_{\text{PDG}} $	< 3.0 MeV
DCA to prim. vertex	< 0.3 cm
Cosine of pointing angle	> 0.9992
$\Lambda$ daughter cuts	
DCA to prim. vertex	> 0.2 cm
Cosine of pointing angle	> 0.0
Cosine of pointing angle to $\Xi$ decay vertex	> 0.9993
OnFlyStatus	false
All other $\Lambda$ and corresponding ( $\pi$ and p) daughter cuts are same as in primary $\Lambda$ selection, and can be found in Sec. 3.4.1	
Bachelor $\pi$ cuts	
$ \eta $	< 0.8
$p_T$	> 0.0 GeV/c
DCA to prim. vertex	> 0.1 cm
Number of clusters in the TPC	> 70
Daughter status	kTPCrefit
TPC and TOF $N\sigma$ Cuts	
$p < 0.5 \text{ GeV}/c$	$N\sigma_{\text{TPC}} < 3$
$p > 0.5 \text{ GeV}/c$	if TOF & TPC available else $N\sigma_{\text{TOF}} < 3$
	$N\sigma_{\text{TPC}} < 3 \& N\sigma_{\text{TOF}} < 3$

**Table 4:**  $\Xi$  selection

**Fig. 7:** Invariant mass ( $m_{\text{inv}}$ ) distribution for all  $\Xi^-$  (a) and  $\bar{\Xi}^+$  (b) candidates immediately before the final invariant mass cut. The bottom figures are zoomed to show the background with fit. The vertical green lines represent the  $m_{\text{inv}}$  cuts used in the analyses, the red vertical lines delineate the regions over which the background was fit, and the blue line shows the background fit. These distributions are used to calculate the collection purities,  $\text{Purity}(\Xi^-) \approx 90\%$  and  $\text{Purity}(\bar{\Xi}^+) \approx 92\%$ .

### 230 3.8 Pair Selection

231 The femtoscopy analysis of two-particle correlation functions relies on the proper formation of particle  
 232 pairs. As such, it is important to obtain true particle pairs in the analysis. In particular, contamination  
 233 from pairs constructed with split or merged tracks, and pairs sharing daughters, can introduce artificial  
 234 signals into the correlation function, obscuring the actual physics. In an effort to remove contamination,

235 we impose two main pair cuts: a shared daughter cut, and an average separation cut.

236 The purpose of the shared daughter cut is to ensure the first particle in the pair is unique from the second.  
 237 For pairs formed of two V0s (e.g.  $\Lambda K_S^0$ ), this cut is implemented by removing all pairs which share  
 238 a daughter. For example, in the  $\Lambda K_S^0$  analysis, if the  $\Lambda$  and  $K_S^0$  in a potential pair claim the same  $\pi^-$   
 239 daughter, the pair is excluded from the analysis. For a pair formed of a single V0 and a charged track  
 240 (e.g.  $\Lambda K^\pm$ ), the cut removes all pairs in which the charged track is also claimed as a daughter of the V0.  
 241 This mistake could only occur if, for instance, either a  $K^\pm$  is misidentified as a  $\pi$  or p and used in the V0  
 242 reconstruction, or a  $\pi$  or p is misidentified as a  $K^\pm$  in the  $K^\pm$  selection. In the case of a pair formed from  
 243 a charged  $\Xi$  and a charged track (e.g.  $\Xi^- K^\pm$ ), the cut removes all pairs in which the charged track is also  
 244 claimed as a daughter of the  $\Xi$ , be it the bachelor- $\pi$  daughter directly, or a daughter of the  $\Lambda$  daughter (a  
 245 granddaughter of the  $\Xi$ ). In the  $\Xi^- K^\pm$  analysis, as in the  $\Lambda K^\pm$  case, this could only occur if there was  
 246 misidentification of a  $K^\pm$  as a  $\pi$  or p, or vice versa.

247 The purpose of the average separation cut is to remove splitting and merging effects, and it is employed  
 248 in the following way. To calculate the average separation between two tracks, the spatial separation is  
 249 determined at several points throughout the TPC (every 20 cm radially from 85 cm to 245 cm), and the  
 250 results averaged. For that  $\Lambda K_S^0$  analysis, which involves two V0 particles, a minimum average separation  
 251 cut of 6 cm between the like-charge daughters in the pairs was imposed (for example, between the p  
 252 daughter of the  $\Lambda$  and the  $\pi^+$  daughter of the  $K_S^0$ ). For the  $\Lambda K^\pm$  analyses, a minimum average separation  
 253 cut of 8 cm was enforced between the  $K^\pm$  and the  $\Lambda$  daughter sharing the same charge (for example,  
 254 in the  $\Lambda K^+$  analysis, between the p daughter of the  $\Lambda$  and the  $K^+$ ). Finally, for the  $\Xi^- K^\pm$  analysis, a  
 255 minimum average separation cut of 8 cm was enforced between any daughter of the  $\Xi$  sharing the same  
 256 charge as the  $K^\pm$  in the pair (for example, in the  $\Xi^- K^-$  analysis, between the  $\pi^-$  granddaughter which  
 257 decayed from the  $\Lambda$  daughter and the  $K^-$ , and between the bachelor- $\pi^-$  daughter and the  $K^-$ ).

258 The motivation for the values used in these cuts can be seen in Figures 8, 9, and 10, in which average sep-  
 259 aration correlation functions are presented. The average separation correlation functions are formed just  
 260 as for our relative-momentum correlation functions, but we instead bin in average separation. Looking at  
 261 these average separation correlation functions for like-charge tracks, at lowest average separation we see  
 262 an enhancement due to track splitting, followed by (at slightly higher average separation) a suppression  
 263 due to track merging. When the average separation correlation function stabilizes to unity, these effects  
 264 are no longer abundant, and we choose our cut value. Splitting and merging effects between oppositely  
 265 charged tracks was found to be negligible, therefore no cuts on unlike-charge tracks were imposed. To  
 266 summarize:

### 267 Average Separation Cuts ( $\Delta r$ )

#### 268 (a) $\Lambda K_S^0$ Analyses

- 269 –  $\Delta r > 6.0$  cm for like-charge sign daughters
- 270 – No cut for unlike-charge daughters

#### 271 (b) $\Lambda K^\pm$ Analyses

- 272 –  $\Delta r > 8.0$  cm for daughter of  $\Lambda(\bar{\Lambda})$  sharing charge sign of  $K^\pm$
- 273 – No cut for unlike-charge

#### 274 (c) $\Xi^- K^\pm$ Analyses

- 275 –  $\Delta r > 8.0$  cm for any daughter of  $\Xi$  sharing charge sign of  $K^\pm$
- 276 – No cut for unlike-charge

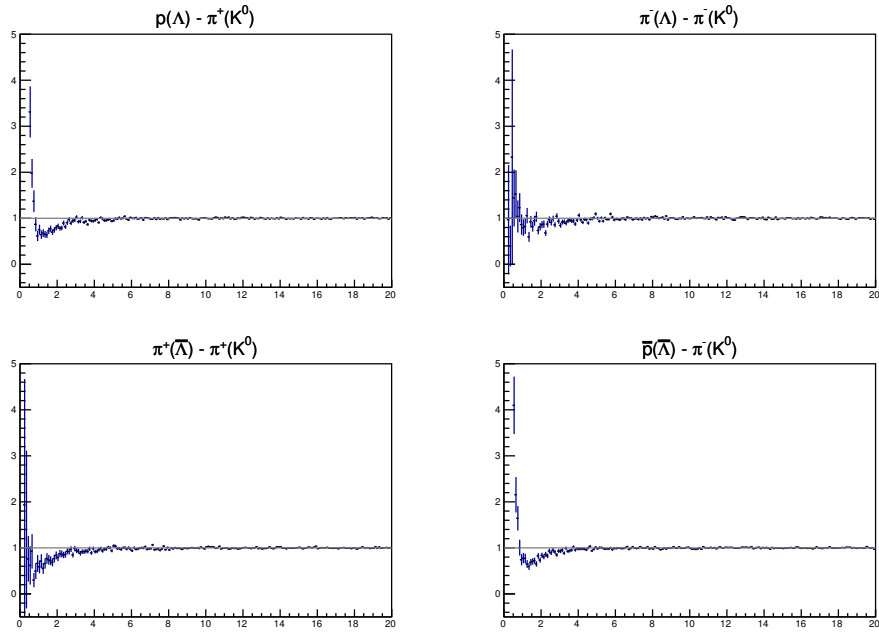


**Fig. 8:** Average separation (cm) correlation functions of  $\Lambda(\bar{\Lambda})$  and  $K_S^0$  Daughters. Only like-sign daughter pairs are shown (the distributions for unlike-signs were found to be flat). The title of each subfigure shows the daughter pair, as well as the mother of each daughter (in “()”), ex. top left is  $p$  from  $\Lambda$  with  $\pi^+$  from  $K_S^0$ .

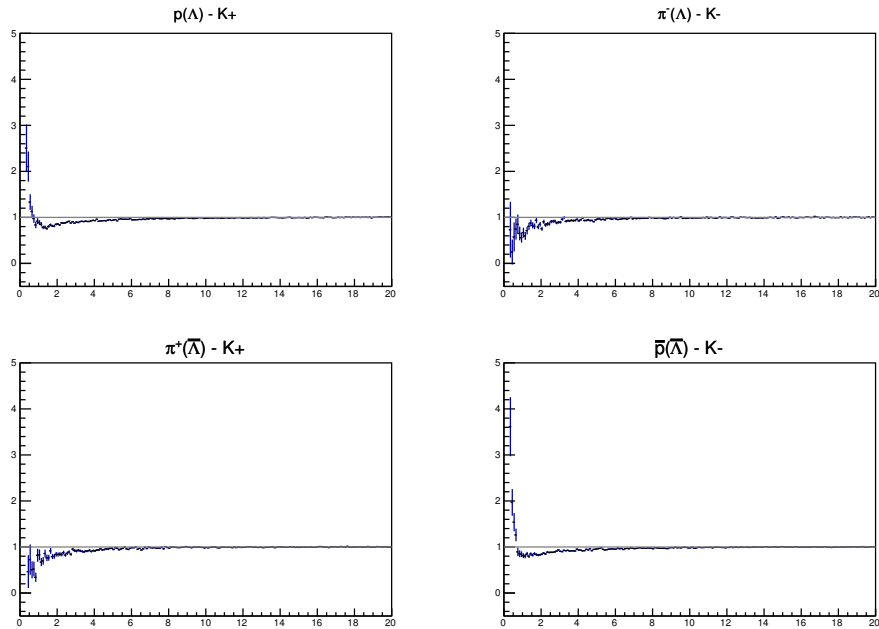


**Fig. 9:** Average separation (cm) correlation functions of  $\Lambda(\bar{\Lambda})$  Daughter and  $K^\pm$ . Only like-sign pairs are shown (unlike-signs were flat). In the subfigure titles, the particles in “()” represent the mothers, ex. top left is  $p$  from  $\Lambda$  with  $K^+$ .

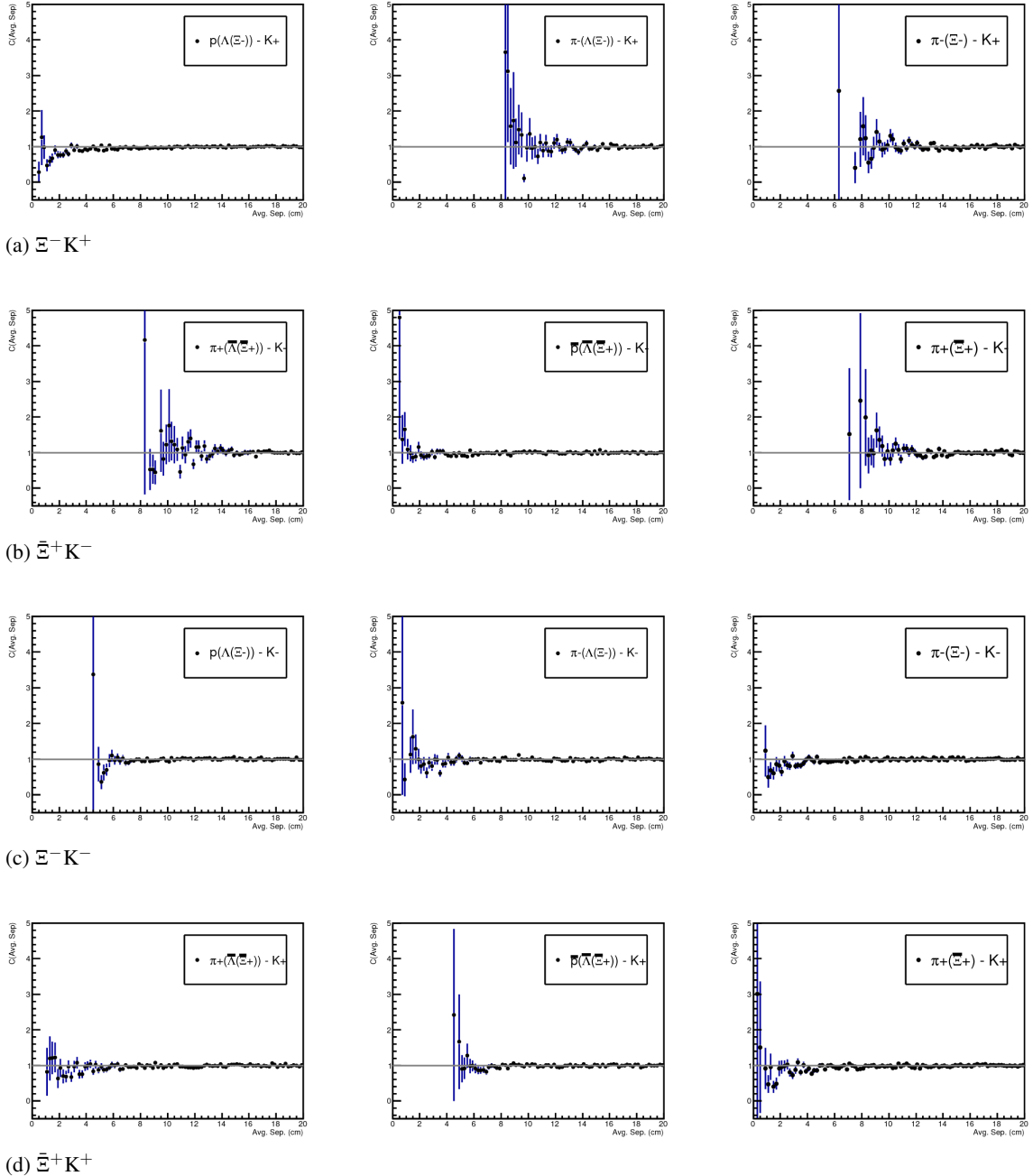


**Fig. 10:** Average separation (cm) correlation functions of  $\Xi$  Daughter and  $K^\pm$ . In the subfigure titles, the particles in “()” represent the mothers, ex. top left is  $p$  from  $\Lambda$  from  $\Xi^-$  with  $K^+$ .

277 **4 Correlation Functions**

278 This analysis studies the momentum correlations of both  $\Lambda K$  and  $\Xi^- K^\pm$  pairs using the two-particle  
 279 correlation function, defined as  $C(k^*) = A(k^*)/B(k^*)$ , where  $A(k^*)$  is the signal distribution,  $B(k^*)$  is the  
 280 reference (or background) distribution, and  $k^*$  is the momentum of one of the particles in the pair rest  
 281 frame. In practice,  $A(k^*)$  is constructed by binning in  $k^*$  pairs from the same event. Ideally,  $B(k^*)$  is  
 282 similar to  $A(k^*)$  in all respects excluding the presence of femtoscopic correlations [2]; as such,  $B(k^*)$   
 283 is used to divide out the phase-space effects, leaving only the femtoscopic effects in the correlation  
 284 function.

285 This analysis presents correlation functions for three centrality bins (0-10%, 10-30%, and 30-50%), and  
 286 is currently pair transverse momentum ( $k_T = 0.5|\mathbf{p}_{T,1} + \mathbf{p}_{T,2}|$ ) integrated (i.e. not binned in  $k_T$ ). The  
 287 correlation functions are constructed separately for the two magnetic field configurations, and, after  
 288 assuring consistency, are combined using a weighted average:

$$C_{combined}(k^*) = \frac{\sum_i w_i C_i(k^*)}{\sum_i w_i} \quad (3)$$

289 where the sum runs over the correlation functions to be combined, and the weight,  $w_i$ , is the number of  
 290 numerator pairs in  $C_i(k^*)$ . Here, the sum is over the two field configurations (++ and - -).

291 **4.1 Typical Correlation Function Construction**

292 In practice,  $B(k^*)$  is typically obtained by forming mixed-event pairs, i.e. particles from a given event  
 293 are paired with particles from  $N_{mix}$ (= 5) other events, and these pairs are then binned in  $k^*$ . In forming  
 294 the background distribution, it is important to mix only similar events; mixing events with different  
 295 phase-spaces can result in an unreliable background distribution, and can introduce artificial signals in  
 296 the correlation function. Therefore, in this analysis, we bin our events both in primary vertex location (2  
 297 cm bin width) and in centrality (5% bin width), and we only mix events within a given bin; i.e. we only  
 298 mix events of like centrality and of like primary vertex location. Also note, a vertex correction is also  
 299 applied to each event, which essentially recenters the the primary vertices to  $z = 0$ .

300 Figures 11a, 11b, 11c show the correlation functions for all centralities studied for  $\Lambda K^+(\bar{\Lambda} K^-)$ ,  $\Lambda K^-(\bar{\Lambda} K^+)$ ,  
 301 and  $\Lambda(\bar{\Lambda})K_S^0$ , respectively. All were normalized in the range  $0.32 < k^* < 0.4$  GeV/c. It is interesting to  
 302 note that the average of the  $\Lambda K^+(\bar{\Lambda} K^-)$  and  $\Lambda K^-(\bar{\Lambda} K^+)$  correlation functions is consistent with our  
 303  $\Lambda K_S^0(\bar{\Lambda} K_S^0)$  measurement.

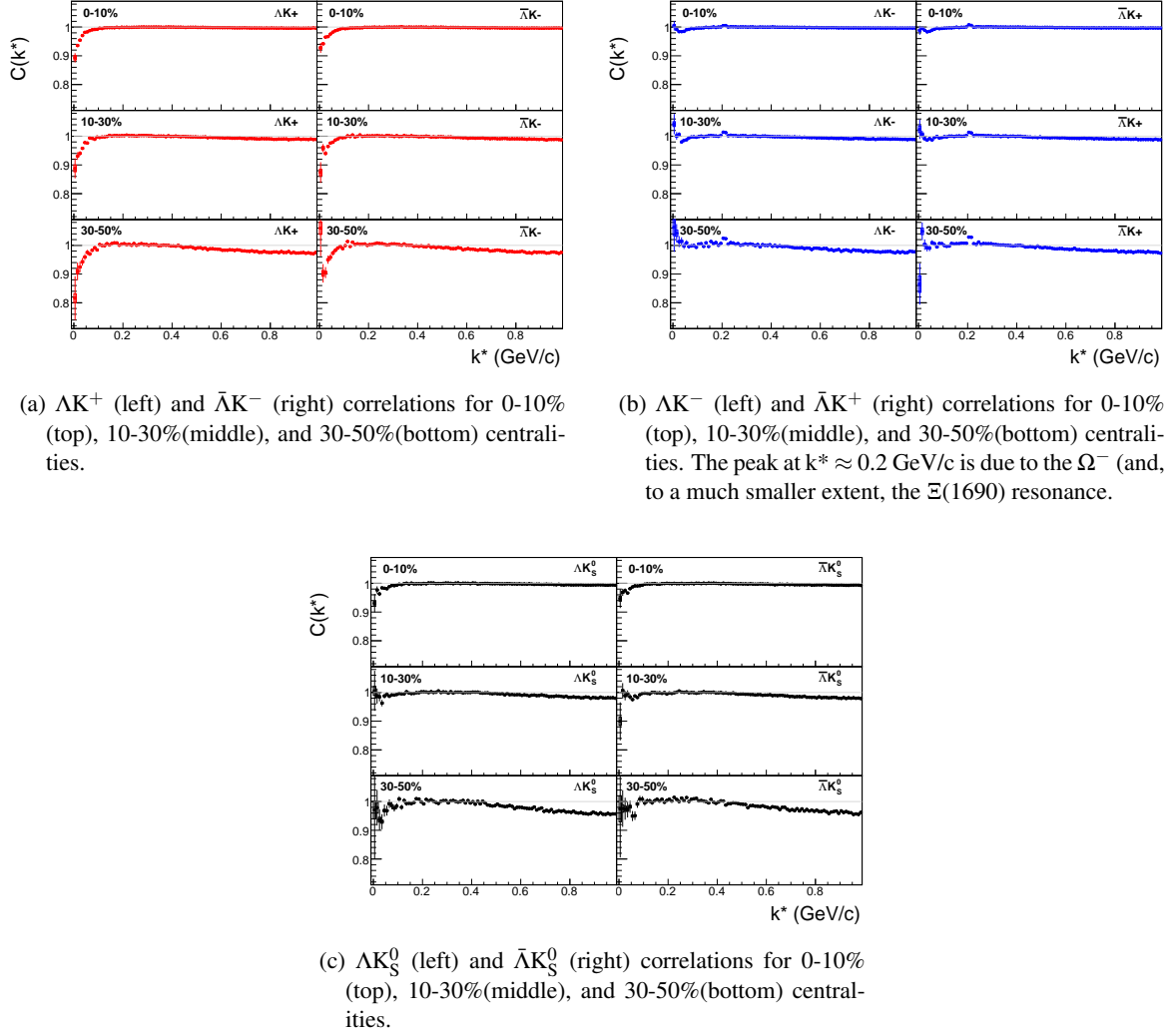


**Fig. 11:**  $\Lambda K$  and  $\bar{\Lambda} \bar{K}$  correlation functions for 0-10%, 10-30%, and 30-50% centralities. The lines represent the statistical errors, while the boxes represent the systematic errors.

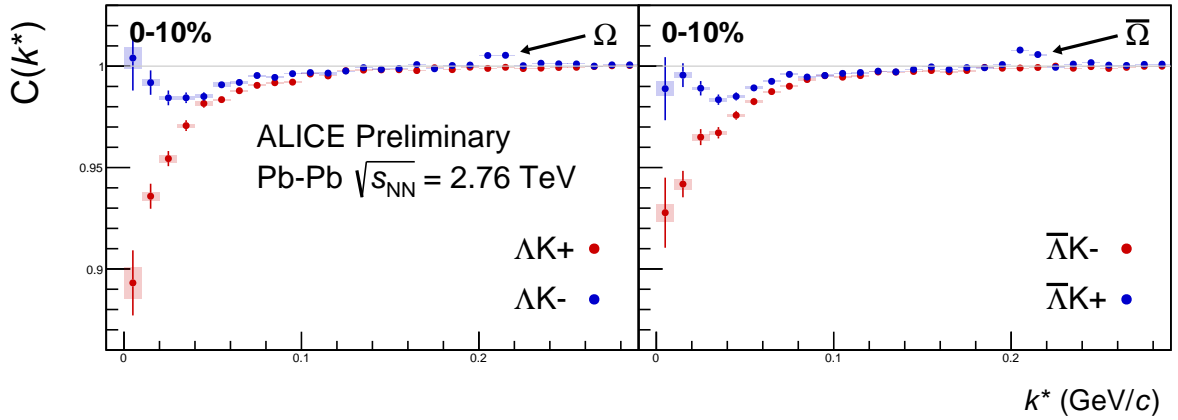


**Fig. 12:** Correlation Functions:  $\Lambda K^+$  vs  $\Lambda K^-$  ( $\bar{\Lambda} K^+$  vs  $\bar{\Lambda} K^-$ ) for 0-10% centrality. The peak in  $\Lambda K^- (\bar{\Lambda} K^+)$  at  $k^* \approx 0.2$  GeV/c is due to the  $\Omega^-$  (and, to a much smaller extent, the  $\Xi(1690)$  resonance. The lines represent the statistical errors, while boxes represent systematic errors.

**304 4.2 Stavinskiy Correlation Function Construction**

305 The purpose of the Stavinskiy method is to rid the correlation functions of the non-femtoscopic back-  
306 ground. More specifically, this method is intended to handle background contributions from elliptic  
307 flow, and other sources having reflection symmetry in the transverse plane. With the Stavinskiy method,  
308 mixed-event pairs are not used for the background ( $B(k^*)$ ); instead, same-event pseudo-pairs, formed  
309 by rotating one particle in a real pair by  $180^\circ$  in the transverse plane, are used as a background. This  
310 rotation rids the pairs of any femtoscopic correlation, while maintaining correlations due to elliptic flow  
311 (and other suitably symmetric contributors).

312 The results of correctly implementing such a procedure are shown in Figure 13. The figure shows the  
313 Stavinskiy method does a very good job of ridding the  $\Lambda K^\pm$  correlations of their non-femtoscopic back-  
314 grounds. We also see the procedure does not work as well on the  $\Lambda K_S^0$  system.

315 Now, one must be somewhat careful when applying this Stavinskiy method. We found that, in order to  
316 obtain correct results, we had to run our pseudo-pairs through the same pair cuts used in our analyses.  
317 In an ideal world, our pair cut would only remove truly bad pairs results from splitting, merging, etc. In  
318 the real world, the pair cut always throws out some of the good with the bad. For the pseudo-pairs to  
319 form a reliable background, they too must experience the pair cut, and the loss of “good” pseudo-pairs.  
320 We found this issue affected mainly our  $\Lambda K^+$  &  $\bar{\Lambda} K^-$  analysis, as can be seen in Figure 14, which shows  
321 both a correct implementation of the Stavinskiy method, and an incorrect implementation lacking the  
322 additional pair cut on the pseudo-pairs.

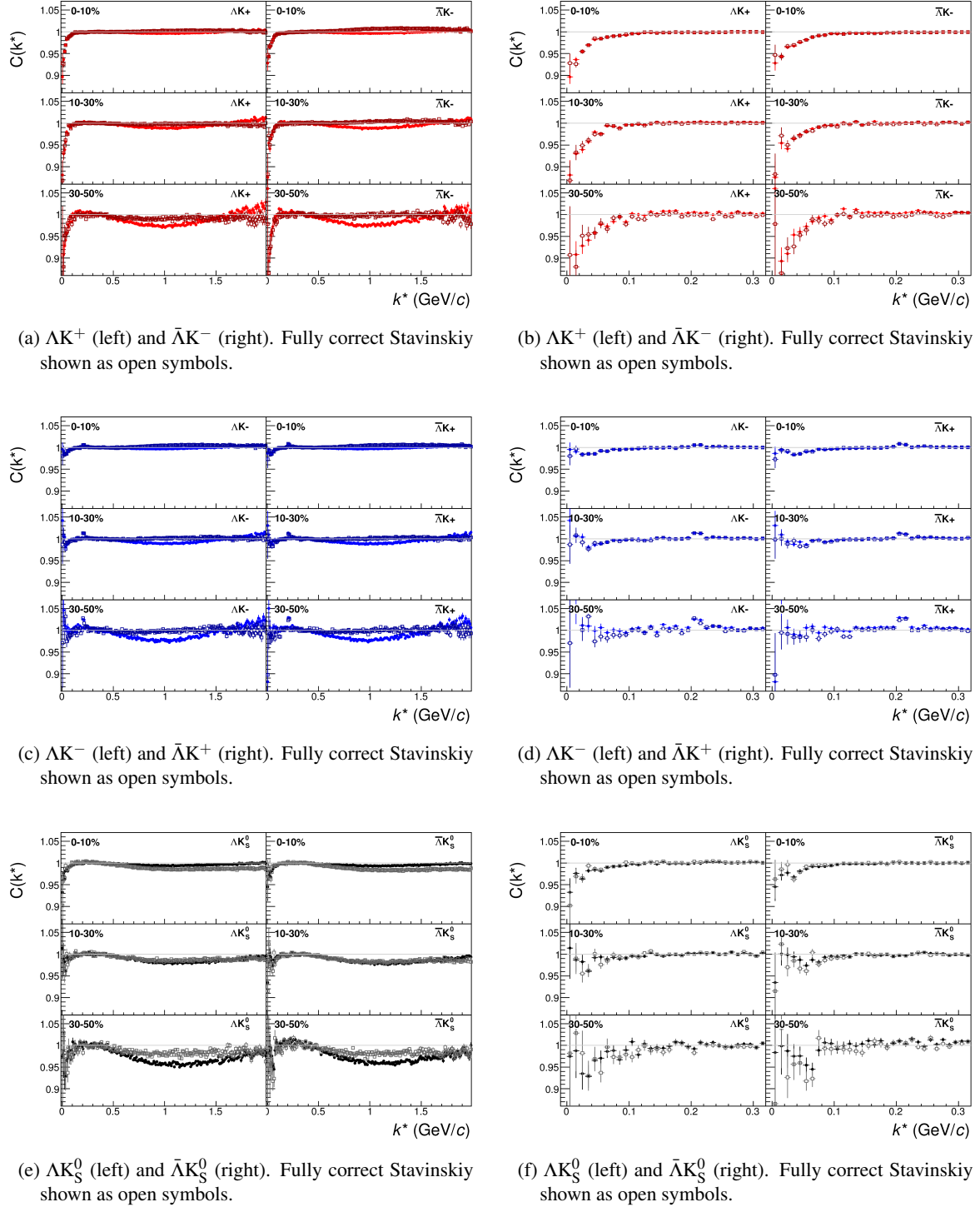


**Fig. 13:**  $\Lambda K$  and  $\bar{\Lambda} \bar{K}$  correlation functions built using the fully correct Stavinskiy method for 0-10%, 10-30%, and 30-50% centralities. In the fully correct method, the pseudo-pairs (same-event pairs with one particle rotated by  $180^\circ$  in the transverse plane) are also run through the pair cuts used in the analysis (an example of an incorrect implementation is shown in Fig. 14. Closed symbols represent correlations built using the normal mixed-event background, while open symbols represent correlations formed using the Stavinskiy same-event pseudo-pairs as a background. Figures in the right column are zoomed-in versions of figures in the left column.

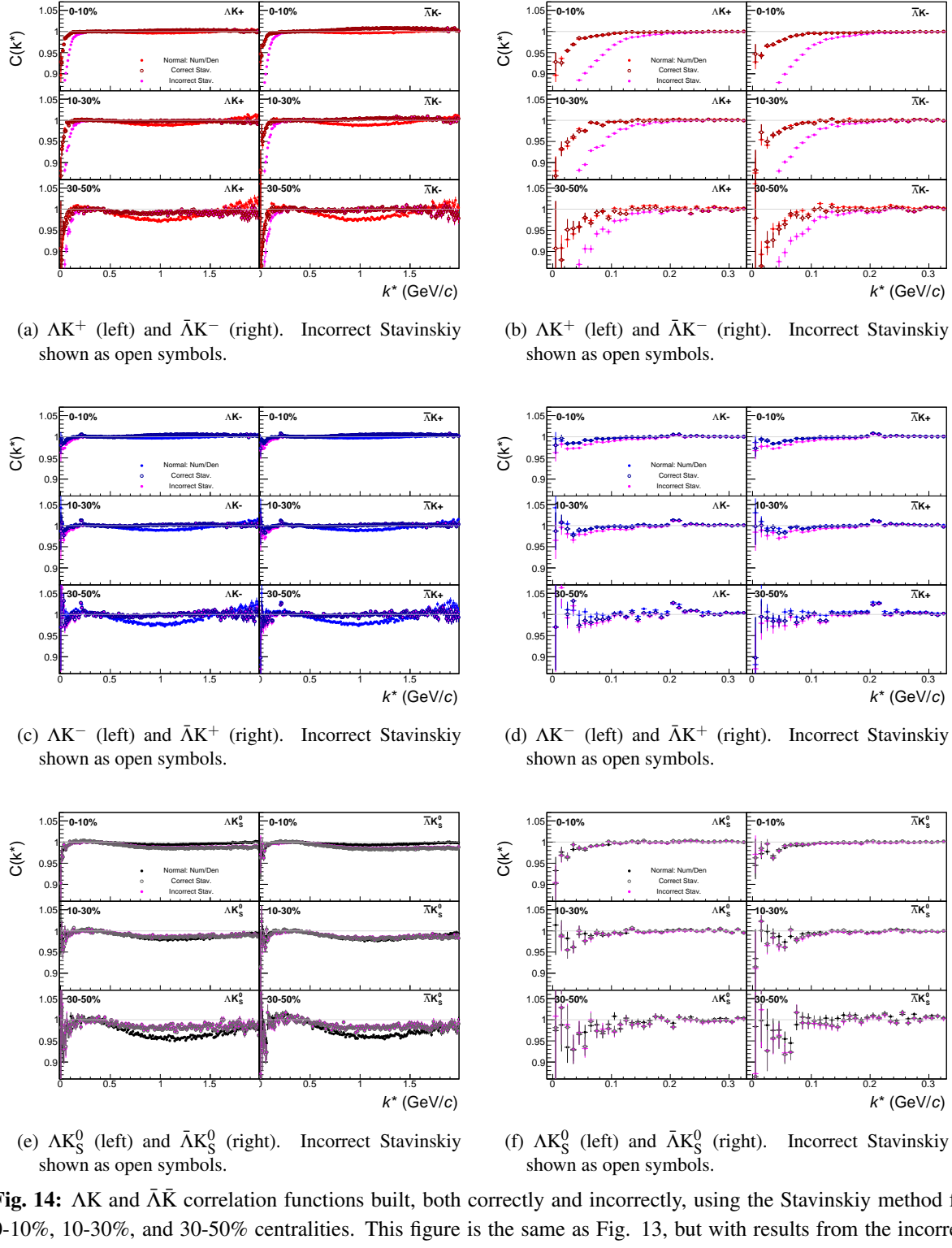


**Fig. 14:**  $\Lambda K$  and  $\bar{\Lambda} \bar{K}$  correlation functions built, both correctly and incorrectly, using the Stavinskiy method for 0-10%, 10-30%, and 30-50% centralities. This figure is the same as Fig. 13, but with results from the incorrect Stavinskiy implementation shown in magenta. The closed, (red, blue, black) symbols represent correlation functions formed using the normal method with mixed-event background pairs. The open, cyan symbols represent correlation functions formed using the correct Stavinskiy method. The closed, magenta symbols represent correlation functions formed using the incorrect Stavinskiy method. In the correct method, the pseudo-pairs (same-event pairs with one particle rotated by  $180^\circ$  in the transverse plane) are also run through the pair cuts used in the analysis; in the incorrect method, they are not. Figures in the right column are zoomed-in versions of figures in the left column.

323 **5 Fitting**

324 **5.1 Model:  $\Lambda K_S^0, \Lambda K^\pm, \Xi^- K_S^0$**

325 The two-particle relative momentum correlation function may be written theoretically by the Koonin-  
326 Pratt equation [3, 4]:

$$C(\mathbf{k}^*) = \int S(\mathbf{r}^*) |\Psi_{\mathbf{k}^*}(\mathbf{r}^*)|^2 d^3 \mathbf{r}^* \quad (4)$$

327 where  $S(\mathbf{r}^*)$  is the pair source distribution,  $\Psi_{\mathbf{k}^*}(\mathbf{r}^*)$  is the two-particle wave-function, and  $k^*$  is the  
328 momentum of one particle in the pair rest frame. In the absence of Coulomb effects, and assuming a  
329 spherically Gaussian source of width  $R$ , and s-wave scattering, the 1D femtoscopic correlation function  
330 can be calculated analytically using:

$$C(k^*) = 1 + C_{QI}(k^*) + C_{FSI}(k^*) \quad (5)$$

331  $C_{QI}$  describes plane-wave quantum interference:

$$C_{QI}(k^*) = \alpha \exp(-4k^{*2}R^2) \quad (6)$$

332 where  $\alpha = (-1)^{2j}/(2j+1)$  for identical particles with spin  $j$ , and  $\alpha = 0$  for non-identical particles. For  
333 all analyses presented in this note,  $\alpha = 0$ .  $C_{FSI}$  describes the s-wave strong final state interaction between  
334 the particles:

$$\begin{aligned} C_{FSI}(k^*) &= (1 + \alpha) \left[ \frac{1}{2} \left| \frac{f(k^*)}{R} \right|^2 \left( 1 - \frac{d_0}{2\sqrt{\pi}R} \right) + \frac{2\Re f(k^*)}{\sqrt{\pi}R} F_1(2k^*R) - \frac{\Im f(k^*)}{R} F_2(2k^*R) \right] \\ f(k^*) &= \left( \frac{1}{f_0} + \frac{1}{2} d_0 k^{*2} - ik^* \right)^{-1}; \quad F_1(z) = \int_0^z \frac{e^{x^2-z^2}}{z} dx; \quad F_2(z) = \frac{1-e^{-z^2}}{z} \end{aligned} \quad (7)$$

335 where  $R$  is the source size,  $f(k^*)$  is the s-wave scattering amplitude,  $f_0$  is the complex scattering length,  
336 and  $d_0$  is the effective range of the interaction.

337 An additional parameter  $\lambda$  is typically included in the femtoscopic fit function to account for the purity  
338 of the pair sample. In the case of no residual correlations (to be discussed in Section 5.4), the fit function  
339 becomes:

$$C(k^*) = 1 + \lambda [C_{QI}(k^*) + C_{FSI}(k^*)] \quad (8)$$

340 **5.2 Model:  $\Xi^- K^\pm$**

341 The two-particle correlation function may be written as:

$$C(\mathbf{k}^*) = \sum_S \rho_S \int S(\mathbf{r}^*) |\Psi_{\mathbf{k}^*}^S(\mathbf{r}^*)|^2 d^3 \mathbf{r}^* \quad (9)$$

342 where  $\rho_S$  is the normalized emission probability of particles in a state with spin  $S$ ,  $S(\mathbf{r}^*)$  is the pair  
343 emission source distribution (assumed to be Gaussian), and  $\Psi_{\mathbf{k}^*}^S(\mathbf{r}^*)$  is the two-particle wave-function  
344 including both strong and Coulomb interactions [5]:

$$\Psi_{\mathbf{k}^*}(\mathbf{r}^*) = e^{i\delta_c} \sqrt{A_c(\eta)} [e^{i\mathbf{k}^*\cdot\mathbf{r}^*} F(-i\eta, 1, i\xi) + f_c(k^*) \frac{\tilde{G}(\rho, \eta)}{r^*}] \quad (10)$$

where  $\rho = k^*r^*$ ,  $\eta = (k^*a_c)^{-1}$ ,  $\xi = \mathbf{k}^* \cdot \mathbf{r}^* + k^*r^* \equiv \rho(1 + \cos\theta^*)$ , and  $a_c = (\mu z_1 z_2 e^2)^{-1}$  is the two-particle Bohr radius (including the sign of the interaction).  $\delta_c$  is the Coulomb s-wave phase shift,  $A_c(\eta)$  is the Coulomb penetration factor,  $\tilde{G} = \sqrt{A_c}(G_0 + iF_0)$  is a combination of the regular ( $F_0$ ) and singular ( $G_0$ ) s-wave Coulomb functions.  $f_c(k^*)$  is the s-wave scattering amplitude:

$$f_c(k^*) = \left[ \frac{1}{f_0} + \frac{1}{2} d_0 k^{*2} - \frac{2}{a_c} h(\eta) - ik^* A_c(\eta) \right]^{-1} \quad (11)$$

where, the “h-function”,  $h(\eta)$ , is expressed through the digamma function,  $\psi(z) = \Gamma'(z)/\Gamma(z)$  as:

$$h(\eta) = 0.5[\psi(i\eta) + \psi(-i\eta) - \ln(\eta^2)] \quad (12)$$

In this case, the  $\lambda$  parameter may be included as:

$$C(\mathbf{k}^*) = (1 - \lambda) + \lambda \sum_S \rho_S \int S(\mathbf{r}^*) |\Psi_{\mathbf{k}^*}^S(\mathbf{r}^*)|^2 d^3\mathbf{r}^* \quad (13)$$

### 5.3 Momentum Resolution Corrections

Finite track momentum resolution causes the reconstructed momentum of a particle to smear around the true value. This, of course, also holds true for V0 particles. The effect is propagated up to the pairs of interest, which causes the reconstructed relative momentum ( $k_{\text{Rec}}^*$ ) to differ from the true momentum ( $k_{\text{True}}^*$ ). Smearing of the momentum typically will result in a suppression of the signal. More specifically, the smearing will broaden the signal, which would cause a decrease in the extracted radius of the system.

The effect of finite momentum resolution can be investigated using the HIJING MC data, for which both the true and reconstructed momenta are available. Figure 15 shows sample  $k_{\text{True}}^*$  vs.  $k_{\text{Rec}}^*$  plots for  $\Lambda K^\pm$  0-10% analyses; Figure 15a was generated using same-event pairs, while Figure 15b was generated using mixed-event pairs (with  $N_{\text{mix}} = 5$ ).

If there are no contaminations in our particle collection, the plots in Figure 15 should be smeared around  $k_{\text{True}}^* = k_{\text{Rec}}^*$ ; this is mostly true in our analyses. However, there are some interesting features of our results which demonstrate a small (notice the log-scale on the z-axis) contamination in our particle collection. The structure around  $k_{\text{Rec}}^* = k_{\text{True}}^* - 0.15 \text{ GeV}/c$  is mainly caused by  $K_S^0$  contamination in our  $\Lambda(\bar{\Lambda})$  sample. The remaining structure not distributed about  $k_{\text{Rec}}^* = k_{\text{True}}^*$  is due to  $\pi$  and  $e$  contamination in our  $K^\pm$  sample. These contaminations are more visible in Figure 16, which show  $k_{\text{Rec}}^*$  vs.  $k_{\text{True}}^*$  plots (for a small sample of the  $\Lambda K^\pm$  0-10% central analysis), for which the MC truth (i.e. true, known identity of the particle) was used to eliminate misidentified particles in the  $K^+(a)$  and  $\Lambda(b)$  collections. (NOTE: This is an old figure and is for a small sample of the data. A new version will be generated shortly. It, nonetheless, demonstrates the point well).

Information gained from looking at  $k_{\text{Rec}}^*$  vs  $k_{\text{true}}$  can be used to apply corrections to account for the effects of finite momentum resolution on the correlation functions. A typical method (“Ratio” method) involves using the MC HIJING data to build two correlation functions,  $C_{\text{Rec}}(k^*)$  and  $C_{\text{True}}(k^*)$ , using the generator-level momentum ( $k_{\text{True}}^*$ ) and the measured detector-level momentum ( $k_{\text{Rec}}^*$ ). The data is then corrected by multiplying by the ratio,  $C_{\text{True}}/C_{\text{Rec}}$ , before fitting. This essentially unsmears the data, which then can be compared directly to theoretical predictions and fits. Although this is conceptually simple, there are a couple of big disadvantages to this method. First, HIJING does not incorporate final-state interactions, so weights must be used when building same-event (numerator) distributions. These weights account for the interactions, and, in the absence of Coulomb interactions, can be calculated using Eq. 5. Of course, these weights are valid only for a particular set of fit parameters. Therefore, in the fitting process, during which the fitter explores a large parameter set, the corrections will not remain valid. As

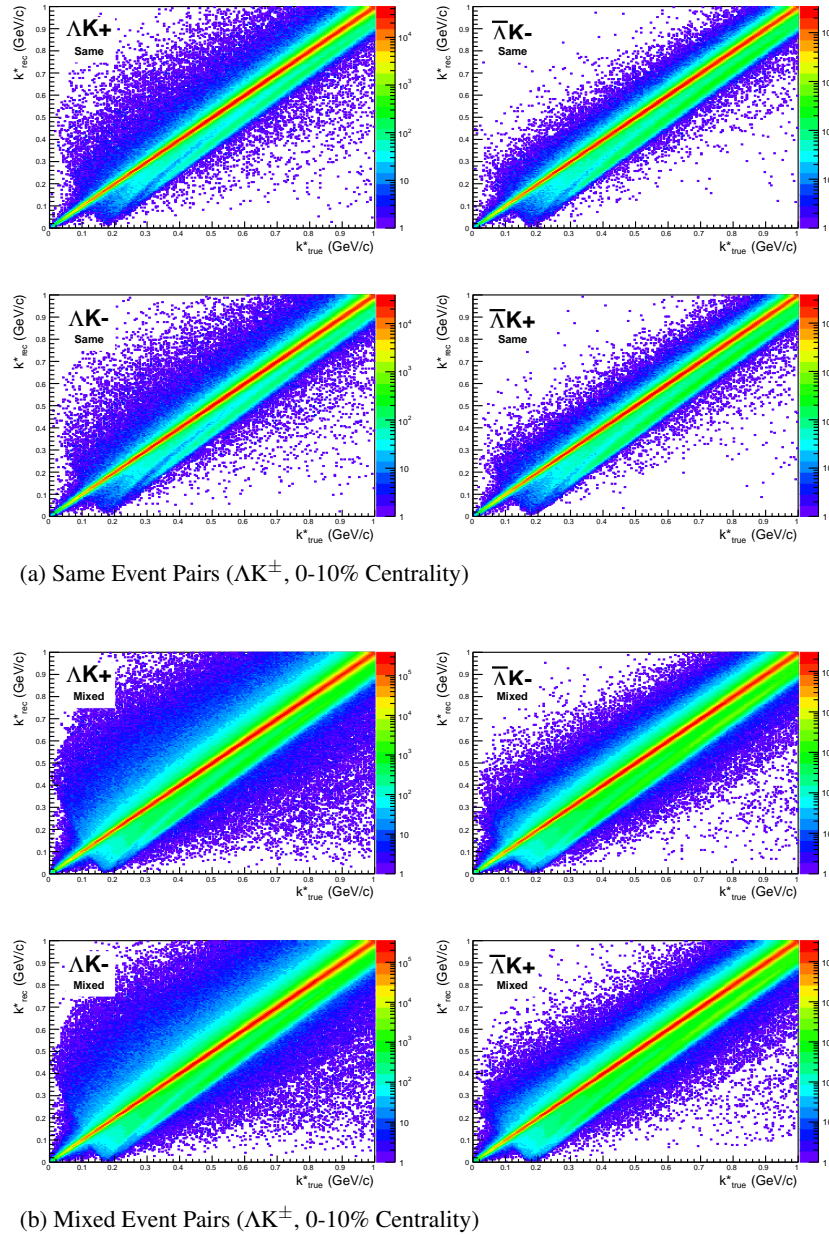
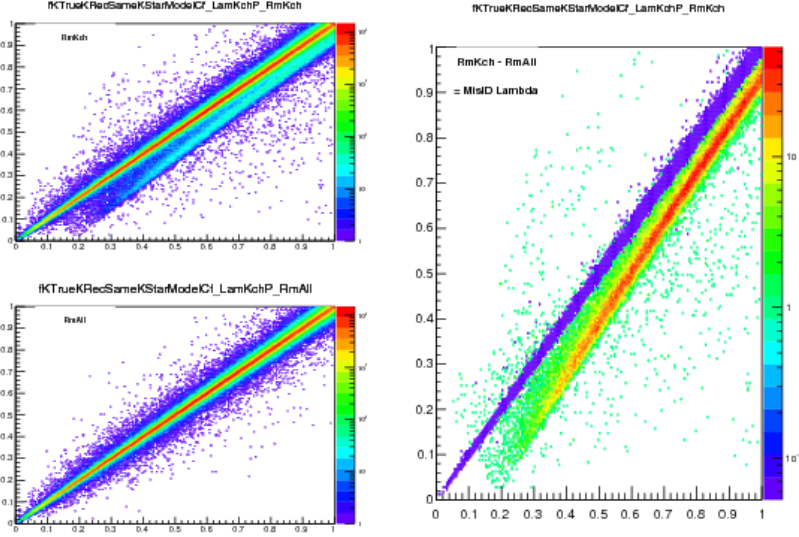
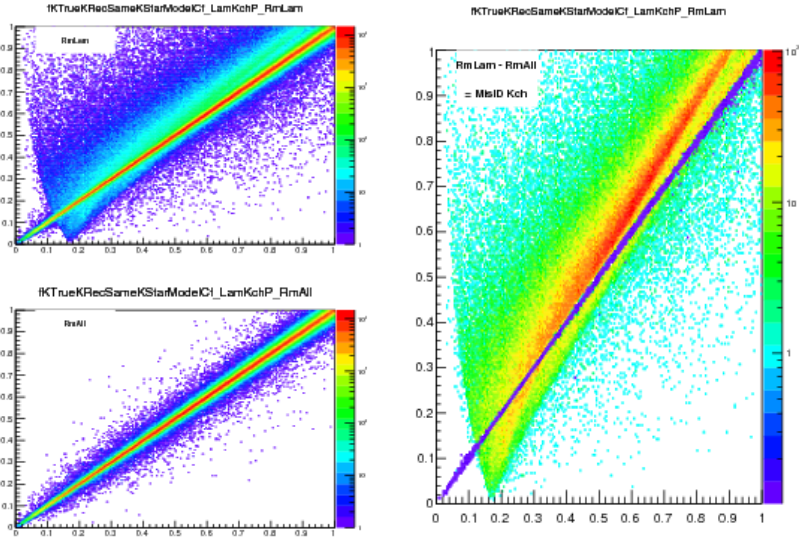


**Fig. 15:** Sample  $k_{\text{True}}^*$  vs.  $k_{\text{Rec}}^*$  plots from MC HIJING events for  $\Lambda K^\pm$  0-10% analyses. The structure which appears around  $k_{\text{Rec}}^* = k_{\text{True}}^* - 0.15 \text{ GeV}/c$  is mainly caused by  $K_S^0$  contamination in our  $\Lambda(\bar{\Lambda})$  sample. The remaining structure not distributed about  $k_{\text{Rec}}^* = k_{\text{True}}^*$  is due to  $\pi$  and  $e$  contamination in our  $K^\pm$  sample. These contaminations are more clearly visible in Figure 16

such, applying the momentum resolution correction and fitting becomes a long and drawn out iterative process. An initial parameter set is obtained (through fitting without momentum resolution corrections, theoretical models, or a good guess), then the MC data is analyzed to obtain correlation functions needed to calculate the correction factor, the data is fit using the correction factor, a refined parameter set is extracted, the MC data is analyzed again to obtain the new correction factor, etc. This process continues until the parameter set stabilizes. The second issue concerns statistics. With the MC data available on the grid, we were not able to generate the statistics necessary to use the raw  $C_{\text{True}}/C_{\text{Rec}}$  ratio. The ratio was not stable, and when applied to the data, obscured the signal. Attempting to fit the ratio to use to generate the corrections also proved problematic. However, as HIJING does not include final-state interactions, the same-event and mixed-event pairs are very similar (with the exception of things like



(a) (Top Left) All misidentified  $K^+$  excluded. (Bottom Left) All misidentified  $\Lambda$  and  $K^+$  excluded. (Right) The difference of (Top Left) - (Bottom Left), which reveals the contamination in our  $\Lambda$  collection. The structure which appears around  $k_{\text{Rec}}^* = k_{\text{True}}^* - 0.15 \text{ GeV}/c$  is mainly caused by  $K_S^0$  contamination in our  $\Lambda(\bar{\Lambda})$  sample.



(b) (Top Left) All misidentified  $\Lambda$  excluded. (Bottom Left) All misidentified  $\Lambda$  and  $K^+$  excluded. (Right) The difference of (Top Left) - (Bottom Left), which reveals the contamination in our  $K^+$  collection. The structure not distributed about  $k_{\text{Rec}}^* = k_{\text{True}}^*$  is due to  $\pi$  and  $e^-$  contamination in our  $K^\pm$  sample.

**Fig. 16:** In the figure, the y-axis =  $k_{\text{Rec}}^*$ , and the x-axis =  $k_{\text{True}}^*$ . (Left)  $k_{\text{Rec}}^*$  vs.  $k_{\text{True}}^*$  plots for a small sample of the  $\Lambda K^+$  0-10% central analysis, MC truth was used to eliminate misidentified particles in the  $K^+$  (a) and  $\Lambda$  (b) collections. (Right) The difference of the top left and bottom left plots. Contaminations in our particle collections are clearly visible. Figure (a) demonstrates a  $K_S^0$  contamination in our  $\Lambda$  collection; Figure (b) demonstrates a  $\pi$  and  $e^-$  contamination in our  $K^\pm$  collection.

392 energy and momentum conservation, etc). Therefore, one may build the numerator distribution using  
 393 mixed-event pairs. This corresponds, more or less, to simply running the weight generator through the  
 394 detector framework.

395 A second approach (“Matrix” method) is to use information gained from plots like those in Figure 15,

396 which can be considered response matrices. The response matrix describes quantitatively how each  
 397  $k_{\text{Rec}}^*$  bin receives contributions from multiple  $k_{\text{True}}^*$  bins, and can be used to account for the effects of  
 398 finite momentum resolution. With this approach, the resolution correction is applied on-the-fly during  
 399 the fitting process by propagating the theoretical correlation function (fit) through the response matrix,  
 400 according to:

$$C_{\text{Fit}}(k_{\text{Rec}}^*) = \frac{\sum_{k_{\text{True}}^*} M_{k_{\text{Rec}}^*, k_{\text{True}}^*} C_{\text{Fit}}(k_{\text{True}}^*)}{\sum_{k_{\text{True}}^*} M_{k_{\text{Rec}}^*, k_{\text{True}}^*}} \quad (14)$$

401 where  $M_{k_{\text{Rec}}^*, k_{\text{True}}^*}$  is the response matrix (Figure 15),  $C_{\text{Fit}}(k_{\text{True}}^*)$  is the fit binned in  $k_{\text{True}}^*$ , and the denominator normalizes the result.

403 Equation 14 describes that, for a given  $k_{\text{Rec}}^*$  bin, the observed value of  $C(k_{\text{Rec}}^*)$  is a weighted average of  
 404 all  $C(k_{\text{True}}^*)$  values, where the weights are the normalized number of counts in the  $[k_{\text{Rec}}^*, k_{\text{True}}^*]$  bin. As  
 405 seen in Figure 15, overwhelmingly the main contributions comes from the  $k_{\text{Rec}}^* = k_{\text{True}}^*$  bins. Although  
 406 the correction is small, it is non-negligible for the low- $k^*$  region of the correlation function.

407 Here, the momentum resolution correction is applied to the fit, not the data. In other words, during  
 408 fitting, the theoretical correlation function is smeared just as real data would be, instead of unsmearing  
 409 the data. This may not be ideal for the theorist attempting to compare a model to experimental data, but  
 410 it leaves the experimental data unadulterated. The current analyses use this second approach to applying  
 411 momentum resolution corrections because of two major advantages. First, the MC data must be analyzed  
 412 only once, and no assumptions about the fit are needed. Secondly, the momentum resolution correction  
 413 is applied on-the-fly by the fitter, delegating the iterative process to a computer instead of the user.

414 The two methods described above, Ratio and Matrix, should reproduce the same results at the parameter  
 415 set used to generate the  $C_{\text{True}}/C_{\text{Rec}}$  needed for the Ratio method. Figure 17 shows that the two methods  
 416 converge as the binning size is decreased.

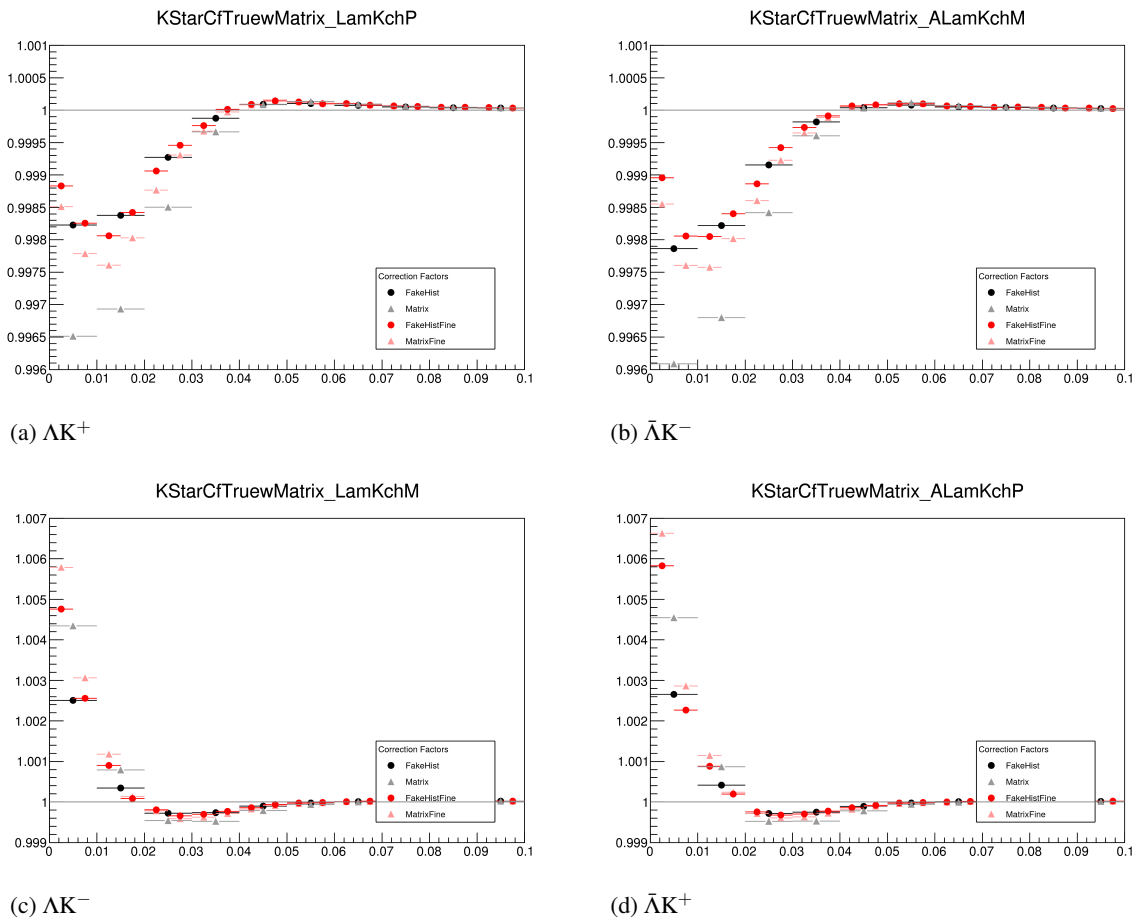


**Fig. 17:** Comparison of the two methods, Ratio and Matrix, for accounting for momentum resolution effects with HIJING. The Ratio method corresponds to the “FakeHist” histograms (circles), while the Matrix method corresponds to the “Matrix” histograms (triangles). Black shows a course binning, while red shows a finer binning.

417 **5.4 Residual Correlations**

418 The purpose of this analysis is study the interaction and scale of the emitting source of the primary  
 419 ΛK pairs. In order to obtain correct results, it is desirable for our particle collections to consist of  
 420 primary particles. In practice, this is impossible to achieve; many of our particles are not primary,  
 421 but originate as decay products from other resonances. Some of our Λ hyperons decay from  $\Sigma^0$ ,  $\Xi^0$ ,  
 422  $\Xi^-$  and  $\Sigma^{*(+,-,0)}(1385)$  parents, and some of our K mesons decay from  $K^{*(+,-,0)}(892)$  parents. In  
 423 these decays, the daughter carries away a momentum very similar to that of its parent. As a result,  
 424 the correlations between the particles in the daughter pair will be sensitive to, and dependent upon, the  
 425 interaction between the parents. In effect, the correlation between the parents will be visible, although  
 426 smeared out, in the daughters' signal. We call this a residual correlation resulting from feed-down. The  
 427 contributions from the primary correlation, residual correlations, and fake pairs on the finally measure  
 428 data is shown schematically in Figure 18. Residual correlations are important in an analysis when three  
 429 criteria are met [6]: i) the parent correlation signal is large, ii) a large fraction of pairs in the sample  
 430 originate from the particular parent system, and iii) the decay momenta are comparable to the expected  
 431 correlation width in  $k^*$ .

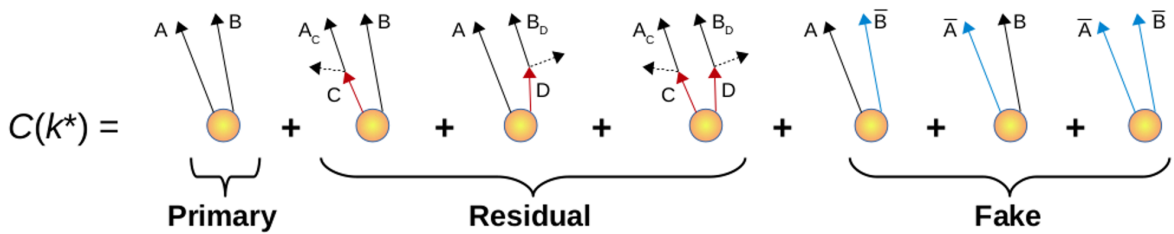


**Fig. 18:** A schematic representation of the contributions to the finally measured data from the primary correlation, residual correlations, and fake pairs.

432 As it is difficult for us to eliminate these residual correlations in our analyses, we must attempt to account  
 433 for them in our fit. The genuine ΛK correlation function may be combined with the contributions from  
 434 residual feed-down and misidentified particles to obtain the final, measured correlation function:

$$C_{\text{measured}}(k_{\Lambda K}^*) = 1 + \lambda'_{\Lambda K}[C_{\Lambda K}(k_{\Lambda K}^*) - 1] + \sum_{i,j} \lambda'_{ij}[C_{ij}(k_{\Lambda K}^*) - 1] \quad (15)$$

$$\begin{aligned} \lambda'_{ij} &= \lambda_{\text{Fit}} \lambda_{ij} \\ \sum_{i,j} \lambda'_{ij} &= \lambda_{\text{Fit}} \sum_{i,j} \lambda_{ij} = \lambda_{\text{Fit}} \end{aligned}$$

435 where the  $\Lambda K$  term represents the genuine  $\Lambda K$  correlation, and the  $i, j$  terms denote the contributions  
 436 from residual feed-down and possible impurities. More specifically,  $C_{ij}(k_{\Lambda K}^*)$  is the correlation function  
 437 between parents of particle species  $i$  and  $j$ , expressed in the basis of the relative momentum of the  
 438 observed daughter  $\Lambda K$  pairs. The  $\lambda$  parameters serve as weight dictating the strength of the parent  
 439 contribution to the daughter pair, and are normalized to unity. The individual  $\lambda_{ij}$  are fixed (and whose  
 440 values can be found in Table 5), but the parameter  $\lambda_{\text{Fit}}$  is left free. The  $\lambda_{\text{Fit}}$  parameter serves as an overall  
 441 normalization shared by all contributors.

442 In order to obtain the parent correlation function expressed in the relative momentum of the daughter  
 443 pair, one must use a transform matrix. The transform matrix describes the decay kinematics of the parent  
 444 system into the daughter, and maps the  $k^*$  of the parent pair onto that of the daughter. Using this matrix,  
 445 the transformed residual correlation function can be obtained:

$$C_{ij}(k_{\Lambda K}^*) \equiv \frac{\sum_{k_{ij}^*} C_{ij}(k_{ij}^*) T(k_{ij}^*, k_{\Lambda K}^*)}{\sum_{k_{ij}^*} T(k_{ij}^*, k_{\Lambda K}^*)} \quad (16)$$

The transform matrix is generated with the THERMINATOR 2 [?] simulation. It is formed for a given parent pair,  $ij$ , by taking all  $\Lambda K$  pairs originating from  $ij$ , calculating the relative momentum of the parents ( $k_{ij}^*$ ) and daughters ( $k_{\Lambda K}^*$ ), and filling a two-dimensional histogram with the values. The transform matrix is essentially an unnormalized probability distribution mapping the  $k^*$  of the parent pair to that of the daughter pair when one or both parents decay. An example of such transform matrices can be found in Figures 19 and 20.

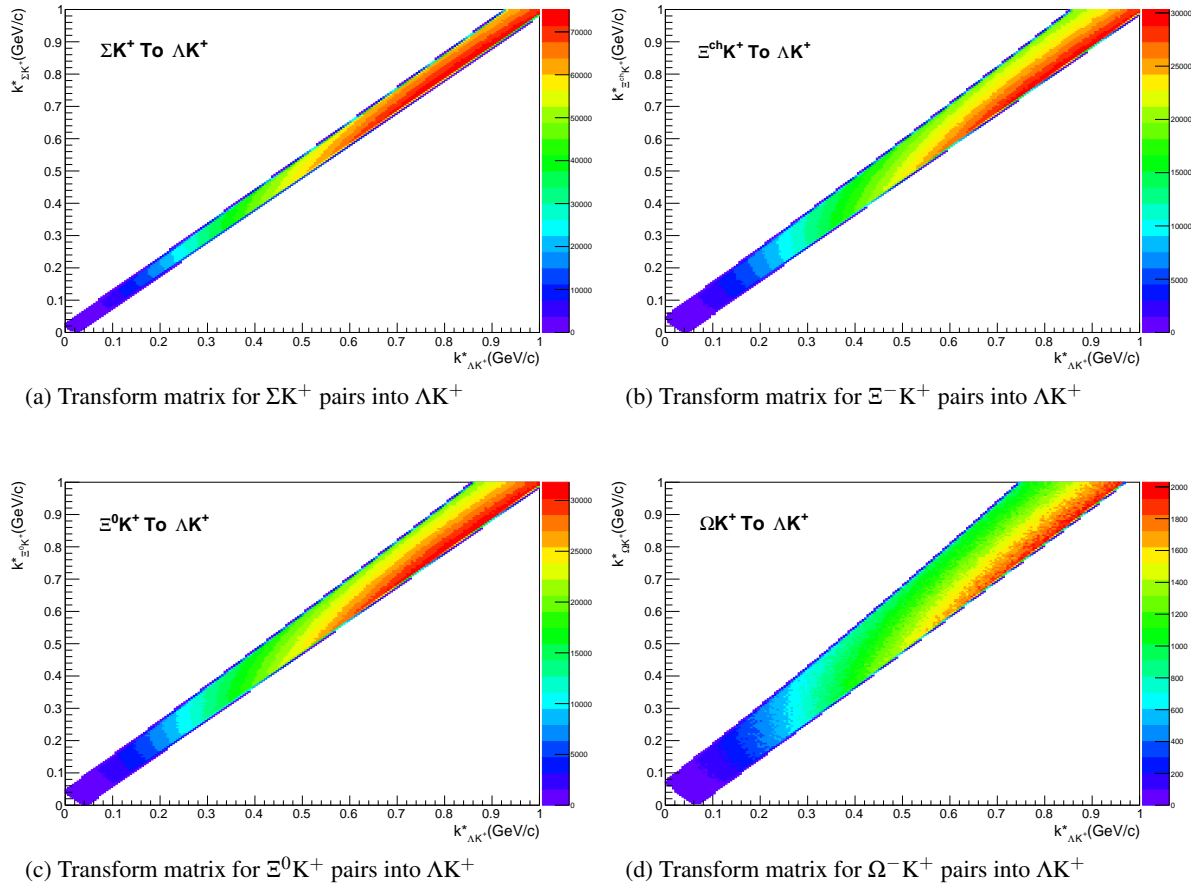


**Fig. 19:** Sample Transform Matrices generated with THERMINATOR for  $\Lambda K^+$  Analysis

Femtoscopic analyses are sensitive to the pair emission structure at kinetic freeze-out. Therefore, in the eyes of femtoscopy, any particle born from a resonance decay before last rescattering is seen as primary. For our study, when including three residual contributors, we consider a particle to be primary if its parent has a proper decay length of  $c\tau < 10$  fm. When including ten residual contributors, we must reduce this number to  $c\tau < 4$  fm for consistency. Moving to ten contributors, we introduce feed-down from  $\Sigma^*$  and  $K^*$  resonances, with proper decay lengths of  $c\tau \approx 5$  fm and  $c\tau \approx 4$  fm, respectively. As these are considered non-primary for the case of ten contributors, so must any resonance with  $c\tau > 4$  fm.

As previously stated, the  $\lambda$  parameters dictate the strength of the parent contribution to the daughter pair. Therefore, the  $\lambda$  parameter for parent system AB can be estimated as the total number of  $\Lambda K$  pairs in our

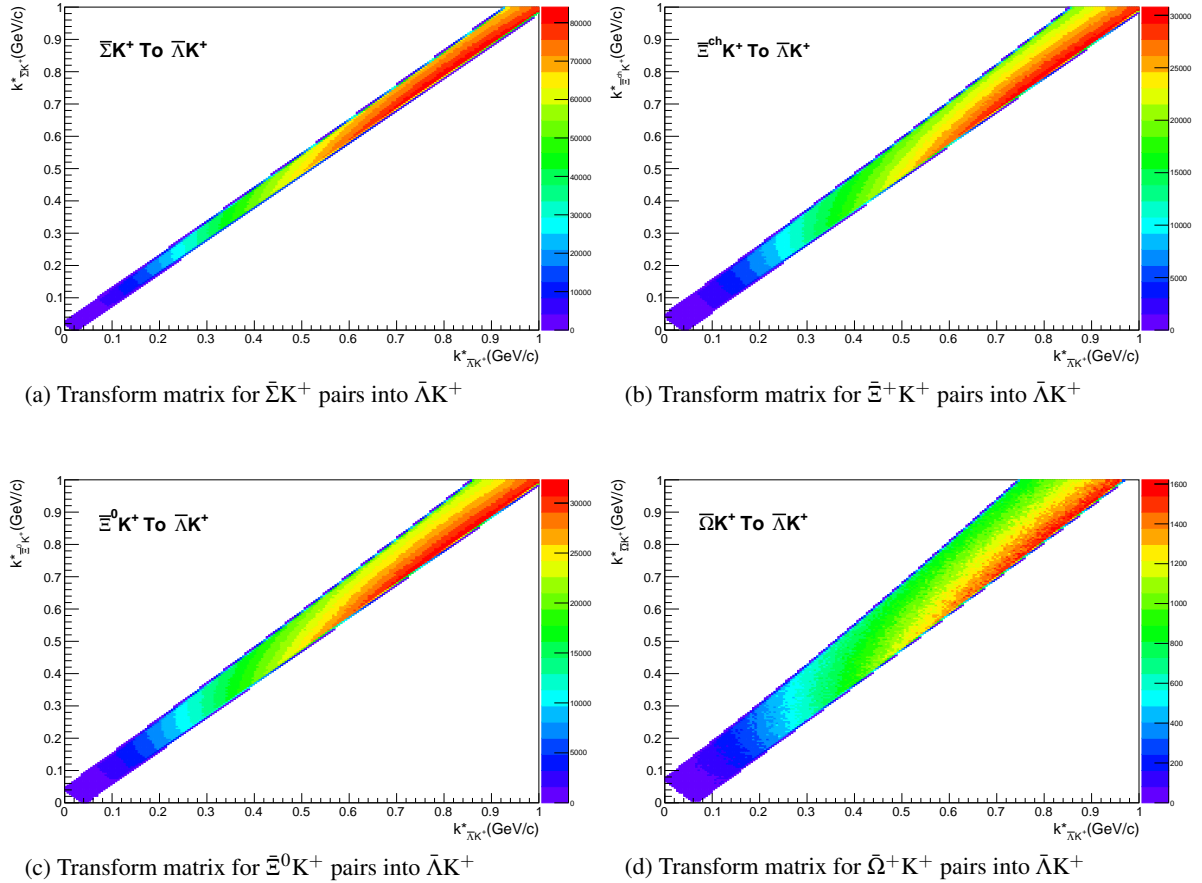


**Fig. 20:** Sample Transform Matrices generated with THERMINATOR for  $\bar{\Lambda}K^+$  Analysis

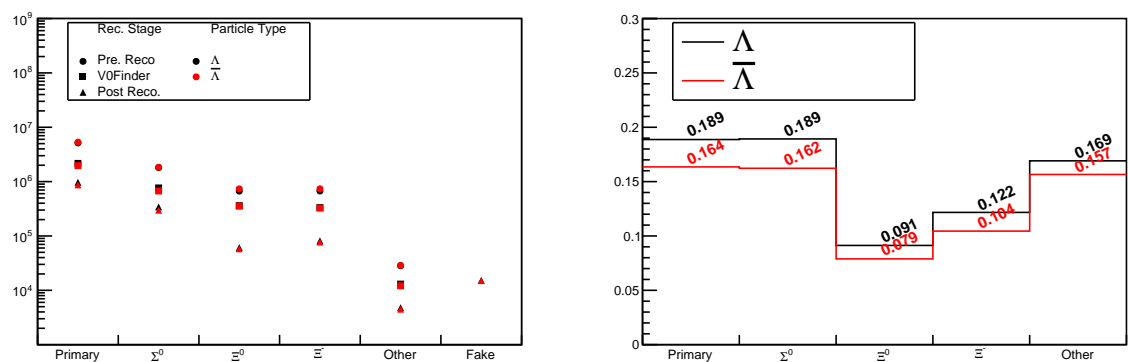
experimental sample originating from AB ( $N_{AB}$ ) divided by the total number of  $\Lambda K$  pairs ( $N_{Total}$ ):

$$\lambda_{AB} = \frac{N_{AB}}{N_{Total}} \quad (17)$$

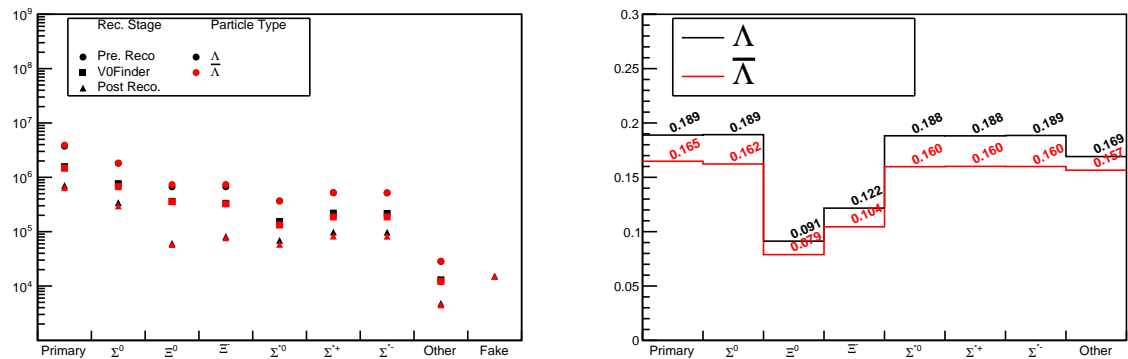
The particle yields can be estimated using THERMINATOR 2 simulation ( $N_{ij}^{THERM}$ ), while the reconstruction efficiencies ( $RE_{ij}$ ) are estimated with MC HIJING data, which has been run through GEANT to simulate the detector response (Fig. 21). Thus, the  $\lambda$  parameters are estimated as:

$$\lambda_{AB} = \frac{N_{AB}}{N_{Total}} = \frac{N_{AB}^{THERM} RE_{AB}^{HIJING}}{\sum_{ij} N_{ij}^{THERM} RE_{ij}^{HIJING}} \quad (18)$$

The  $\lambda$  values used can be found in Table 5, for the case of both three and ten residual contributors. In the table, we also list the  $\lambda$  values used for “Other” and “Fakes”. The “Other” category contains pairs which are not primary, and which do not originate from the (3 or 10) residual pairs included in the fit. The “Fakes” category represents pairs that are mistakenly identified as  $\Lambda K$ . To estimate this  $\lambda_{Fakes}$  value, we assumed that the number of fake pairs was equal to the total number of pairs multiplied by the  $\Lambda$  purity (i.e. assuming perfect purity for the kaons); or, more simply,  $\lambda_{Fakes} = 1.0 - \text{Purity}(\Lambda)$ . For both of these contributors (“Other” and “Fakes”), we assume that these correlations average to unity, and therefore do not contribute to the final correlation function.



(a) Reconstruction Efficiencies (3 Residuals)



(b) Reconstruction Efficiencies (10 Residuals)

**Fig. 21:** Reconstruction Efficiencies

$\Lambda K^+$ residuals		$\bar{\Lambda}K^-$ residuals		$\Lambda K^-$ residuals		$\bar{\Lambda}K^+$ residuals		$\Lambda K_S^0$ residuals		$\bar{\Lambda}K_S^0$ residuals	
Pair System	$\lambda$ value	Pair System	$\lambda$ value	Pair System	$\lambda$ value	Pair System	$\lambda$ value	Pair System	$\lambda$ value	Pair System	$\lambda$ value
3 Residuals (Max Parent $c\tau_{\text{decay}} = 10 \text{ fm}$ )											
$\Lambda K^+$	0.527	$\bar{\Lambda}K^-$	0.526	$\Lambda K^-$	0.526	$\bar{\Lambda}K^+$	0.527	$\Lambda K_S^0$	0.543	$\bar{\Lambda}K_S^0$	0.544
$\Sigma^0 K^+$	0.111	$\bar{\Sigma}^0 K^-$	0.110	$\Sigma^0 K^-$	0.110	$\bar{\Sigma}^0 K^+$	0.111	$\Sigma^0 K_S^0$	0.120	$\bar{\Sigma}^0 K_S^0$	0.120
$\Xi^0 K^+$	0.039	$\bar{\Xi}^0 K^-$	0.035	$\Xi^0 K^-$	0.038	$\bar{\Xi}^0 K^+$	0.036	$\Xi^0 K_S^0$	0.042	$\bar{\Xi}^0 K_S^0$	0.039
$\Xi^- K^+$	0.050	$\bar{\Xi}^+ K^-$	0.046	$\Xi^- K^-$	0.050	$\bar{\Xi}^+ K^+$	0.046	$\Xi^- K_S^0$	0.054	$\bar{\Xi}^+ K_S^0$	0.050
Other	0.226	Other	0.235	Other	0.228	Other	0.233	Other	0.194	Other	0.199
Fakes	0.048	Fakes	0.048	Fakes	0.048	Fakes	0.048	Fakes	0.048	Fakes	0.048
10 Residuals (Max Parent $c\tau_{\text{decay}} = 4 \text{ fm}$ )											
$\Lambda K^+$	0.180	$\bar{\Lambda}K^-$	0.180	$\Lambda K^-$	0.179	$\bar{\Lambda}K^+$	0.181	$\Lambda K_S^0$	0.192	$\bar{\Lambda}K_S^0$	0.193
$\Sigma^0 K^+$	0.116	$\bar{\Sigma}^0 K^-$	0.114	$\Sigma^0 K^-$	0.115	$\bar{\Sigma}^0 K^+$	0.116	$\Sigma^0 K_S^0$	0.125	$\bar{\Sigma}^0 K_S^0$	0.124
$\Xi^0 K^+$	0.040	$\bar{\Xi}^0 K^-$	0.037	$\Xi^0 K^-$	0.040	$\bar{\Xi}^0 K^+$	0.037	$\Xi^0 K_S^0$	0.043	$\bar{\Xi}^0 K_S^0$	0.040
$\Xi^- K^+$	0.052	$\bar{\Xi}^+ K^-$	0.047	$\Xi^- K^-$	0.052	$\bar{\Xi}^+ K^+$	0.048	$\Xi^- K_S^0$	0.056	$\bar{\Xi}^+ K_S^0$	0.052
$\Sigma^{*+} K^+$	0.054	$\bar{\Sigma}^{*-} K^-$	0.051	$\Sigma^{*+} K^-$	0.053	$\bar{\Sigma}^{*-} K^+$	0.051	$\Sigma^{*+} K_S^0$	0.058	$\bar{\Sigma}^{*-} K_S^0$	0.055
$\Sigma^{*-} K^+$	0.048	$\bar{\Sigma}^{*+} K^-$	0.050	$\Sigma^{*-} K^-$	0.048	$\bar{\Sigma}^{*+} K^+$	0.050	$\Sigma^{*-} K_S^0$	0.052	$\bar{\Sigma}^{*+} K_S^0$	0.054
$\Sigma^{*0} K^+$	0.048	$\bar{\Sigma}^{*0} K^-$	0.045	$\Sigma^{*0} K^-$	0.048	$\bar{\Sigma}^{*0} K^+$	0.045	$\Sigma^{*0} K_S^0$	0.052	$\bar{\Sigma}^{*0} K_S^0$	0.048
$\Lambda K^{*0}$	0.046	$\bar{\Lambda}K^{*0}$	0.047	$\Lambda \bar{K}^{*0}$	0.046	$\bar{\Lambda}K^{*0}$	0.047	$\Lambda K^{*0}$	0.022	$\bar{\Lambda}K^{*0}$	0.022
$\Sigma^0 K^{*0}$	0.041	$\bar{\Sigma}^0 \bar{K}^{*0}$	0.041	$\Sigma^0 \bar{K}^{*0}$	0.041	$\bar{\Sigma}^0 K^{*0}$	0.041	$\Sigma^0 K^{*0}$	0.019	$\bar{\Sigma}^0 K^{*0}$	0.019
$\Xi^0 K^{*0}$	0.014	$\bar{\Xi}^0 \bar{K}^{*0}$	0.013	$\Xi^0 \bar{K}^{*0}$	0.014	$\bar{\Xi}^0 K^{*0}$	0.013	$\Xi^0 K^{*0}$	0.007	$\bar{\Xi}^0 K^{*0}$	0.006
$\Xi^- K^{*0}$	0.018	$\bar{\Xi}^+ \bar{K}^{*0}$	0.017	$\Xi^- \bar{K}^{*0}$	0.018	$\bar{\Xi}^+ K^{*0}$	0.017	$\Xi^- K^{*0}$	0.009	$\bar{\Xi}^+ K^{*0}$	0.008
Other	0.295	Other	0.310	Other	0.299	Other	0.307	Other	0.318	Other	0.330
Fakes	0.048	Fakes	0.048	Fakes	0.048	Fakes	0.048	Fakes	0.048	Fakes	0.048

**Table 5:**  $\lambda$  values for the individual components of the  $\Lambda K$  correlation functions for the case of 3 and 10 residual contributions.

473 In practice, we model the correlation function of the parents (ex.  $\Sigma^0 K^+$ ), and run the correlation function  
474 through the appropriate transform matrix to determine the contribution to the daughter correlation func-  
475 tion (ex.  $\Lambda K^+$ ). In an ideal world, we would simply look up the parent interaction in some table, and  
476 input this into our model, and form the parent correlation function,  $C_{ij}$ , through the Lednicky equation  
477 (for the case of one or more charge neutral particle in the pair), or via the CoulombFitter machinery  
478 described in Sec.5.2. Unfortunately, the world in which we live is not perfect, such a table does not  
479 exist, and little is known about the interaction between the particles in the residual pairs of this study.  
480 Additionally, introducing a unique set of scattering parameters and radii for each residual system would  
481 introduce a large number of additional fit parameters, for which we do not have many constraints, and  
482 would cause our fitter to be too unconstrained and yield untrustworthy results. Therefore, for this analy-  
483 sis, we assume all residual pairs have the same source size as the daughter pair. Furthermore, we assume  
484 Coulomb-neutral residual pairs share the same scattering parameters as the daughter pair. Therefore, for  
485 Coulomb-neutral pairs, such as  $\Sigma^0 K$ , and  $\Xi^0 K$ ,  $C_{ij}(k_{ij}^*)$  is calculated from Eqn. 5, with the help of Eqn. 7;  
486  $C_{ij}(k_{\Lambda K}^*)$  is then obtained by transforming  $C_{ij}(k_{ij}^*)$  with Eq. 16, using the appropriate transform matrix.

487 For residual pairs affected by both the strong and Coulomb interactions, things are a bit more compli-  
488 cated. This is due to the fact that, for the case of both strong and Coulomb interaction, we no longer  
489 have a nice analytical form with which to fit. Generating a correlation function including both is also  
490 time consuming, as described further in Sec.5.2. This increase in formation time is not an issue in gen-  
491 erating single correlation functions, however, it does become a problem when including the method in  
492 the fit process, where thousands of generated correlation functions are needed (the parallelization of the  
493 process across a large number of GPU cores, to drastically decrease run-time, is currently underway).  
494 Therefore, when modeling  $\Xi^- K^\pm$  residual correlations, we use the experimental  $\Xi^- K^\pm$  data; in this case,  
495 there is no need to make any assumptions about scattering parameters or source sizes. The downside is  
496 that, especially in the 30-50% centrality bin, the statistics are low and error bars large. For the other  
497 cases, we assume the strong interaction is negligible, and generate the parent correlation assuming a  
498 Coulomb-only scenario (see Sec.5.2 for more details). This approximation is well justified here as a  
499 Coulomb-only description of the system describes, reasonably well, the broad features of the  $\Xi^{ch} K^{ch}$   
500 correlation; the strong interaction is necessary for the fine details. However, as these correlations are  
501 run through a transform matrix, which largely flattens out and fine details, a Coulomb-only description  
502 should be sufficient.

503 In practice, the Coulomb-only scenario is achieved by first building a large number of Coulomb-only  
504 correlations for various radii and  $\lambda$  parameter values, and interpolating from this grid during the fitting  
505 process. This allows us to generate the correlations functions with the speed needed to converge on  
506 fit results within a reasonable amount of time. We find consistent results between using the  $\Xi K$  data  
507 and the Coulomb-only interpolation method. When quantifying the  $\Xi^- K^\pm$  residual contribution, the  
508 experimental  $\Xi^- K^\pm$  data is always used. When the number of residual pairs used is increased to 10,  
509 so that contributors such as  $\Sigma^{*+} K^-$  enter the picture, the Coulomb-only interpolation method is used.  
510 In other words, the  $\Xi K$  experimental data is only used to model the  $\Xi K$  residual contribution, all other  
511 charged pairs are treated with the Coulomb-only interpolation method.

512 Two examples of how very different transform matrices can alter a correlation function are shown in  
513 Figures 22 and 23 below. These figures were taken using parameter values obtained from fits to the data.  
514 In the top left corner of the figures, the input correlation function (closed symbols) is shown together  
515 with the output, transformed, correlation function (open symbols). In the bottom left, the transformed  
516 correlation is shown by itself (with zoomed y-axis). This is especially helpful when the  $\lambda$  parameter is  
517 very small, in which case the contribution in the top left can look flat, but the zoomed in view in the  
518 bottom left shows the structure. The right two plots in each figure show the transform matrix without  
519 (top right) and with (bottom right) a log-scale on the z-axis. Note, more examples of these transforms  
520 can be found in Sec. 9.

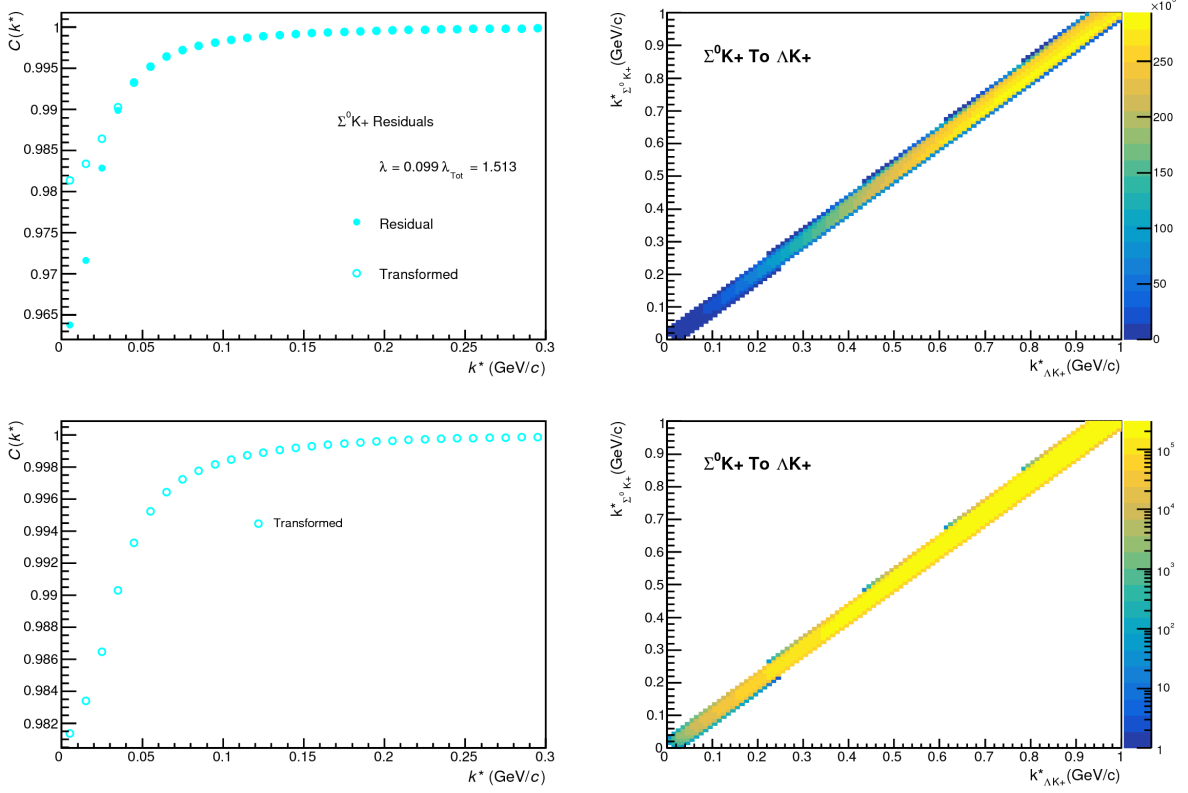


**Fig. 22:**  $\Sigma^0 K^+$  Transform. These figures were taken using parameter values obtained from fits to the data. In the top left corner of the figures, the input correlation function (closed symbols) is shown together with the output, transformed, correlation function (open symbols). In the bottom left, the transformed correlation is shown by itself. The right two plots in each figure show the transform matrix without (top right) and with (bottom right) a log-scale on the z-axis.

Concerning the radii of the residual parent pairs, it was suggested that these should be set to smaller values than those of the daughter pair. In the interest of minimizing the number of parameters in the fitter, we tested this by introducing an  $m_T$ -scaling of the parents' radii. The motivation for this scaling comes from the approximate  $m_T$ -scaling of the radii observed in 30. To achieve this scaling, we assume the radii follow an inverse-square-root distribution:  $R_{AB} = \alpha m_T^{-1/2}$ . Then, it follows that we should scale the parent radii as:

$$R_{AB} = R_{\Lambda K} \left( \frac{m_{T,AB}}{m_{T,\Lambda K}} \right)^{-1/2} \quad (19)$$

The values of  $m_T$  for each pair system were taken from THERMINATOR. As the fitter dances around parameter space and selects a new radius for the  $\Lambda K$  system, the radii of the residuals is simply the  $\Lambda K$  radius scaled by the appropriate factor, given above (Eq.19). In the end, this scaling factor made no significant difference in our fit results, so this complication is excluded from our final results. Note that this is not surprising, as the most extreme scaling factor was, in the case of using 10 residual systems, between  $\Lambda K^+$  with  $m_{T,\Lambda K^+} \approx 1.4 \text{ GeV}/c^2$  and  $\Xi^- K^{*0}$  with  $m_{T,\Xi^- K^{*0}} \approx 1.8 \text{ GeV}/c^2$ , resulting in a scale factor of  $\approx 0.9$ .

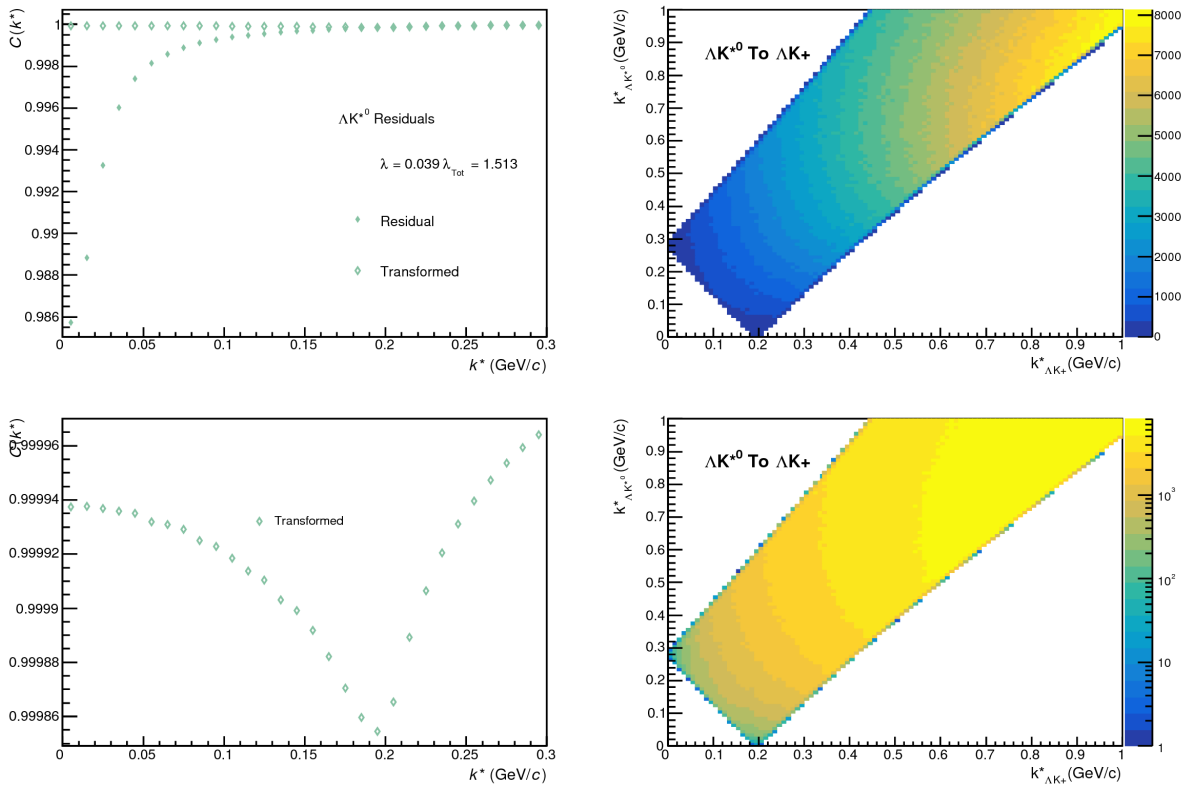


**Fig. 23:**  $\Lambda K^{*0}$  Transform. These figures were taken using parameter values obtained from fits to the data. In the top left corner of the figures, the input correlation function (closed symbols) is shown together with the output, transformed, correlation function (open symbols). In the bottom left, the transformed correlation is shown by itself. The right two plots in each figure show the transform matrix without (top right) and with (bottom right) a log-scale on the z-axis.

534 **5.5 Non-Flat Background**

535 We observe a significant non-femtoscopic, non-flat, background in all of our correlations at large  $k^*$ .  
 536 This background increases with decreasing centrality, is the same amongst all  $\Lambda K^\pm$  pairs, and is more  
 537 pronounced in the  $\Lambda K_S^0$  system, as can be seen in Fig. 24. Figure 25a shows that THERMINATOR 2  
 538 simulation does a good job of describing the difference in backgrounds between  $\Lambda K^\pm$  and  $\Lambda K_S^0$ .

539 Before beginning, it is important to note that the difference in  $\Lambda K^\pm$  and  $\Lambda K_S^0$  backgrounds is due mainly  
 540 to the difference in kinematic cuts, not due to any interesting physics. Figure 25b shows that, for THER-  
 541 MINATOR simulation, when restrictions are imposed on the  $p_T$  of the  $K_S^0$  to more closely match the  
 542  $K^\pm$  cuts, the backgrounds align much better. Therefore, we conclude that the difference in background  
 543 between  $\Lambda K^\pm$  and  $\Lambda K_S^0$  observed in our experimental data is simply due to a difference in kinematic cuts  
 544 between  $K^\pm$  and  $K_S^0$  particles.

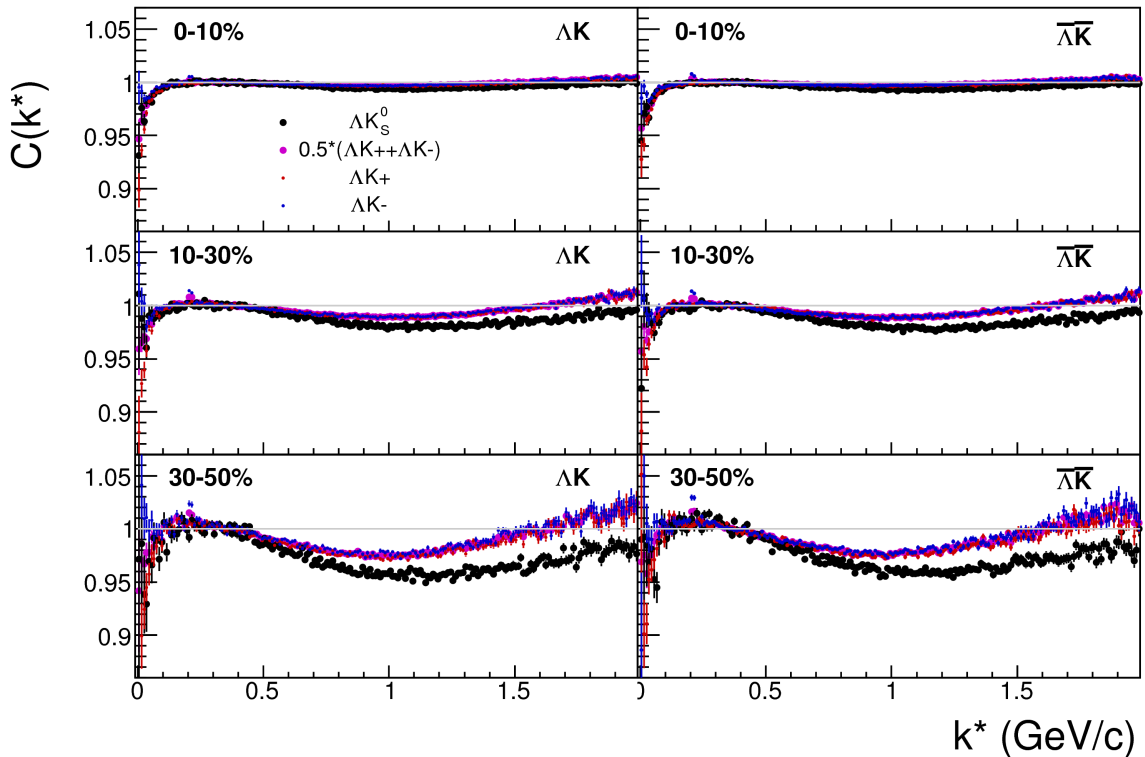


**Fig. 24:** A comparison on the non-femtoscopic backgrounds observed in our our  $\Lambda K$  experimental data.

545 It is suggested that this background effect is due primarily to particle collimation associated with elliptic  
 546 flow [8]. More specifically, these backgrounds result from mixing events with unlike event-plane angles  
 547 ( $\Psi_{EP}$ ). As explained in [8], when elliptic flow is present, all particles are more likely to be emitted  
 548 in a specific direction (in-plane), as opposed to a perpendicular direction. Therefore, the difference in  
 549 momenta for pairs of particles tends to be smaller, compared to the case of no flow. In the case of mixed-  
 550 event pairs, the two events used do not share an event-plane, and therefore there is no collimation effect  
 551 in the pairs from flow. As a result, pairs with larger momentum are more likely when mixed-events are  
 552 used, causing the correlation function to be observed below unity. In general, a dip below unity, at a given  
 553  $k^*$ , means it is more probable to find a pair at that  $k^*$  when the daughters are taken from mixed-events, as  
 554 compared to when they are taken from the same event.

555 This same reasoning suggests that the background should lead to an enhancement at low- $k^*$ . The en-  
 556 hancement at high- $k^*$  ( $k^* \gtrsim 1.5 \text{ GeV}/c$ ) does not result from the collective flow of the system. We are not

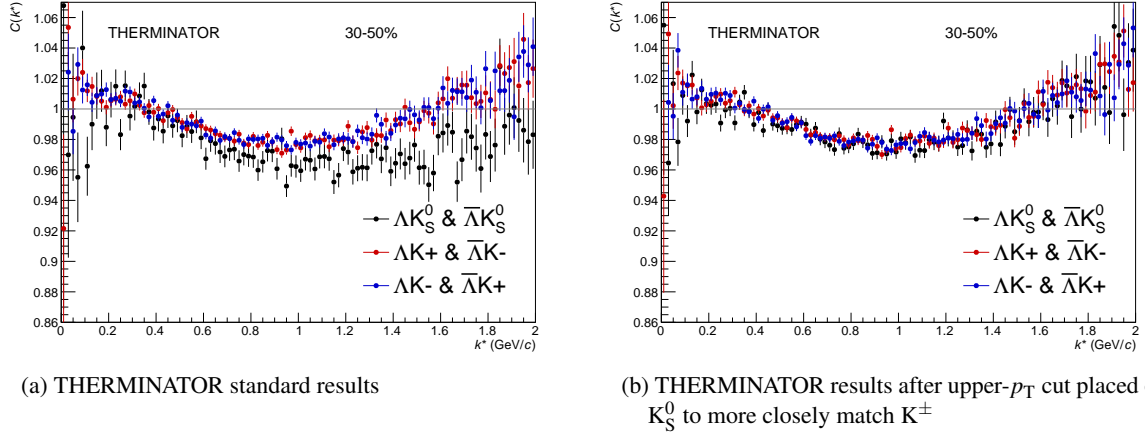


**Fig. 25:** THERMINATOR 2 simulation for  $\Lambda K^+$  (red),  $\Lambda K^-$  (blue), and  $\Lambda K_S^0$  (black). In 25a, we show the standard THERMINATOR 2 results. THERMINATOR 2 does a good job describing qualitatively the different between the  $\Lambda K^\pm$  and  $\Lambda K_S^0$  backgrounds. In 25b, an upper- $p_T$  cut was placed on the  $K_S^0$  particles to more closely match the  $K^\pm$  kinematic cuts. After this tweak, the  $\Lambda K^\pm$  and  $\Lambda K_S^0$  backgrounds agree much better.

557 certain what causes this enhancement, but typical suspects are jet-like correlations and resonance decays.  
 558 We can split our correlation functions into three main regions. First, the low- $k^*$  region ( $k^* \lesssim 0.3$  GeV/ $c$ )  
 559 contains the femtoscopic correlations, as well as a likely enhancement from the background. The  
 560 intermediate- $k^*$  region ( $0.3 \lesssim k^* \lesssim 1.5$  GeV/ $c$ ) contains a suppression from the background. Finally,  
 561 the high- $k^*$  region ( $k^* \gtrsim 1.5$  GeV/ $c$ ) contains an enhancement with unknown origin.  
 562 THERMINATOR 2 simulation has been shown to reproduce the background features in a  $\pi K$  analysis  
 563 [8]. As the background effect can be attributed mainly to elliptic flow, which is a global feature of the  
 564 system, we suspected THERMINATOR 2 could also, at least qualitatively, describe our backgrounds.  
 565 After ensuring each simulated event received a random event-plane angle ( $\Psi_{EP}$ )<sup>1</sup>, we found THERMI-  
 566 NATOR 2 did a good job of describing our data qualitatively, and, in many cases, quantitatively. Figure  
 567 26 shows the THERMINATOR 2 simulation (gold) together with experimental data (red, blue, or black).  
 568 The figure also shows a 6<sup>th</sup>-order polynomial fit to the simulation (gold), as well as the fit polynomial  
 569 scaled to match the data (red, blue, black).

570 Figure 27 shows three different correlation function generated using THERMINATOR 2 simulation (“Cf  
 571 w/o Bgd (A)”, “Cf w. Bgd (B)”, “Bgd(C)”), as well as two histograms describing the relation between  
 572 the three (“Ratio (B/C)”, “1+Diff(B-C)”). “Cf w/o Bgd (A)” shows a correlation function with a femto-  
 573 scopic correlation, but without background. When THERMINATOR 2 is run without randomizing event  
 574 planes, and therefore having all events share a common event plane, no background is observed, as ex-  
 575 pected. The femtoscopic correlation effect was introduced by assuming a set of scattering parameters for  
 576 the system, and weighting the numerators appropriately. The second correlation, ”Cf w. Bgd (B)”, shows  
 577 a correlation function with both a femtoscopic correlation and a background (most closely matches our  
 578 situation in experiment). To generate the background, each event was given a random event-plane angle,  
 579 as is given to us in experiment. To generate the femtoscopic correlation, the same numerator weighting  
 580 procedure was used. Finally, ”Bgd (C)”, shows a correlation function with a non-femtoscopic back-  
 581 ground, but no femtoscopic correlation, i.e. background only. This is generated just as ”Cf w. Bgd (B)”,  
 582 with randomized event planes, but unit weights are used when filling the numerators, so no femtoscopic  
 583 effects are included.

<sup>1</sup>default was for all events to share a common event plane

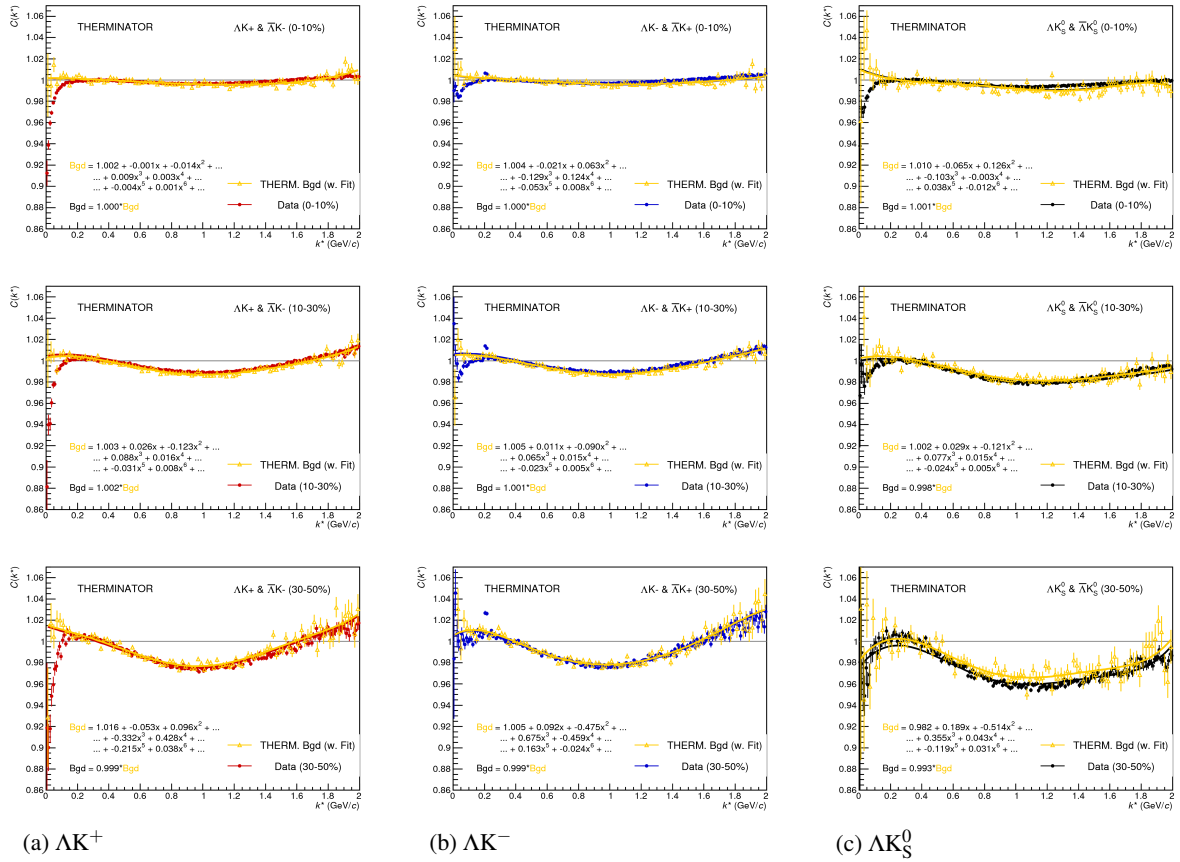


**Fig. 26:** THERMINATOR 2 simulation (gold) together with experimental data (red, blue, or black). The left column shows results for  $\Lambda K^+$  (26a), middle for  $\Lambda K^-$  (26b), and right for  $\Lambda K_S^0$  (26c). A 6<sup>th</sup>-order polynomial fit to the simulation is shown as a solid gold line, and whose fit parameters are printed on the lower left of each plot. This polynomial is scaled to match the experimental data; the value of this scale is printed in the lower left corner of each plot. The polynomial fit with scale factor applied is drawn in a color matching the experimental data (red, blue, black).

584 The main point of Fig. 27 is that the black points match the blue (and purple) points; or, equivalently:

$$C_{fw/oBgd} = \frac{C_{fw.Bgd}}{Bgd} \rightarrow C_{theory} = \frac{C_{exp}}{F_{Bgd}} \rightarrow C_{exp} = C_{theory} \cdot F_{Bgd} \quad (20)$$

585 As shown and described in Fig 27 and Eq. 20, THERMINATOR 2 simulation shows the non-femtosscopic  
 586 background affects the correlation function as a separable scale factor. We expect this behavior to be  
 587 roughly the same in the experimental data.

588 Figure 28 demonstrates the use of the Stavinskiy method with THERMINATOR 2. In the figure, unit  
 589 weights were used for all numerators, so no femtoscopy signal is included, only background effects.  
 590 The black points show an ideal, experimentally unreachable, situation of aligning all of the event-plane  
 591 angles. With THERMINATOR 2, when the event-planes are aligned, the background signal is killed.  
 592 The green points show the case of random event-plane angles, a situation more closely matching that  
 593 of experiment. The purple points show the affect of applying the Stavinskiy method to the case of  
 594 random event-planes. The figure shows that this method effectively kills the non-flat background (i.e.  
 595 the procedure takes the green points to the purple). Finally, the blue points show the effect of applying  
 596 the Stavinskiy method when all of the event-planes are aligned. This shows that the Stavinskiy method

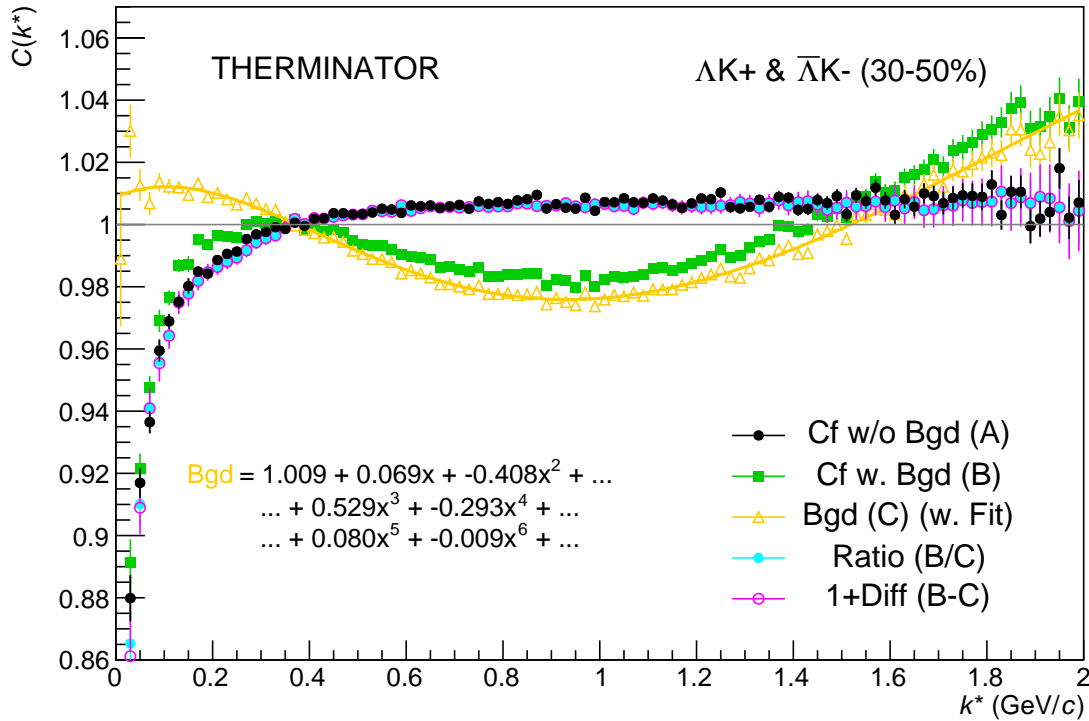


**Fig. 27:** Correlation with background decomposition with THERMINATOR. "Cf w/o Bgd (A)" shows a correlation function with a femtoscopic correlation, but without background. "Cf w. Bgd (B)", shows a correlation function with both a femtoscopic correlation and a background (most closely matches our situation in experiment). "Bgd (C)", shows a correlation function with a non-femtoscopic background, but no femtoscopic correlation, i.e. background only.

597 does not introduce any signal to an already flat background.

## 598 5.6 LednickyFitter

599 The code developed to fit the data is called "LednickyFitter", and utilizes the ROOT TMinuit implementation  
600 of the MINUIT fitting package. In short, given a function with a number of parameters, the fitter  
601 explores the parameter space searching for the minimum of the function. In this implementation, the  
602 function to be minimized should represent the difference between the measured and theoretical corre-  
603 lation functions. However, a simple  $\chi^2$  test is inappropriate for fitting correlation functions, as the ratio of  
604 two Poisson distributions does not result in a Poisson distribution. Instead, a log-likelihood fit function  
605 of the following form is used [2]:

$$\chi_{PML}^2 = -2 \left[ A \ln \left( \frac{C(A+B)}{A(C+1)} \right) + B \ln \left( \frac{A+B}{B(C+1)} \right) \right] \quad (21)$$

606 where  $A$  is the experimental signal distribution (numerator),  $B$  is the experimental background distribu-  
607 tion (denominator), and  $C$  is the theoretical fit correlation function.

608 The LednickyFitter uses Equations 5 – 7 to build the theoretical fit, and Equation 21 as the statistic  
609 quantifying the quality of the fit. The parameters to be varied by MINUIT are:  $\lambda$ ,  $R$ ,  $f_0$  ( $\mathbb{R}f_0$  and  $\mathbb{I}f_0$   
610 separately),  $d_0$ , and normalization  $N$ . The fitter currently includes methods to correct for momentum  
611 resolution and a non-flat background. These corrections are applied to the fit function, the data is never

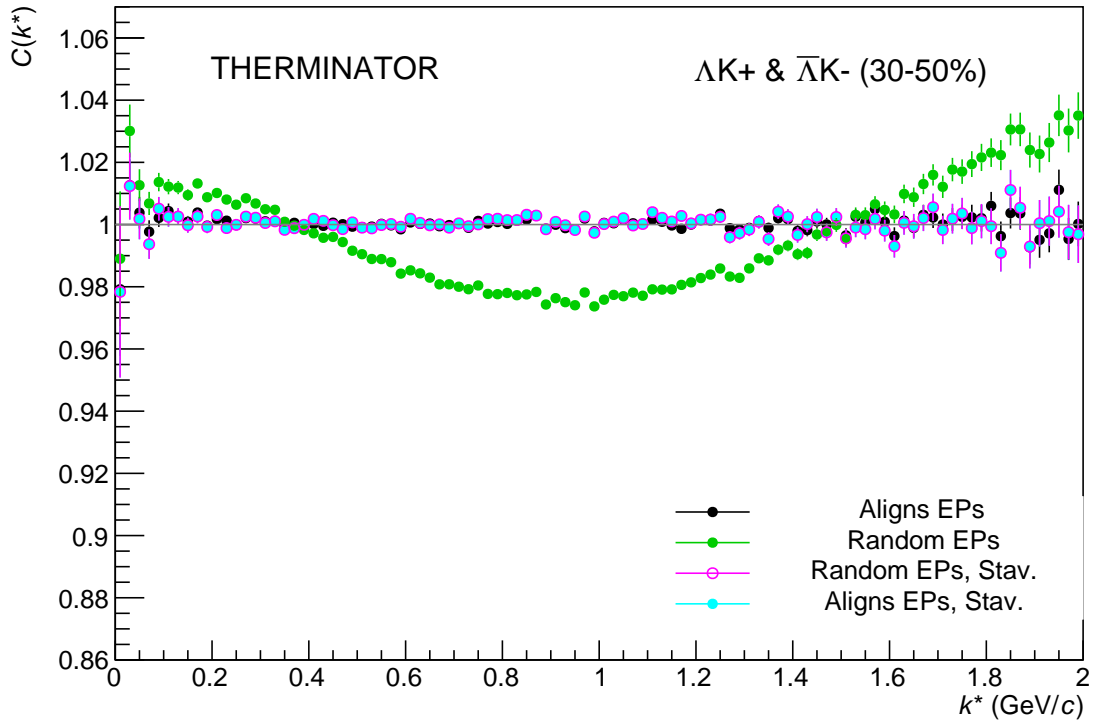


**Fig. 28:** The use of the Stavinskiy method with THERMINATOR 2. Unit weights were used for all numerators, so no femtoscopic signal is included, only background effects. The black points show an ideal, experimentally unreachable, situation of aligning all of the event-plane angles. The green points show the experimental situation of random event-plane angles. The purple points shown the affect of applying the Stavinskiy method to the case of random event-planes. Finally, the blue points show the effect of applying the Stavinskiy method when all of the event-planes are aligned.

- 612 touched. The fitter is able to share parameters between different analyses and fit all simultaneously.  
 613 In a typical fit, a given pair is fit with its conjugate (ex.  $\Lambda K^+$  with  $\bar{\Lambda} K^-$ ) across all centralities (0-10%,  
 614 10-30%, 30-50%), for a total of 6 simultaneous analyses. Each analysis has a unique  $\lambda$  and normalization  
 615 parameter. The radii are shared between analyses of like centrality, as these should have similar source  
 616 sizes. The scattering parameters ( $\mathbb{R}f_0, \mathbb{I}f_0, d_0$ ) are shared amongst all.  
 617 Initially, we left open the possibility for the  $\Lambda K^+(\bar{\Lambda} K^-)$  and  $\Lambda K^-(\bar{\Lambda} K^+)$  systems to have different source  
 618 radii. After always finding these two to be consistent, we decided to join the radii parameters between these  
 619 systems. So, now, in a typical fit of our  $\Lambda K^\pm$  data, all  $\Lambda K^\pm$  analyses ( $\Lambda K^+, \bar{\Lambda} K^-, \Lambda K^-, \bar{\Lambda} K^+$ ) are fit  
 620 simultaneously across all centralities. Scattering parameters are shared between pair-conjugate systems  
 621 (i.e. a parameter set describing the  $\Lambda K^+ & \bar{\Lambda} K^-$  system, and a separate set describing the  $\Lambda K^- & \bar{\Lambda} K^+$   
 622 system). For each centrality, a radius and  $\lambda$  parameters are shared amongst all pairs. Each analysis has a  
 623 unique normalization parameter.  
 624 In the case of fitting with residuals, the  $\lambda_{Fit}$  parameter serves as an overall normalization shared by all  
 625 contributors, such that Eqn 15 becomes:

$$\begin{aligned}
C_{measured}(k_{\Lambda K}^*) &= 1 + \sum_i \lambda'_i [C_i(k_{\Lambda K}^*) - 1] \\
\lambda'_i &= \lambda_{Fit} \lambda_i \\
\sum_i \lambda'_i &= \lambda_{Fit} \sum_i \lambda_i = \lambda_{Fit}
\end{aligned} \tag{22}$$

where  $\lambda_i$  is obtained from THERMINATOR, as explained in Section 5.4, and whose values are presented in Table 5. For Coulomb-neutral pairs, such as  $\Lambda K$ ,  $\Sigma^0 K$ , and  $\Xi^0 K$ ,  $C_i(k_{\Lambda K}^*)$  is calculated from Eqn. 5, with the help of Eqn. 7. For those residual pairs which include a Coulomb interaction,  $C_i(k_{\Lambda K}^*)$  is either calculated using the CoulombFitter method (Sections 5.2 and 5.7) with no strong interaction, or by using the  $\Xi^{ch} K^{ch}$  data directly. Unless otherwise stated, the  $\Xi^{ch} K^{ch}$  residual contribution is modeled using the experimental  $\Xi^{ch} K^{ch}$  data, and all other charged contributors (ex.  $\Sigma^{*ch} K^{ch}$ ) are modeled using the CoulombFitter technique with no strong interaction contribution.

To summarize, the complete fit function is constructed as follows:

1. The uncorrected, primary, correlation function,  $C_{\Lambda K}(k_{True}^*)$ , is constructed using Eq. 22 (with the help of Eqns. 5 and 7)
2. If residuals are included:
  - the parent correlation functions are obtained using:
    - Eq. 22 (with the help of Eqns. 5 and 7) for the case of Coulomb-neutral pairs
    - $\Xi^- K^\pm$  experimental data for  $\Xi^- K^\pm$  contributions
    - a Coulomb-only curve, with the help of Secs. 5.2 and 5.7, for pairs including the Coulomb interaction
  - the contribution to the  $\Lambda K$  correlation function is found by running the parent correlation function through the appropriate transform, via Eq. 16
3. The primary and residual correlations are combined, via Eq. 15, to form  $C'_{Fit}(k_{True}^*)$ 
  - in the case of no residual contributions included in the fit,  $\lambda_i = \lambda_{\Lambda K}$  in Eq. 22 is set equal to 1. Then, the extracted  $\lambda_{Fit}$  parameter should be roughly equal to the pair purity
  - when residuals are included, the  $\lambda_i$  values are presented in Table 5
4. The correlation function is corrected to account for momentum resolution effects using Eq. 14

$$C'_{fit}(k_{Rec}^*) = \frac{\sum_{k_{True}^*} M_{k_{Rec}^*, k_{True}^*} C'_{fit}(k_{True}^*)}{\sum_{k_{True}^*} M_{k_{Rec}^*, k_{True}^*}}$$

5. Finally, the non-flat background correction is applied, and the final fit function is obtained

$$C_{Fit}(k_{Rec}^*) = C'_{Fit}(k_{Rec}^*) * F_{Bgd}(k_{Rec}^*)$$

Figures 45, 46, and 47 (31, 32, and 33, or 38, 39, and 40), in Section 7, show experimental data with fits for all studied centralities for  $\Lambda K_S^0 (\bar{\Lambda} K_S^0)$ ,  $\Lambda K^+ (\bar{\Lambda} K^-)$ , and  $\Lambda K^- (\bar{\Lambda} K^+)$ , respectively. In the figures, the black solid line represents the “raw” fit, i.e. not corrected for momentum resolution effects nor non-flat background. The green line shows the fit to the non-flat background. The purple points show the fit after momentum resolution, non-flat background, and residual correlations (if applicable) corrections have been applied. The extracted fit values with uncertainties are also printed on the figures.

658 **5.7 Coulomb Fitter**

659 When fitting the  $\Xi^-(\bar{\Xi}^+)K^\pm$  results, it is necessary to include both strong and Coulomb effects. In this  
 660 case, Equation 5 is no longer valid, and, in fact, there is no analytical form with which to fit. We therefore  
 661 must take a more basic approach, and integrate out Eq.4 by hand. To achieve this, one has two options.  
 662 The first option is to numerically integrate Eq.4. The second option is to simulate a large sample of  
 663 particle pairs, calculate the wave function describing the interaction, and average to obtain the integral.  
 664 Having no experience with either of these options, we elected the latter of simulating pairs. The code  
 665 developed to achieve this functionality is called “CoulombFitter”. Currently, in order to generate the  
 666 statistics needed for a stable fit, we find that  $\sim 10^4$  simulated pairs per 10 MeV bin are necessary. The  
 667 nature of this process means that the “CoulombFitter” takes much longer to run than the “LednickyFitter”  
 668 of Section 5.1.

669 Unfortunately, with this analysis, we are not sensitive to, and therefore not able to distinguish between,  
 670 the iso-spin singlet and triplet states. We proceed with our analysis, but the results must be interpreted  
 671 as iso-spin averaged scattering parameters.

672 As stated before, to generate a fit correlation function, we must simulate a large number of pairs, calculate  
 673 the wave-function, and average  $\Psi^2$  over all pairs in a given  $k^*$  bin. Essentially, we calculate Equation 9  
 674 by hand:

$$\begin{aligned} C(\mathbf{k}^*) &= \sum_S \rho_S \int S(\mathbf{r}^*) |\Psi_{\mathbf{k}^*}^S(\mathbf{r}^*)|^2 d^3\mathbf{r}^* \\ &\longrightarrow C(|\mathbf{k}^*|) \equiv C(k^*) = \sum_S \rho_S \langle |\Psi^S(\mathbf{k}_i^*, \mathbf{r}_i^*)|^2 \rangle_i \\ &\longrightarrow C(k^*) = \lambda \sum_S \rho_S \langle |\Psi^S(\mathbf{k}_i^*, \mathbf{r}_i^*)|^2 \rangle_i + (1 - \lambda) \end{aligned} \quad (23)$$

675 where  $\langle \rangle_i$  represents an average over all pairs in a given  $k^*$  bin.

676 In summary, for a given  $k^*$  bin, we must draw  $N_{pairs} \sim 10^4$  pairs, and for each pair:

677 1. Draw a random  $\mathbf{r}^*$  vector according to our Gaussian source distribution  $S(\mathbf{r}^*)$

678 2. Draw a random  $\mathbf{k}^*$  vector satisfying the  $|\mathbf{k}^*|$  restriction of the bin

679 – We draw from real  $k^*$  vectors obtained from the data

680 – However, we find that drawing from a distribution flat in  $k^*$  gives similar results

681 3. Construct the wave-function  $\Psi$

682 After all pairs for a given  $k^*$  bin are simulated and wave-functions obtained, the results are averaged to  
 683 give the fit result.

684 Construction of the wave-functions, Equation 10, involves a number of complex functions not included  
 685 in standard C++ or ROOT libraries (namely,  $h(\eta)$ ,  $\tilde{G}(\rho, \eta)$ ), and  $F(-i\eta, 1, i\xi)$ . These functions were  
 686 even difficult to find and implement from elsewhere. Our solution was to embed a Mathematica kernel  
 687 into our C++ code to evaluate these functions. However, having Mathematica work on-the-fly with the  
 688 fitter was far too time consuming (fitter would have taken days, maybe weeks to finish). Our solution  
 689 was to use Mathematica to create matrices representing these functions for different parameter values.  
 690 During fitting, these matrices were then interpolated and the results used to build the wave-functions.  
 691 This method decreased the running time dramatically, and we are not able to generate results in under  $\sim$   
 692 1 hour. This process will be explained in more detail in future versions of the note.

## 6 Systematic Errors

In order to understand my systematic uncertainties, the analysis code was run many times using slightly different values for a number of important cuts, and the results were compared. To quantify the systematic errors on the data, all correlation functions built using all varied cut values were bin-by-bin averaged, and the resulting variance of each bin was taken as the systematic error. The cuts which were utilized in this study are presented in Sections 6.1.1 ( $\Lambda K_S^0$ ) and 6.2.1 ( $\Lambda K^\pm$ ).

Similarly, the fit parameters extracted from all of these correlation functions were averaged, and the resulting variances were taken as the systematic errors for the fit parameters. As with the systematic errors on the data, this was performed for all varied cut values. Additionally, a systematic analysis was done on our fit method (which, for now, just includes our choice of fit range and functional form used to model the non-femtoscopic background). These two sources of uncertainty were combined in quadrature to obtain the final systematic uncertainties on the extracted fit parameters.

### 6.1 Systematic Errors: $\Lambda K_S^0$

#### 6.1.1 Particle and Pair Cuts

The cuts included in the systematic study, as well as the values used in the variations, are listed below. Note, the central value corresponds to that used in the analysis.

$\Lambda K_S^0$ systematics	
DCA $\Lambda(\bar{\Lambda})$	4, 5, 6 mm
DCA $K_S^0$	2, 3, 4 mm
DCA $\Lambda(\bar{\Lambda})$ Daughters	3, 4, 5 mm
DCA $K_S^0$ Daughters	2, 3, 4 mm
$\Lambda(\bar{\Lambda})$ Cosine of Pointing Angle	0.9992, 0.9993, 0.9994
$K_S^0$ Cosine of Pointing Angle	0.9992, 0.9993, 0.9994
DCA to Primary Vertex of $p(\bar{p})$ Daughter of $\Lambda(\bar{\Lambda})$	0.5, 1, 2 mm
DCA to Primary Vertex of $\pi^-(\pi^+)$ Daughter of $\Lambda(\bar{\Lambda})$	2, 3, 4 mm
DCA to Primary Vertex of $\pi^+$ Daughter of $K_S^0$	2, 3, 4 mm
DCA to Primary Vertex of $\pi^-$ Daughter of $K_S^0$	2, 3, 4 mm
Average Separation of Like-Charge Daughters	5, 6, 7 cm

**Table 6:**  $\Lambda K_S^0$  systematics

#### 6.1.2 Non-Flat Background

We fit our non-flat background with a linear function. To study the contribution of this choice to our systematic errors, we also fit with a quadratic and Gaussian form. The resulting uncertainties are combined with the uncertainties arising from our particle cuts.

#### 6.1.3 Fit Range

Our choice of  $k^*$  fit range was varied by  $\pm 25\%$ . The resulting uncertainties in the extracted parameter sets were combined with our uncertainties arising from our particle and pair cuts.

716 **6.2 Systematic Errors:  $\Lambda K^\pm$**

717 **6.2.1 Particle and Pair Cuts**

718 The cuts included in the systematic study, as well as the values used in the variations, are listed below.  
 719 Note, the central value corresponds to that used in the analysis.

$\Lambda K^\pm$ systematics	
DCA $\Lambda(\bar{\Lambda})$	4, 5, 6 mm
DCA $\Lambda(\bar{\Lambda})$ Daughters	3, 4, 5 mm
$\Lambda(\bar{\Lambda})$ Cosine of Pointing Angle	0.9992, 0.9993, 0.9994
DCA to Primary Vertex of $p(\bar{p})$ Daughter of $\Lambda(\bar{\Lambda})$	0.5, 1, 2 mm
DCA to Primary Vertex of $\pi^-(\pi^+)$ Daughter of $\Lambda(\bar{\Lambda})$	2, 3, 4 mm
Average Separation of $\Lambda(\bar{\Lambda})$ Daughter with Same Charge as $K^\pm$	7, 8, 9 cm
Max. DCA to Primary Vertex in Transverse Plane of $K^\pm$	1.92, 2.4, 2.88
Max. DCA to Primary Vertex in Longitudinal Direction of $K^\pm$	2.4, 3.0, 3.6

Table 7:  $\Lambda K^\pm$  systematics

720 **6.2.2 Non-Flat Background**

721 We fit our non-flat background with a linear function. To study the contribution of this choice to our sys-  
 722 tematic errors, we also fit with a quadratic and Gaussian form. The resulting uncertainties are combined  
 723 with the uncertainties arising from our particle cuts.

724 **6.2.3 Fit Range**

725 Our choice of  $k^*$  fit range was varied by  $\pm 25\%$ . The resulting uncertainties in the extracted parameter  
 726 sets were combined with our uncertainties arising from our particle and pair cuts.

727 **6.3 Systematic Errors:  $\Xi K^\pm$**

728 **6.3.1 Particle and Pair Cuts**

729 The cuts included in the systematic study, as well as the values used in the variations, are listed below.  
 730 Note, the central value corresponds to that used in the analysis.

$\Xi^- K^\pm$  systematics

	$\Xi^- K^\pm$ systematics
Max. DCA $\Xi(\bar{\Xi})$	2, 3, 4 mm
Max. DCA $\Xi(\bar{\Xi})$ Daughters	2, 3, 4 mm
Min. $\Xi(\bar{\Xi})$ Cosine of Pointing Angle to Primary Vertex	0.9991, 0.9992, 0.9993
Min. $\Lambda(\bar{\Lambda})$ Cosine of Pointing Angle to $\Xi(\bar{\Xi})$ Decay Vertex	0.9992, 0.9993, 0.9994
Min. DCA Bachelor $\pi$	0.5, 1, 2 mm
Min. DCA $\Lambda(\bar{\Lambda})$	1, 2, 3 mm
Max. DCA $\Lambda(\bar{\Lambda})$ Daughters	3, 4, 5 mm
Min. DCA to Primary Vertex of $p(\bar{p})$ Daughter of $\Lambda(\bar{\Lambda})$	0.5, 1, 2 mm
Min. DCA to Primary Vertex of $\pi^-(\pi^+)$ Daughter of $\Lambda(\bar{\Lambda})$	2, 3, 4 mm
Min. Average Separation of $\Lambda(\bar{\Lambda})$ Daughter and $K^\pm$ with like charge	7, 8, 9 cm
Min. Average Separation of Bachelor $\pi$ and $K^\pm$ with like charge	7, 8, 9 cm
Max. DCA to Primary Vertex in Transverse Plane of $K^\pm$	1.92, 2.4, 2.88
Max. DCA to Primary Vertex in Longitudinal Direction of $K^\pm$	2.4, 3.0, 3.6

**Table 8:**  $\Xi^- K^\pm$  systematics

731 **7 Results and Discussion**

732 **7.1 Results:  $\Lambda K_S^0$  and  $\Lambda K^\pm$**

733 In the following sections, we present results assuming (i) three residual contributors (Sec. 7.1.1), (ii) ten  
 734 residual contributors (Sec. 7.1.2), and (iii) no residual correlations (Sec. 7.1.3).

735 For the results shown, unless otherwise noted, the following hold true: All correlation functions were  
 736 normalized in the range  $0.32 < k^* < 0.40$  GeV/c, and fit in the range  $0.0 < k^* < 0.30$  GeV/c. For the  $\Lambda K^-$   
 737 and  $\bar{\Lambda} K^+$  analyses, the region  $0.19 < k^* < 0.23$  GeV/c was excluded from the fit to exclude the bump  
 738 caused by the  $\Omega^-$  resonance. The non-femtoscopic backgrounds for the  $\Lambda K^+$  and  $\Lambda K^-$  systems were  
 739 modeled by a (6<sup>th</sup>-order polynomial fit to THERMINATOR simulation, while those for the  $\Lambda K_S^0$  were  
 740 fit with a simple linear form. The  $\Lambda K^+(\bar{\Lambda} K^-)$  radii are shared with  $\Lambda K^-(\bar{\Lambda} K^+)$ , while the  $\Lambda K_S^0(\bar{\Lambda} K_S^0)$   
 741 radii are unique. In the figures showing experimental correlation functions with fits, the black solid line  
 742 represents the primary ( $\Lambda K$ ) correlation's contribution to the fit. The green line shows the fit to the non-  
 743 flat background. The purple points show the fit after all residuals' contributions have been included, and  
 744 momentum resolution and non-flat background corrections have been applied.

745 Before beginning, I first collect a summary of my final results in Figure 29. In the summary plot, we  
 746 show the extracted scattering parameters in the form of a  $\text{Im}[f_0]$  vs  $\text{Re}[f_0]$  plot, which includes the  $d_0$   
 747 values to the right side. We also show the  $\lambda$  vs. radius parameters for all three of our studied centrality  
 748 bins. In Fig. 29, three residual contributors were used. For the  $\Lambda K_S^0$  results shown in the figure, the  $\Lambda K_S^0$   
 749 and  $\bar{\Lambda} K_S^0$  analyses were fit simultaneously across all centralities (0-10%, 10-30%, 30-50%); scattering  
 750 parameters and a single  $\lambda$  parameter were shared amongst all, the radii were shared amongst results  
 751 of like-centrality, and each has a unique normalization parameter. For the  $\Lambda K^\pm$  results shown, all four  
 752 pair combinations were fit simultaneously ( $\Lambda K^+, \bar{\Lambda} K^-, \Lambda K^-, \bar{\Lambda} K^+$ ) across all centralities. Scattering  
 753 parameters were shared between pair-conjugate systems (i.e. a parameter set describing  $\Lambda K^+$  &  $\bar{\Lambda} K^-$ ,  
 754 and a separate set describing  $\Lambda K^-$  &  $\bar{\Lambda} K^+$ ). For each centrality, a radius and  $\lambda$  parameters were shared  
 755 between all pairs. Each analysis has a unique normalization parameter.

756 **7.1.1 3 Residual Correlations Included in Fit**

757 Figure 29 nicely collects and summarizes all of our extracted fit parameters for the case of 3 included  
 758 residual contributors. Figure 30 presents our extracted fit radii, along with those of other systems previ-  
 759 ously analyzed by ALICE [9], as a function of pair transverse mass ( $m_T$ ). Figures 31, 32, and 33 show the  
 760 experimental correlation functions with fits, assuming 3 residual contributors, for all studied centralities  
 761 for  $\Lambda K_S^0$  with  $\bar{\Lambda} K_S^0$ ,  $\Lambda K^+$  with  $\bar{\Lambda} K^-$ , and  $\Lambda K^-$  with  $\bar{\Lambda} K^+$ , respectively. The parameter sets extracted  
 762 from the fits can be found in Tables 13 and 14.

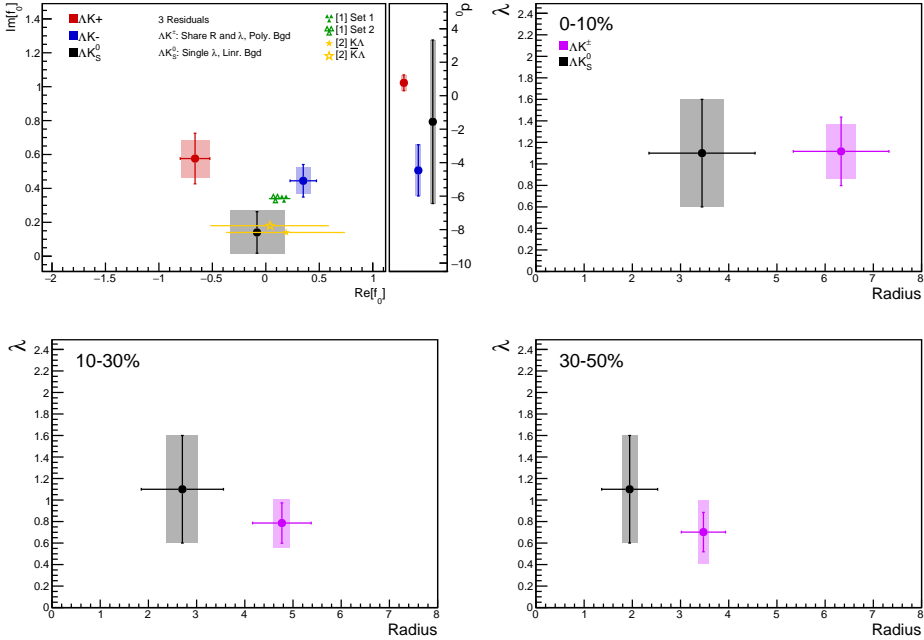


**Fig. 29:** Extracted scattering parameters for the case of 3 residual contributors for all of our AK systems. [Top Left]:  $\text{Im}[f_0]$  vs.  $\text{Re}[f_0]$ , together with  $d_0$  to the right. [Top Right (Bottom Left, Bottom Right)]:  $\lambda$  vs. Radius for the 0-10% (10-30%, 30-50%) bin. The green [10] and yellow [11] points show theoretical predictions made using chiral perturbation theory.

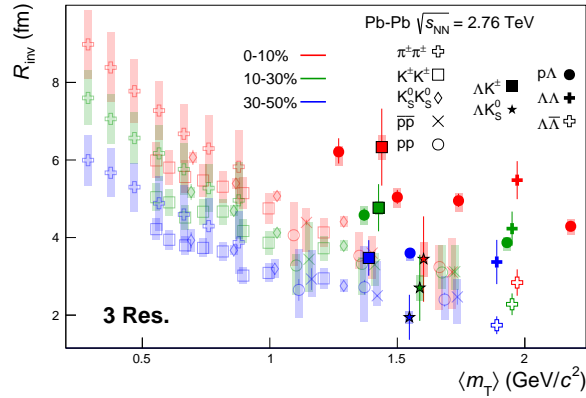
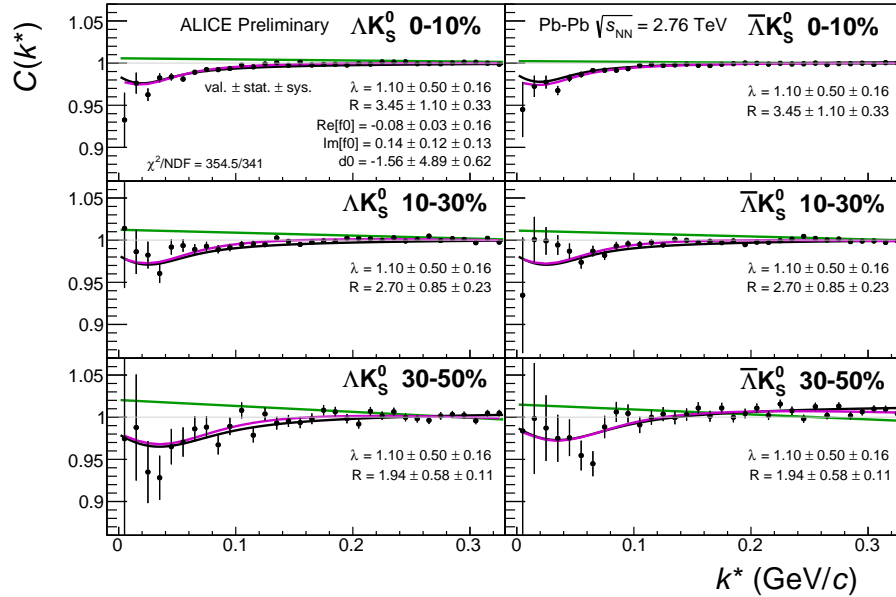
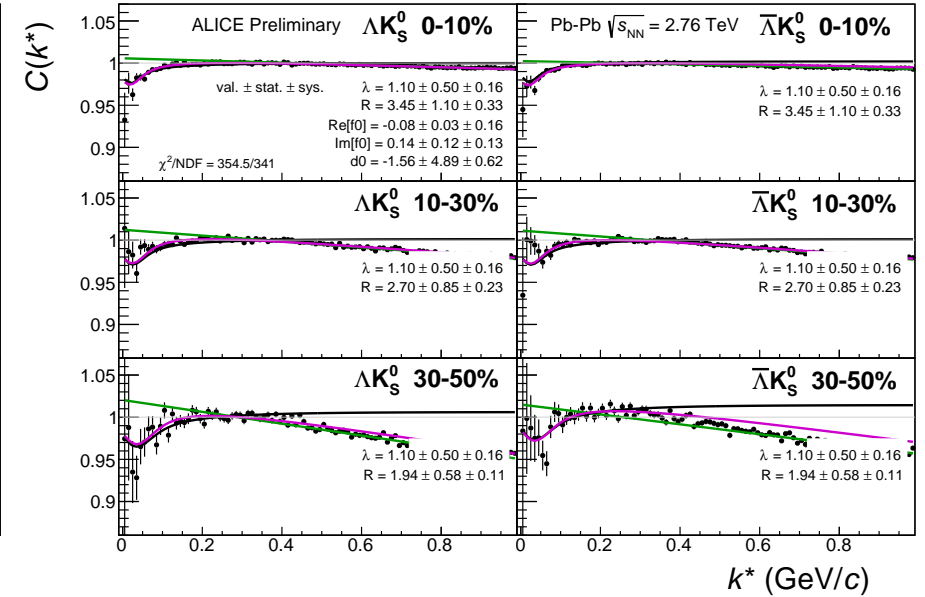


**Fig. 30:** 3 residual correlations in AK fits. Extracted fit  $R_{\text{inv}}$  parameters as a function of pair transverse mass ( $m_T$ ) for various pair systems over several centralities. The ALICE published data [9] is shown with transparent, open symbols. The new AK results are shown with opaque, filled symbols. In the left, the  $\Lambda K^+$  (with its conjugate pair) results are shown separately from the  $\Lambda K^-$  (with its conjugate pair) results. In the right, all  $\Lambda K^\pm$  results are averaged.

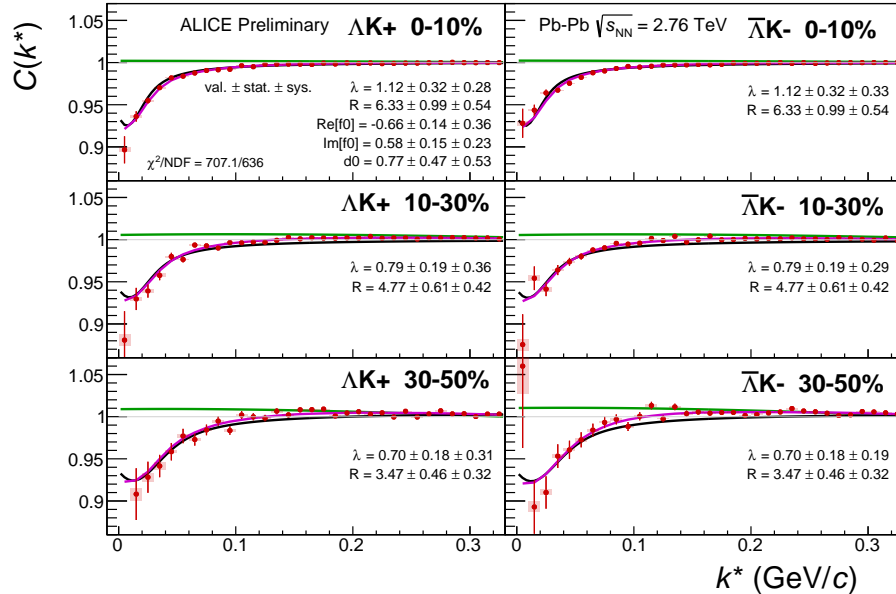


(a) Signal region view ( $k^* \lesssim 0.3 \text{ GeV}/c$ )

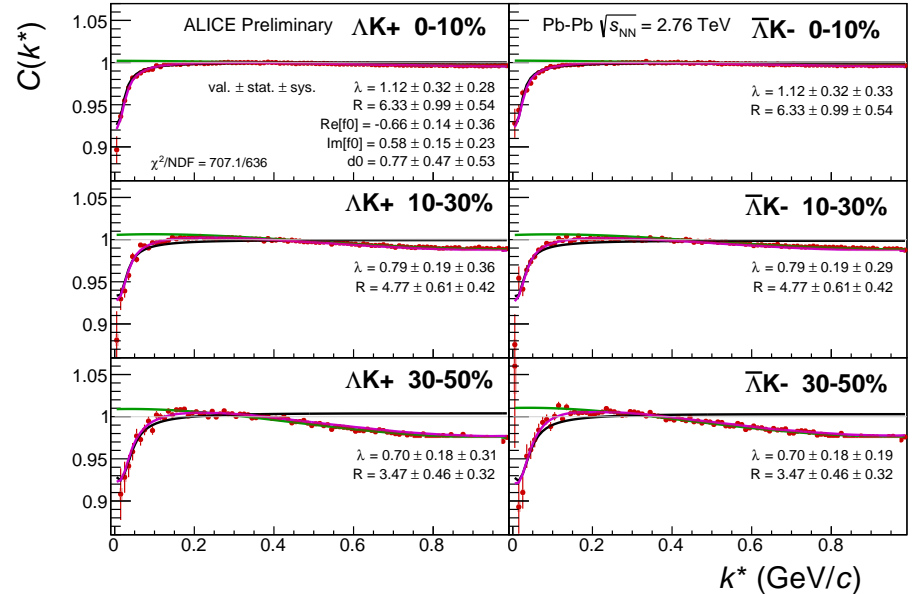


(b) Wide view ( $k^* \lesssim 1.0 \text{ GeV}/c$ )

**Fig. 31:** Fits, with 3 residual correlations included, to the  $\Lambda K_s^0$  (left) and  $\bar{\Lambda} K_s^0$  (right) data for the centralities 0-10% (top), 10-30% (middle), and 30-50% (bottom). The lines represent the statistical errors, while the boxes represent the systematic errors. A single  $\lambda$  parameter is shared amongst all. Each analysis has a unique normalization parameter. The radii are shared between analyses of like centrality, as these should have similar source sizes. The scattering parameters ( $\mathbb{R} f_0, \mathbb{I} f_0, d_0$ ) are shared amongst all. The background is modeled by a (6<sup>th</sup>-degree polynomial fit to THERMINATOR simulation. The black solid line represents the primary ( $\Lambda K$ ) correlation's contribution to the fit. The green line shows the fit to the non-flat background. The purple points show the fit after all residuals' contributions have been included, and momentum resolution and non-flat background corrections have been applied. The extracted fit values with uncertainties are printed.

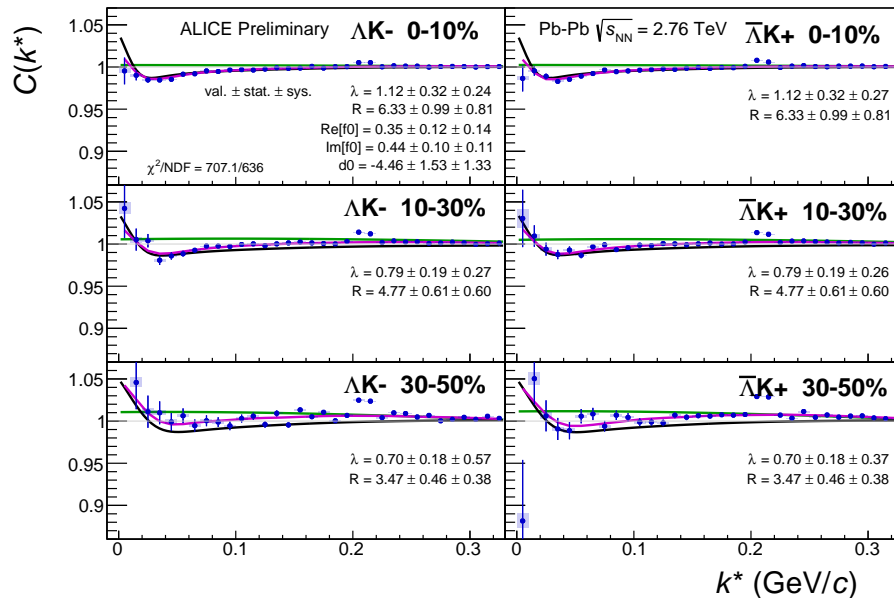


(a) Signal region view ( $k^* \lesssim 0.3 \text{ GeV}/c$ )

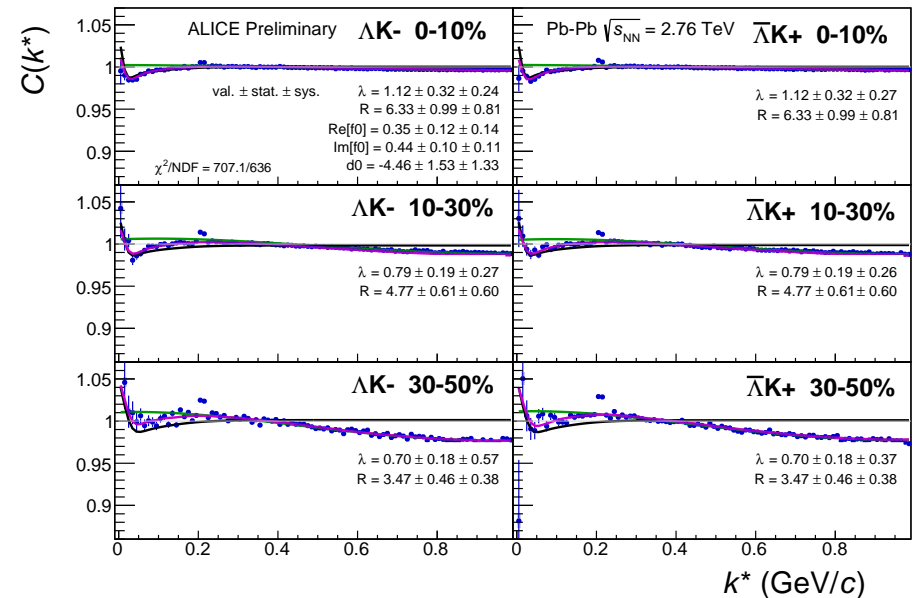


(b) Wide view ( $k^* \lesssim 1.0 \text{ GeV}/c$ )

**Fig. 32:** Fits, with 3 residual correlations included, to the  $\Delta K^+$  (left) and  $\bar{\Delta}K^-$  (right) data for the centralities 0-10% (top), 10-30% (middle), and 30-50% (bottom). The lines represent the statistical errors, while the boxes represent the systematic errors. All  $\Delta K^\pm$  analyses are fit simultaneously across all centralities (0-10%, 10-30%, 30-50%). Scattering parameters ( $\text{Re}[f_0]$ ,  $\text{Im}[f_0]$ ,  $d_0$ ) are shared between pair-conjugate systems (i.e. a parameter set describing the  $\Delta K^+$  &  $\bar{\Delta}K^-$  system, and a separate set describing the  $\Delta K^-$  &  $\bar{\Delta}K^+$  system). For each centrality, a radius and  $\lambda$  parameters are shared between all pairs ( $\Delta K^+$ ,  $\bar{\Delta}K^-$ ,  $\Delta K^-$ ,  $\bar{\Delta}K^+$ ). Each analysis has a unique normalization parameter. The background is modeled by a (6<sup>th</sup>-degree polynomial fit to THERMINATOR simulation. The black solid line represents the primary ( $\Delta K$ ) correlation's contribution to the fit. The green line shows the fit to the non-flat background. The purple points show the fit after all residuals' contributions have been included, and momentum resolution and non-flat background corrections have been applied. The extracted fit values with uncertainties are printed.



(a) Signal region view ( $k^* \lesssim 0.3 \text{ GeV}/c$ )



(b) Wide view ( $k^* \lesssim 1.0 \text{ GeV}/c$ )

**Fig. 33:** Fits, with 3 residual correlations included, to the  $\Lambda K^-$  (left) with  $\bar{\Lambda} K^+$  (right) data for the centralities 0-10% (top), 10-30% (middle), and 30-50% (bottom). The lines represent the statistical errors, while the boxes represent the systematic errors. All  $\Lambda K^\pm$  analyses are fit simultaneously across all centralities (0-10%, 10-30%, 30-50%). Scattering parameters ( $Re[f_0]$ ,  $Im[f_0]$ ,  $d_0$ ) are shared between pair-conjugate systems (i.e. a parameter set describing the  $\Lambda K^+$  &  $\bar{\Lambda} K^-$  system, and a separate set describing the  $\Lambda K^-$  &  $\bar{\Lambda} K^+$  system). For each centrality, a radius and  $\lambda$  parameters are shared between all pairs ( $\Lambda K^+$ ,  $\bar{\Lambda} K^-$ ,  $\Lambda K^-$ ,  $\bar{\Lambda} K^+$ ). Each analysis has a unique normalization parameter. The background is modeled by a (6<sup>th</sup>-)degree polynomial fit to THERMINATOR simulation. The black solid line represents the “raw” fit, i.e. not corrected for momentum resolution effects nor non-flat background. The green line shows the fit to the non-flat background. The purple points show the fit after momentum resolution and non-flat background corrections have been applied. The extracted fit values with uncertainties are printed.

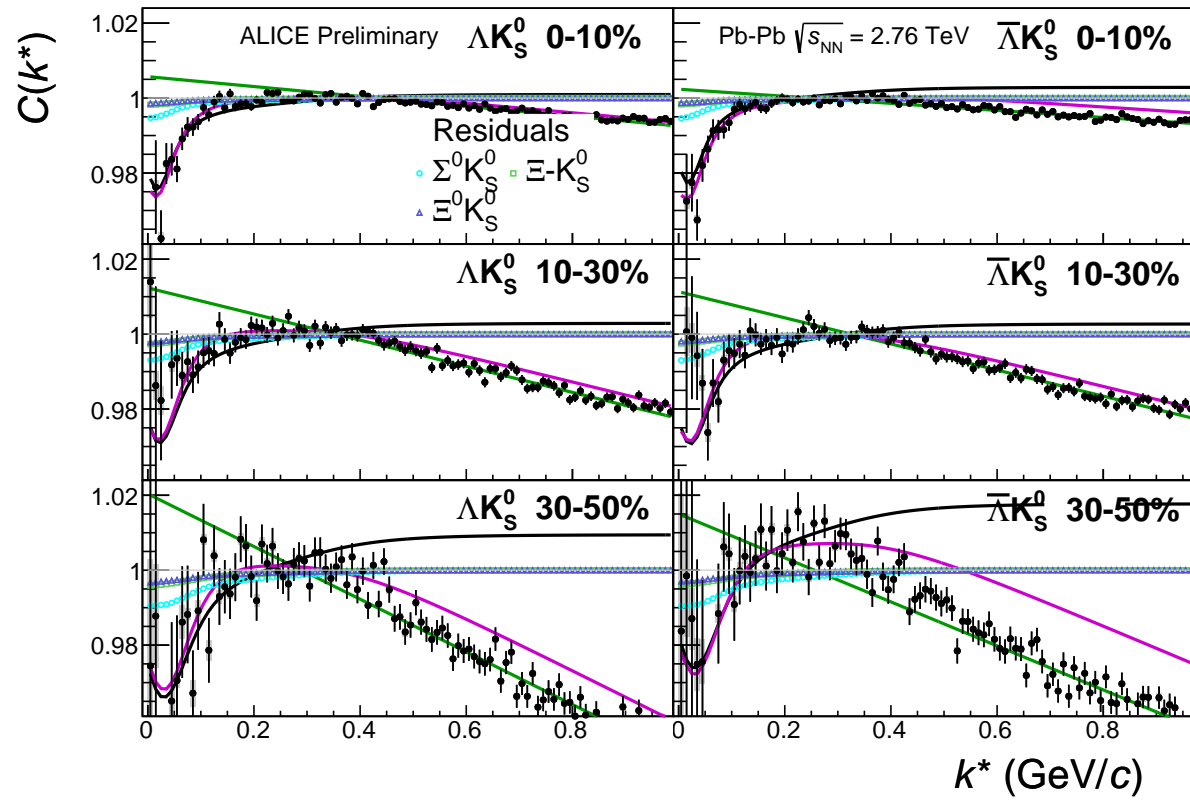
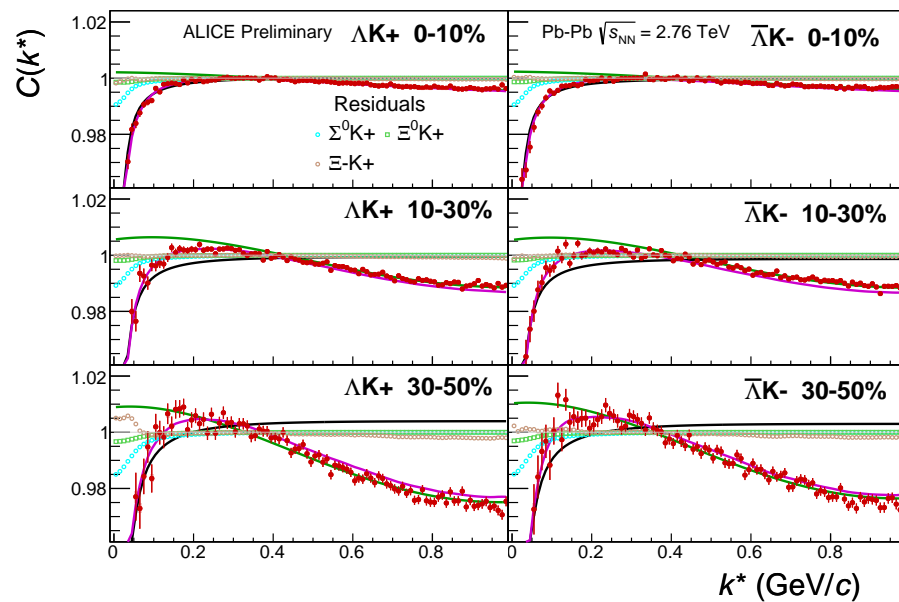
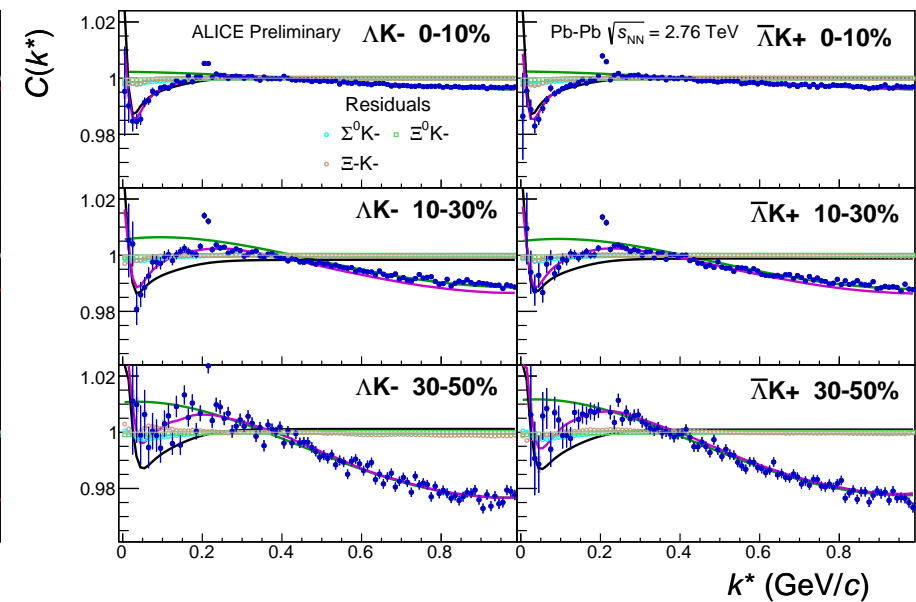


**Fig. 34:** Fits, with 3 residual correlations included and shown, to the  $\Lambda K_S^0$  (left) and  $\bar{\Lambda} K_S^0$  (right) data for the centralities 0-10% (top), 10-30% (middle), and 30-50% (bottom). The three parent pairs used for the residual correction to the  $\Lambda K_S^0$  ( $\bar{\Lambda} K_S^0$ ) fit are  $\Sigma^0 K_S^0$ ,  $\Xi^0 K_S^0$ , and  $\Xi^- K_S^0$  ( $\bar{\Sigma}^0 K_S^0$ ,  $\bar{\Xi}^0 K_S^0$ , and  $\bar{\Xi}^+ K_S^0$ ).



(a)  $\Lambda K^+(\bar{\Lambda} K^-)$  fits with residual contributions shown for the centralities 0-10% (top), 10-30% (middle), and 30-50% (bottom)



(b)  $\Lambda K^-(\bar{\Lambda} K^+)$  fits with residual contributions shown for the centralities 0-10% (top), 10-30% (middle), and 30-50% (bottom)

**Fig. 35:** Fits, with 3 residual correlations included and shown, to the  $\Lambda K^+$  &  $\bar{\Lambda} K^-$  (left) and  $\Lambda K^-$  &  $\bar{\Lambda} K^+$  (right) data for the centralities 0-10% (top), 10-30% (middle), and 30-50% (bottom). The three parent pairs used for the residual correction to the  $\Lambda K^+(\bar{\Lambda} K^-)$  fit are  $\Sigma^0 K^+$ ,  $\Xi^0 K^+$ , and  $\Xi^- K^+$  ( $\bar{\Sigma}^0 K^-$ ,  $\bar{\Xi}^0 K^-$ , and  $\bar{\Xi}^+ K^-$ ).

Fit Results $\Lambda(\bar{\Lambda})K_S^0$						
System	Centrality	Fit Parameters				
		$\lambda$	$R$	$\mathbb{R}f_0$	$\mathbb{I}f_0$	$d_0$
$\Lambda K_S^0 \& \bar{\Lambda} K_S^0$	0-10%			$3.45 \pm 1.10$ (stat.) $\pm 0.45$ (sys.)		
	10-30%	$1.10 \pm 0.50$ (stat.) $\pm 0.50$ (sys.)	$2.70 \pm 0.85$ (stat.) $\pm 0.32$ (sys.)	$-0.08 \pm 0.03$ (stat.) $\pm 0.25$ (sys.)	$0.14 \pm 0.12$ (stat.) $\pm 0.13$ (sys.)	$-1.56 \pm 4.89$ (stat.) $\pm 3.53$ (sys.)
	30-50%			$1.94 \pm 0.58$ (stat.) $\pm 0.16$ (sys.)		

**Table 9:** Fit Results  $\Lambda(\bar{\Lambda})K_S^0$ , with 3 residual correlations included. Each pair is fit simultaneously with its conjugate (ie.  $\Lambda K_S^0$  with  $\bar{\Lambda} K_S^0$ ) across all centralities (0-10%, 10-30%, 30-50%), for a total of 6 simultaneous analyses in the fit. A single  $\lambda$  parameter is shared amongst all. Each analysis has a unique normalization parameter. The radii are shared between analyses of like centrality, as these should have similar source sizes. The scattering parameters ( $\mathbb{R}f_0$ ,  $\mathbb{I}f_0$ ,  $d_0$ ) are shared amongst all. The background is fit with a linear form in the range  $0.6 < k^* < 0.9$  GeV/c. The fit is done on the data with only statistical error bars. The errors marked as “stat.” are those returned by MINUIT. The errors marked as “sys.” are those which result from my systematic analysis (as outlined in Section 6).

Fit Results $\Lambda(\bar{\Lambda})K^\pm$						
System	Centrality	Fit Parameters				
		$\lambda$	$R$	$\mathbb{R}f_0$	$\mathbb{I}f_0$	$d_0$
$\Lambda K^+ \& \bar{\Lambda} K^-$	0-10%	$1.12 \pm 0.32$ (stat.) $\pm 0.25$ (sys.)	$6.33 \pm 0.99$ (stat.) $\pm 0.31$ (sys.)	$-0.66 \pm 0.14$ (stat.) $\pm 0.13$ (sys.)	$0.58 \pm 0.15$ (stat.) $\pm 0.11$ (sys.)	$0.77 \pm 0.47$ (stat.) $\pm 1.66$ (sys.)
	10-30%	$0.79 \pm 0.19$ (stat.) $\pm 0.23$ (sys.)	$4.77 \pm 0.61$ (stat.) $\pm 0.17$ (sys.)			
$\Lambda K^+ \& \bar{\Lambda} K^-$	30-50%	$0.70 \pm 0.18$ (stat.) $\pm 0.30$ (sys.)	$3.47 \pm 0.46$ (stat.) $\pm 0.10$ (sys.)	$0.35 \pm 0.12$ (stat.) $\pm 0.07$ (sys.)	$0.44 \pm 0.10$ (stat.) $\pm 0.08$ (sys.)	$-4.46 \pm 1.53$ (stat.) $\pm 1.36$ (sys.)

**Table 10:** Fit Results  $\Lambda(\bar{\Lambda})K^\pm$ , with 3 residual correlations included. All  $\Lambda K^\pm$  analyses are fit simultaneously across all centralities (0-10%, 10-30%, 30-50%). Scattering parameters ( $\mathbb{R}f_0$ ,  $\mathbb{I}f_0$ ,  $d_0$ ) are shared between pair-conjugate systems (i.e. a parameter set describing the  $\Lambda K^+ \& \bar{\Lambda} K^-$  system, and a separate set describing the  $\Lambda K^- \& \bar{\Lambda} K^+$  system). For each centrality, a radius and  $\lambda$  parameters are shared between all pairs ( $\Lambda K^+, \bar{\Lambda} K^-, \Lambda K^-, \bar{\Lambda} K^+$ ). Each analysis has a unique normalization parameter. The background is modeled by a (6<sup>th</sup>-)degree polynomial fit to THERMINATOR simulation. The fit is done on the data with only statistical error bars. The errors marked as “stat.” are those returned by MINUIT. The errors marked as “sys.” are those which result from my systematic analysis (as outlined in Section 6).

763 **7.1.2 10 Residual Correlations Included in Fit**

764 Figure 36 nicely collects and summarizes all of our extracted fit parameters for the case of 10 included  
 765 residual contributors. Figure 37 presents our extracted fit radii, along with those of other systems pre-  
 766 viously analyzed by ALICE [9], as a function of pair transverse mass ( $m_T$ ). Figures 38, 39, and 40  
 767 show the experimental correlation functions with fits, assuming 10 residual contributors, for all studied  
 768 centralities for  $\Lambda K_S^0$  with  $\bar{\Lambda} K_S^0$ ,  $\Lambda K^+$  with  $\bar{\Lambda} K^-$ , and  $\Lambda K^-$  with  $\bar{\Lambda} K^+$ , respectively. The parameter sets  
 769 extracted from the fits can be found in Tables 11 and 12.

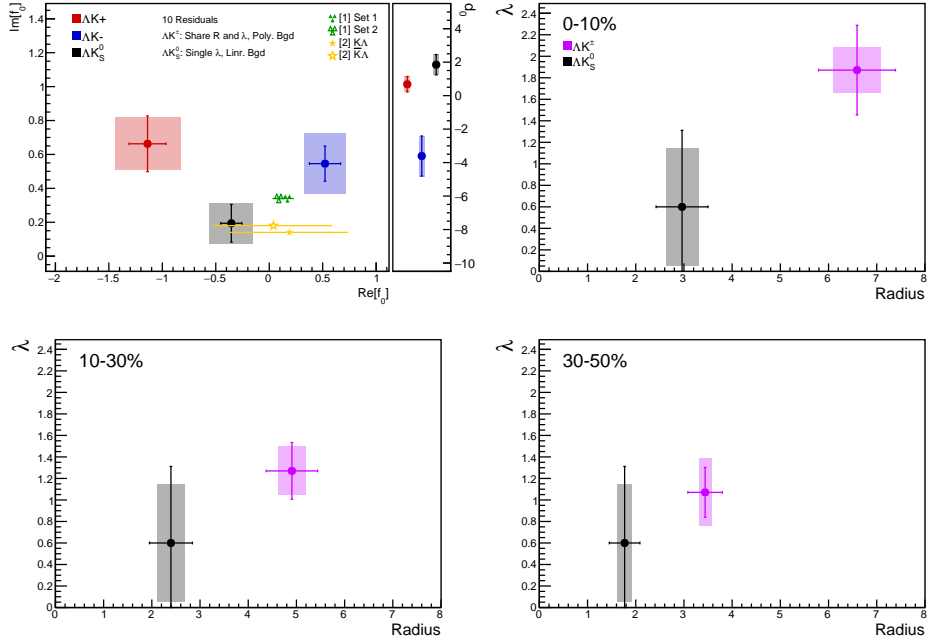


**Fig. 36:** Extracted scattering parameters for the case of 10 residual contributors for all of our AK systems. [Top Left]:  $\text{Im}(f_0)$  vs.  $\text{Re}(f_0)$ , together with  $d_0$  to the right. [Top Right (Bottom Left, Bottom Right)]:  $\lambda$  vs. Radius for the 0-10% (10-30%, 30-50%) bin. The green [10] and yellow [11] points show theoretical predictions made using chiral perturbation theory.

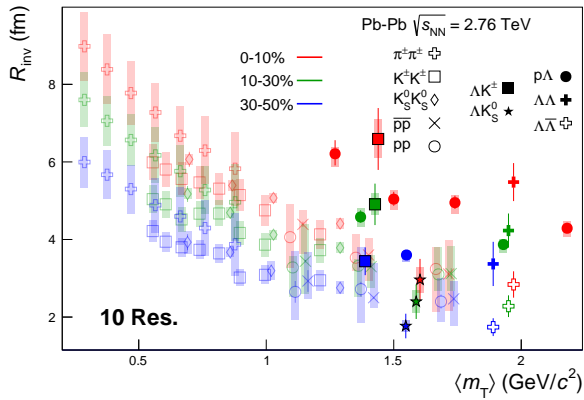
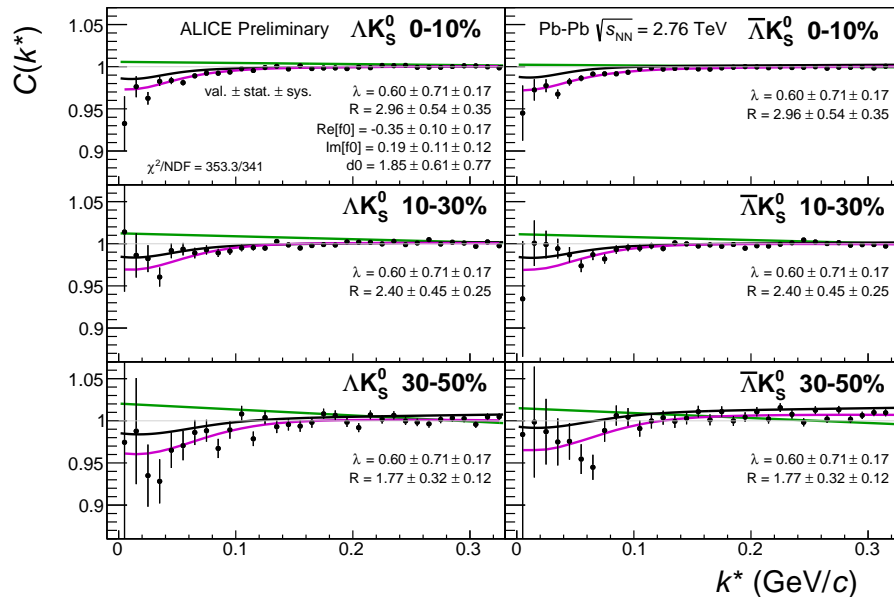
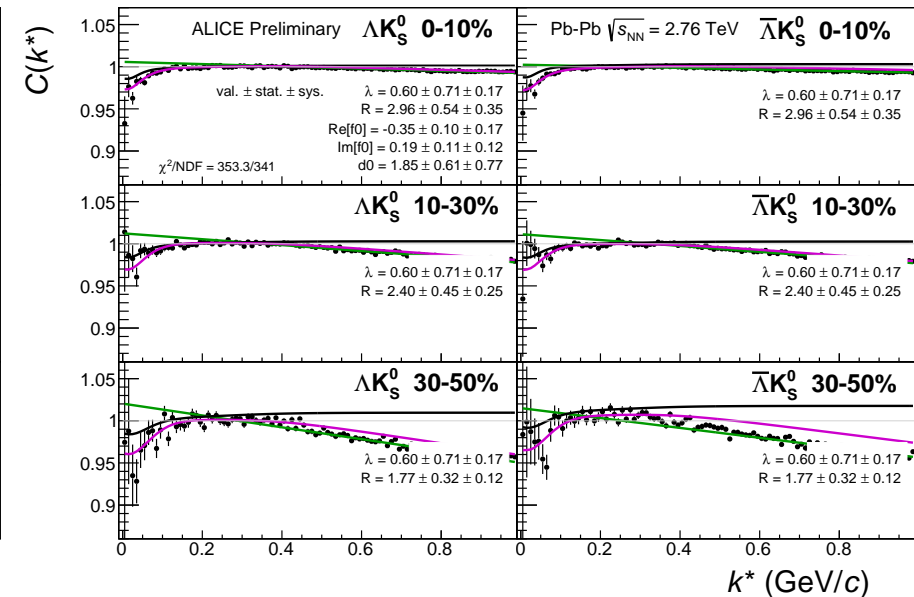


**Fig. 37:** 10 residual correlations in AK fits. Extracted fit  $R_{\text{inv}}$  parameters as a function of pair transverse mass ( $m_T$ ) for various pair systems over several centralities. The ALICE published data [9] is shown with transparent, open symbols. The new AK results are shown with opaque, filled symbols. In the left, the  $\Lambda K^+$  (with its conjugate pair) results are shown separately from the  $\Lambda K^-$  (with its conjugate pair) results. In the right, all  $\Lambda K^\pm$  results are averaged.

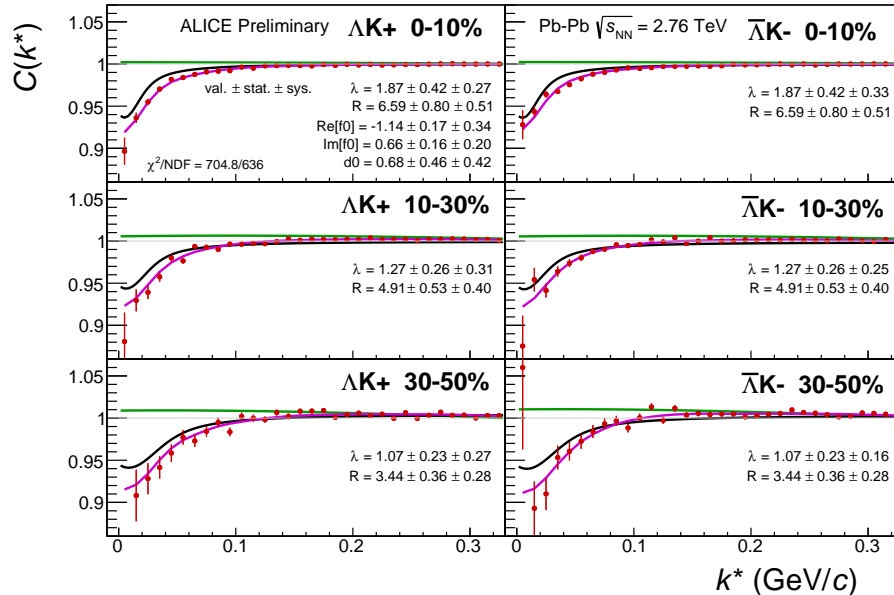


(a) Signal region view ( $k^* \lesssim 0.3$  GeV/c)

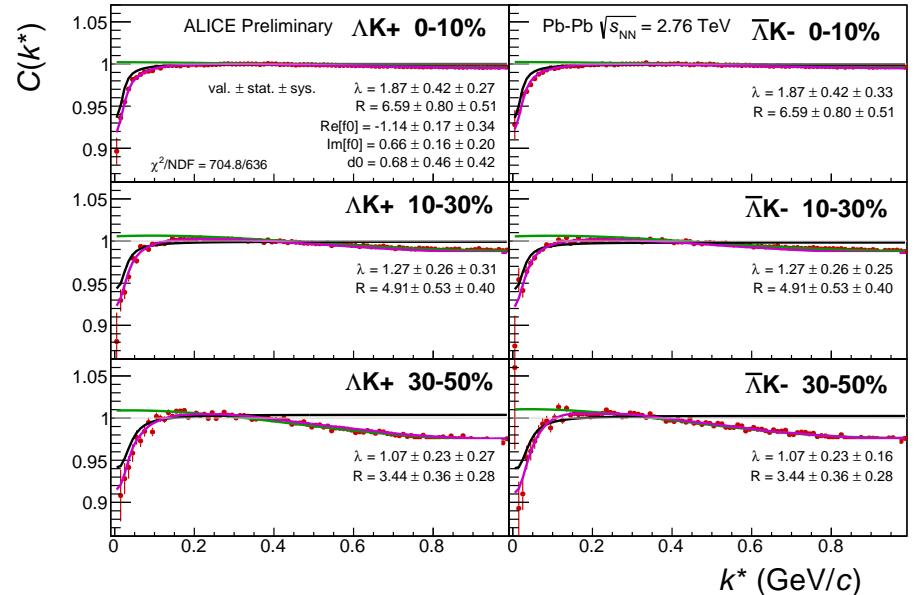


(b) Wide view ( $k^* \lesssim 1.0$  GeV/c)

**Fig. 38:** Fits, with 10 residual correlations included, to the  $\Lambda K_s^0$  (left) and  $\bar{\Lambda} K_s^0$  (right) data for the centralities 0-10% (top), 10-30% (middle), and 30-50% (bottom). The lines represent the statistical errors, while the boxes represent the systematic errors. A single  $\lambda$  parameter is shared amongst all. Each analysis has a unique normalization parameter. The radii are shared between analyses of like centrality, as these should have similar source sizes. The scattering parameters ( $\mathbb{R}f_0$ ,  $\mathbb{I}f_0$ ,  $d_0$ ) are shared amongst all. The background is modeled by a (6<sup>th</sup>-degree polynomial fit to THERMINATOR simulation. The black solid line represents the primary ( $\Lambda K$ ) correlation's contribution to the fit. The green line shows the fit to the non-flat background. The purple points show the fit after all residuals' contributions have been included, and momentum resolution and non-flat background corrections have been applied. The extracted fit values with uncertainties are printed.

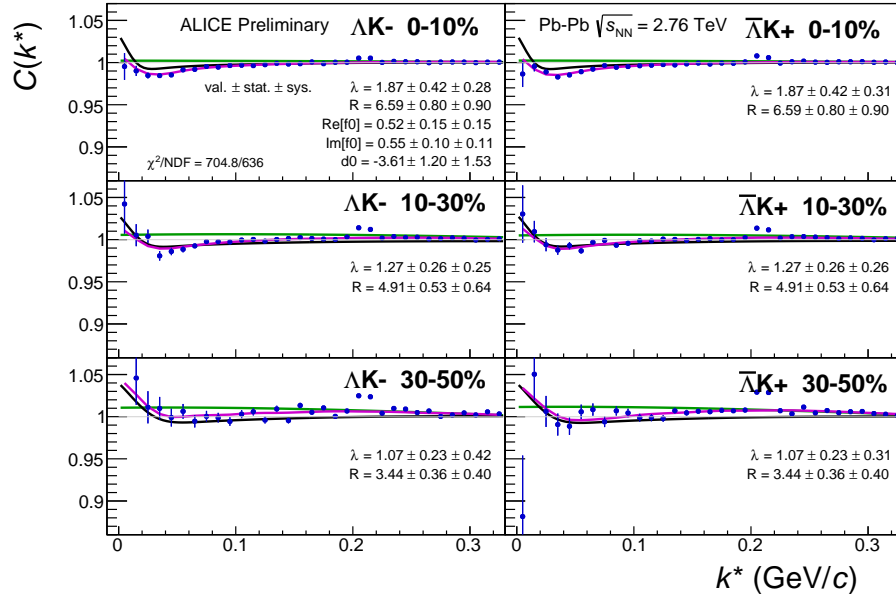


(a) Signal region view ( $k^* \lesssim 0.3 \text{ GeV}/c$ )

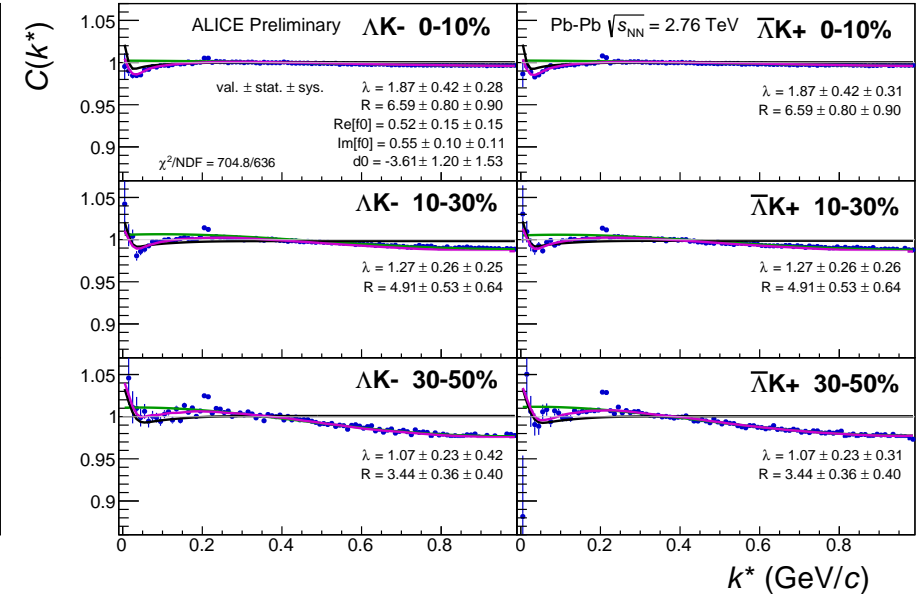


(b) Wide view ( $k^* \lesssim 1.0 \text{ GeV}/c$ )

**Fig. 39:** Fits, with 10 residual correlations included, to the  $\Delta K^+$  (left) and  $\bar{\Delta} K^-$  (right) data for the centralities 0-10% (top), 10-30% (middle), and 30-50% (bottom). The lines represent the statistical errors, while the boxes represent the systematic errors. All  $\Delta K^\pm$  analyses are fit simultaneously across all centralities (0-10%, 10-30%, 30-50%). Scattering parameters ( $\mathbb{R}f_0$ ,  $\mathbb{I}f_0$ ,  $d_0$ ) are shared between pair-conjugate systems (i.e. a parameter set describing the  $\Delta K^+$  &  $\bar{\Delta} K^-$  system, and a separate set describing the  $\Delta K^-$  &  $\bar{\Delta} K^+$  system). For each centrality, a radius and  $\lambda$  parameters are shared between all pairs ( $\Delta K^+$ ,  $\bar{\Delta} K^-$ ,  $\Delta K^-$ ,  $\bar{\Delta} K^+$ ). Each analysis has a unique normalization parameter. The background is modeled by a (6<sup>th</sup>-degree polynomial fit to THERMINATOR simulation. The black solid line represents the primary ( $\Delta K$ ) correlation's contribution to the fit. The green line shows the fit to the non-flat background. The purple points show the fit after all residuals' contributions have been included, and momentum resolution and non-flat background corrections have been applied. The extracted fit values with uncertainties are printed.



(a) Signal region view ( $k^* \lesssim 0.3 \text{ GeV}/c$ )



(b) Wide view ( $k^* \lesssim 1.0 \text{ GeV}/c$ )

**Fig. 40:** Fits, with 10 residual correlations included, to the  $\Lambda K^-$  (left) with  $\bar{\Lambda} K^+$  (right) data for the centralities 0-10% (top), 10-30% (middle), and 30-50% (bottom). The lines represent the statistical errors, while the boxes represent the systematic errors. All  $\Lambda K^\pm$  analyses are fit simultaneously across all centralities (0-10%, 10-30%, 30-50%). Scattering parameters ( $\mathbb{R}f_0$ ,  $\mathbb{I}f_0$ ,  $d_0$ ) are shared between pair-conjugate systems (i.e. a parameter set describing the  $\Lambda K^+$  &  $\bar{\Lambda} K^-$  system, and a separate set describing the  $\Lambda K^-$  &  $\bar{\Lambda} K^+$  system). For each centrality, a radius and  $\lambda$  parameters are shared between all pairs ( $\Lambda K^+$ ,  $\bar{\Lambda} K^-$ ,  $\Lambda K^-$ ,  $\bar{\Lambda} K^+$ ). Each analysis has a unique normalization parameter. The background is modeled by a (6<sup>th</sup>-degree polynomial fit to THERMINATOR simulation. The black solid line represents the primary ( $\Lambda K$ ) correlation's contribution to the fit. The green line shows the fit to the non-flat background. The purple points show the fit after all residuals' contributions have been included, and momentum resolution and non-flat background corrections have been applied. The extracted fit values with uncertainties are printed.

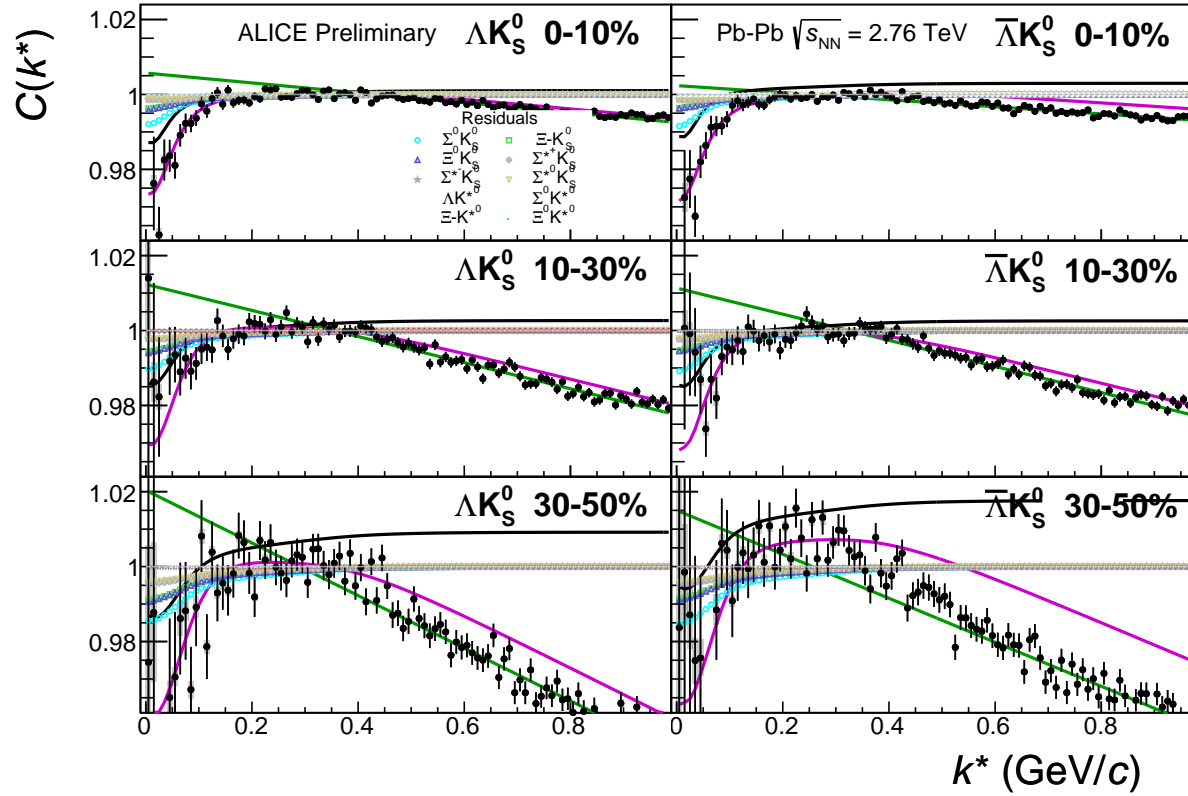
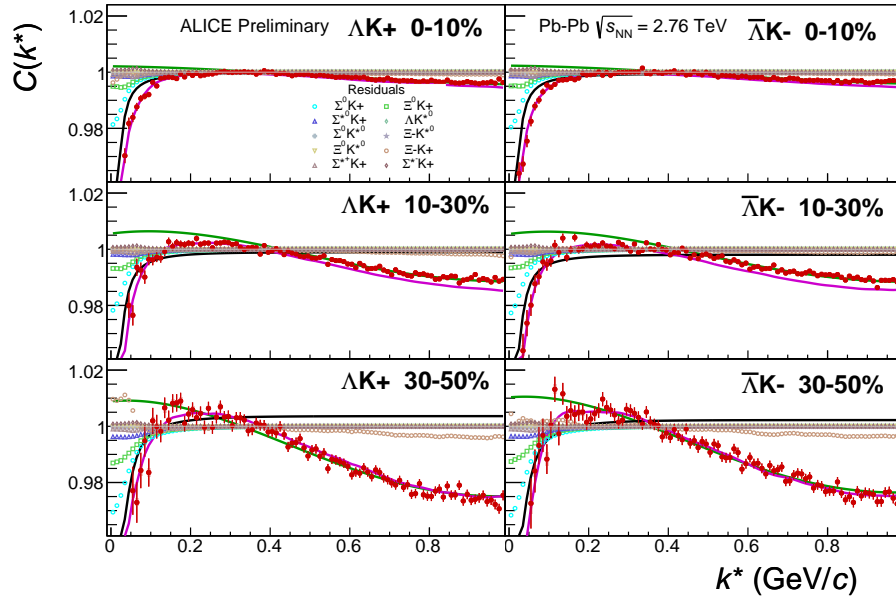
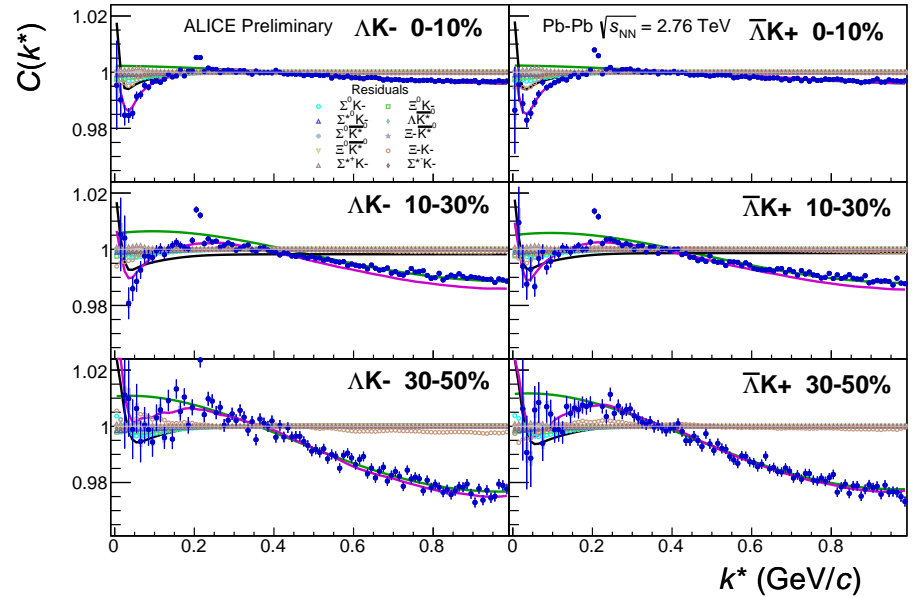


**Fig. 41:** Fits, with 10 residual correlations included and shown, to the  $\Lambda K_s^0$  (left) and  $\bar{\Lambda} K_s^0$  (right) data for the centralities 0-10% (top), 10-30% (middle), and 30-50% (bottom). The ten parent pairs used for the residual correction to the  $\Lambda K_s^0$  ( $\bar{\Lambda} K_s^0$ ) fit are  $\Sigma^0 K_S^0$ ,  $\Xi^0 K_S^0$ ,  $\Xi^- K_S^0$ ,  $\Sigma^{*(+,-,0)} K_S^0$ ,  $\Lambda K^{*0}$ ,  $\Sigma^0 K^{*0}$ ,  $\Xi^0 K^{*0}$ , and  $\Xi^- K^{*0}$  ( $\bar{\Sigma}^0 K_S^0$ ,  $\bar{\Xi}^0 K_S^0$ ,  $\bar{\Xi}^+ K_S^0$ ,  $\bar{\Sigma}^{*(+,-,0)} K_S^0$ ,  $\bar{\Lambda} \bar{K}^{*0}$ ,  $\bar{\Sigma}^0 \bar{K}^{*0}$ ,  $\bar{\Xi}^0 \bar{K}^{*0}$ , and  $\bar{\Xi}^+ \bar{K}^{*0}$ ).



(a)  $\Lambda K^+(\bar{\Lambda}K^-)$  fits with residual contributions shown for the centralities 0-10% (top), 10-30% (middle), and 30-50% (bottom)



(b)  $\Lambda K^-(\bar{\Lambda}K^+)$  fits with residual contributions shown for the centralities 0-10% (top), 10-30% (middle), and 30-50% (bottom)

**Fig. 42:** Fits, with 10 residual correlations included and shown, to the  $\Lambda K^+$  &  $\bar{\Lambda}K^-$  (left) and  $\Lambda K^-$  &  $\bar{\Lambda}K^+$  (right) data for the centralities 0-10% (top), 10-30% (middle), and 30-50% (bottom). The ten parent pairs used for the residual correction to the  $\Lambda K^+(\bar{\Lambda}K^-)$  fit are  $\Sigma^0 K^+$ ,  $\Xi^0 K^+$ ,  $\Xi^- K^+$ ,  $\Sigma^{*(+,-,0)} K^+$ ,  $\Lambda K^{*0}$ ,  $\Sigma^0 K^{*0}$ ,  $\Xi^0 K^{*0}$ , and  $\Xi^- K^{*0}$  ( $\Sigma^0 K^-$ ,  $\Xi^0 K^-$ ,  $\Xi^+ K^-$ ,  $\Sigma^{*(+,-,0)} K^-$ ,  $\bar{\Lambda}K^{*0}$ ,  $\Sigma^0 \bar{K}^{*0}$ ,  $\Xi^0 \bar{K}^{*0}$ , and  $\Xi^- \bar{K}^{*0}$ ).

Fit Results $\Lambda(\bar{\Lambda})K_S^0$						
System	Centrality	Fit Parameters				
		$\lambda$	$R$	$\mathbb{R}f_0$	$\mathbb{I}f_0$	$d_0$
$\Lambda K_S^0 \text{ & } \bar{\Lambda} K_S^0$	0-10%			$2.96 \pm 0.54 \text{ (stat.)} \pm 0.33 \text{ (sys.)}$		
	10-30%	$0.60 \pm 0.71 \text{ (stat.)} \pm 0.54 \text{ (sys.)}$	$2.40 \pm 0.45 \text{ (stat.)} \pm 0.29 \text{ (sys.)}$	$-0.35 \pm 0.10 \text{ (stat.)} \pm 0.21 \text{ (sys.)}$	$0.19 \pm 0.11 \text{ (stat.)} \pm 0.12 \text{ (sys.)}$	$1.85 \pm 0.61 \text{ (stat.)} \pm 2.68 \text{ (sys.)}$
	30-50%			$1.77 \pm 0.32 \text{ (stat.)} \pm 0.15 \text{ (sys.)}$		

**Table 11:** Fit Results  $\Lambda(\bar{\Lambda})K_S^0$ , with 10 residual correlations included. Each pair is fit simultaneously with its conjugate (ie.  $\Lambda K_S^0$  with  $\bar{\Lambda} K_S^0$ ) across all centralities (0-10%, 10-30%, 30-50%), for a total of 6 simultaneous analyses in the fit. A single  $\lambda$  parameter is shared amongst all. Each analysis has a unique normalization parameter. The radii are shared between analyses of like centrality, as these should have similar source sizes. The scattering parameters ( $\mathbb{R}f_0$ ,  $\mathbb{I}f_0$ ,  $d_0$ ) are shared amongst all. The background is fit with a linear form in the range  $0.6 < k^* < 0.9$  GeV/c. The fit is done on the data with only statistical error bars. The errors marked as “stat.” are those returned by MINUIT. The errors marked as “sys.” are those which result from my systematic analysis (as outlined in Section 6).

Fit Results $\Lambda(\bar{\Lambda})K^\pm$						
System	Centrality	Fit Parameters				
		$\lambda$	$R$	$\mathbb{R}f_0$	$\mathbb{I}f_0$	$d_0$
$\Lambda K^+ \text{ & } \bar{\Lambda} K^-$	0-10%	$1.87 \pm 0.42 \text{ (stat.)} \pm 0.21 \text{ (sys.)}$	$6.59 \pm 0.80 \text{ (stat.)} \pm 0.49 \text{ (sys.)}$	$-1.14 \pm 0.17 \text{ (stat.)} \pm 0.31 \text{ (sys.)}$	$0.66 \pm 0.16 \text{ (stat.)} \pm 0.15 \text{ (sys.)}$	$0.68 \pm 0.46 \text{ (stat.)} \pm 0.53 \text{ (sys.)}$
	10-30%	$1.27 \pm 0.26 \text{ (stat.)} \pm 0.23 \text{ (sys.)}$	$4.91 \pm 0.53 \text{ (stat.)} \pm 0.28 \text{ (sys.)}$			
$\Lambda K^+ \text{ & } \bar{\Lambda} K^-$	30-50%	$1.07 \pm 0.23 \text{ (stat.)} \pm 0.32 \text{ (sys.)}$	$3.44 \pm 0.36 \text{ (stat.)} \pm 0.13 \text{ (sys.)}$	$0.52 \pm 0.15 \text{ (stat.)} \pm 0.19 \text{ (sys.)}$	$0.55 \pm 0.10 \text{ (stat.)} \pm 0.18 \text{ (sys.)}$	$-3.61 \pm 1.20 \text{ (stat.)} \pm 1.02 \text{ (sys.)}$

**Table 12:** Fit Results  $\Lambda(\bar{\Lambda})K^\pm$ , with 10 residual correlations included. All  $\Lambda K^\pm$  analyses are fit simultaneously across all centralities (0-10%, 10-30%, 30-50%). Scattering parameters ( $\mathbb{R}f_0$ ,  $\mathbb{I}f_0$ ,  $d_0$ ) are shared between pair-conjugate systems (i.e. a parameter set describing the  $\Lambda K^+ \text{ & } \bar{\Lambda} K^-$  system, and a separate set describing the  $\Lambda K^- \text{ & } \bar{\Lambda} K^+$  system). For each centrality, a radius and  $\lambda$  parameters are shared between all pairs ( $\Lambda K^+, \bar{\Lambda} K^-, \Lambda K^-, \bar{\Lambda} K^+$ ). Each analysis has a unique normalization parameter. The background is modeled by a (6<sup>th</sup>-degree polynomial fit to THERMINATOR simulation. The fit is done on the data with only statistical error bars. The errors marked as “stat.” are those returned by MINUIT. The errors marked as “sys.” are those which result from my systematic analysis (as outlined in Section 6).

770 **7.1.3 No Residual Correlations Included in Fit**

771 Figure 43 nicely collects and summarizes all of our extracted fit parameters for the case of no included  
 772 residual contributors. Figure 44 presents our extracted fit radii, along with those of other systems pre-  
 773 viously analyzed by ALICE [9], as a function of pair transverse mass ( $m_T$ ). Figures 45, 46, and 47  
 774 show the experimental correlation functions with fits, assuming no residual contributors, for all studied  
 775 centralities for  $\Lambda K_S^0$  with  $\bar{\Lambda} K_S^0$ ,  $\Lambda K^+$  with  $\bar{\Lambda} K^-$ , and  $\Lambda K^-$  with  $\bar{\Lambda} K^+$ , respectively. The parameter sets  
 776 extracted from the fits can be found in Tables 13 and 14.

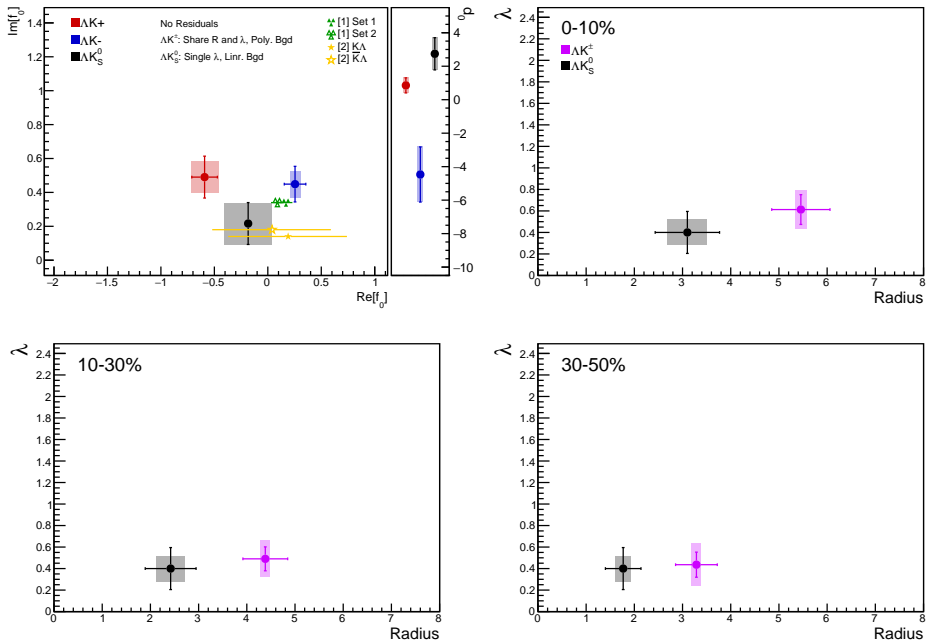


**Fig. 43:** Extracted scattering parameters for the case of NO residual contributors for all of our AK systems. [Top Left]:  $\text{Im}[f_0]$  vs.  $\text{Re}[f_0]$ , together with  $d_0$  to the right. [Top Right (Bottom Left, Bottom Right)]:  $\lambda$  vs. Radius for the 0-10% (10-30%, 30-50%) bin. The green [10] and yellow [11] points show theoretical predictions made using chiral perturbation theory.

777 Figure 44 shows extracted  $R_{\text{inv}}$  parameters as a function of transverse mass ( $m_T$ ) for various pair systems  
 778 over several centralities. The published ALICE data [9] is shown with transparent, open symbols. The  
 779 new AK results are shown with opaque, filled symbols. The radii shown an increasing size with increas-  
 780 ing centrality, as is expected from the simple geometric picture of the collisions. The radii decrease  
 781 in size with increasing  $m_T$ , and we see an approximate scaling of the radii with transverse mass, as is  
 782 expected in the presence of collective flow in the system.

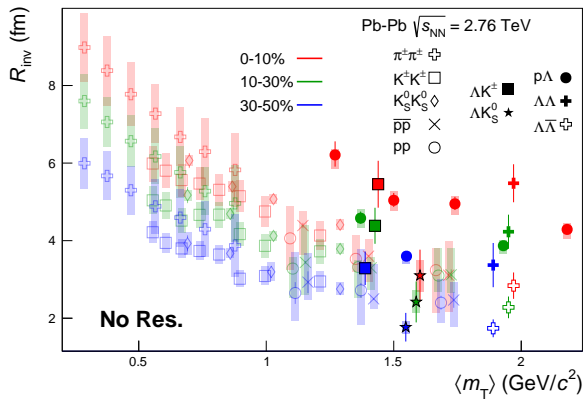
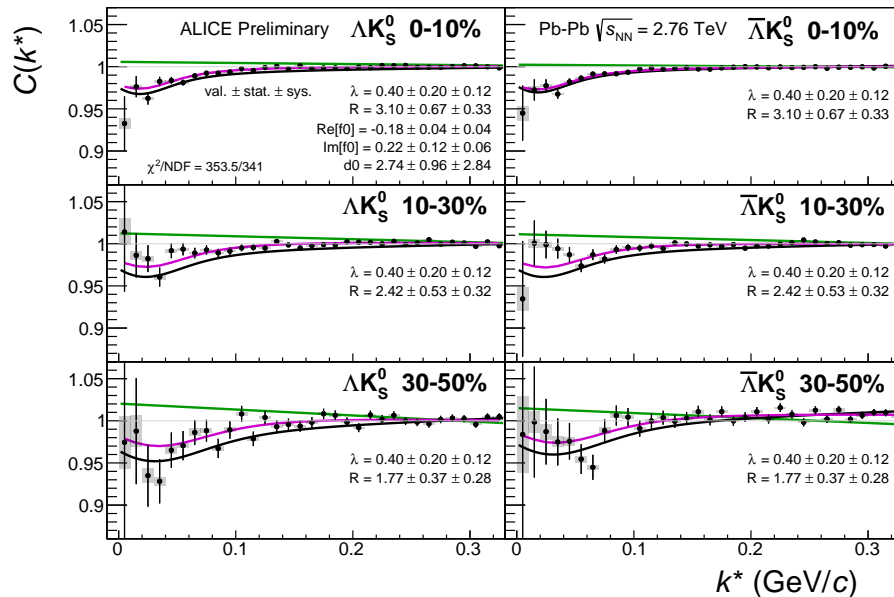
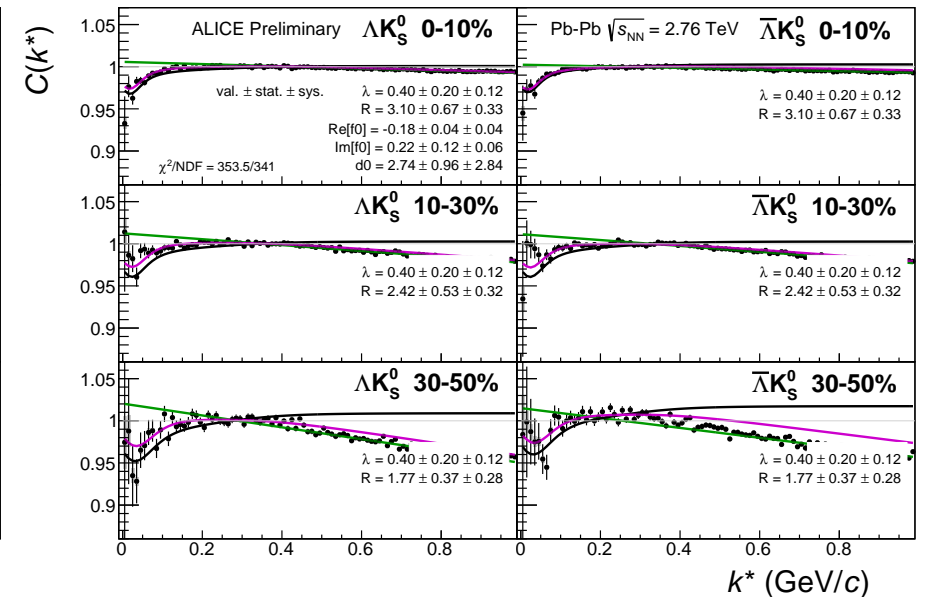


**Fig. 44:** No residual correlations in  $\Lambda K$  fits. Extracted fit  $R_{\text{inv}}$  parameters as a function of pair transverse mass ( $m_T$ ) for various pair systems over several centralities. The ALICE published data [9] is shown with transparent, open symbols. The new  $\Lambda K$  results are shown with opaque, filled symbols. In the left, the  $\Lambda K^+$  (with its conjugate pair) results are shown separately from the  $\Lambda K^-$  (with its conjugate pair) results. In the right, all  $\Lambda K^\pm$  results are averaged.

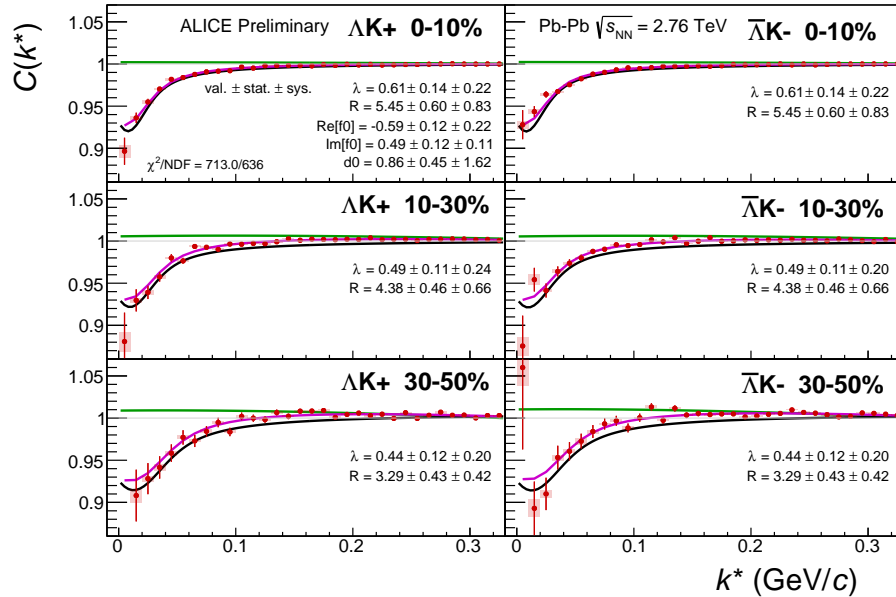


(a) Signal region view ( $k^* \lesssim 0.3 \text{ GeV}/c$ )

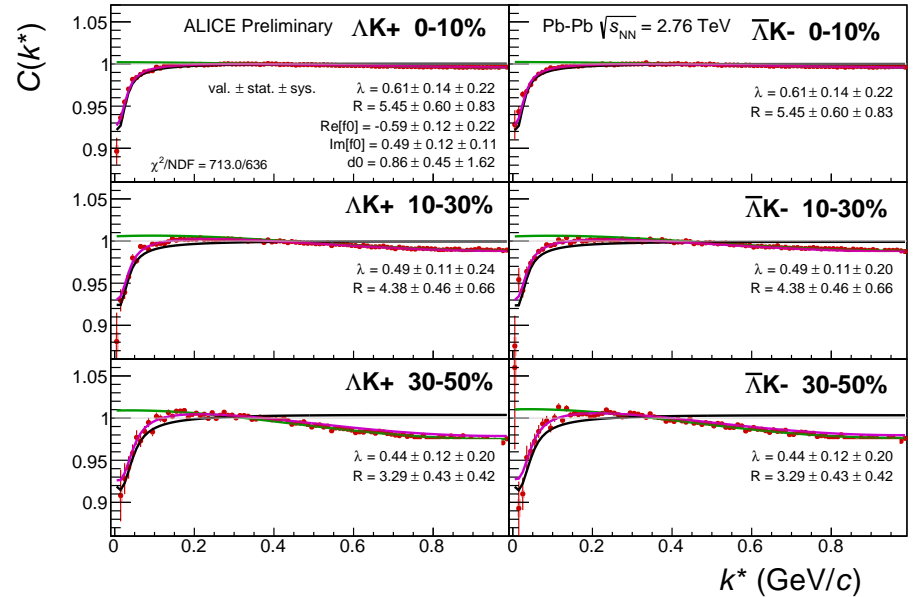


(b) Wide view ( $k^* \lesssim 1.0 \text{ GeV}/c$ )

**Fig. 45:** Fits, with NO residual correlations included, to the  $\Lambda K_s^0$  (left) and  $\bar{\Lambda} K_s^0$  (right) data for the centralities 0-10% (top), 10-30% (middle), and 30-50% (bottom). The lines represent the statistical errors, while the boxes represent the systematic errors. A single  $\lambda$  parameter is shared amongst all. Each analysis has a unique normalization parameter. The radii are shared between analyses of like centrality, as these should have similar source sizes. The scattering parameters ( $\mathbb{R}f_0$ ,  $\mathbb{I}f_0$ ,  $d_0$ ) are shared amongst all. The background is modeled by a (6<sup>th</sup>-)degree polynomial fit to THERMINATOR simulation. The black solid line represents the “raw” primary fit, i.e. not corrected for momentum resolution effects nor non-flat background. The green line shows the fit to the non-flat background. The purple points show the fit after momentum resolution and non-flat background corrections have been applied. The extracted fit values with uncertainties are printed.

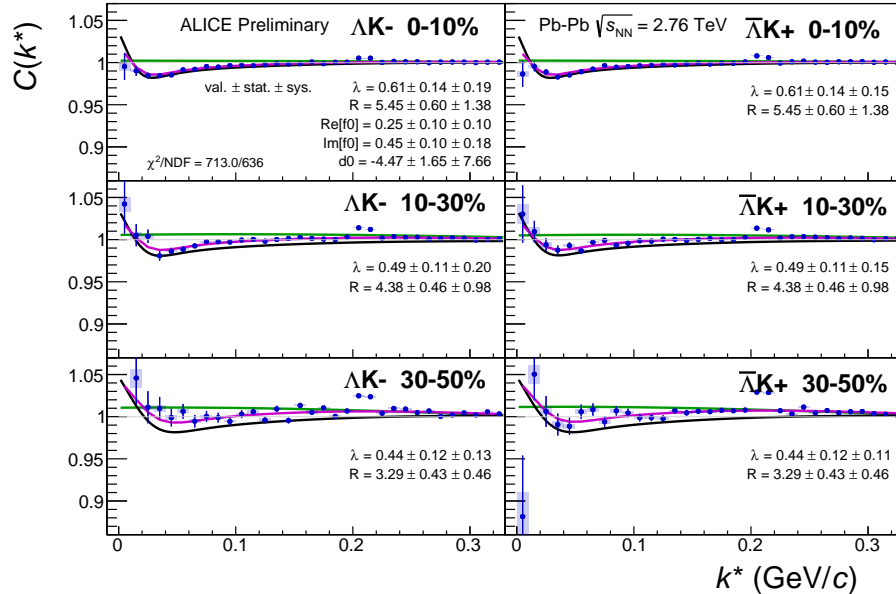


(a) Signal region view ( $k^* \lesssim 0.3 \text{ GeV}/c$ )

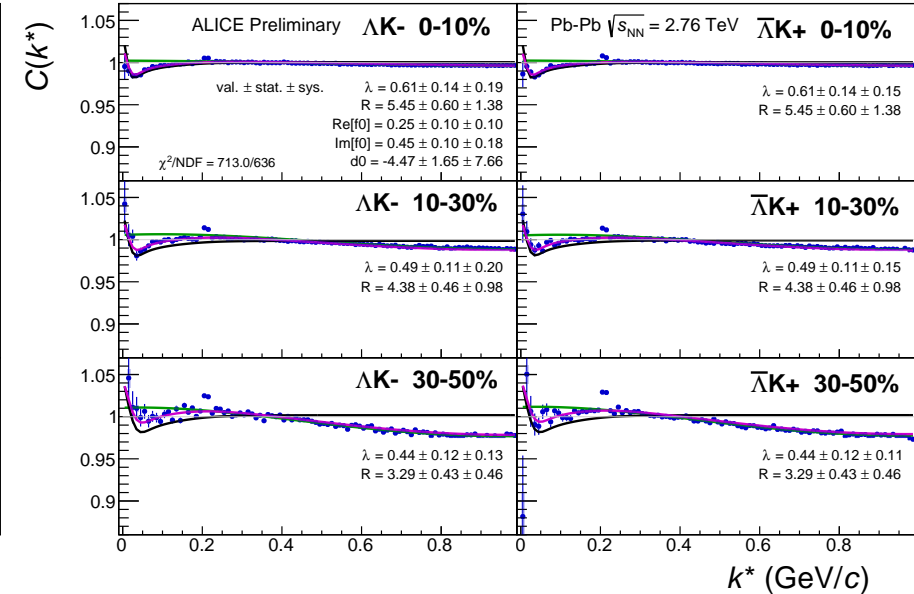


(b) Wide view ( $k^* \lesssim 1.0 \text{ GeV}/c$ )

**Fig. 46:** Fits to the  $\Delta K^+$  (left) and  $\bar{\Delta} K^-$  (right) data for the centralities 0-10% (top), 10-30% (middle), and 30-50% (bottom). The lines represent the statistical errors, while the boxes represent the systematic errors. All  $\Delta K^\pm$  analyses are fit simultaneously across all centralities (0-10%, 10-30%, 30-50%). Scattering parameters ( $\mathbb{R}f_0$ ,  $\mathbb{I}f_0$ ,  $d_0$ ) are shared between pair-conjugate systems (i.e. a parameter set describing the  $\Delta K^+$  &  $\bar{\Delta} K^-$  system, and a separate set describing the  $\Delta K^-$  &  $\bar{\Delta} K^+$  system). For each centrality, a radius and  $\lambda$  parameters are shared between all pairs ( $\Delta K^+$ ,  $\bar{\Delta} K^-$ ,  $\Delta K^-$ ,  $\bar{\Delta} K^+$ ). Each analysis has a unique normalization parameter. The background is modeled by a (6<sup>th</sup>-)degree polynomial fit to THERMINATOR simulation. The black solid line represents the “raw” primary fit, i.e. not corrected for momentum resolution effects nor non-flat background. The green line shows the fit to the non-flat background. The purple points show the fit after momentum resolution and non-flat background corrections have been applied. The extracted fit values with uncertainties are printed.



(a) Signal region view ( $k^* \lesssim 0.3 \text{ GeV}/c$ )



(b) Wide view ( $k^* \lesssim 1.0 \text{ GeV}/c$ )

**Fig. 47:** Fits, with NO residual correlations included, to the  $\Lambda K^-$  (left) with  $\bar{\Lambda} K^+$  (right) data for the centralities 0-10% (top), 10-30% (middle), and 30-50% (bottom). The lines represent the statistical errors, while the boxes represent the systematic errors. All  $\Lambda K^\pm$  analyses are fit simultaneously across all centralities (0-10%, 10-30%, 30-50%). Scattering parameters ( $\mathbb{R}f_0$ ,  $\mathbb{I}f_0$ ,  $d_0$ ) are shared between pair-conjugate systems (i.e. a parameter set describing the  $\Lambda K^+$  &  $\bar{\Lambda} K^-$  system, and a separate set describing the  $\Lambda K^-$  &  $\bar{\Lambda} K^+$  system). For each centrality, a radius and  $\lambda$  parameters are shared between all pairs ( $\Lambda K^+$ ,  $\bar{\Lambda} K^-$ ,  $\Lambda K^-$ ,  $\bar{\Lambda} K^+$ ). Each analysis has a unique normalization parameter. The background is modeled by a (6<sup>th</sup>-)degree polynomial fit to THERMINATOR simulation. The black solid line represents the “raw” primary fit, i.e. not corrected for momentum resolution effects nor non-flat background. The green line shows the fit to the non-flat background. The purple points show the fit after momentum resolution and non-flat background corrections have been applied. The extracted fit values with uncertainties are printed.

Fit Results $\Lambda(\bar{\Lambda})K_S^0$						
System	Centrality	Fit Parameters				
		$\lambda$	$R$	$\mathbb{R}f_0$	$\mathbb{I}f_0$	$d_0$
$\Lambda K_S^0 \text{ & } \bar{\Lambda} K_S^0$	0-10%			$3.10 \pm 0.67 \text{ (stat.)} \pm 0.41 \text{ (sys.)}$		
	10-30%	$0.40 \pm 0.20 \text{ (stat.)} \pm 0.12 \text{ (sys.)}$	$2.42 \pm 0.53 \text{ (stat.)} \pm 0.29 \text{ (sys.)}$	$-0.18 \pm 0.04 \text{ (stat.)} \pm 0.22 \text{ (sys.)}$	$0.22 \pm 0.12 \text{ (stat.)} \pm 0.12 \text{ (sys.)}$	$2.74 \pm 0.96 \text{ (stat.)} \pm 1.28 \text{ (sys.)}$
	30-50%			$1.77 \pm 0.37 \text{ (stat.)} \pm 0.16 \text{ (sys.)}$		

**Table 13:** Fit Results  $\Lambda(\bar{\Lambda})K_S^0$ , with no residual correlations included. Each pair is fit simultaneously with its conjugate (ie.  $\Lambda K_S^0$  with  $\bar{\Lambda} K_S^0$ ) across all centralities (0-10%, 10-30%, 30-50%), for a total of 6 simultaneous analyses in the fit. A single  $\lambda$  parameter is shared amongst all. Each analysis has a unique normalization parameter. The radii are shared between analyses of like centrality, as these should have similar source sizes. The scattering parameters ( $\mathbb{R}f_0$ ,  $\mathbb{I}f_0$ ,  $d_0$ ) are shared amongst all. The background is fit with a linear form in the range  $0.6 < k^* < 0.9 \text{ GeV}/c$ . The fit is done on the data with only statistical error bars. The errors marked as “stat.” are those returned by MINUIT. The errors marked as “sys.” are those which result from my systematic analysis (as outlined in Section 6).

Fit Results $\Lambda(\bar{\Lambda})K^\pm$						
System	Centrality	Fit Parameters				
		$\lambda$	$R$	$\mathbb{R}f_0$	$\mathbb{I}f_0$	$d_0$
$\Lambda K^+ \text{ & } \bar{\Lambda} K^-$	0-10%	$0.61 \pm 0.14 \text{ (stat.)} \pm 0.18 \text{ (sys.)}$	$5.45 \pm 0.60 \text{ (stat.)} \pm 0.12 \text{ (sys.)}$	$-0.59 \pm 0.12 \text{ (stat.)} \pm 0.13 \text{ (sys.)}$	$0.49 \pm 0.12 \text{ (stat.)} \pm 0.09 \text{ (sys.)}$	$0.86 \pm 0.45 \text{ (stat.)} \pm 1.63 \text{ (sys.)}$
	10-30%	$0.49 \pm 0.11 \text{ (stat.)} \pm 0.17 \text{ (sys.)}$	$4.38 \pm 0.46 \text{ (stat.)} \pm 0.10 \text{ (sys.)}$			
$\Lambda K^+ \text{ & } \bar{\Lambda} K^-$	30-50%	$0.44 \pm 0.12 \text{ (stat.)} \pm 0.20 \text{ (sys.)}$	$3.29 \pm 0.43 \text{ (stat.)} \pm 0.10 \text{ (sys.)}$	$0.25 \pm 0.10 \text{ (stat.)} \pm 0.05 \text{ (sys.)}$	$0.45 \pm 0.10 \text{ (stat.)} \pm 0.08 \text{ (sys.)}$	$-4.47 \pm 1.65 \text{ (stat.)} \pm 1.60 \text{ (sys.)}$

**Table 14:** Fit Results  $\Lambda(\bar{\Lambda})K^\pm$ , with no residual correlations included. All  $\Lambda K^\pm$  analyses are fit simultaneously across all centralities (0-10%, 10-30%, 30-50%). Scattering parameters ( $\mathbb{R}f_0$ ,  $\mathbb{I}f_0$ ,  $d_0$ ) are shared between pair-conjugate systems (i.e. a parameter set describing the  $\Lambda K^+ \text{ & } \bar{\Lambda} K^-$  system, and a separate set describing the  $\Lambda K^- \text{ & } \bar{\Lambda} K^+$  system). For each centrality, a radius and  $\lambda$  parameters are shared between all pairs ( $\Lambda K^+, \bar{\Lambda} K^-, \Lambda K^-, \bar{\Lambda} K^+$ ). Each analysis has a unique normalization parameter. The background is modeled by a (6<sup>th</sup>-degree polynomial fit to THERMINATOR simulation. The fit is done on the data with only statistical error bars. The errors marked as “stat.” are those returned by MINUIT. The errors marked as “sys.” are those which result from my systematic analysis (as outlined in Section 6).

783 **7.1.4 Fit Method Comparisons**

784 In Figure 48, we show extracted fit parameters for the case of  $\Lambda K^+(\bar{\Lambda}K^-)$  sharing radii with  $\Lambda K^-(\bar{\Lambda}K^+)$ .  
 785 The figure shows results for three different treatments of the non-femtoscopic background: a polynomial  
 786 fit to THERMINATOR 2 simulation to model the background (circles), a linear fit to the data to model  
 787 the background (squares), and the Stavinskiy method (crosses).

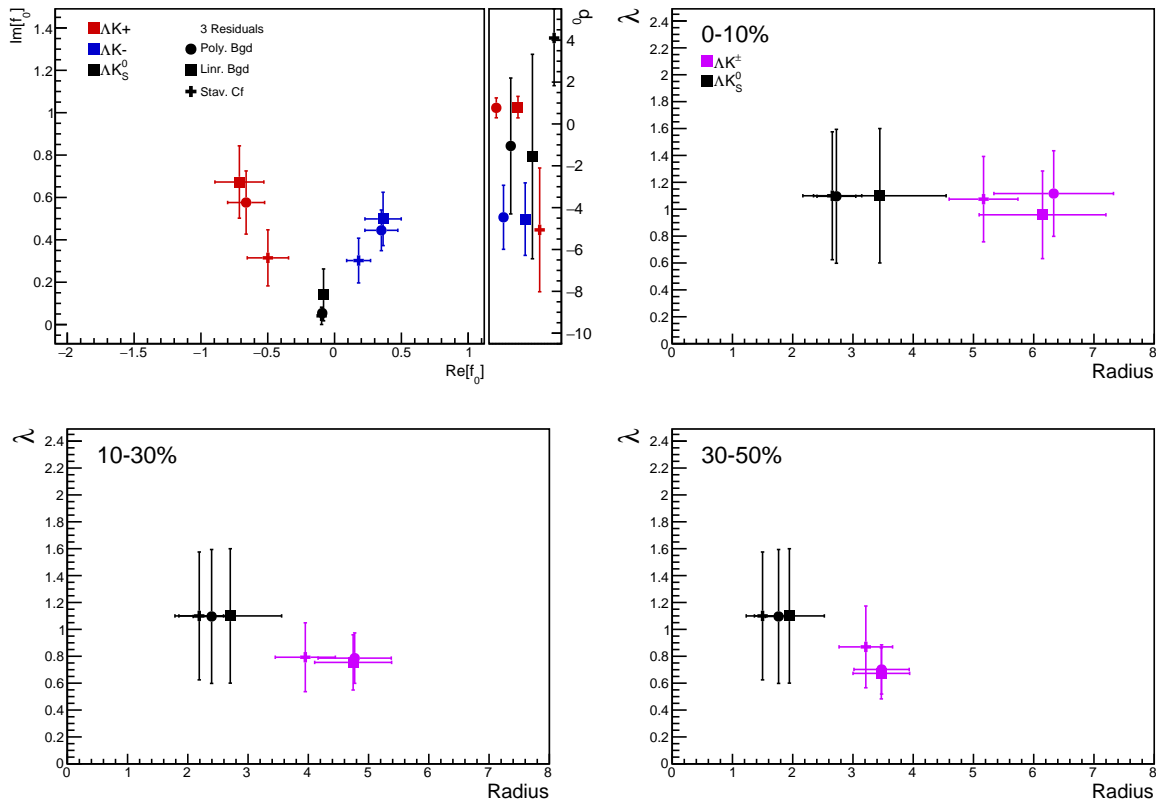


**Fig. 48:** Compare Fit Parameters: Background treatment: Extracted fit results for all of our  $\Lambda(\bar{\Lambda})K^\pm$  systems across all studied centrality bins (0-10%, 10-30%, 30-50%). The  $\Lambda K^+(\bar{\Lambda}K^-)$  and  $\Lambda K^-(\bar{\Lambda}K^+)$  systems share both a radius and a  $\lambda$  parameter for each centrality bin (i.e. 3 total radius parameters, 3 total  $\lambda$  parameters). The figure shows results for three different treatments of the non-femtoscopic background: a polynomial fit to THERMINATOR 2 simulation to model the background (circles), a linear fit to the data to model the background (squares), and the Stavinskiy method (crosses). The green [10] and yellow [11] points show theoretical predictions made using chiral perturbation theory.

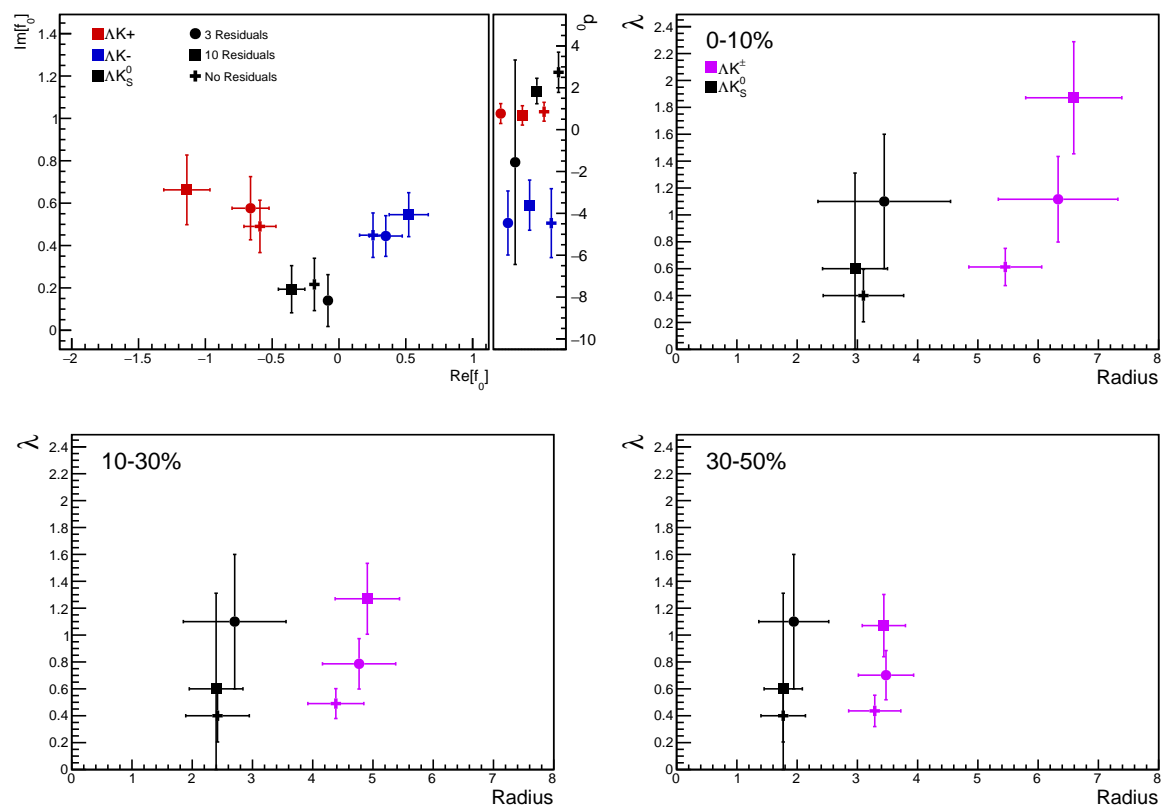
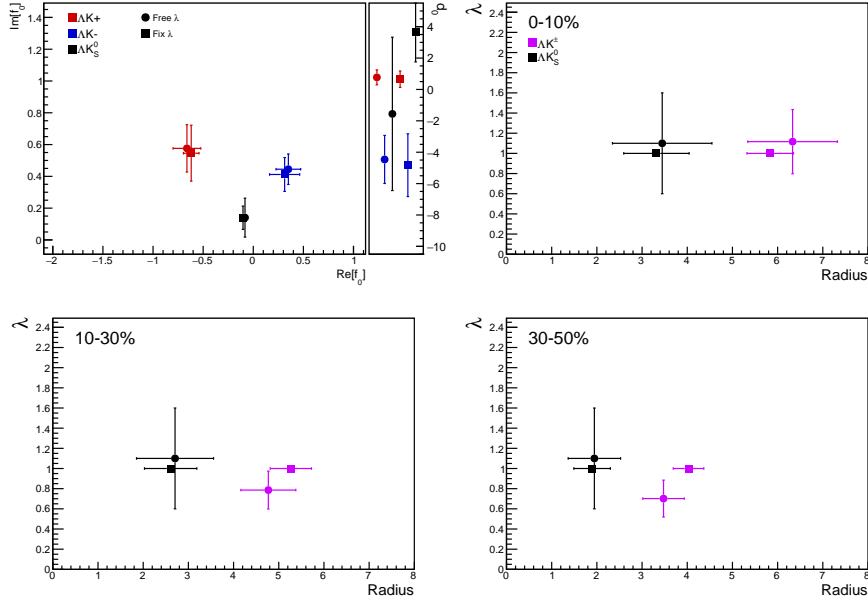
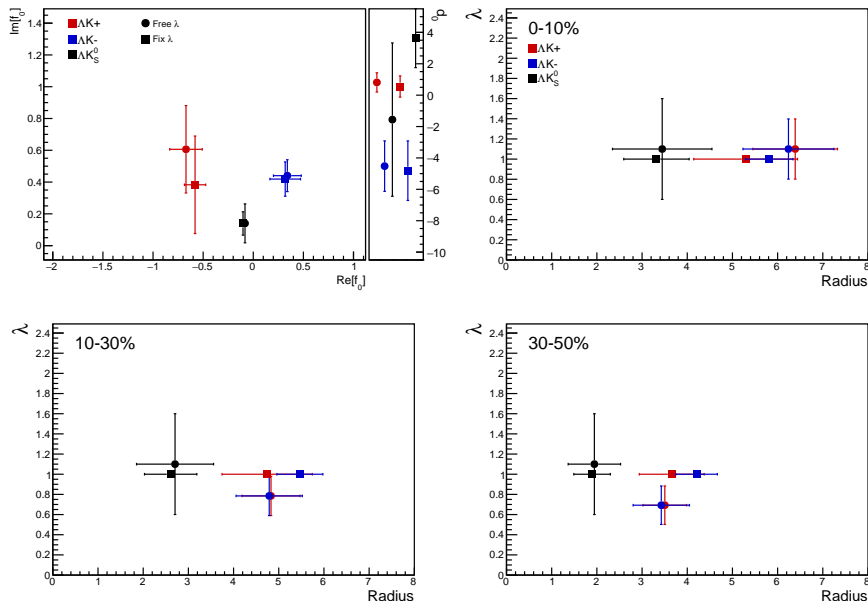


**Fig. 49:** Compare Fit Parameters: Number of residuals: Results shown for the case of 3 (+), 10 (X), and no (circles) residual contributors.



(a) Shared radii



(b) Separate radii

**Fig. 50:** Compare Fit Parameters: Free vs fixed  $\lambda$ : Results shown for  $\lambda$  parameters left free (filled symbols) and fixed to 1 (open symbols). In the top plot (50a), the  $\Lambda K^+$  and  $\Lambda K^-$  analyses share radii, whereas in the bottom (50b) they have unique radii.

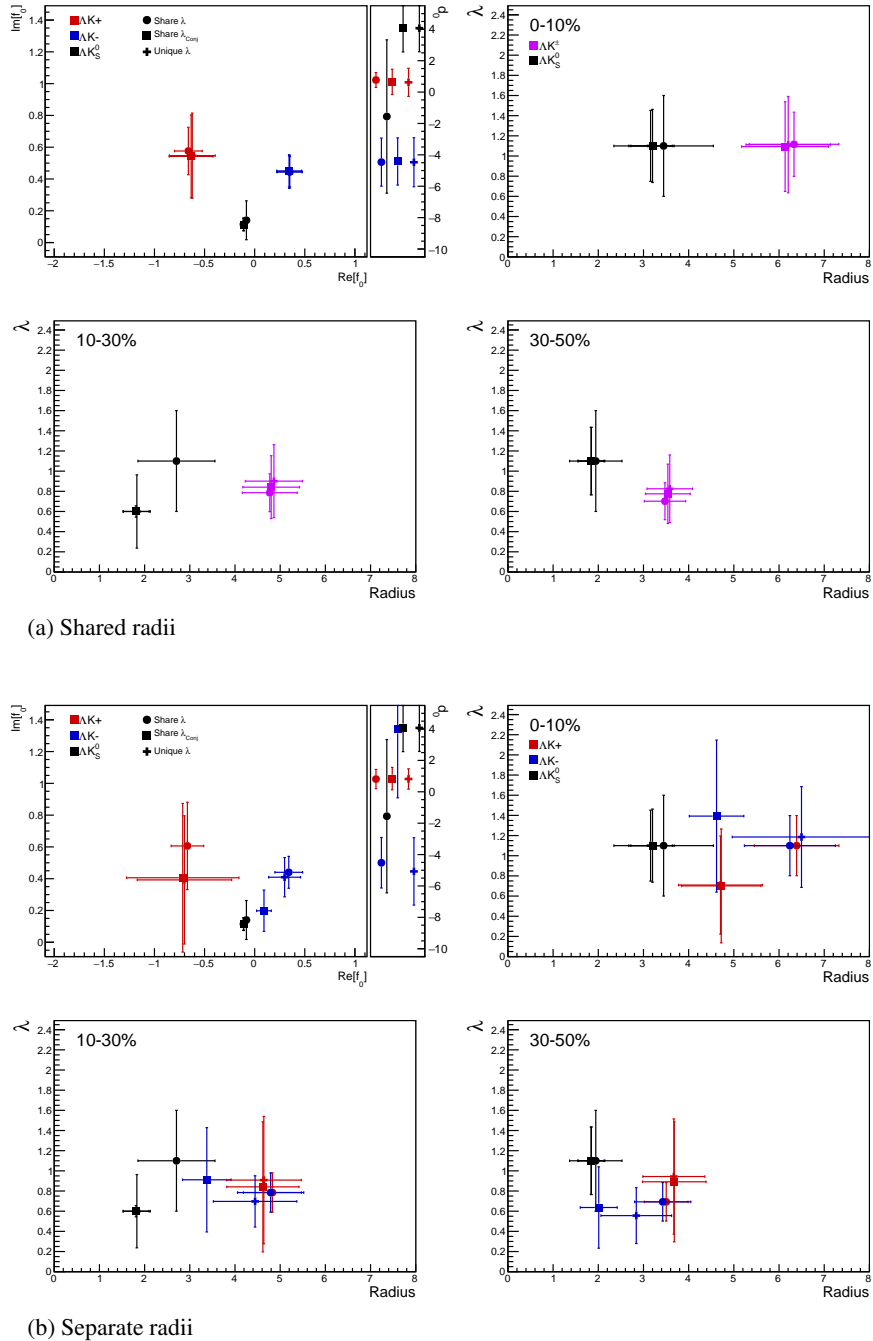
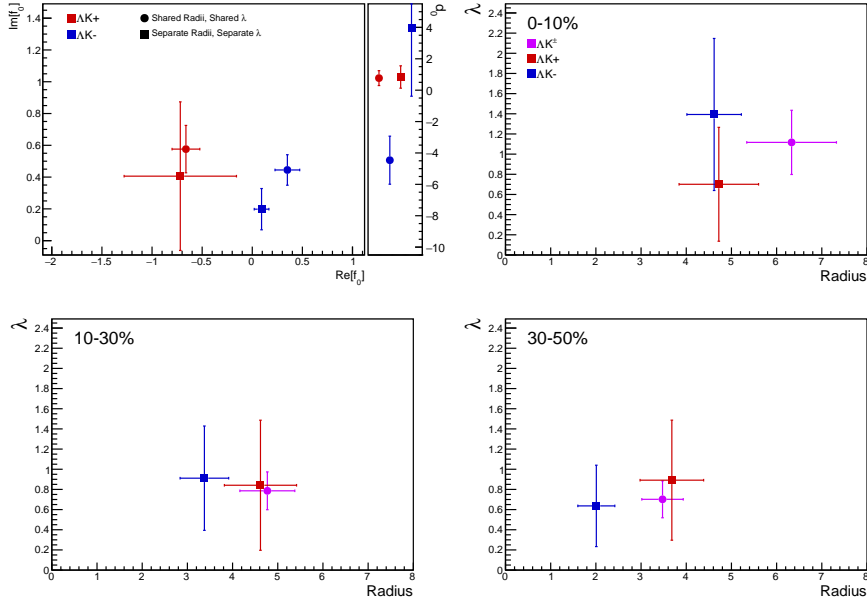
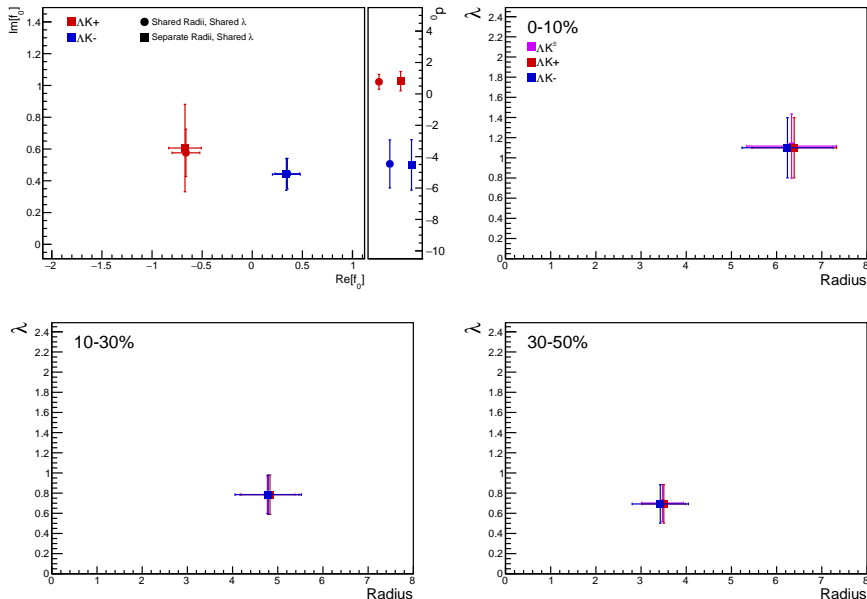


**Fig. 51:** Compare Fit Parameters: Shared vs unique  $\lambda$ : Results shown for different sharing of the  $\lambda$  parameters between analyses and systems. In the top (51a), the  $\Lambda K^+$  and  $\Lambda K^-$  analyses share radii, whereas in the bottom (51b), they do not. “Share  $\lambda$ ” (circles) is the case where a single  $\lambda$  is shared amongst all analyses for a given centrality bin (i.e., in 51a, 3 radius parameters and 3  $\lambda$  parameters). “Share  $\lambda_{Conj}$ ” (squares) means that conjugate pairs (ex.  $\Lambda K^+$  and  $\bar{\Lambda} K^-$ ) share a  $\lambda$  parameter for each centrality. This corresponds to 6 total  $\lambda$  parameters (for each of the 3 centrality bins, the  $\Lambda K^+(\bar{\Lambda} K^-)$  receives a unique  $\lambda$ , as does  $\Lambda K^-(\bar{\Lambda} K^+)$ ). Finally, in “Unique  $\lambda$ ” (+), each analysis received its own unique  $\lambda$  parameter. This corresponds to 12  $\lambda$  parameters (for each of the 3 centrality bins, each  $\Lambda K^+$ ,  $\bar{\Lambda} K^-$ ,  $\Lambda K^-$ , and  $\bar{\Lambda} K^+$  receives a unique  $\lambda$ ).



(a) Shared radii



(b) Separate radii

**Fig. 52:** Compare Fit Parameters: Shared vs. Separate Radii: Results shown for the case of radii being shared between  $\Delta K^+$  and  $\Delta K^-$  (circles) vs not shared (squares). In (a), when the radii are not shared between  $\Delta K^+$  and  $\Delta K^-$ , neither are the  $\lambda$  parameters. In (b), the  $\lambda$  parameters are always shared between  $\Delta K^+$  and  $\Delta K^-$

788 **7.1.5 Discussion of  $m_T$ -Scaling**

789 It is clear from the results presented in the previous sections, that the  $\Lambda K$  systems do not conform to the  
 790 approximate  $m_T$ -scaling of the pair source sizes. At first thought, this may appear to be a troubling result;  
 791 the approximate scaling is an observed consequence of the collective behavior of the soft (low- $p_T$ ) sector  
 792 of the produced system. The  $\Lambda$  and  $K$  particles certainly participate in the collective expansion of the  
 793 QGP medium, so why do their extracted femtoscopy radii not behave as expected? To get straight to the  
 794 point: the  $\Lambda K$  systems are (obviously) comprised on non-identical particles, each with its own and unique  
 795 single particle source. Each source is, in general, unique in both its overall size, and in its space-time po-  
 796 sition within the produced medium. The hydrodynamic nature of the medium produces the approximate  
 797  $m_T$ -scaling with respect to these single-particle sources, not the pair sources. The combination of these  
 798 effects, when probing correlations between non-identical particle pairs, leads to extracted radii falling  
 799 outside of the (identical particle femtoscopy)  $m_T$ -scaling trend. Figure 53 (which contains the same data  
 800 as Fig.30), shows again the  $R_{\text{inv}}$  vs  $m_T$  plot, but also highlights (with arrows) the approximate individual  
 801  $\langle m_T \rangle$  values of the single particle distributions. The grey circles show how to single particle sizes change  
 802 with  $m_T$ .

803 Taking a close look at Fig. 53, one can see that the previously published data (transparent points) are  
 804 for identical particle analyses only. For these cases, the pair source, probed through femtoscopy, is  
 805 comprised of two identical sources laying on top of each other. The extracted femtoscopy radii are  
 806 related to the single particle source sizes by a factor of  $\sqrt{2}$ , and of course follow the  $m_T$ -scaling trend.  
 807 The other (unpublished) non-identical particle femtoscopy study ( $p\Lambda$ ) included in the figure, also shows  
 808 radii deviating from the  $m_T$ -scaling band. Drawing a comparison with the  $\Lambda\bar{\Lambda}$  study shown in Fig. 30  
 809 is a bit more complicated; the  $\Lambda\bar{\Lambda}$  system, although containing non-identical particles, does contain a  
 810 particle with its antiparticle, for which annihilation could conceivably alter the pair source distribution.  
 811 It would be more surprising if the non-identical analyses did happen to conform to the scaling; although,  
 812 this could occur for a non-identical analysis in which the particles have similar masses as well as similar  
 813  $m_T$  distributions. For the case presented here, the result differing from  $m_T$ -scaling is not surprising.

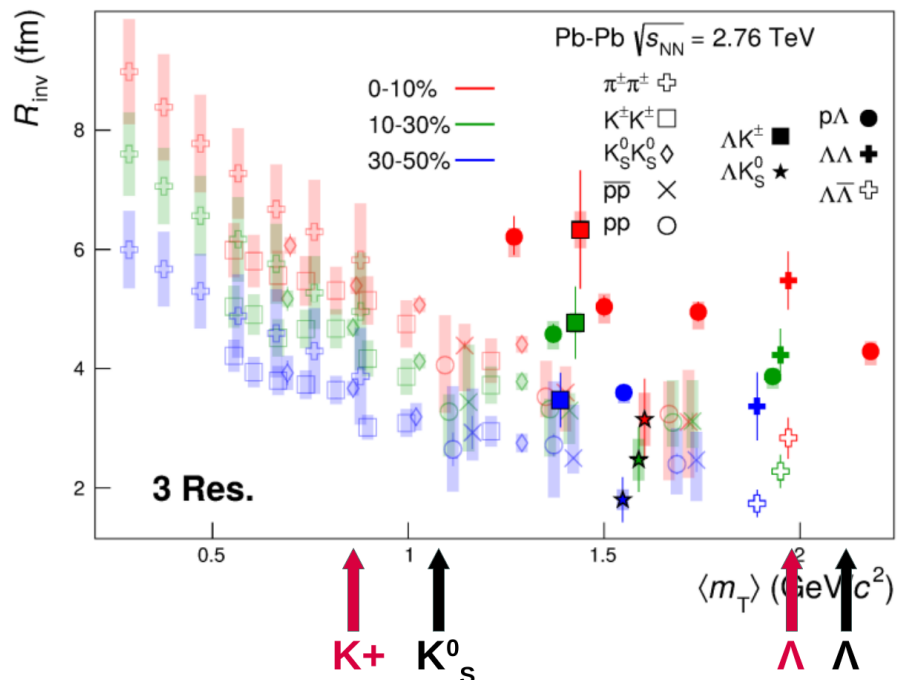


**Fig. 53:** Same as Fig. 30, but with the individual  $m_T$  values for the single particle distributions identified. The grey circles show how the single particle sizes are expected to change with  $m_T$ .

I will also briefly point out that it is not automatically clear where a non-identical study should be placed on such a  $R_{\text{inv}}$  vs  $m_T$  plot. Each single particle distribution has a well-defined  $\langle m_T \rangle$ , which, to a large extent, determines the single particle region of homogeneity. When combining two sources with different spatio-temporal characteristics, originating from particles of different  $m_T$ , how should one define the pair  $m_T$ ? A simple mathematical expression for the pair  $m_T$  is easy to come up with, but that's not exactly what I'm hinting at here. With respect to this  $m_T$ -scaling picture, the  $m_T$  value dictates the source size, and one desires the same for non-identical particles. However, do the two unequal sized sources both contribute equally to the extracted femtoscopic size? Or does the larger (smaller) source more closely dictate the femtoscopic signal? If the contribution is equal, then it seems natural to simply more-or-less average the two, single particle,  $m_T$  values. If the contribution is unequal, then there should be introduced some sort of weighting in the pair  $m_T$  calculation reflecting this fact. In any case, in our study we use the most straightforward definition of pair  $m_T$ , defined as:

$$m_{T,\text{pair}}^2 = \left( \frac{m_{\text{inv}}}{2} \right)^2 + \left( \frac{1}{2} |\mathbf{p}_{T,1} + \mathbf{p}_{T,2}| \right)^2 \quad (24)$$

Many times, the equation for non-identical particle pair  $m_T$  is defined with the average mass replacing  $m_{\text{inv}}/2$ . However, the above Eq. 24 is more directly analogous to the single particle  $m_T$ :

$$m_T^2 = m^2 + \mathbf{p}_T^2 = (p^0)^2 - (p^3)^2 \quad (25)$$

as, Eq. 24 may be rewritten as:

$$\begin{aligned} m_{T,\text{pair}}^2 &= (K^0)^2 - (K^3)^2 \\ K^\mu &\equiv \frac{1}{2} (p_1^\mu + p_2^\mu) \end{aligned} \quad (26)$$

Identical particle femtoscopic studies are able to probe only the size of the emitting region, or, more precisely, the second moments of the emission function. In addition to this, non-identical particle studies are able to measure the relative emission shifts, the first moments of the emission function. One method to extract information about the emission asymmetries in the system is via a spherical decomposition of the correlation function. With this method, one can draw a wealth of information from just a few components of the decomposition. More specifically, the  $C_{00}$  component is similar to the 1D correlation functions typically studied, and probes the overall size of the source. The  $\Re C_{11}$  component probes the asymmetry in the system; a non-zero value reveals the asymmetry.

In Fig. 54 we show results for the  $C_{00}$  and  $\Re C_{11}$  components from the spherical decomposition of our  $\Lambda K^+$  system in the 0-10% centrality bin (red circles). Results from a number of other components within the decomposition, as well as for our  $\Lambda K_S^0$  and  $\Lambda K^-$  systems, are contained in 9.2. Along with the experimental data in Fig. 54, we have also included results from THERMINATOR simulation for an impact parameter of  $b = 2$  fm (gold stars). As THERMINATOR does not include any final state effects, we assumed scattering parameters  $(\Re f_0, \Im f_0, d_0) = (-1.16, 0.51, 1.08)$  and weighted the numerator pairs with  $|\Psi|^2$ , as discussed previously. As seen in the figure, the  $C_{00}$  signal is similar to that observed in our one-dimensional study. The  $\Re C_{11}$  component shows a clear deviation from zero, and the negative value signifies that the  $\Lambda$  particles are, on average, emitted further out and/or earlier than the  $K$  mesons.

Fig. 55 shows a closer look at the THERMINATOR simulation, whose spherical harmonic decomposition was shown along with the data in Fig. 54. The top left of Fig. 55a shows a fit to the one-dimensional correlation function from THERMINATOR. The scattering parameters are known precisely here, as they served as the weights used in the simulation, and are kept constant in the fit. We are interested in looking

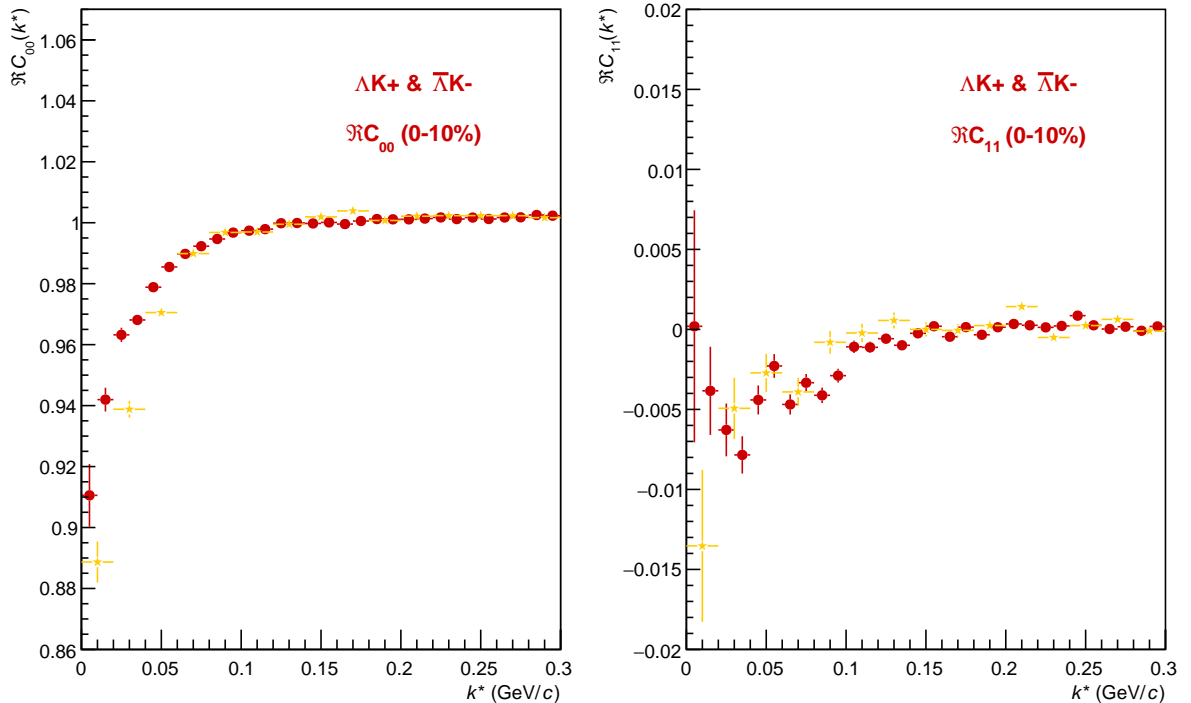
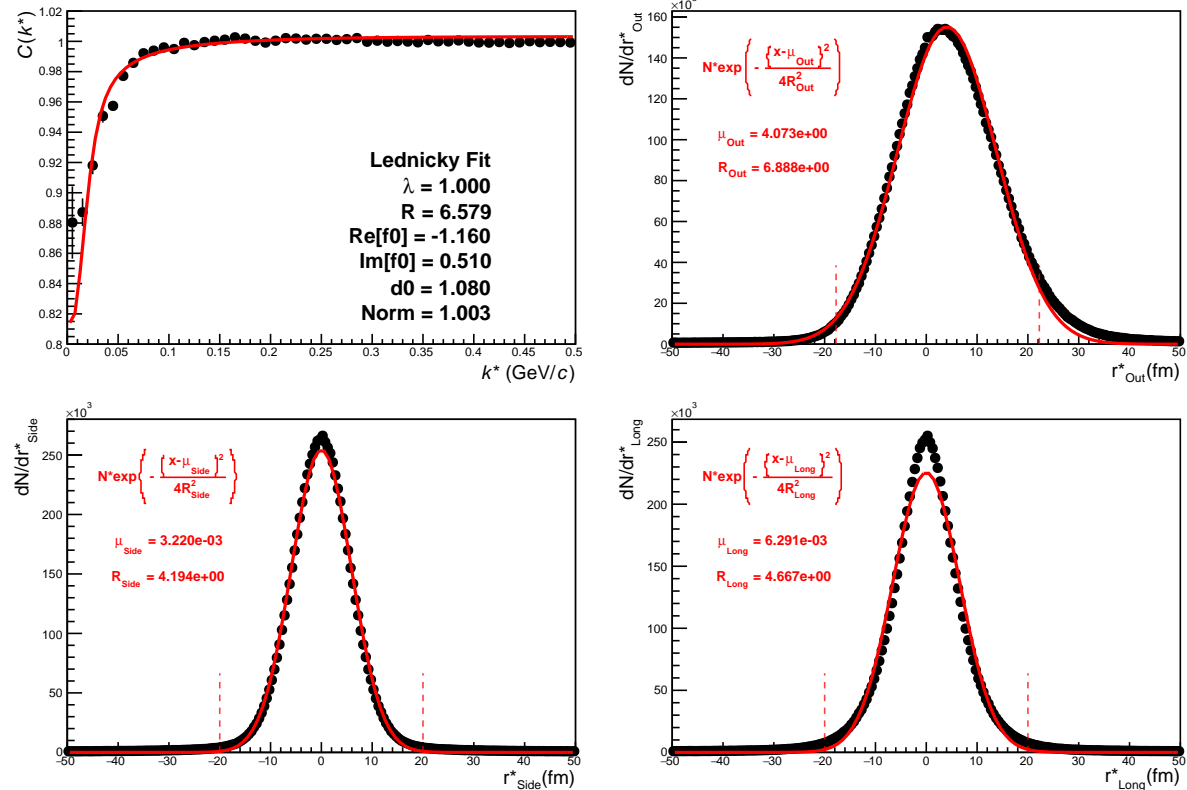


**Fig. 54:**  $C_{00}$  (left) and  $\Re C_{11}$  (right) components of a spherical harmonic decomposition of the  $\Lambda K^+$  correlation function for the 0-10% centrality bin. The  $C_{00}$  component is similar to the 1D correlation functions typically studied, and probes the overall size of the source. The  $\Re C_{11}$  component probes the asymmetry in the system; a non-zero value reveals the asymmetry

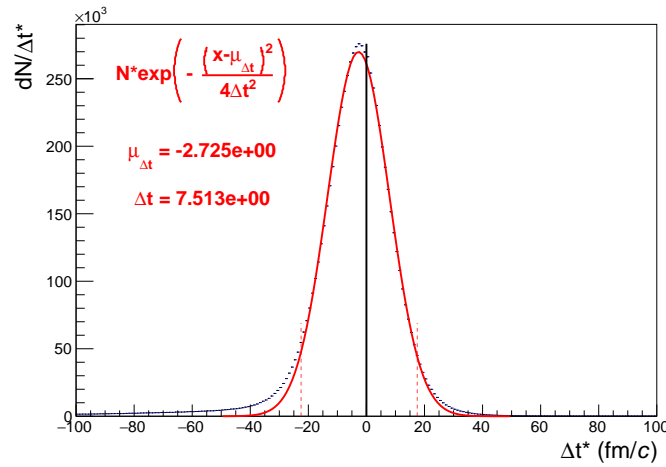
at the extracted one-dimensional source size here, so the  $\lambda$  parameter is also fixed at unity. The other three plots in Fig. 55a show the source distribution in the out (top right), side (bottom left), and long (bottom right) directions (all in the PRF). The source distributions have all been fitted with a Gaussian form, the result of which is printed within the respective plot. One immediately sees a significant shift in the out direction,  $\mu_{\text{out}} \approx 4$  fm, and negligible shift in the other two directions,  $\mu_{\text{side}} \approx \mu_{\text{long}} \approx 0$  fm. The figure demonstrates that, within the THERMINATOR model, the  $\Lambda$  is, on average, emitted further out than its K partner. Finally, Fig. 55b shows the distribution of the relative time of emittance, again in the PRF. The figure shows that the  $\Lambda$  is, on average, emitted earlier than its K partner.

We end this section with a brief look at how a spatial separation of the single particle sources affects the radii extracted from a femtoscopic analysis. To achieve this, we use THERMINATOR in a similar fashion as described above, but with one important difference. Instead of taking the source information from THERMINATOR, we instead draw the source from a pre-determined Gaussian distribution. In all cases, we take  $R_{\text{out}} = R_{\text{side}} = R_{\text{long}} = 5$  fm, and  $\mu_{\text{side}} = \mu_{\text{long}} = 0$  fm. Figure 56 shows an example of results obtained from THERMINATOR following this procedure, where  $\mu_{\text{out}} = 3$  fm.

In Figure 57, we show results for the case of  $\mu_{\text{out}} = 1$  fm,  $\mu_{\text{out}} = 3$  fm, and  $\mu_{\text{out}} = 6$  fm. In this figure, we do not show the side and long distributions, as they appear identical to those shown in Fig. 56. The figure demonstrates that as the separation  $\mu_{\text{out}}$  increases, so do the extracted femtoscopic radii.



(a) Caption 1



(b) Caption 2

**Fig. 55:** Long Overall

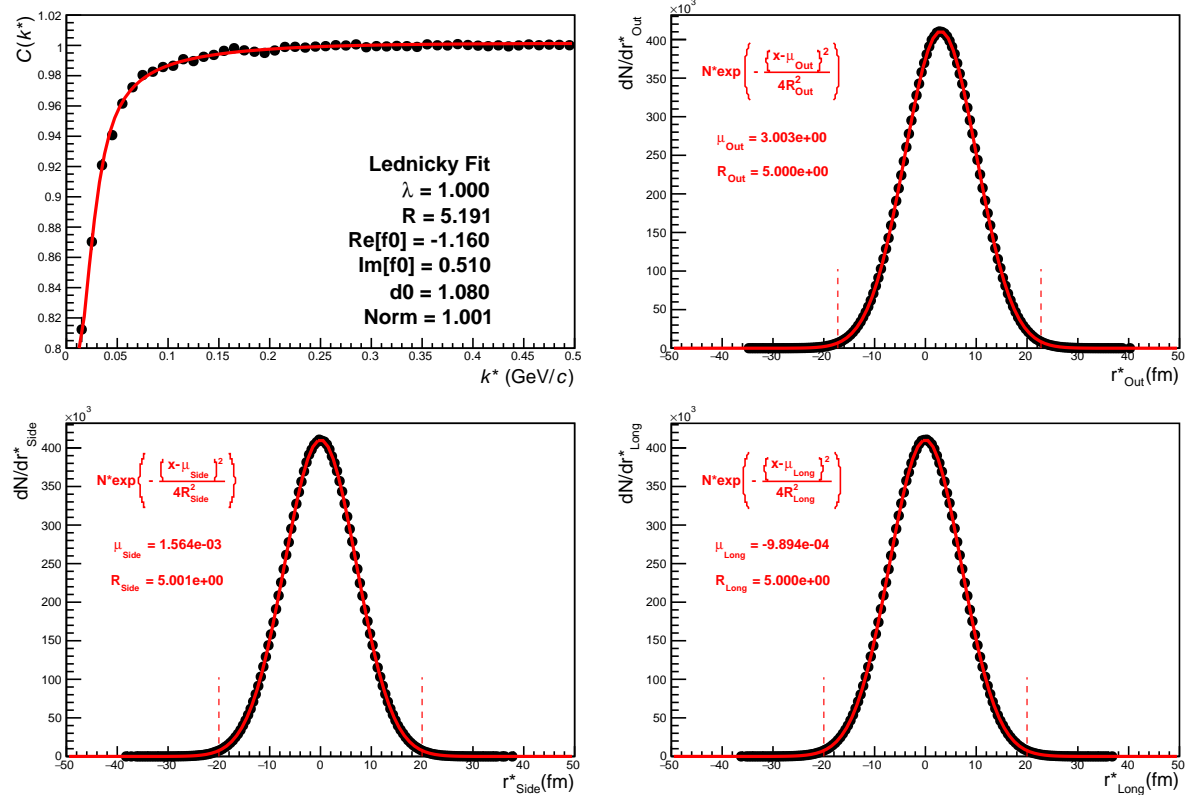


**Fig. 56:** Long Caption

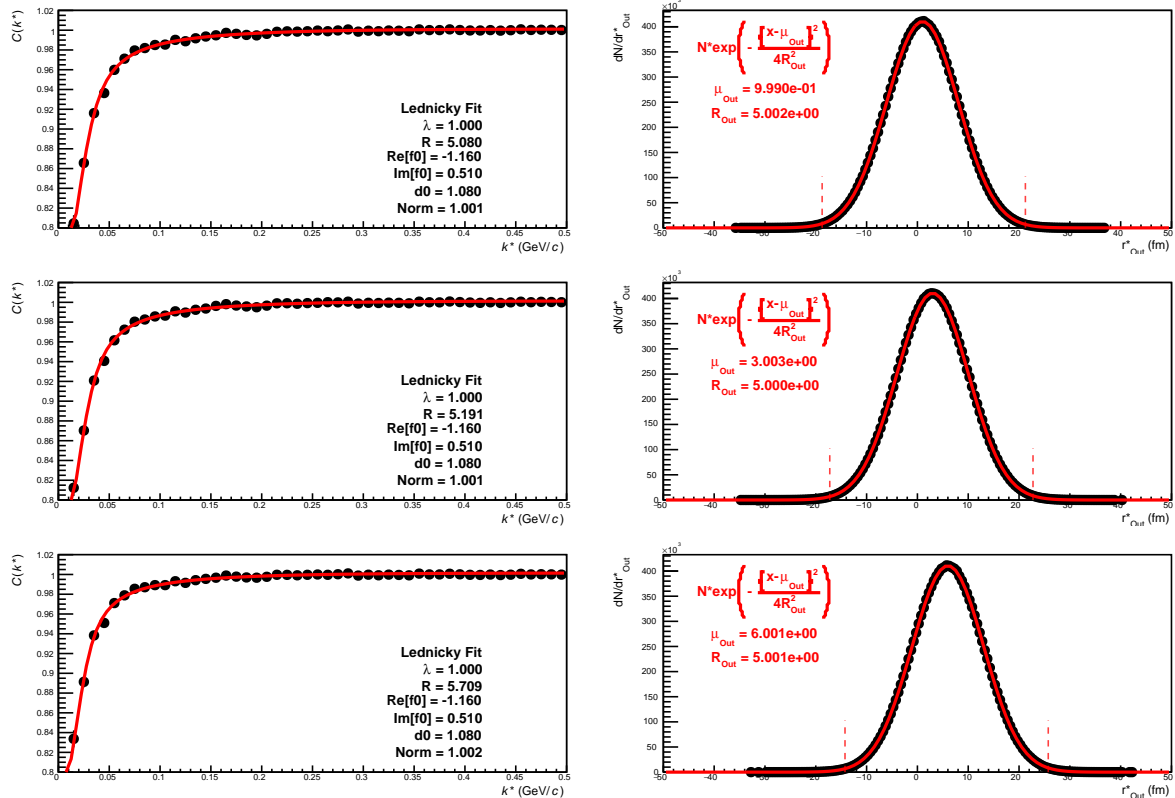


**Fig. 57:** Long Caption

## 867 7.2 Results: $\Xi K^\pm$

868 Even without any fits to the data, the fact that the  $\Xi^- K^+$  data dips below unity (Fig. 58) is exciting, as  
 869 this cannot occur purely from a Coulomb interaction. We hope that this dip signifies that we are able to  
 870 peer through the overwhelming contribution from the Coulomb interaction to see the effects arising from  
 871 the strong interaction.

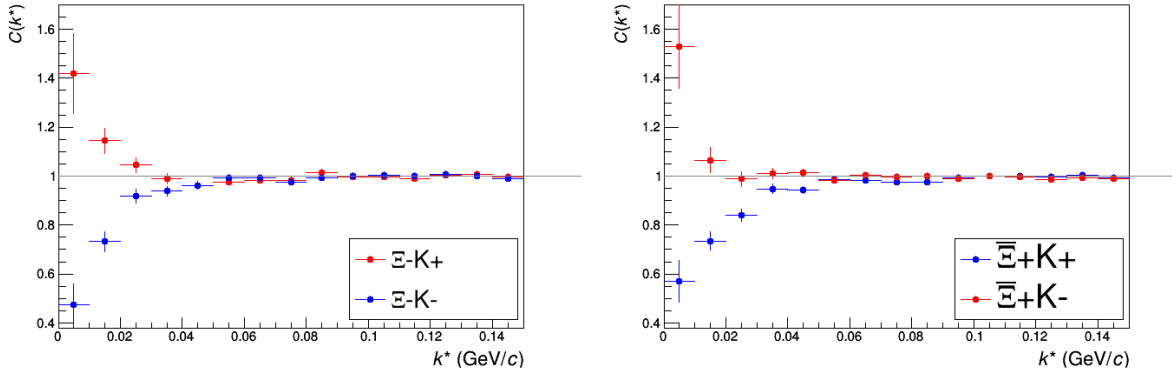
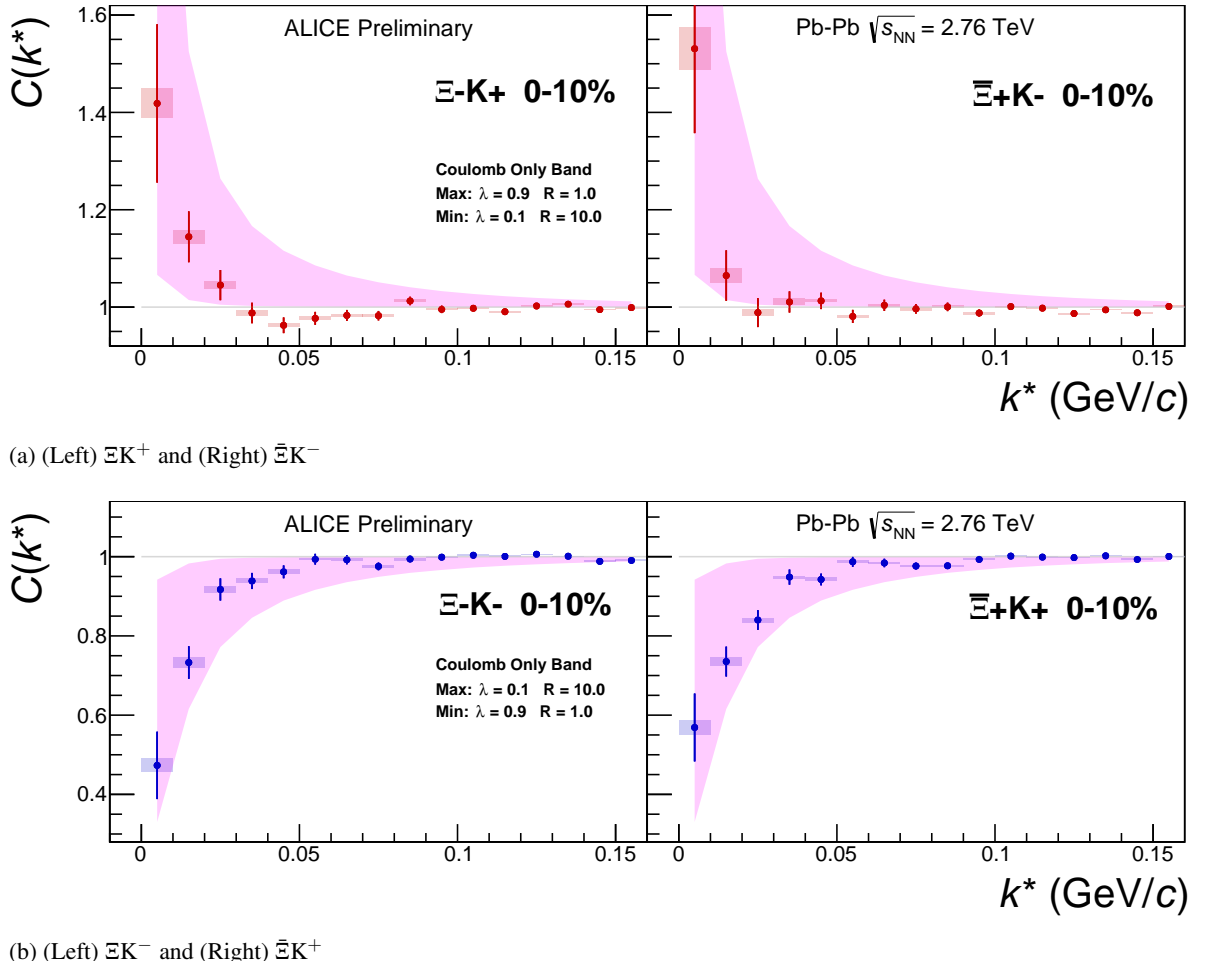


**Fig. 58:**  $\Xi K^\pm$  Results for 0-10% Centrality. (Left)  $\Xi^- K^+$  and  $\Xi^- K^-$  (Right)  $\Xi^+ K^+$  and  $\Xi^+ K^-$

872 Figure 59 demonstrates graphically, that the  $\Xi^- K^+$  results cannot be described by solely the Coulomb  
 873 interaction. In this figure, we present the data along with a Coulomb-only band. The Coulomb-only  
 874 band is spanned by two Coulomb-only curves, whose parameters are given in the figure. The Coulomb-  
 875 only curves were generated using a technique identical to the generation of the fit function, described  
 876 in Sec. 5.2, except, of course, with the nuclear scattering parameters all set to zero. The Coulomb-only  
 877 curves change monotonically with varying  $\lambda$  or varyin radius parametre, therefore, any curves built with  
 878 parameter sets intermediate to those use in the Coulomb-only band will be contained in the band.

879 Including the strong interaction into the simulation can change, sometimes dramatically, the resulting  
 880 correlation function, as shown in Figure 60. In the figure, the solid line represents a Coulomb-only curve,  
 881 i.e. a simulated correlation function with the strong interaction turned off. The dashed lines represent a  
 882 full simulation, including both the strong and Coulomb interactions. The two dashed lines differ only in  
 883 the real part of the assumed scattering length: positive in Set 1, and negative in Set 2. In the top figure,  
 884 for the  $\Xi^- K^+$  simulation, we see that parameter set 2, with a negative real part of the scattering length,  
 885 causes the simulated curve to dip below unity, as is seen in the data. If there is a parallel to be drawn  
 886 between this analysis and the  $\Lambda K$  analysis, we expect to see similar effects in the  $\Lambda K^+$  system and the  
 887  $\Xi^- K^+$  systems. In these systems, we could have an  $s\bar{s}$  annihilation picture. Or, another possible way of  
 888 thinking about these systems is in terms of net strangeness. The  $\Lambda K^+$  system has  $S=0$ , while the  $\Lambda K^-$   
 889 has  $S=-2$ . The  $\Xi^- K^+$  has  $S=-1$ , while the  $\Xi^- K^-$  has  $S=-3$ .

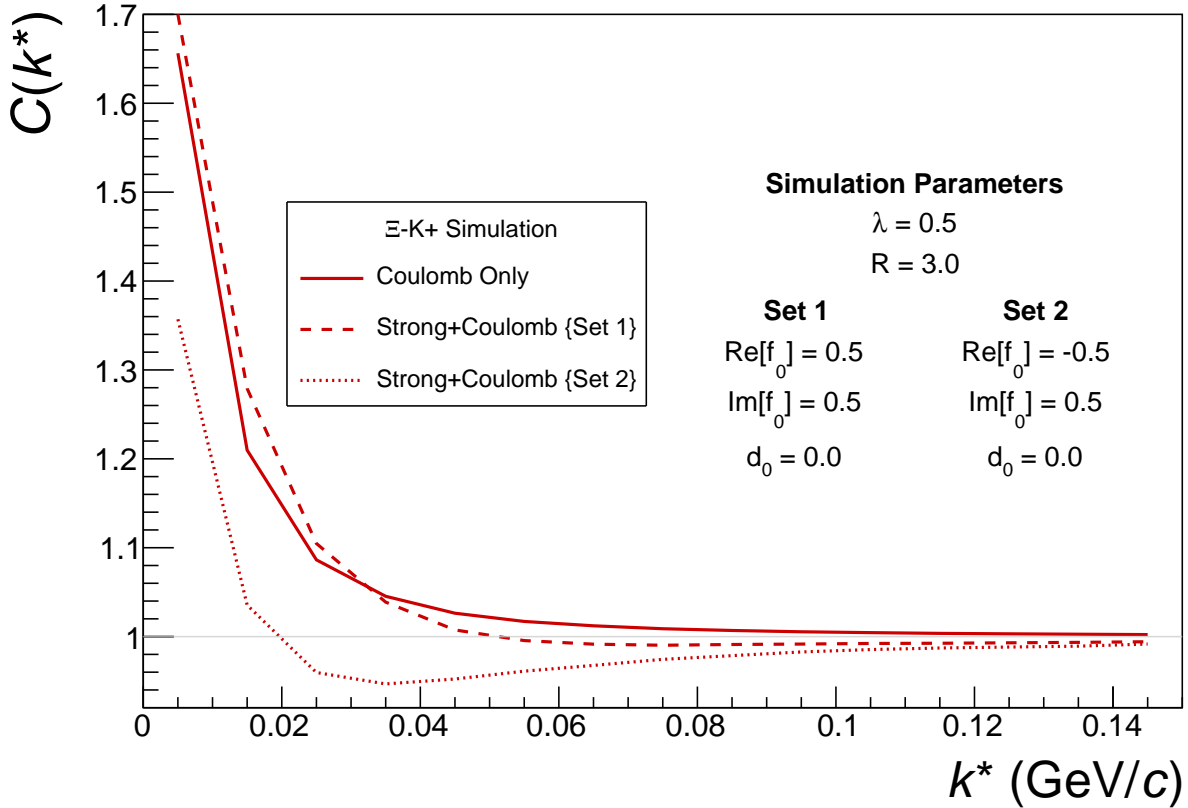
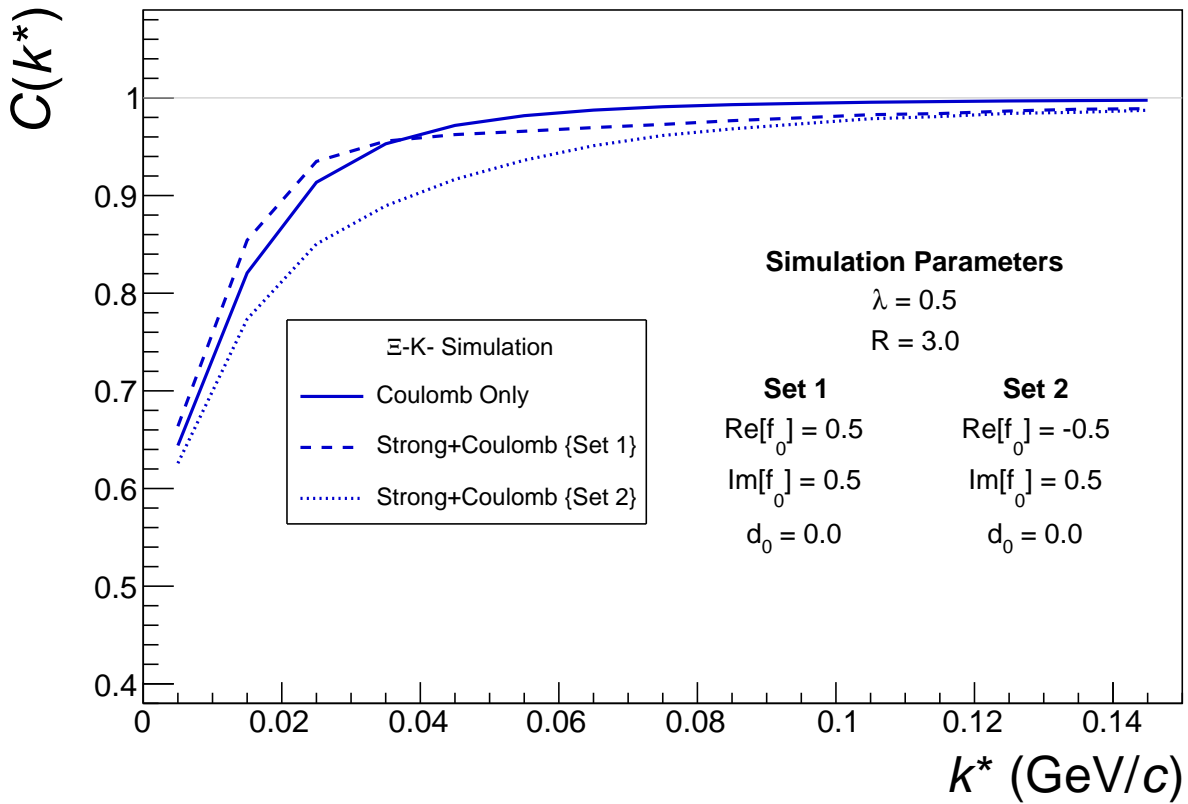
890 The author was asked to perform a global Coulomb-only fit to the data, to ensure that the system truly  
 891 could not be described simply by the Coulomb interaction. In order words, in the fit, the strong force was  
 892 turned off, and the  $\Xi^- K^+$ ,  $\Xi^+ K^-$ ,  $\Xi^- K^-$ ,  $\Xi^+ K^+$  systems all share one sinlge radius parameter, while the  
 893 pair and conjugate pair systems share a  $\lambda$  parameter. The results of this fit are shown in Figures 61 and  
 894 62. In Fig. 61, there was a lower limit of 0.1 fm placed on the radius parameter, and the radius parameter  
 895 was initialized to 3 fm (as seems reasonable, when considering the transverse mass of the system and  
 896 looking at Fig. 30). As is shown in the results, the radius parameter reached this unrealistic lower bound  
 897 of 0.1 fm. In Fig. 62, the parameters were all unbounded, and the radius parameter was initialized to 10  
 898 fm. In this case, the radius parameters reamins high, and ends at an unrealistic value of 10.84 fm. In both  
 899 cases, the  $\lambda$  parameters are too low. From these figures, we conclude that a global Coulomb-only fit is  
 900 not suitable for the data.



**Fig. 59:**  $\Xi K^\pm$  data with Coulomb-only bands for the 0-10% centrality bin. The Coulomb-only bands span two sets of Coulomb-only curves: (1)  $\lambda = 0.9$ ,  $R = 1.0$  fm and (2)  $\lambda = 0.1$ ,  $R = 10.0$  fm. The Coulomb-only curves are simulated correlation functions for the respective pair system assuming only a Coulomb interaction, i.e. ignoring the strong interaction. The Coulomb-only curves change monotonically with varying  $\lambda$  and varying  $R$ , therefore, any intermediate parameter set will fall within this Coulomb-only band.

901 Although the global Coulomb-only fit failed, it is possible that a Coulomb-only fit performed on  $\Xi^- K^+$   
 902 and  $\bar{\Xi}^+ K^-$  separately from  $\Xi^- K^-$  and  $\bar{\Xi}^+ K^+$  could be suitable. The result of such fits are shown in  
 903 Figures 63 and 64. Figure 63, shows that the fit is not able to describe the dip in the  $\Xi^- K^+$  data below  
 904 unity. Of course, this is obviously true for an attractive Coulomb-only fit. The radius parameter of  
 905 8.43 fm extracted from this fit is unrealistically large. In Figure 64 shows the Coulomb-only fit can  
 906 described the  $\Xi^- K^-$  data reasonable well; although the extracted radius of 3.73 fm is somewhat larger  
 907 than expected.

## 908 8 To Do

(a)  $\Xi K^+$  and  $\bar{\Xi} K^-$  simulation(b)  $\Xi K^-$  and  $\bar{\Xi} K^+$  simulation

**Fig. 60:** Effect on the Coulomb-only curve of including the strong interaction for  $\Xi K^\pm$  systems. The solid line represents a Coulomb-only curve, i.e. a simulated correlation function with the strong interaction turned off. The dashed lines represent a full simulation, including both the strong and Coulomb interactions. The two dashed lines differ only in the real part of the assumed scattering length: positive in Set 1, and negative in Set 2.

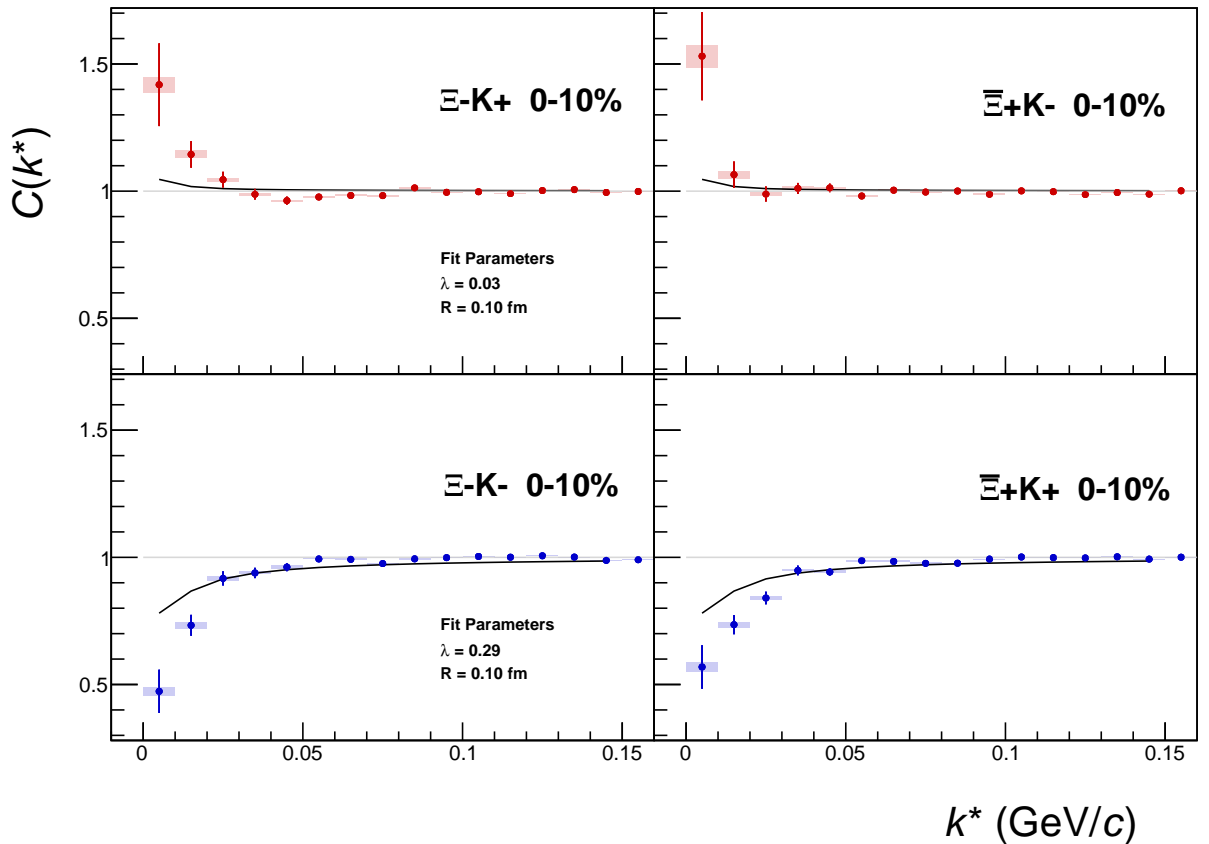


**Fig. 61:**  $\Xi K^\pm$  Global Coulomb-only fit (Set 1) for 0-10% centrality. In this fit, there was a lower limit of 0.1 fm placed on the radius parameter, and the radius parameter was initialized to 3 fm (as seems reasonable, when considering the transverse mass of the system and looking at Fig. 30). As is shown in the results, the radius parameter reached this unrealistic lower bound of 0.1 fm. Also, the extracted  $\lambda$  parameters are too low.

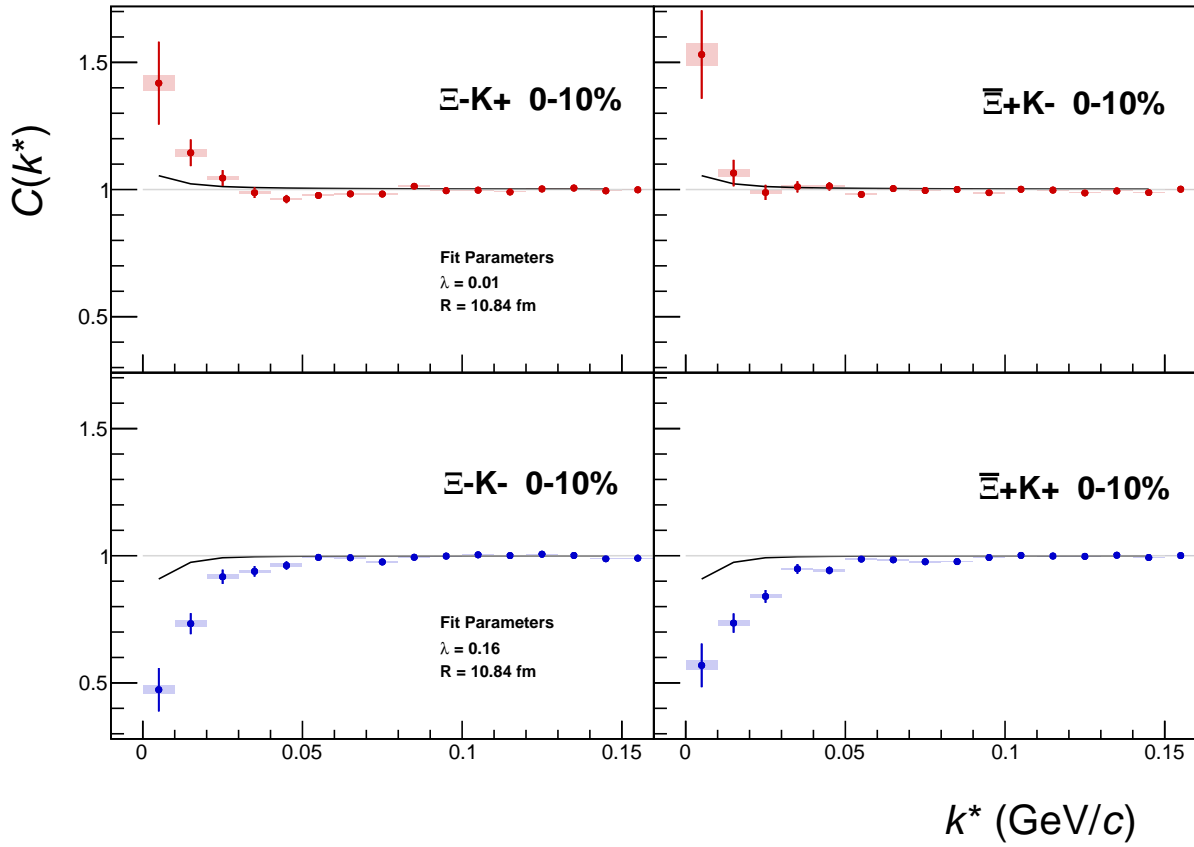


**Fig. 62:**  $\Xi K^\pm$  Global Coulomb-only fit (Set 2) for 0-10% centrality. In this fit, the parameters were all unbounded, and the radius parameter was initialized to 10 fm. In this case, the radius parameters remain high, and ends at an unrealistic value of 10.84 fm. Also, the extracted  $\lambda$  parameters are too low.

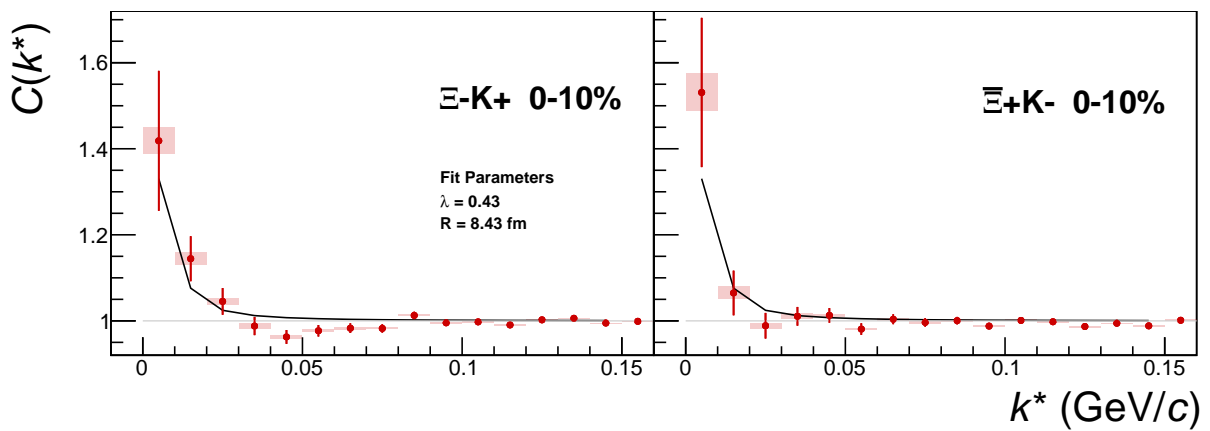


**Fig. 63:**  $\Xi\text{-}K^+$  Coulomb-only fit for 0-10% centrality

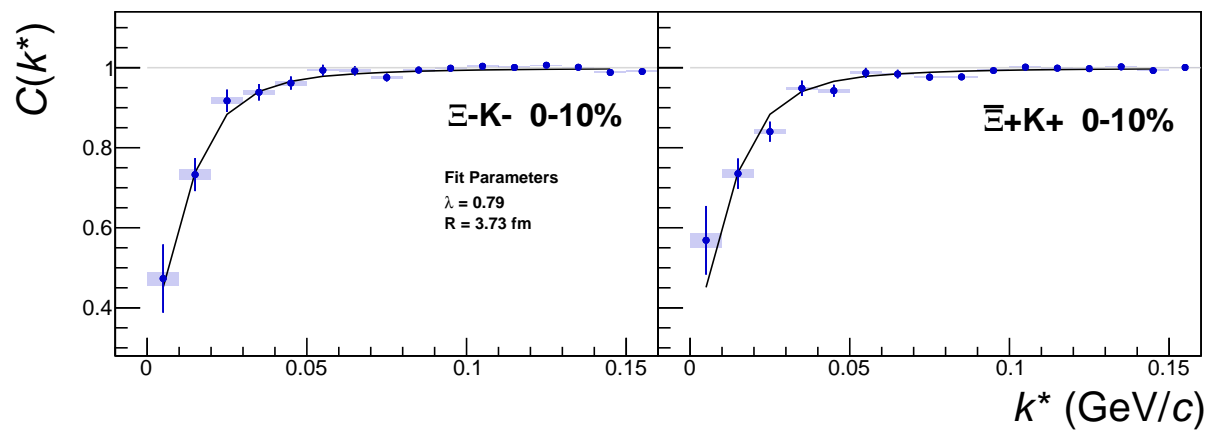
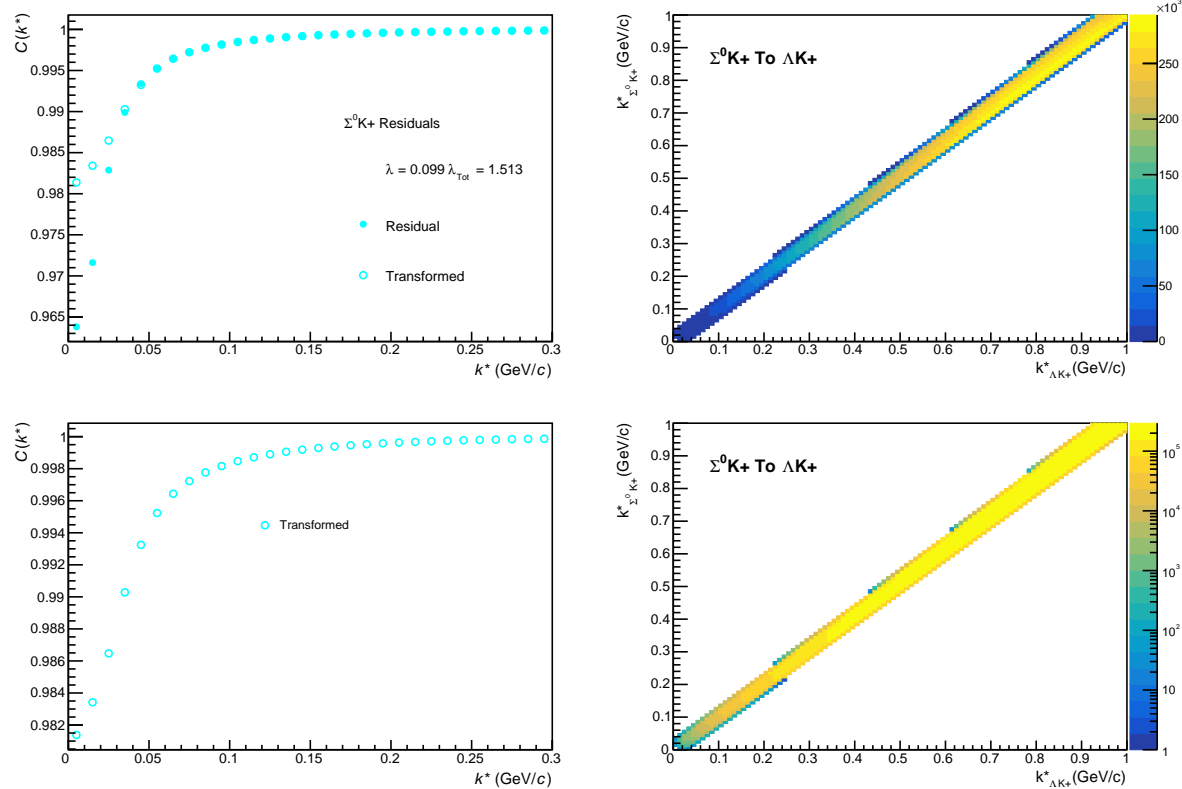


**Fig. 64:**  $\Xi^- K^-$  Coulomb-only fit for 0-10% centrality

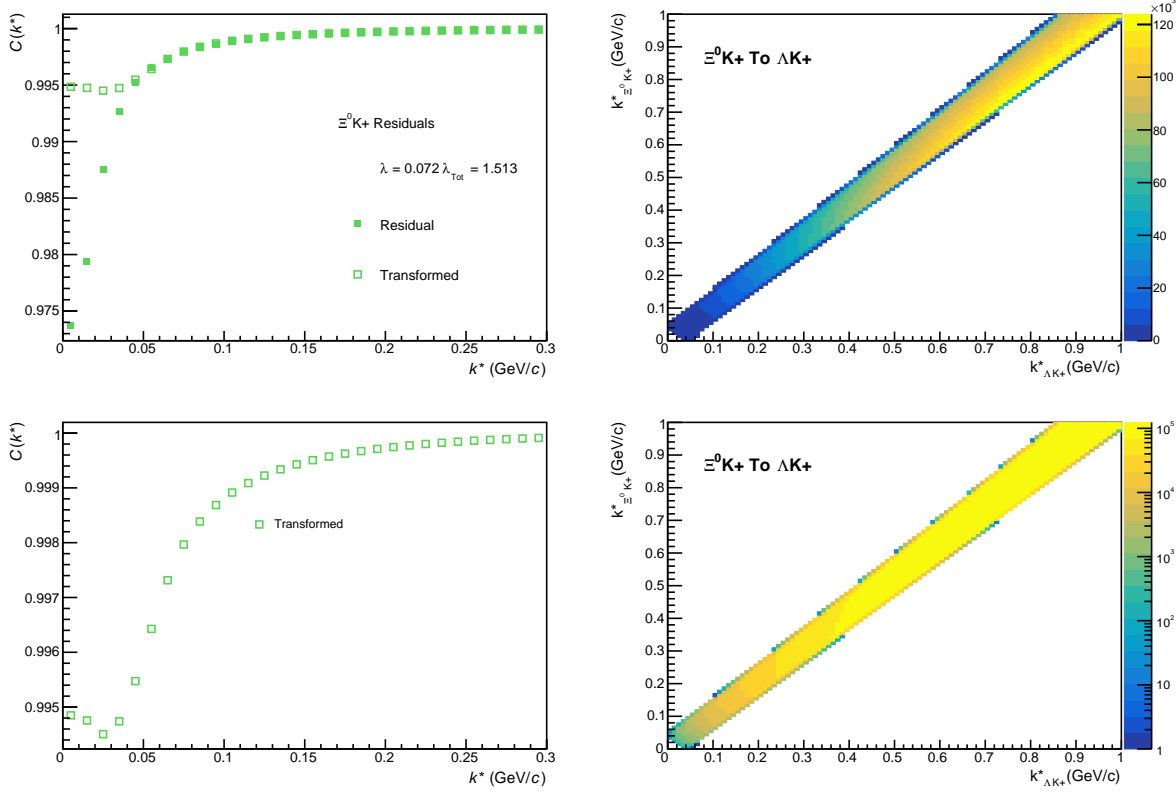
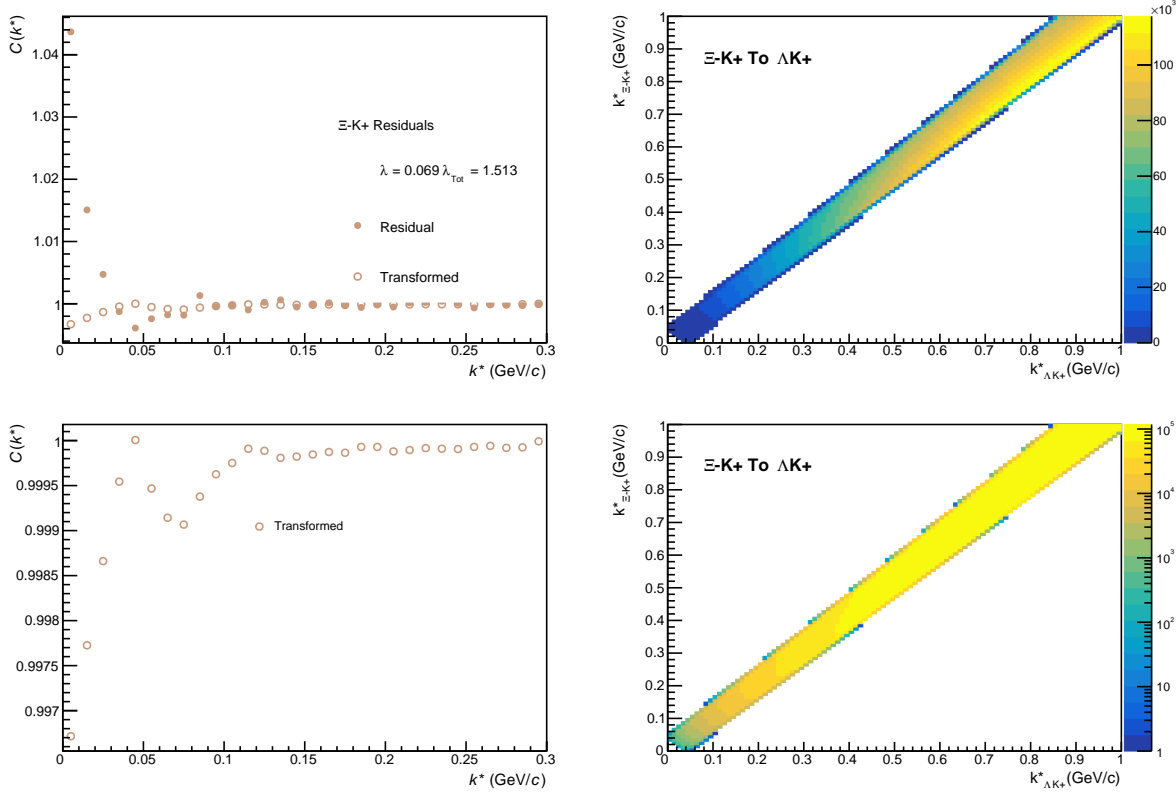
909 **9 Additional Figures**

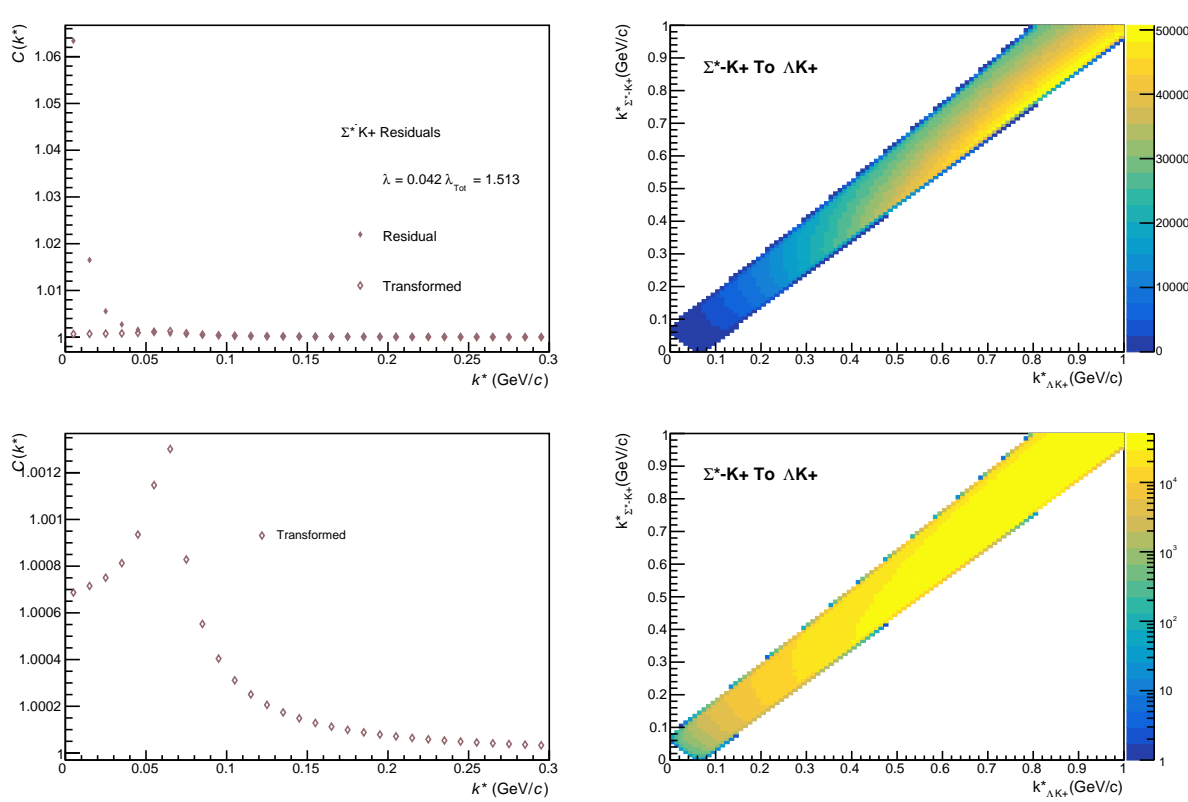
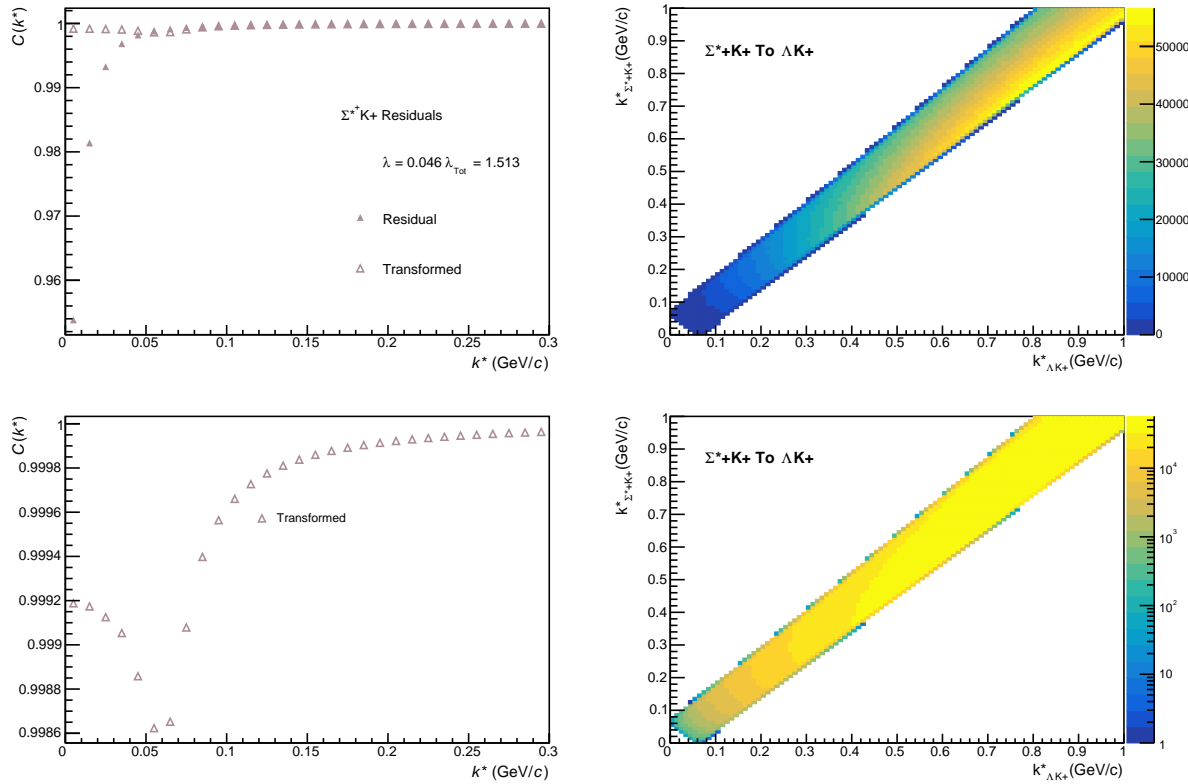
910 **9.1 Residuals**

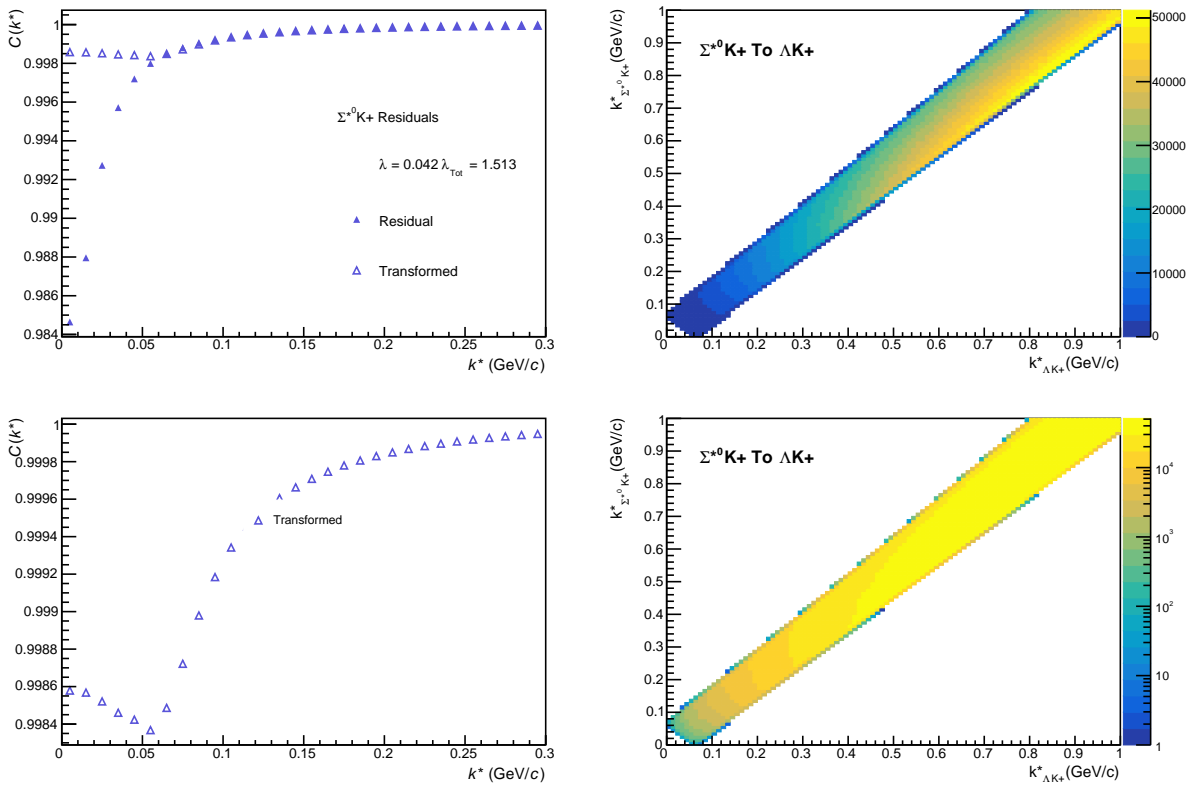
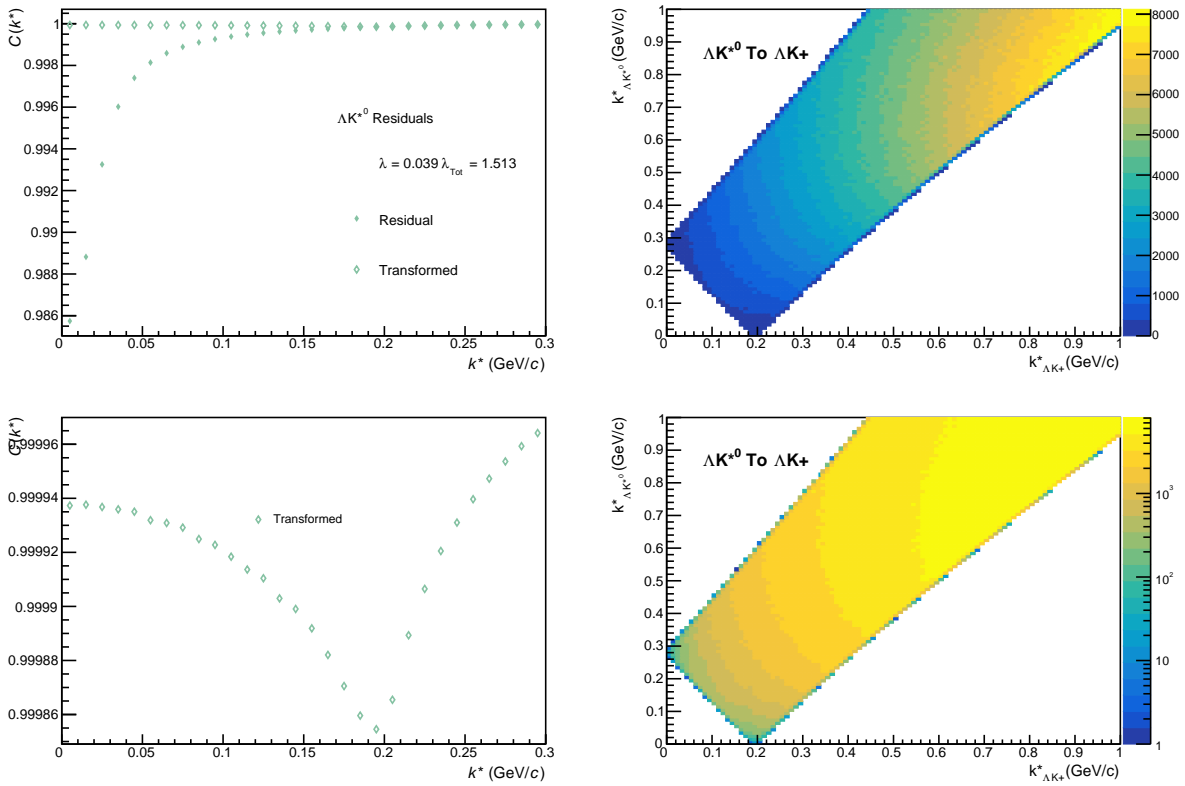
911 **9.1.1  $\Lambda K^+$  Residuals**

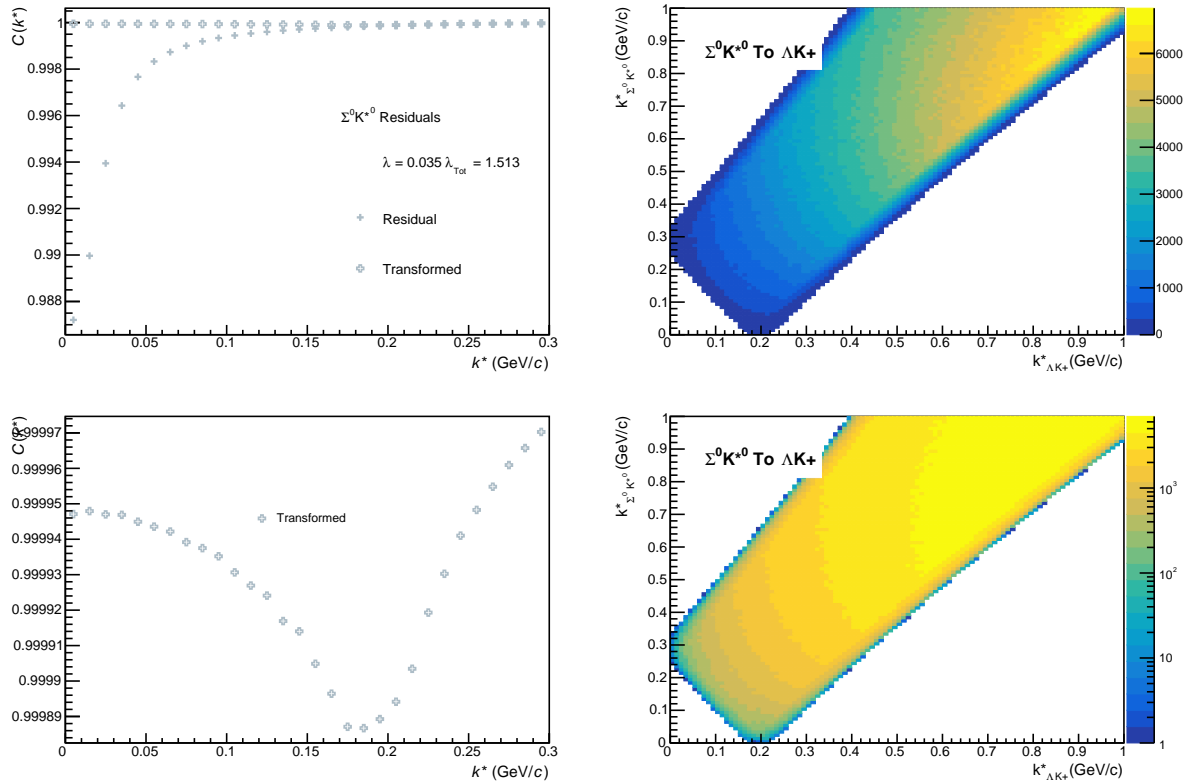


**Fig. 65:** Residuals:  $\Sigma^0 K^+$  to  $\Lambda K^+$  (0-10% Centrality)

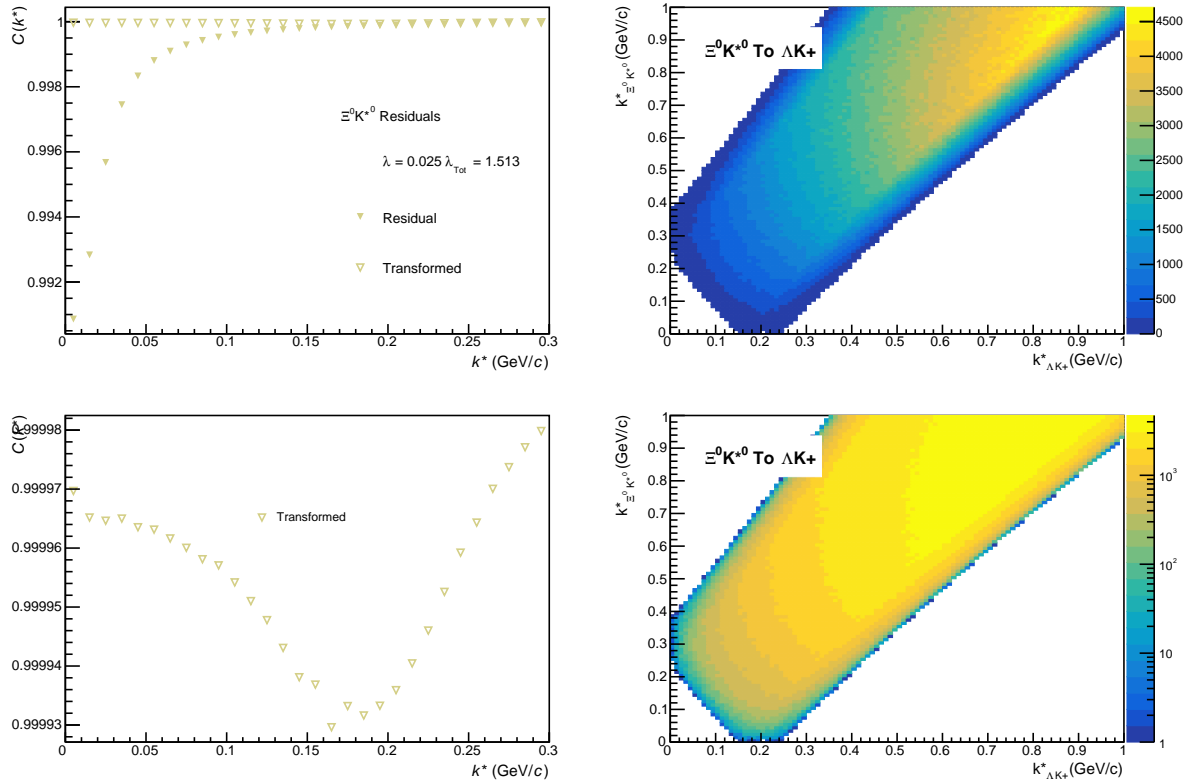

**Fig. 66:** Residuals:  $\Xi^0 K^+$  to  $\Lambda K^+$  (0-10% Centrality)

**Fig. 67:** Residuals:  $\Xi^- K^+$  to  $\Lambda K^+$  (0-10% Centrality)



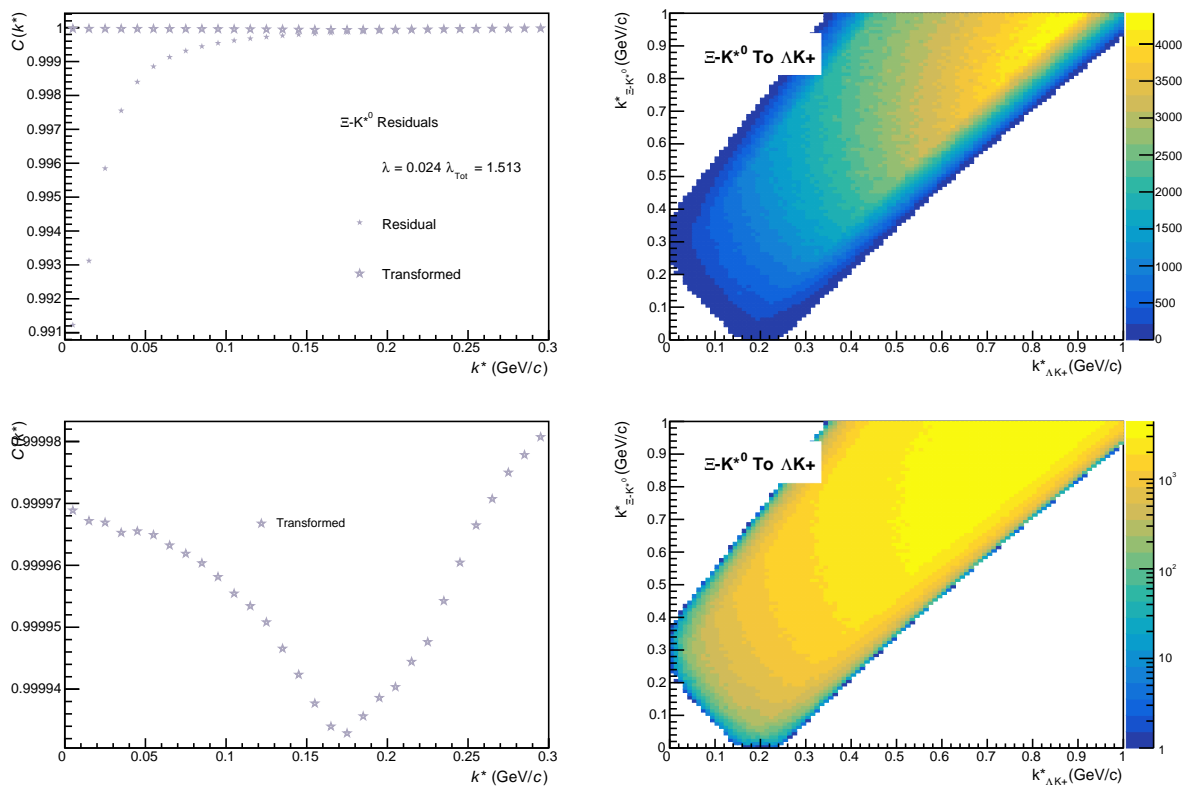

 Fig. 70: Residuals:  $\Sigma^{*0} K^+$  to  $\Lambda K^+$  (0-10% Centrality)

 Fig. 71: Residuals:  $\Lambda K^{*0}$  to  $\Lambda K^+$  (0-10% Centrality)



**Fig. 72:** Residuals:  $\Sigma^0 K^{*0}$  to  $\Lambda K^+$  (0-10% Centrality)

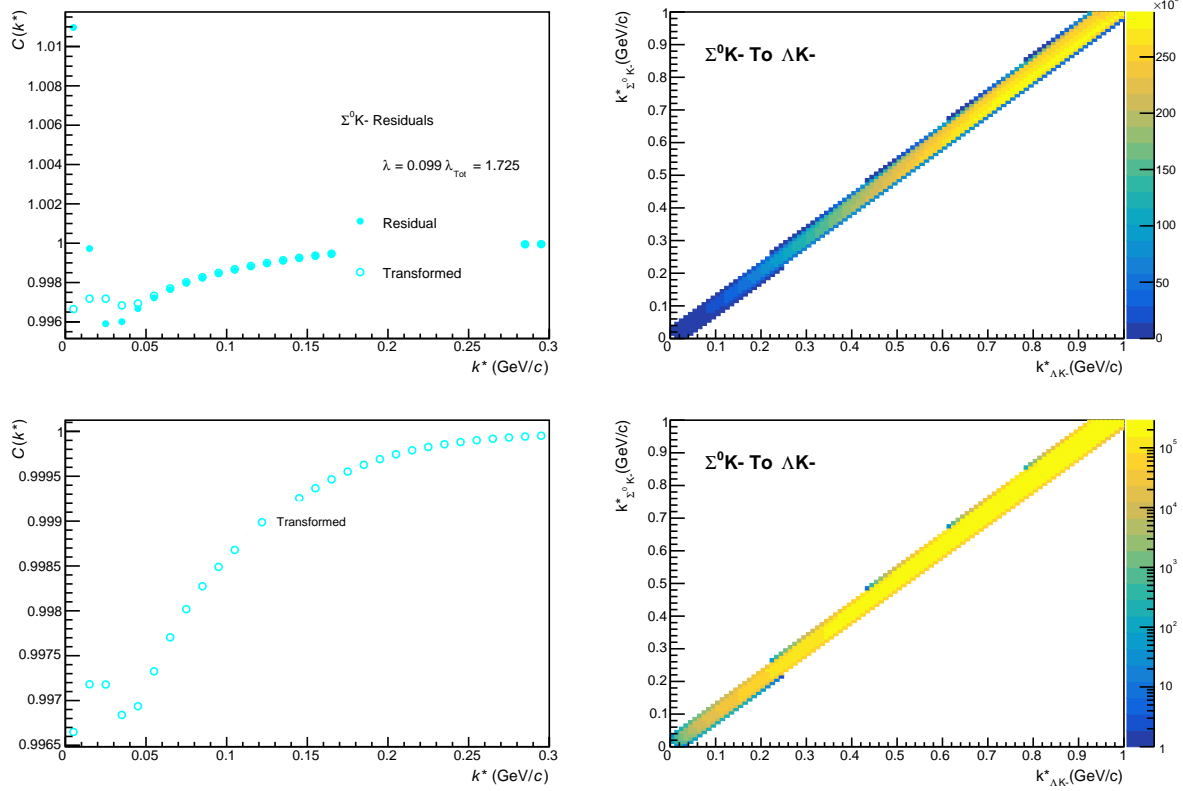


**Fig. 73:** Residuals:  $\Xi^0 K^{*0}$  to  $\Lambda K^+$  (0-10% Centrality)

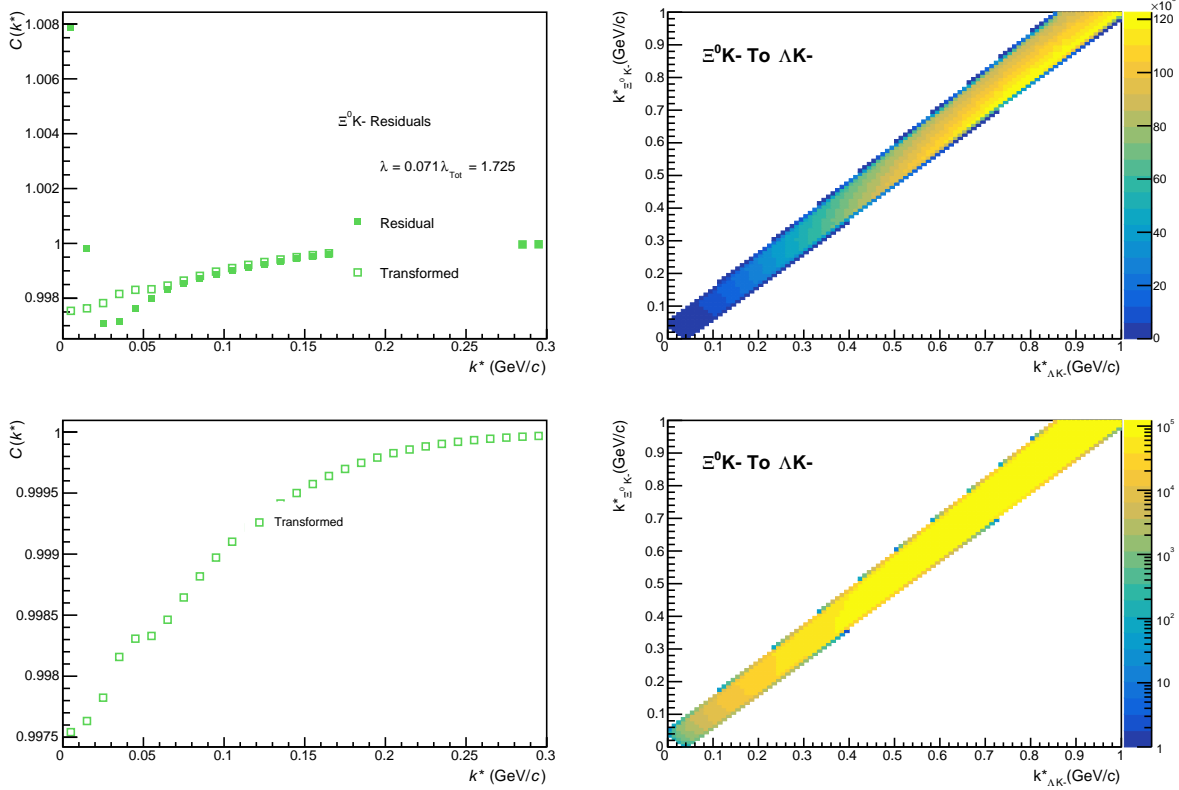


**Fig. 74:** Residuals:  $\Xi\text{-}K^{*0}$  to  $\Lambda K^+$  (0-10% Centrality)

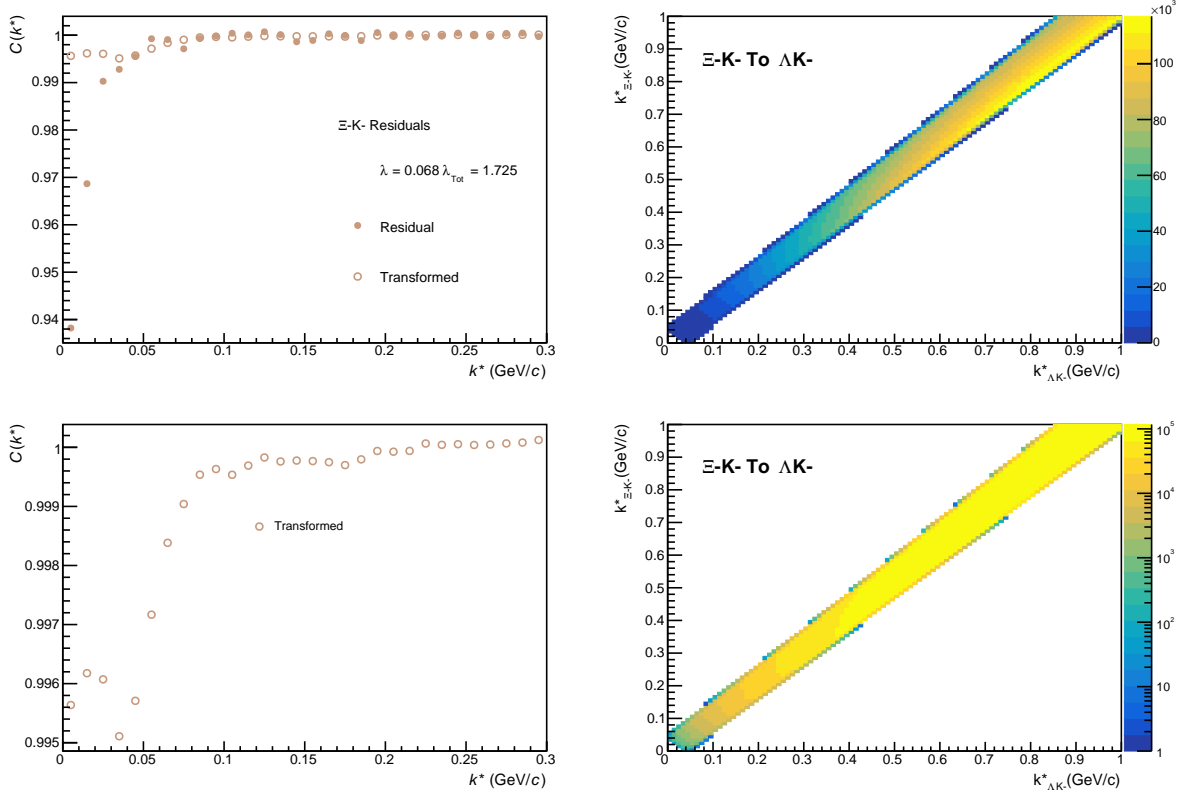
912 **9.1.2  $\Lambda K^-$  Residuals**



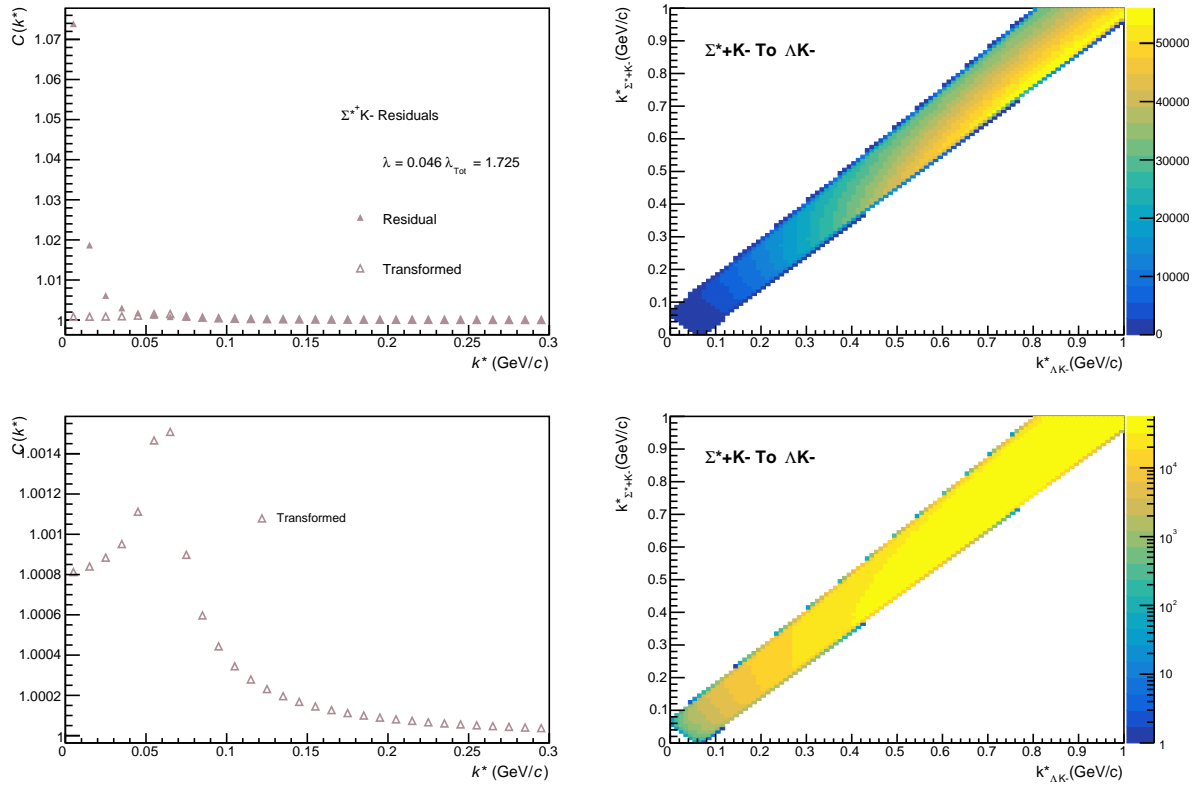
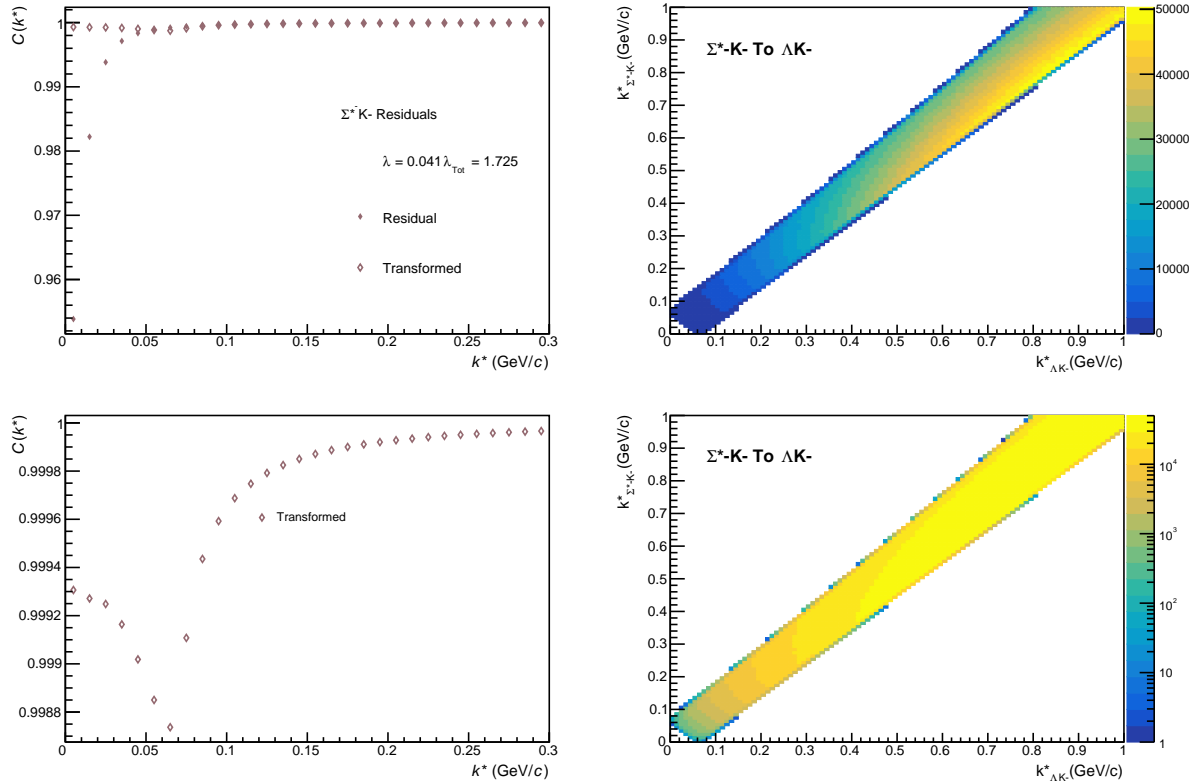
**Fig. 75:** Residuals:  $\Sigma^0 K^-$  to  $\Lambda K^-$  (0-10% Centrality)

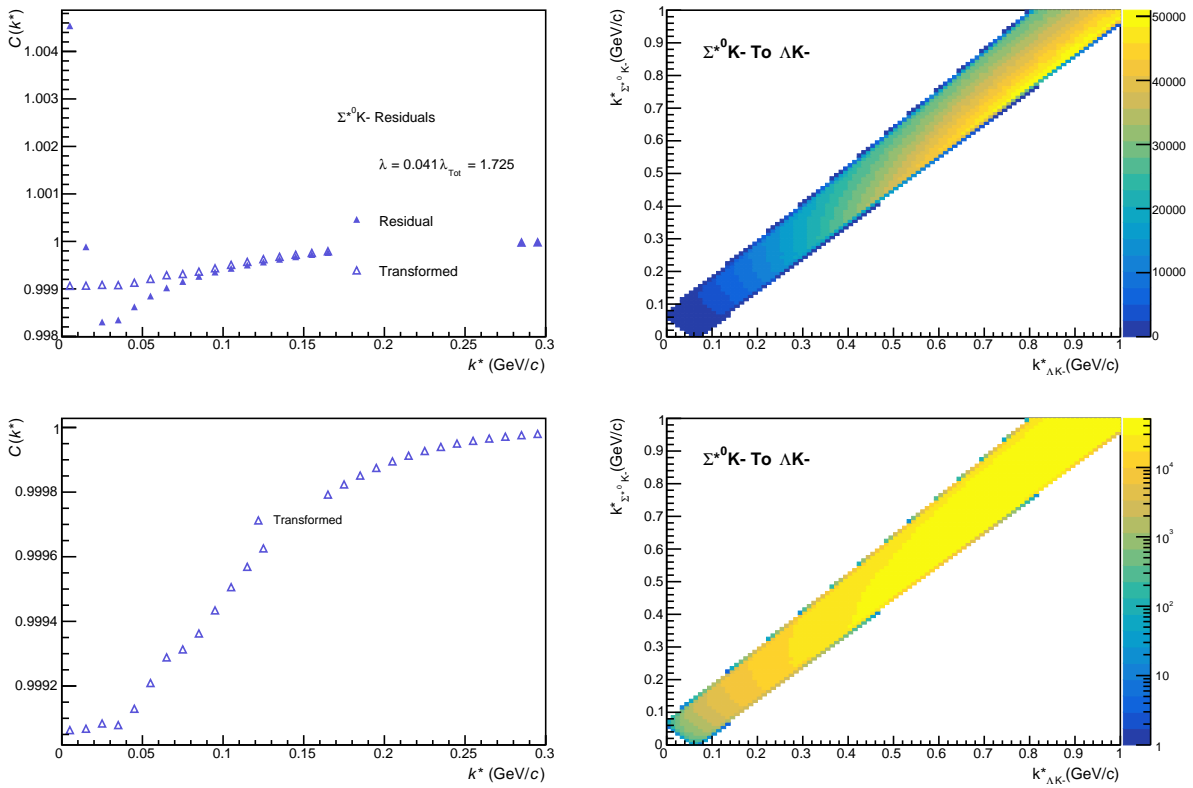
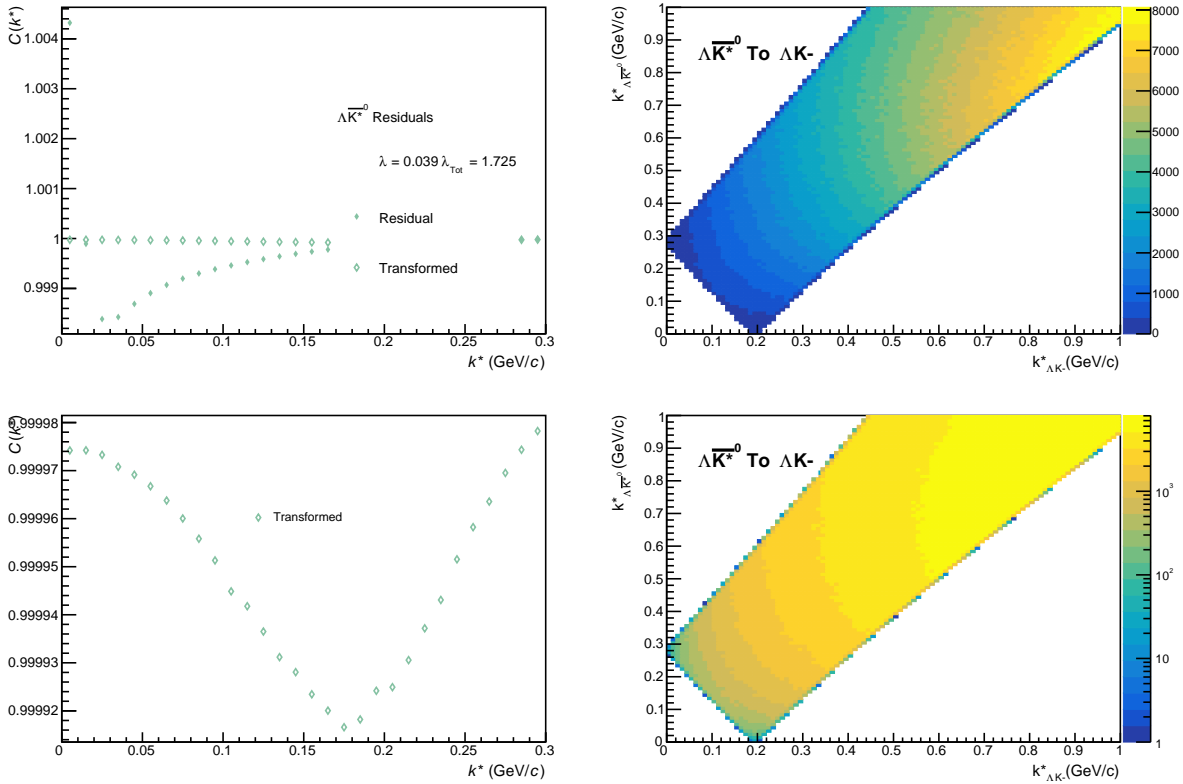


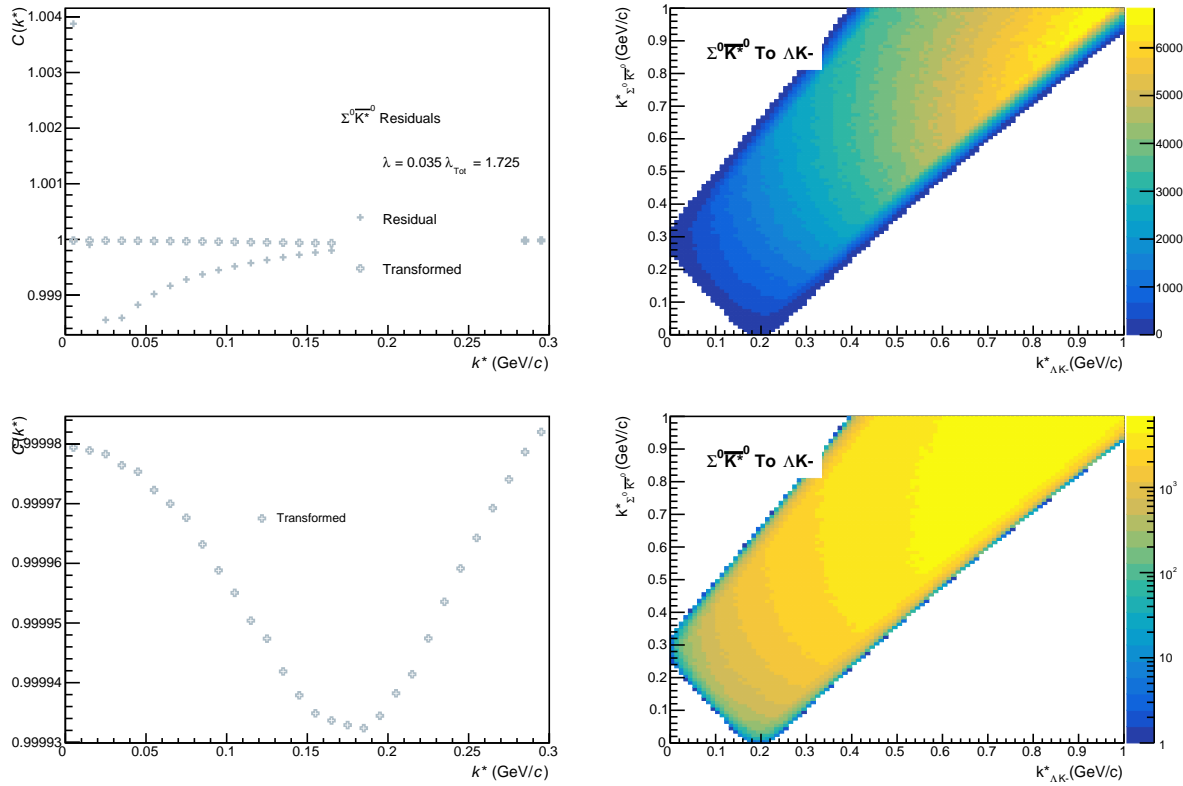
**Fig. 76:** Residuals:  $\Xi^0 \text{K}^-$  to  $\Lambda \text{K}^-$  (0-10% Centrality)



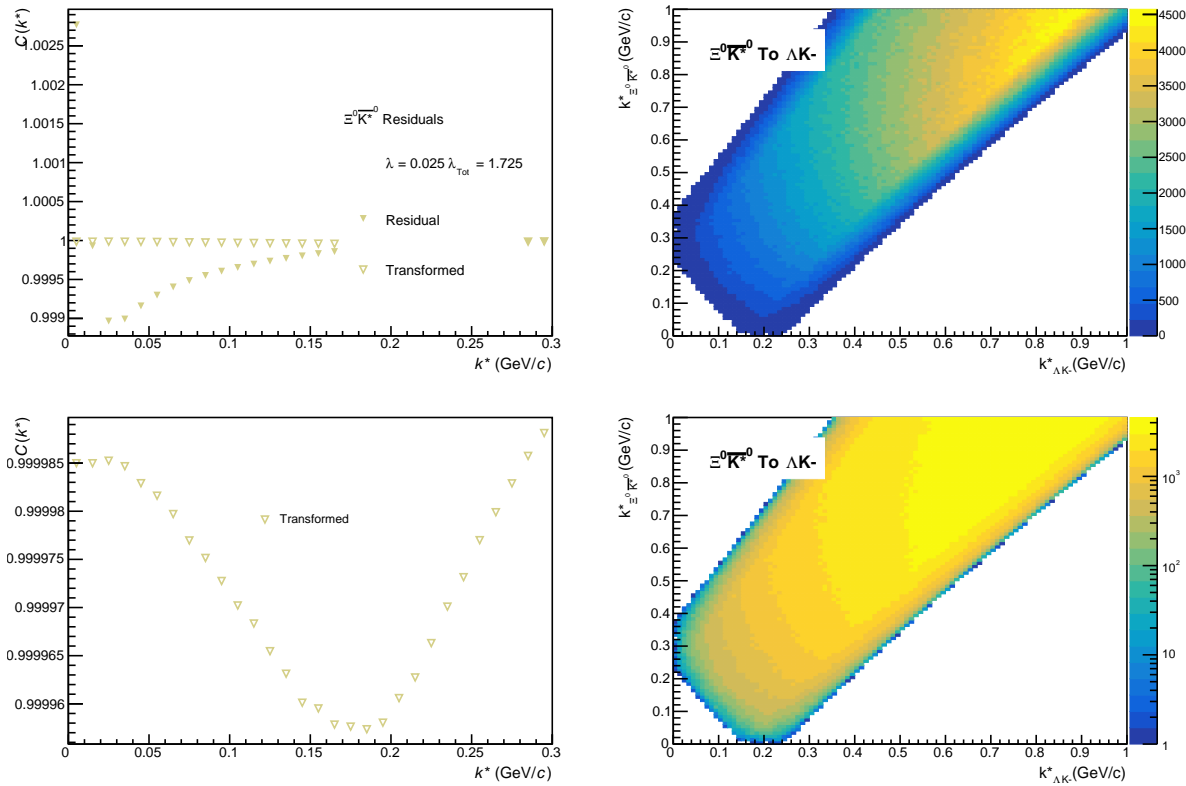
**Fig. 77:** Residuals:  $\Xi^- \text{K}^-$  to  $\Lambda \text{K}^-$  (0-10% Centrality)

Fig. 78: Residuals:  $\Sigma^+K^-$  to  $\Lambda K^-$  (0-10% Centrality)Fig. 79: Residuals:  $\Sigma^-K^-$  to  $\Lambda K^-$  (0-10% Centrality)

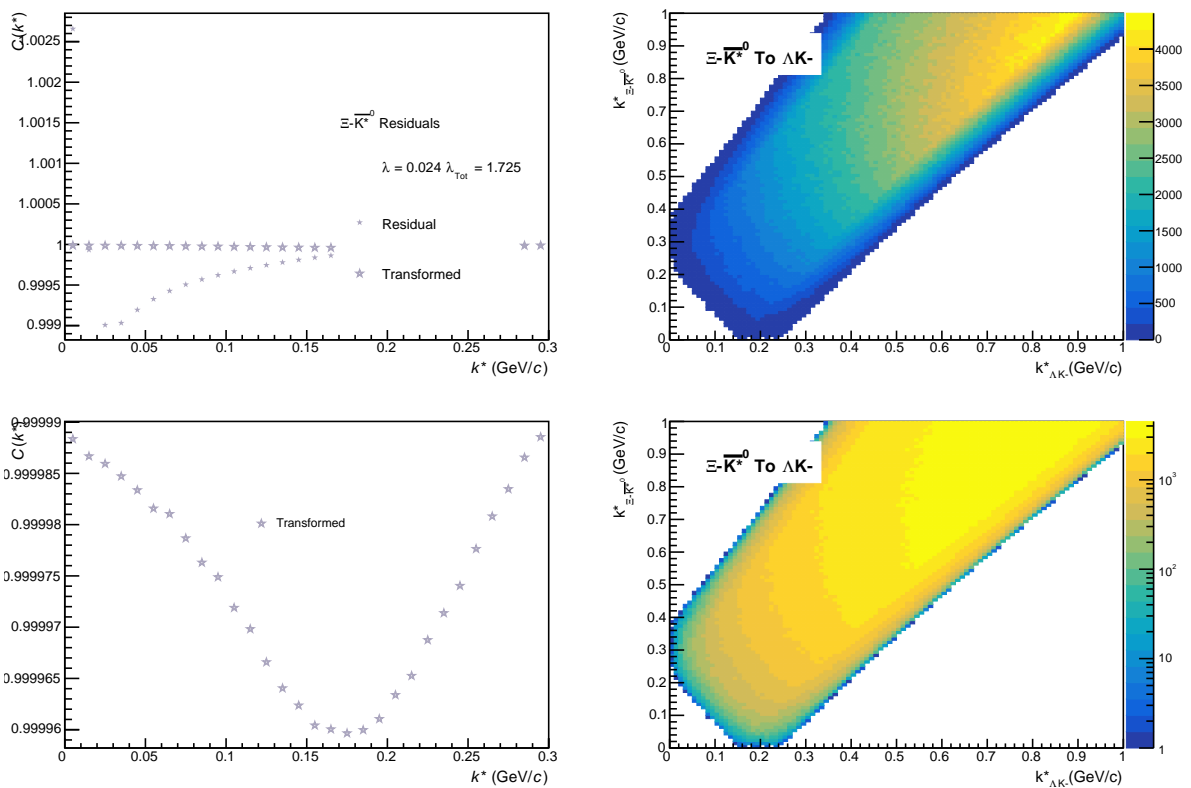

 Fig. 80: Residuals:  $\Sigma^{*0} K^-$  to  $\Lambda K^-$  (0-10% Centrality)

 Fig. 81: Residuals:  $\Lambda \bar{K}^{*0}$  to  $\Lambda K^-$  (0-10% Centrality)



**Fig. 82:** Residuals:  $\Sigma^0 \bar{K}^{*0}$  to  $\Lambda K^-$  (0-10% Centrality)

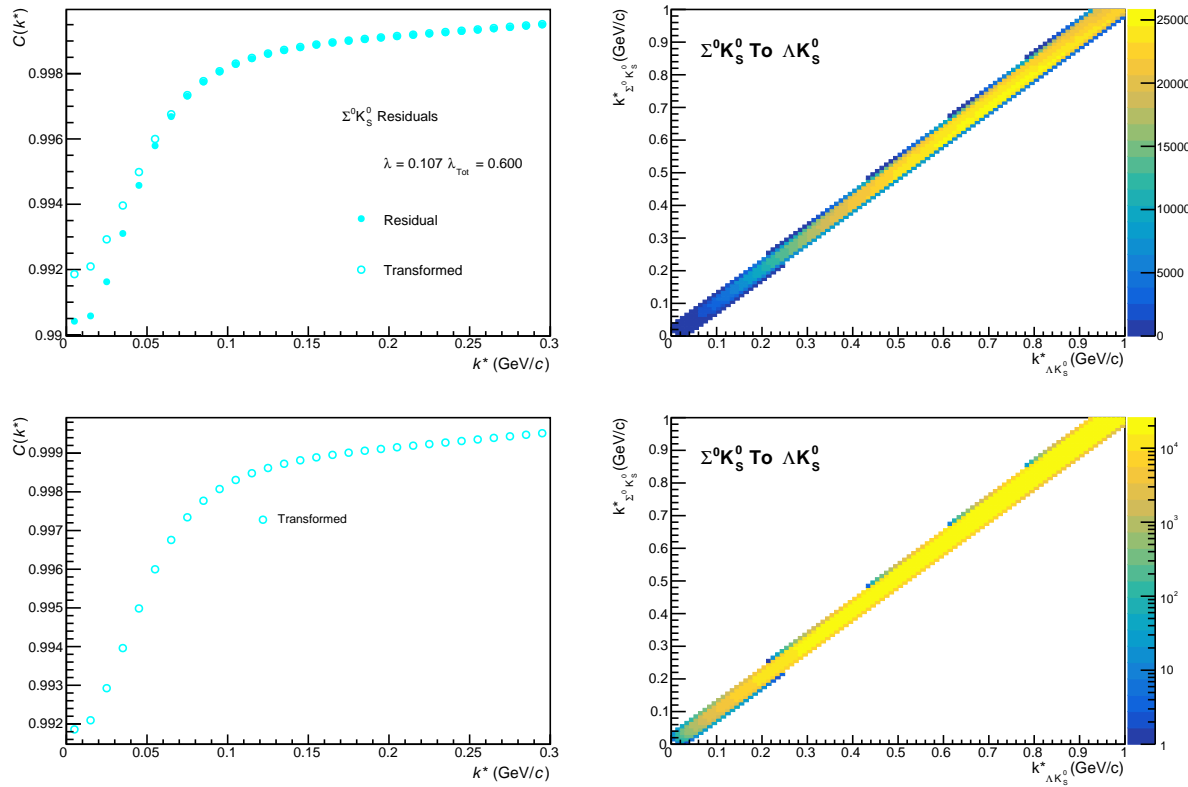


**Fig. 83:** Residuals:  $\Xi^0 \bar{K}^{*0}$  to  $\Lambda K^-$  (0-10% Centrality)

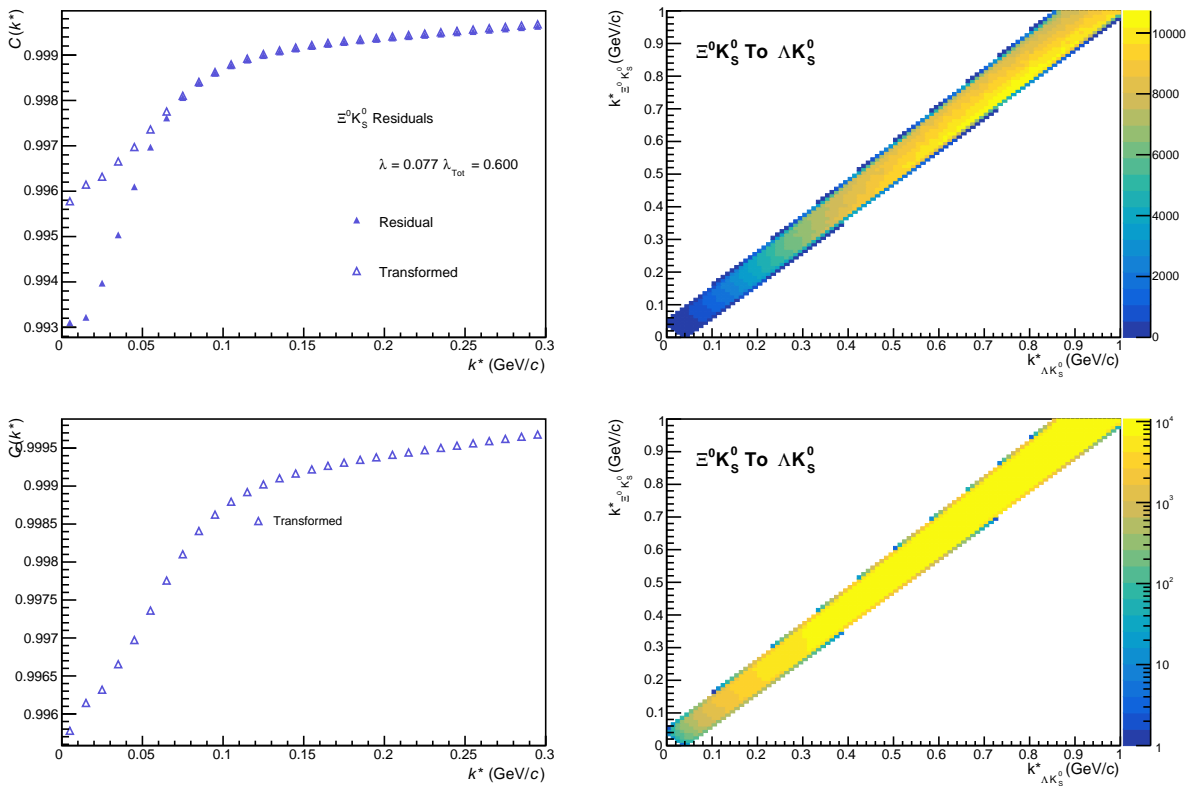
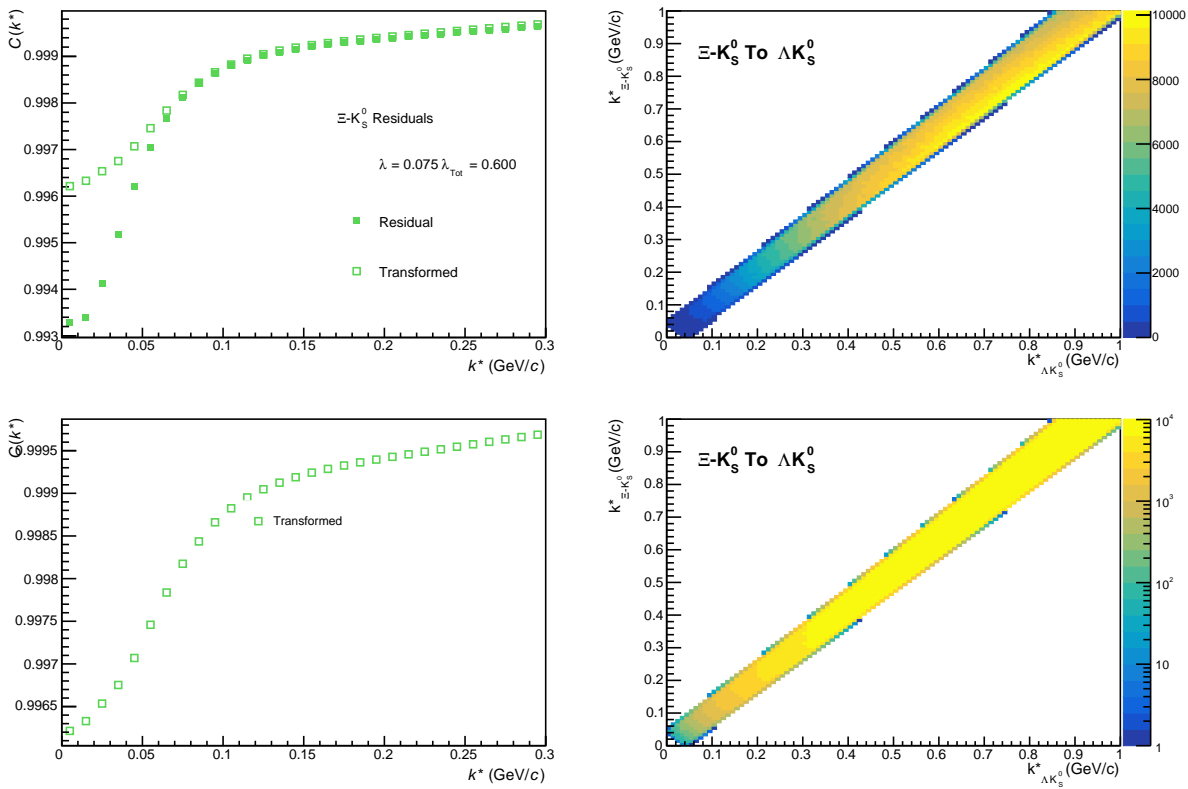


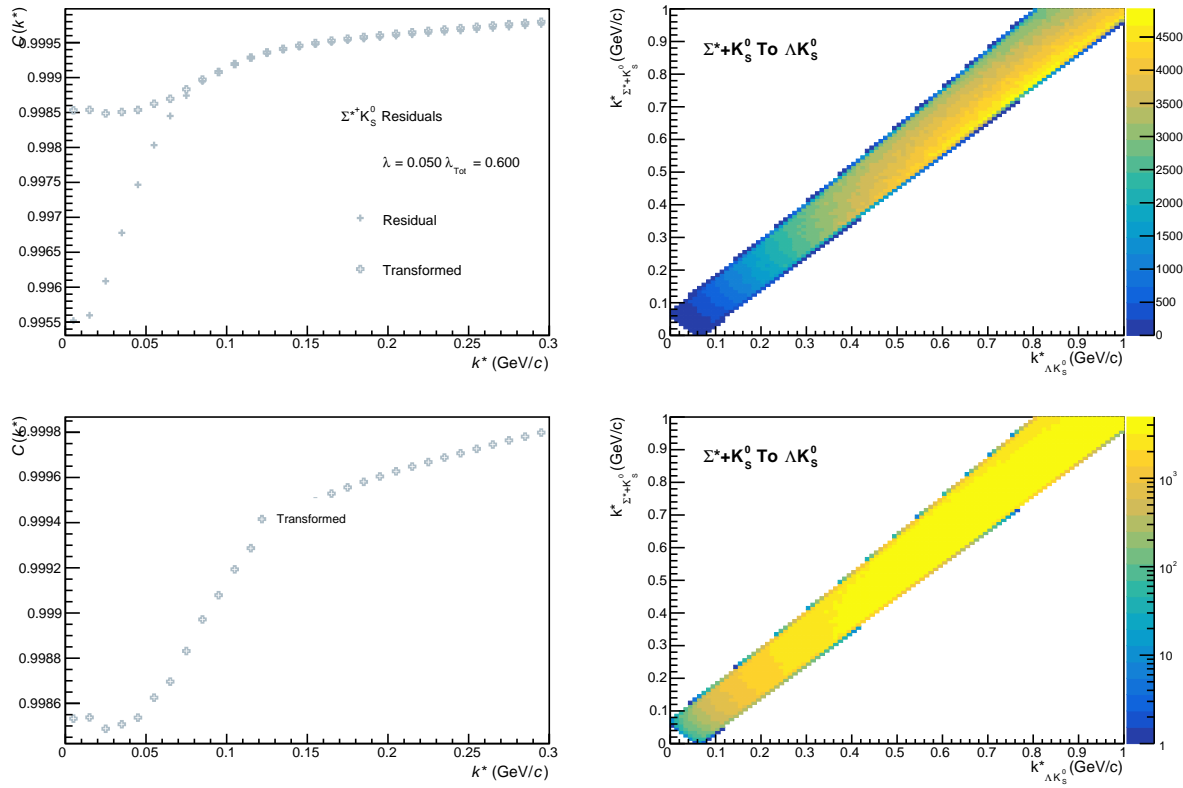
**Fig. 84:** Residuals:  $\Xi\bar{K}^{*0}$  to  $\Lambda K^-$  (0-10% Centrality)

913 **9.1.3  $\Lambda K_S^0$  Residuals**

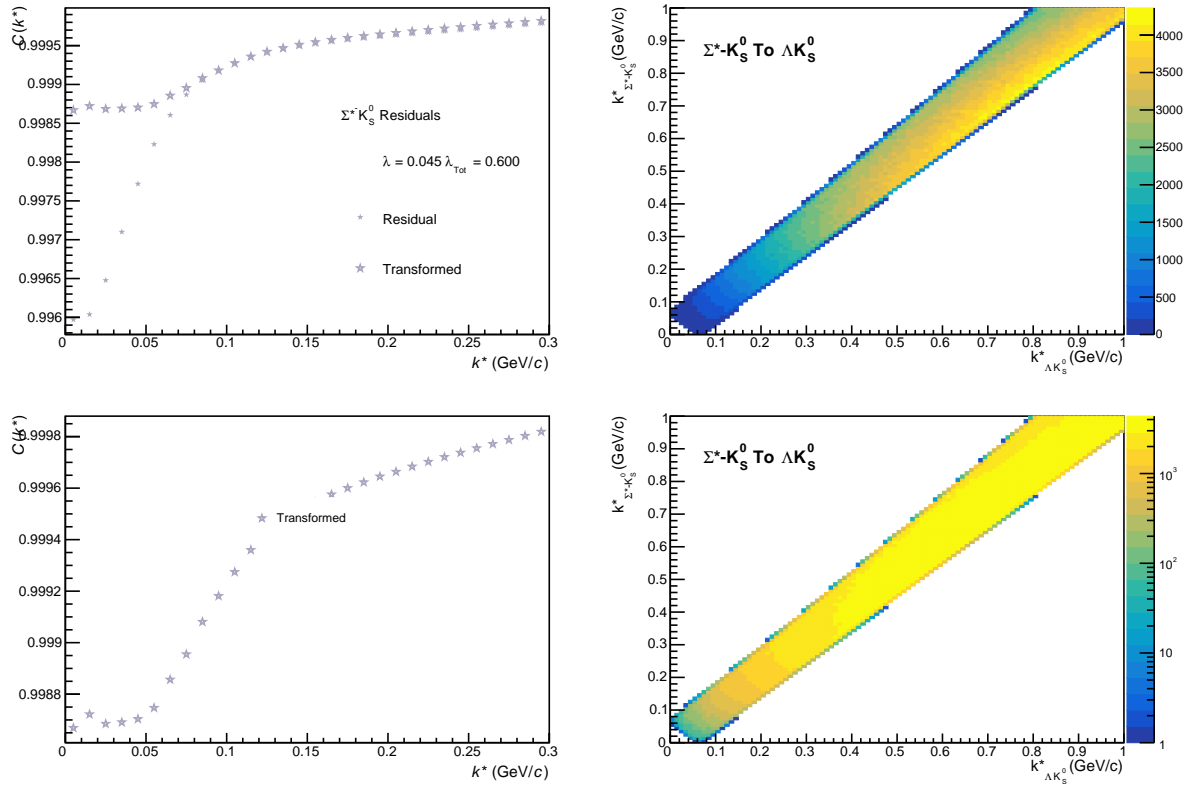


**Fig. 85:** Residuals:  $\Sigma^0 K_S^0$  to  $\Lambda K_S^0$  (0-10% Centrality)

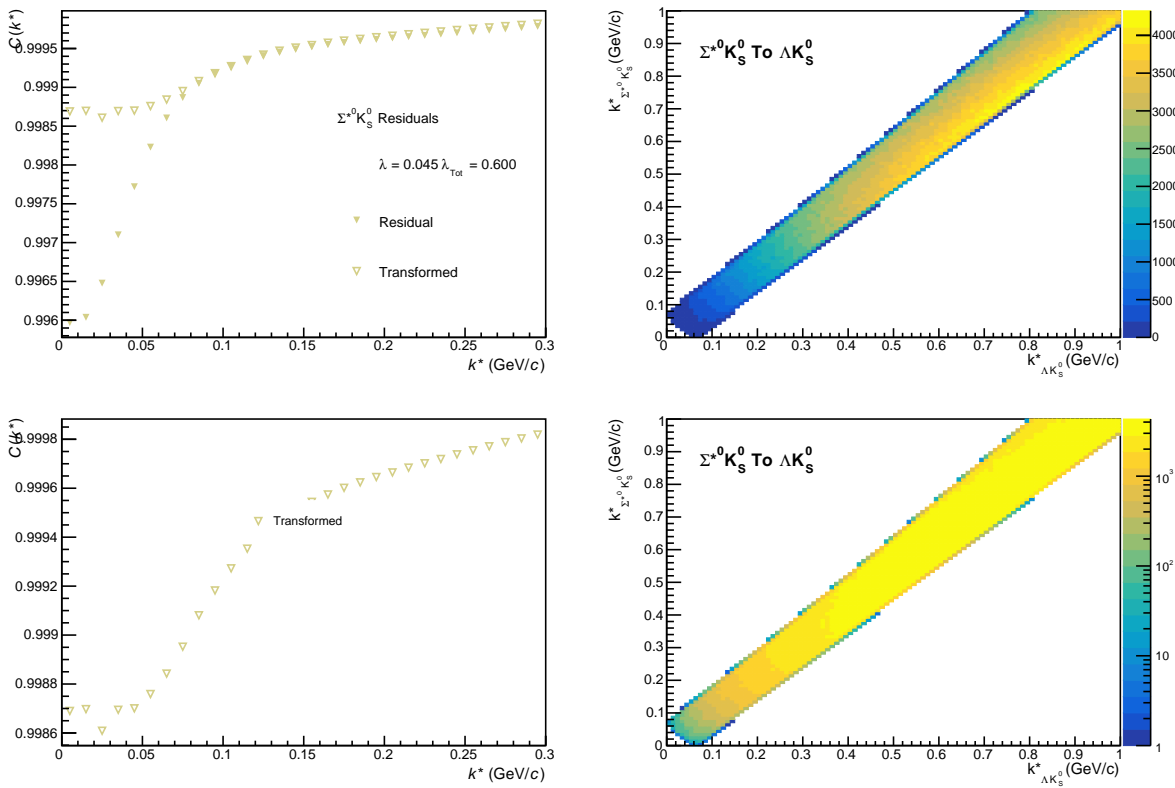
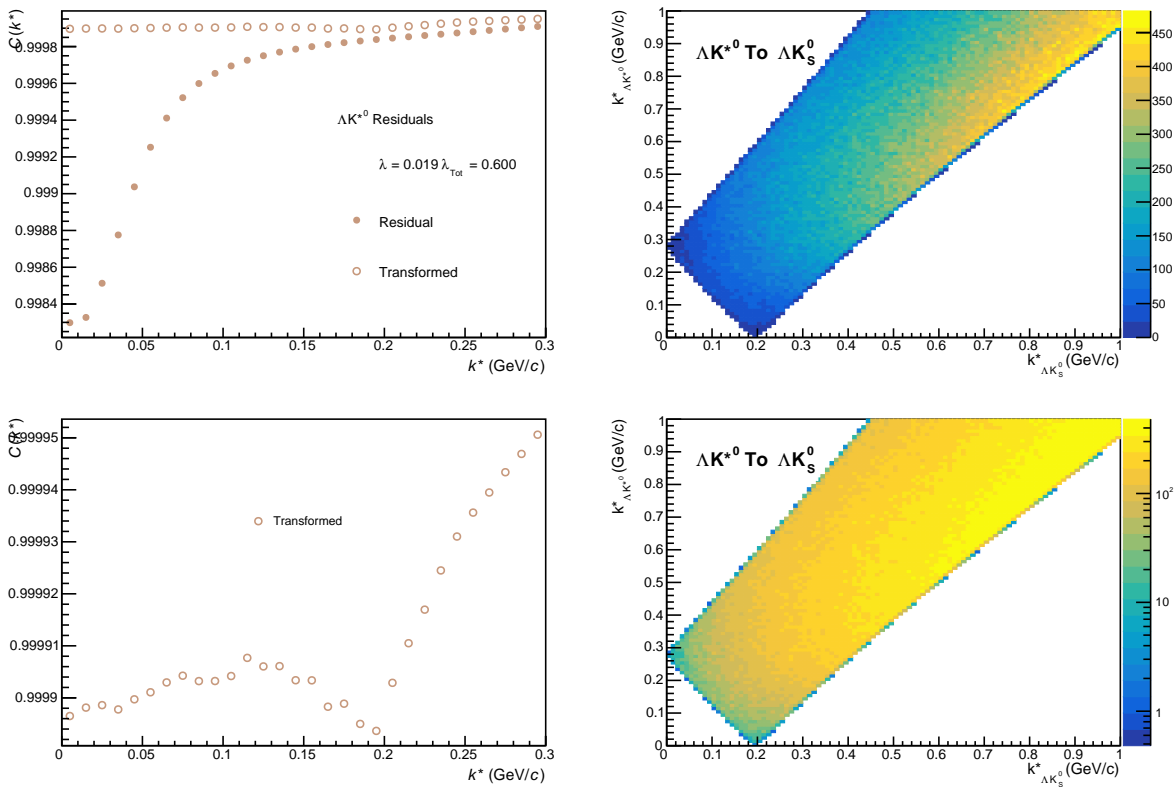

 Fig. 86: Residuals:  $\Xi^0 K_S^0$  to  $\Lambda K_S^0$  (0-10% Centrality)

 Fig. 87: Residuals:  $\Xi^- K_S^0$  to  $\Lambda K_S^0$  (0-10% Centrality)

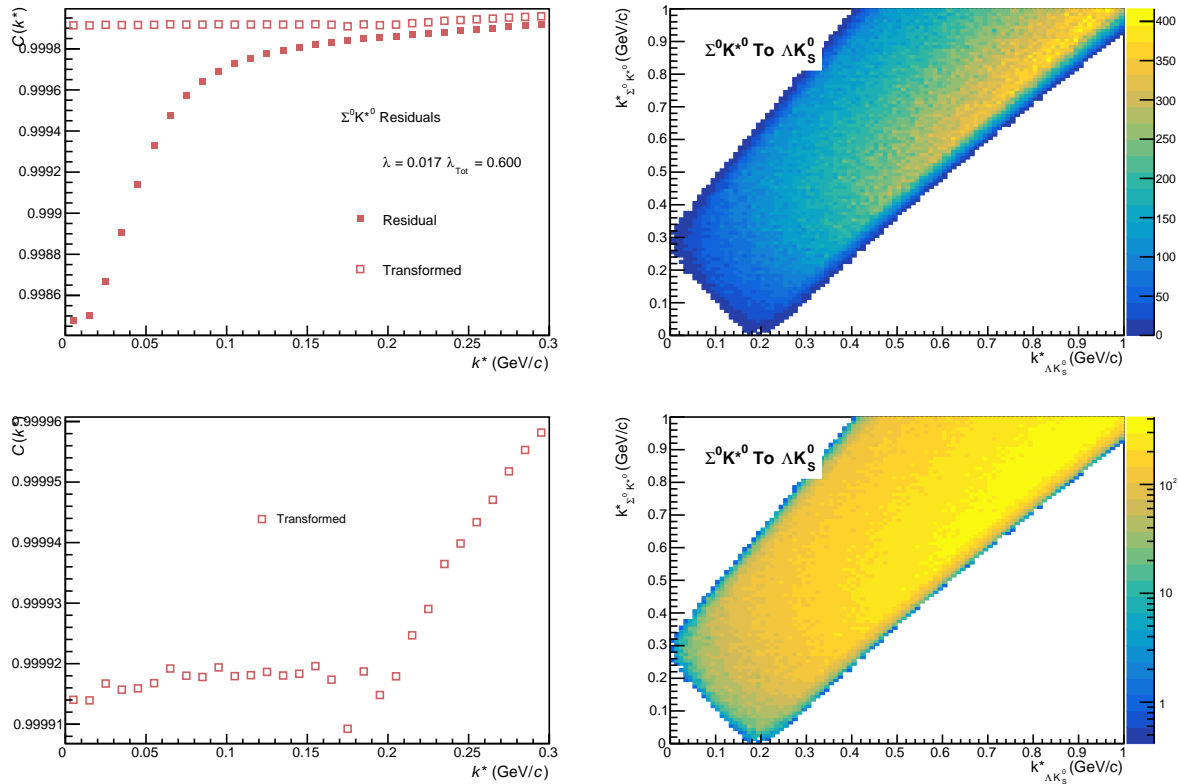


**Fig. 88:** Residuals:  $\Sigma^*+K_S^0$  to  $\Lambda K_S^0$  (0-10% Centrality)

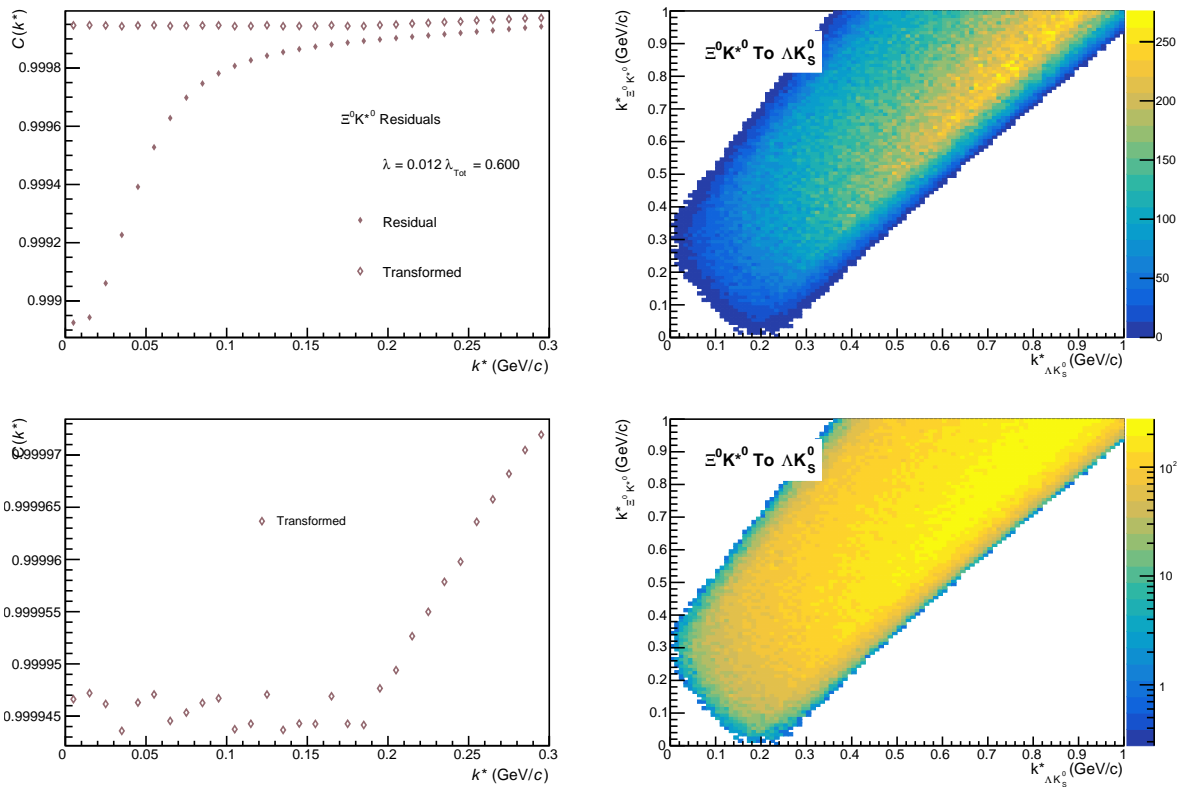


**Fig. 89:** Residuals:  $\Sigma^*+K_S^0$  to  $\Lambda K_S^0$  (0-10% Centrality)

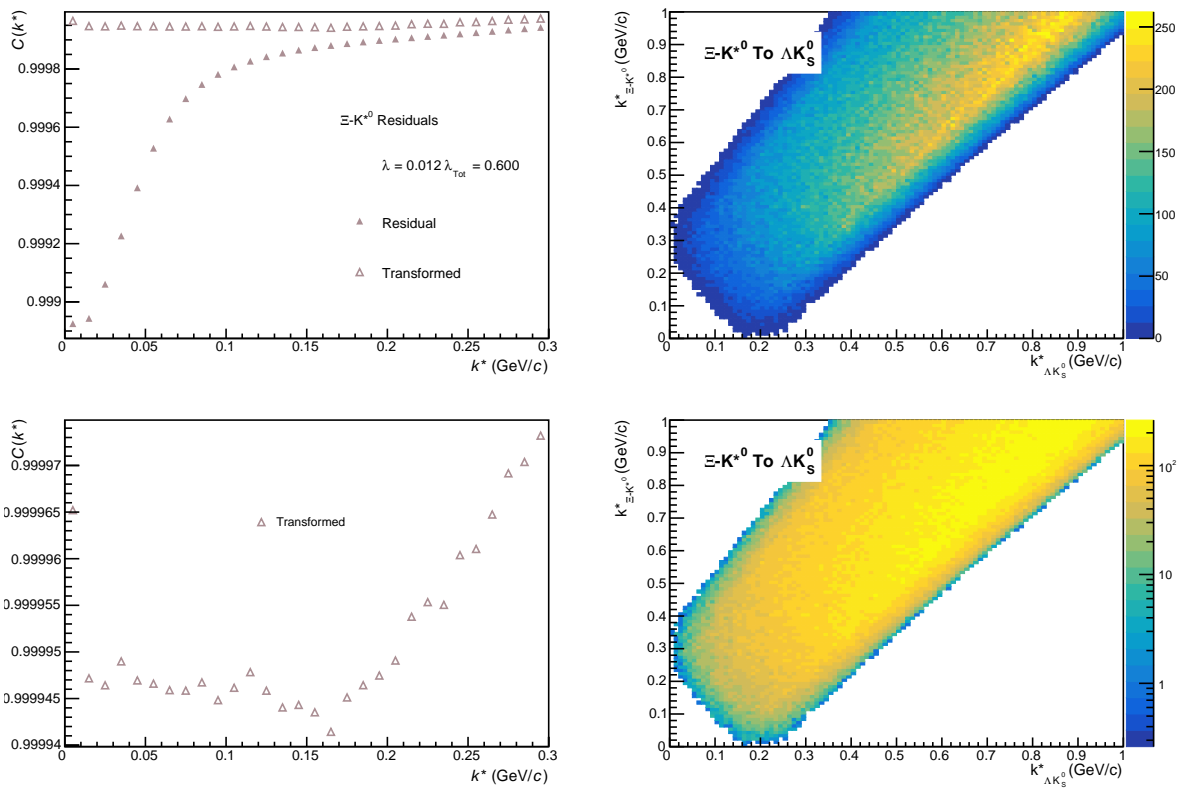

**Fig. 90:** Residuals:  $\Sigma^{*0} K_S^0$  to  $\Lambda K_S^0$  (0-10% Centrality)

**Fig. 91:** Residuals:  $\Lambda K^{*0}$  to  $\Lambda K_S^0$  (0-10% Centrality)



**Fig. 92:** Residuals:  $\Sigma^0 K^{*0}$  to  $\Lambda K_S^0$  (0-10% Centrality)



**Fig. 93:** Residuals:  $\Xi^0 K^{*0}$  to  $\Lambda K_S^0$  (0-10% Centrality)



**Fig. 94:** Residuals:  $\Xi\text{-}K^{*0}$  to  $\Lambda\text{K}_S^0$  (0-10% Centrality)

## 914 9.2 Spherical Harmonics

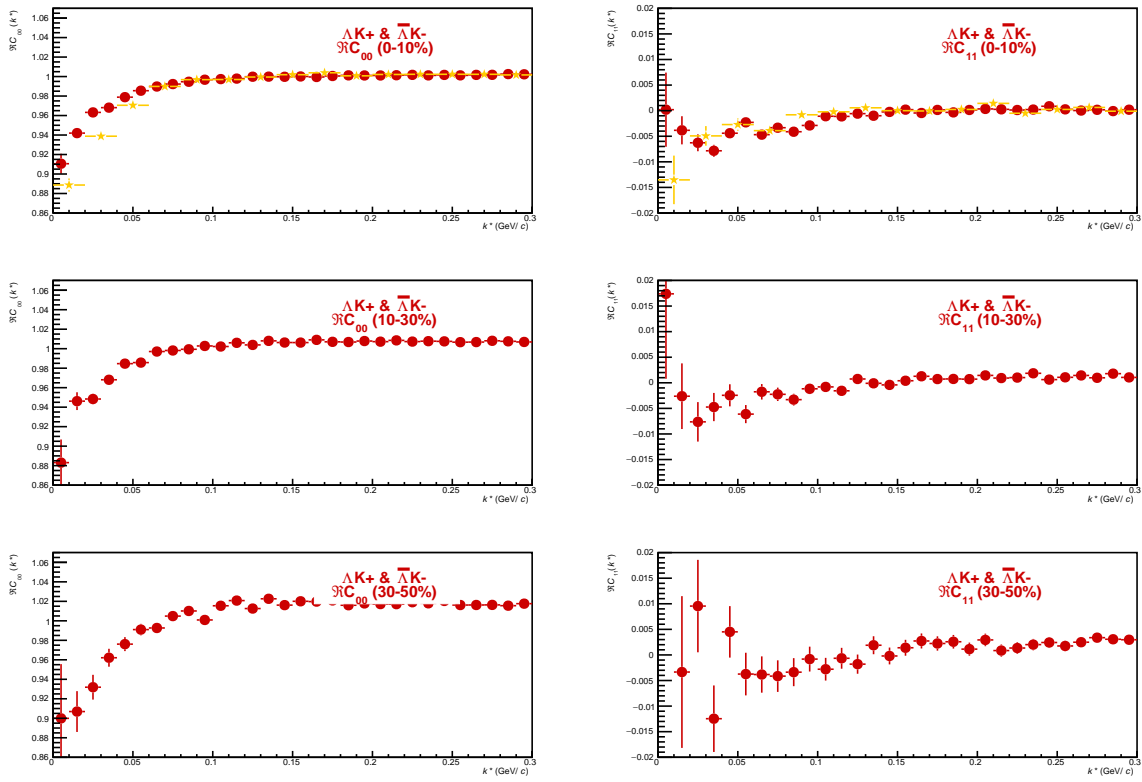


**Fig. 95:**  $C_{00}$  (left) and  $\Re C_{11}$  (right) components of a spherical harmonic decomposition of the  $\Lambda K^+$  correlation function for the 0-10% (top), 10-30% (middle), and 30-50% (bottom) centrality bins

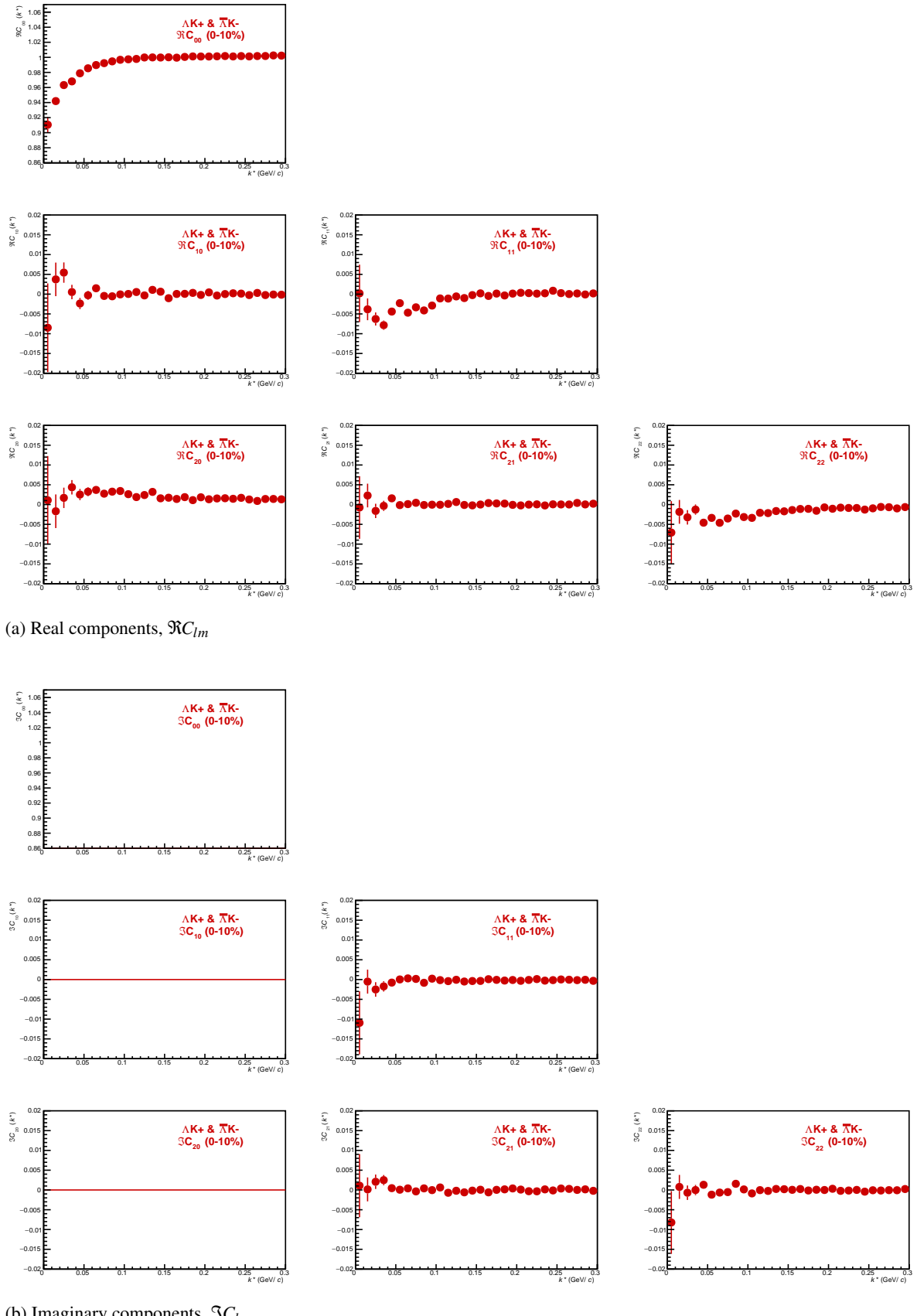


**Fig. 96:** First six components ( $C_{00}, C_{10}, C_{11}, C_{20}, C_{21}, C_{22}$ ) of the spherical harmonic decomposition of the  $\Lambda K^+$  correlation function for the 0-10% centrality bin. Note,  $\Im C_{00}$ ,  $\Im C_{10}$ , and  $\Im C_{20}$  are zero by definition.

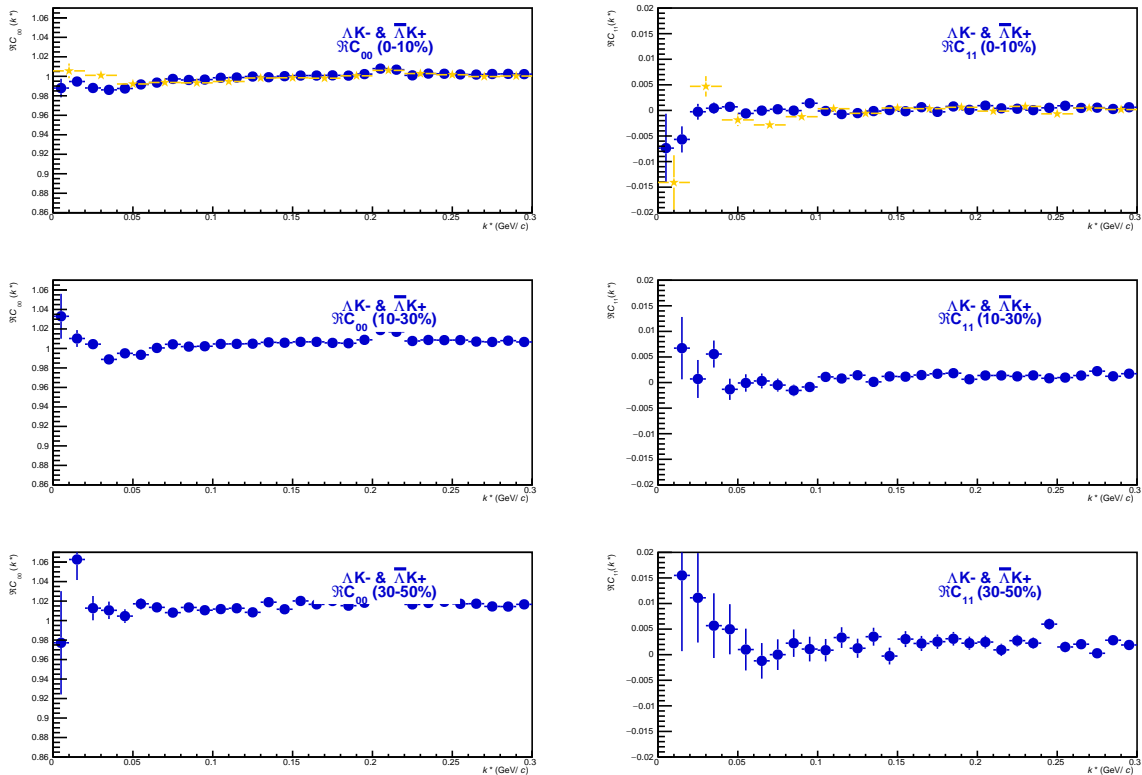


**Fig. 97:**  $C_{00}$  (left) and  $\Re C_{11}$  (right) components of a spherical harmonic decomposition of the  $\Lambda K^-$  correlation function for the 0-10% (top), 10-30% (middle), and 30-50% (bottom) centrality bins

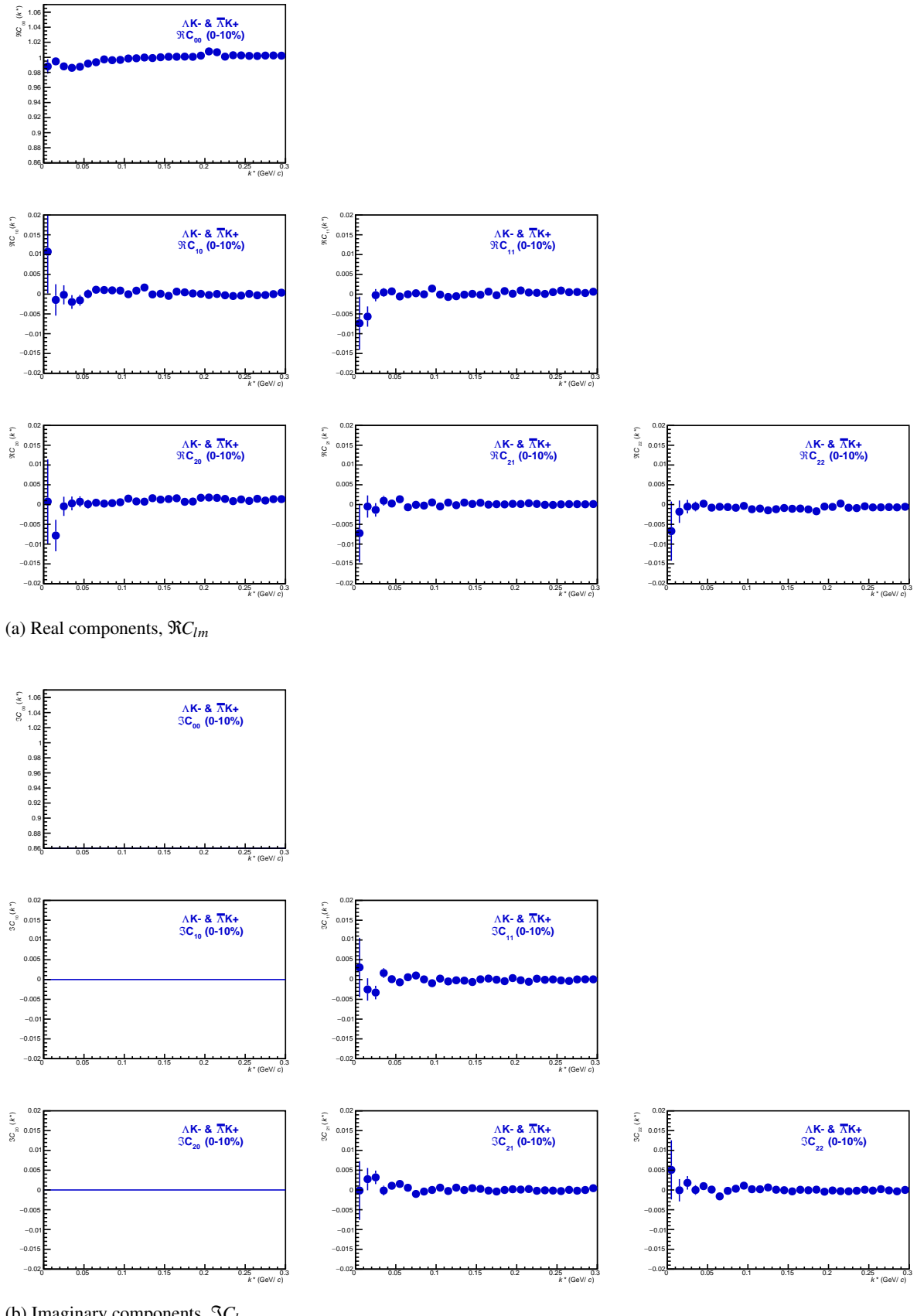


**Fig. 98:** First six components ( $C_{00}, C_{10}, C_{11}, C_{20}, C_{21}, C_{22}$ ) of the spherical harmonic decomposition of the  $\Lambda K^-$  correlation function for the 0-10% centrality bin. Note,  $\Im C_{00}$ ,  $\Im C_{10}$ , and  $\Im C_{20}$  are zero by definition.

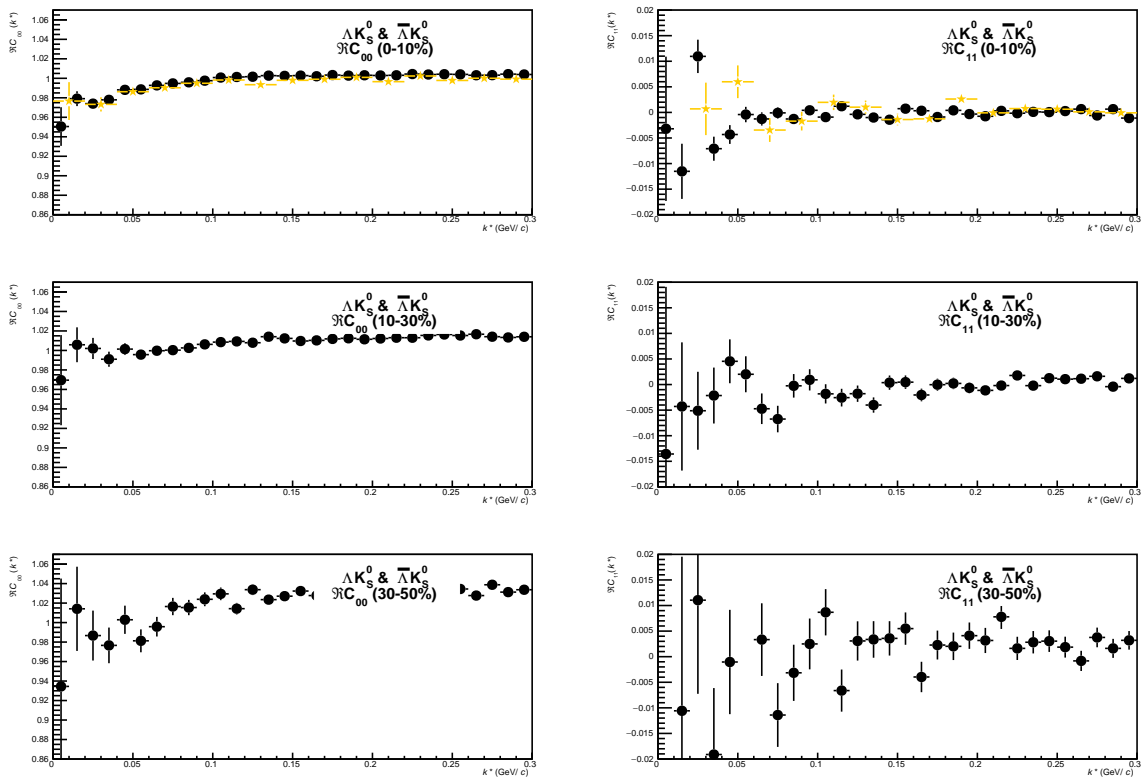


**Fig. 99:**  $C_{00}$  (left) and  $\Re C_{11}$  (right) components of a spherical harmonic decomposition of the  $\Lambda K_S^0$  correlation function for the 0-10% (top), 10-30% (middle), and 30-50% (bottom) centrality bins

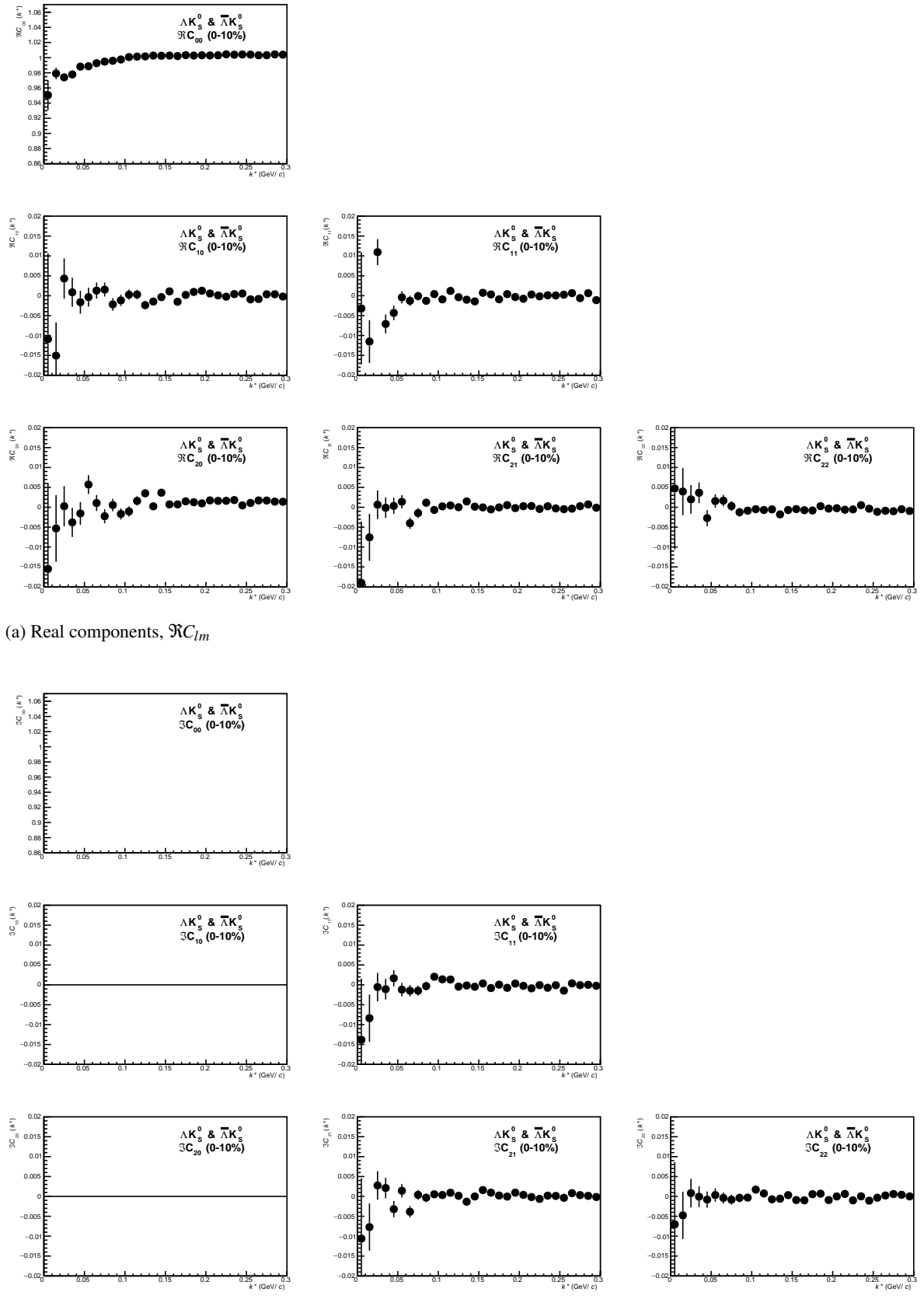


**Fig. 100:** First six components ( $C_{00}, C_{10}, C_{11}, C_{20}, C_{21}, C_{22}$ ) of the spherical harmonic decomposition of the  $\Lambda K_S^0$  correlation function for the 0-10% centrality bin. Note,  $\Im C_{00}$ ,  $\Im C_{10}$ , and  $\Im C_{20}$  are zero by definition.

## References

- [1] R. Lednicky and V. L. Lyuboshitz. *Sov. J. Nucl. Phys.*, 35:770, 1982.
- [2] Michael Annan Lisa, Scott Pratt, Ron Soltz, and Urs Wiedemann. Femtoscopy in relativistic heavy ion collisions. *Ann. Rev. Nucl. Part. Sci.*, 55:357–402, 2005.
- [3] S. E. Koonin. Proton Pictures of High-Energy Nuclear Collisions. *Phys. Lett.*, B70:43–47, 1977.
- [4] S. Pratt, T. Csorgo, and J. Zimanyi. Detailed predictions for two pion correlations in ultrarelativistic heavy ion collisions. *Phys. Rev.*, C42:2646–2652, 1990.
- [5] Richard Lednicky. Finite-size effects on two-particle production in continuous and discrete spectrum. *Phys. Part. Nucl.*, 40:307–352, 2009.
- [6] Adam Kisiel, Hanna Zbroszczyk, and Maciej Szymaski. Extracting baryon-antibaryon strong interaction potentials from  $p\bar{\Lambda}$  femtoscopic correlation functions. *Phys. Rev.*, C89(5):054916, 2014.
- [7] Jai Salzwedel and Thomas Humanic. Lambda femtoscopy in  $\sqrt{s_{NN}} = 2.76$  TeV Pb-Pb collisions at ALICE, Jan 2017. Presented 15 Dec 2016.
- [8] A Kisiel. Non-identical particle correlation analysis in the presence of non-femtoscopic correlations. *Acta Physica Polonica B*, 48:717, 04 2017.
- [9] Jaroslav Adam et al. One-dimensional pion, kaon, and proton femtoscopy in Pb-Pb collisions at  $\sqrt{s_{NN}} = 2.76$  TeV. *Phys. Rev.*, C92(5):054908, 2015.
- [10] Yan-Rui Liu and Shi-Lin Zhu. Meson-baryon scattering lengths in HB chi PT. *Phys. Rev.*, D75:034003, 2007.
- [11] Maxim Mai, Peter C. Bruns, Bastian Kubis, and Ulf-G. Meissner. Aspects of meson-baryon scattering in three and two-flavor chiral perturbation theory. *Phys. Rev.*, D80:094006, 2009.